Iron-based superconductors in high magnetic fields



Matt Bristow

Christ Church College

University of Oxford

A thesis submitted for the degree of

Doctor of Philosophy

2020

"It's the job that's never started as takes longest to finish."
J. R. R. Tolkien

"You know nothing, poor graduate student."
Someone, probably

"Why is it that when one man [physics] *builds a wall, the next man* [us]
immediately needs to know what's on the other side?"
G. R. R. Martin [and me]

Acknowledgements

Completing a doctorate of any form is never the sole endeavour of a single person. The work that will be presented here would not have been possible without the support, professional and otherwise, of a number of people.

The experimental work presented here has been aided by a variety of people in different facilities. First, I must thank all of the staff at the Clarendon Laboratory as part of the Oxford Physics Department. A special thanks go out to the cryomagnetic team, Rob Storey and Kieran McCall, who seem to be able to get any system up and running, and conjure liquid helium from nowhere for a PhD student in need. Much of the essential research presented here was performed at high-magnetic field facilities. For their aid setting up and during experiments I would like to thank William Knafo at the pulsed-field facility at LNCMI Toulouse and David Graf at NHMFL Tallahassee. The bulk of the high-field work was performed at HFML in Nijmegen with Alix McCollam, who deserves a special thanks for her experimental expertise, tolerating my (many) mistakes with a positive attitude and helping me keep what little is left of my sanity on long night shifts. None of the measurements done would have been possible without first having the materials and samples to measure. For providing me with samples of $CaKFe_4As_4$ I thank William Meier and Paul Canfield at Ames Laboratory. Samples of various sulphur substitutions of $FeSe_{1-x}S_x$ have been grown by a number of people. For this I would like to thank Amir Haghighirad, Thomas Wolf and Shiv Singh. I would also like to extend a personal thanks to a post-doc I have had the pleasure of working with, Pascal Reiss, with whom I have spent many hours problem solving (*"Why is the nitrogen always gone?"*) and hypothesising wild theories about iron selenide.

None of this would have been possible without the keen guidance of my two supervisors, Dr Amalia Coldea and Professor Stephen Blundell. I would like to thank Steve for always being there to give advice, point my research in the right direction as well as for showing me the best jazz bars (and pizza) in Boston.

Amalia has taught me most of my knowledge of experimental condensed matter physics, without which the data in this thesis would like have been highly questionable. Dr Coldea also deserves thanks for sitting through the long magnet shifts, frequently on only a few hours of sleep, in Nijmegen, always being able to provide a plethora of literature and being there during the tough times. I would like to thank members of the Coldea and Blundell groups.

The various PhD students, post-doc's and staff in the Clarendon have played a vital role in my time at Oxford, some of whom I have even had the privilege of working alongside. Some of those have provided me with fond memories, such as dramatic readings of 'The Lad and the Gad', and solid advice when it was needed (*"well, sometimes science is hard"*). They were always there to answer my calls, exasperated or otherwise, of 'tea time!?' or 'pub!?'. On that note, it is probably necessary for me to acknowledge the public houses we used to frequent across Oxford, from the Rickety Press to the Cape of Good Hope.

Finally, I would like to express my gratitude to my friends and family who have supported me throughout the last three and a half years, and are definitely fed up of hearing me talk about physics by now (*"what is it you are working on again, biology or semiconductors?"*). Cheers guys.

Declaration

Scientific work is often collaborative. This section will cover work presented in this thesis that has been done, or contributed to, by other people.

Single crystals of $FeSe_{1-x}S_x$ have been grown by Amir Haghighirad and Shiv Singh in Oxford. Single crystals of $CaKFe_4As_4$ were produced in Ames laboratory by William Meier and supplied by Paul Canfield. A powder sample of $CaKFe_4As_4$ used in magnetisation studies was provided by A. Iyo from the National Institute of Advanced Industrial Science and Technology (AIST) in Japan.

Experiments were performed in collaboration with a number of other people in the Oxford Physics department, including Pascal Reiss, Jordan Thompson, Zach Zajicek, Stephen Blundell and Amalia Coldea. High magnetic field experiments at the HFML in Nijmegen were performed with the assistance of Alix McCollam. Data presented by to $45\,\mathrm{T}$ from the NHFML in Tallahassee were taken by Pascal Reiss, Amalia Coldea and David Graf. Pulsed magnetic field experiments up to $90\,\mathrm{T}$ at the LNCMI in Toulouse were performed with the assistance of William Knafo.

Fermi surface calculations of $CaKFe_4As_4$ (presented in figures 5.1**e** and A.1) were done by Amalia I. Coldea, who also produced the relevant figure panels. The data in figure B.6 were gathered by Amalia Coldea, who also produced the relevant figure. Figure B.7 was also produced by Amalia Coldea.

Publications

- **M. Bristow**, P. Reiss, Z. Zajicek, A. A. Haghighirad, M. Watson, A. McCollam, S. J. Blundell and A. I. Coldea, "Upper critical fields and an FFLO state in FeSe", *in preparation* (2020)[1].

- **M. Bristow**, P. Reiss, Z. Zajicek, A. A. Haghighirad, S. J. Singh, A. McCollam, S. J. Blundell and A. I. Coldea, "Evolution of the upper critical fields in the iron-based superconductors $FeSe_{1-x}S_x$", *in preparation* (2020)[1].

- **M. Bristow**, P. Reiss, Z. Zajicek, A. A. Haghighirad, S. J. Blundell and A. I. Coldea, "Persistent two-dimensional superconducting fluctuations across the nematic end point in $FeSe_{1-x}S_x$", *in preparation* (2020)[1].

- **M. Bristow**, W. Knafo, P. Reiss, W. Meier, P. Canfield, S. J. Blundell and A. I. Coldea, "Competing pairing interactions responsible for the large upper critical field in a stoichiometric iron-based superconductor $CaKFe_4As_4$", *Physical Review B* **101**, 134502 (2020).

- **M. Bristow**, P. Reiss, A. A. Haghighirad, Z. Zajicek, S. J. Singh, T. Wolf, D. Graf, W. Knafo, A. McCollam and A. I. Coldea, "Anomalous high-magnetic field electronic state of the nematic superconductors $FeSe_{1-x}S_x$", *Physical Review Research* **2**, 013309 (2020).

- L. Farrar, **M. Bristow**, A. A. Haghighirad, A. McCollam, S. J. Bending and A. I. Coldea, "Suppression of superconductivity and enhanced critical field anisotropy in thin flakes of FeSe", *Nature Physics Journals Quantum Materials* **5**, 29 (2020).

- S. J. Singh, **M. Bristow**, W. R. Meier, P. Taylor, S. J. Blundell, P. Canfield and A. I. Coldea, "Ultrahigh critical current densities, vortex phase diagram and the effect of granularity of the stoichiometric high-T_c superconductor $CaKFe_4As_4$ ", *Physical Review Materials* **2**, 074802 (2018).

[1]Title and author list are subject to change.

- S. J. Singh, S. J. Cassidy, **M. Bristow**, S. J. Blundell, S. J. Clarke and A. I. Coldea, "Optimization of the superconducting properties of the stoichiometric $CaKFe_4As_4$ ", *Superconductor Science and Technology* **33**, 025003 (2020).

- Y. H. Kwan, P. Reiss, Y. Han, **M. Bristow**, D. Prabhakaran, D. Graf, A. McCollam, S. A. Parameswaran and A. I. Coldea, "Quantum oscillations probe the Fermi surface topology of the nodal-line semimetal CaAgAs", *Physical Review Research* **2**, 012005(R) (2020).

- P. Reiss, D. Graf, A. A. Haghighirad, W. Knafo, L. Drigo, **M. Bristow**, A. J. Schofield and A. I. Coldea, "Quenched nematic criticality and two superconducting domes in an iron-based superconductor", *Nature Physics* **16**, 89-94 (2019).

- N. R. Davies, C.V. Topping, H. Jacobsen, A. J. Princep, F. K. K. Kirschner, M. C. Rahn, **M. Bristow**, J. G. Vale, I. da Silva, P. J. Baker, Ch. J. Sahle, Y.-F. Guo, D.-Y. Yan, Y.-G. Shi, S. J. Blundell, D. F. McMorrow and A. T. Boothroyd, "Evidence for a $J_{\text{eff}} = 0$ ground state and defect-induced spin glass behaviour in the pyrochlore osmate $Y_2Os_2O_7$", *Physical Review B* **99**, 174442 (2019).

- F. K. K. Kirschner, D. N. Woodruff, **M. Bristow**, F. Lang, P. J. Baker, S. J. Clarke and S. J. Blundell, "Robuestness of superconducting properties to transition metal substitution and impurity phases in $Fe_{1-x}V_xSe$", *Physical Review B* **100**, 094527 (2019).

- J. R. Soh, F. De Juan, M. G. Vergniory, N. B. M. Schröter, M. C. Rahn, D. Y. Yan, J. Jiang, **M. Bristow**, P. Reiss, J. N. Blandy, Y. F. Guo, Y. G. Shi, T. K. Shi, T. K. Kim, A. McCollam, S. H. Simon, Y. Chen, A. I. Coldea and A. T. Boothroyd, "Ideal Weyl Semimetal induced by magnetic exchange", *Physical Review B* **100**, 201102 (2019).

Acronyms and parameters

List of acronyms:

- AC – alternating current
- AFM – antiferromagnetic
- ARPES – angle resolved photo-emission spectroscopy
- BCS – Bardeen-Cooper-Schrieffer (theory)
- BEC – Bose-Einstein condensate
- BKT – Berezinskii-Kosterlitz-Thouless (transition)
- DC – direct current
- ETO – electrical transport option
- FFLO – Fulde-Ferrell-Larkin-Ovchinnikov (state)
- HFML – high-field magnetic laboratory (Nijmegen)
- GL – Ginzburg-Landau (theory)
- μSR – muon spectroscopy
- NEP – nematic end point
- NHFML – national high-field magnetic laboratory (Tallahassee)
- NMR – nuclear magnetic resonance
- PID – proportional, integral, derivative (temperature control systems)
- PPMS – Physical Properties Measurement System
- RRR – residual resistivity ratio
- SC – superconductivity
- SCF – superconducting fluctuations
- SMP – second magnetisation peak

- STM – scanning tunnelling microscopy
- SQUID – superconducting quantum interference device
- VSM – vibrating sample magnetometry
- VTI – variable temperature insert
- WHH – Werthamer-Helfand-Hohenberg (theory and model)

List of general parameters:

- T – temperature (in kelvin)
- $\mu_0 H$ – magnetic field
- B – internal magnetic field
- m – magnetic moment
- $M \ \ (= m/V)$ – magnetisation, where V is the sample volume
- χ – magnetic susceptibility
- R – resistance
- ρ – resistivity
- σ – conductivity
- $H||c$ – magnetic field parallel to the crystallographic c-axis
- $H||(ab)$ – magnetic field parallel to the crystallographic (ab)-plane (or perpendicular to the c-axis, $H \perp c$)
- $T_{\rm c}$ – superconducting transition temperature
- Δ – superconducting gap
- $\mu_0 H_{\rm c}$ – critical field
- $\mu_0 H_{\rm c1}$ – lower critical field
- $\mu_0 H_{\rm c2}$ – upper critical field
- $\mu_0 H_{\rm c2}^{c}$ – upper critical field when $H||c$
- $\mu_0 H_{\rm c2}^{ab}$ – upper critical field when $H||(ab)$
- $\mu_0 H_{\rm off}$ – upper critical field offset criteria from resistivity measurements
- $\mu_0 H_{\rm mid}$ – midpoint criteria of upper critical field from resistivity measurements (from the peak in the derivative with respect to magnetic field)
- $\mu_0 H_{\rm on}$ – onset upper critical field criteria from resistivity measurements

- $T_{\rm off}$ – offset criteria of the superconducting transition temperature from resistivity
- $T_{\rm mid}$ – midpoint criteria of the superconducting transition temperature from resistivity measurements (peak in the derivative with respect to temperature)
- $T_{\rm on}$ – onset criteria of the superconducting transition temperature from resistivity
- $J_{\rm c}$ – critical current density
- $J_{\rm d}$ – depairing current density
- $F_{\rm P}$ – vortex pinning force density
- $f_{\rm P}$ – normalised vortex pinning force density
- λ – superconducting penetration depth
- ξ – superconducting coherence length
- κ – superconducting order parameter (from Ginzburg-Landau model)
- Γ – superconducting anisotropy of the upper critical field $H_{\rm c2}^{ab}/H_{\rm c2}^{c}$
- λ_{ij} – band coupling parameter
- α $(\alpha_{\rm M})$ – Maki parameter
- v $(v_{\rm F}, v_i)$ – Fermi velocity
- η – Fermi velocity anisotropy (v_2^2/v_1^2)
- τ – scattering time
- $E_{\rm F}$ – Fermi energy
- $k_{\rm F}$ – Fermi wavevector
- ℓ – mean free path
- x – sulphur substitution (with range 0 to 1)
- $\Delta\sigma$ – excess conductivity
- $\sigma_{\rm SCF}$ – conductivity arising from superconducting fluctuations
- Gi – Ginzburg number

Abstract

This thesis presents the results of resistivity, torque magnetometry and magnetisation experiments on two different unconventional high-temperature iron-based superconductors in high magnetic fields. The superconducting phases and normal electronic states are explored. These results provide details about superconductivity in these compounds, and link changes in the superconducting state to those of the electronic state above the superconducting transition.

The first material that will be presented is the high-temperature, stoichiometric, clean and optimally doped iron-based superconductor $CaKFe_4As_4$. Magnetisation experiments on $CaKFe_4As_4$ map the vortex phase diagram and reveal exceptional high critical current densities, the largest in the family of iron-based superconductors. The upper critical fields of $CaKFe_4As_4$ require a two-band description, and become almost isotropic at low temperatures. The large upper critical fields, high critical current densities and strong vortex pinning force in $CaKFe_4As_4$, combined with its high transition temperature, metallic properties and stoichiometry, make it an excellent candidate for practical applications.

The second superconductor that will be considered is FeSe, particularly with isoelectronic sulphur substitution in $FeSe_{1-x}S_x$. This system has been of much interest recently. The sulphur substitution suppresses the nematic transition temperature of FeSe, and superconductivity persists across the entire phase diagram, although the transition temperature is suppressed where nematicity vanishes. These materials offer the opportunity to study the interplay between nematicity and superconductivity where no long-ranged magnetic order is present. This thesis experimentally explores the normal electronic state and superconducting phase of $FeSe_{1-x}S_x$ both inside the nematic state and in the tetragonal phase. The results show significant differences between the nematic and tetragonal phases for both the normal state and superconductivity, which correspond to changes in the Fermi surface. Near the nematic end point an extended region of $\rho \propto T^{1.5}$ resistivity is uncovered. New characteristic signatures of nematicity have been found in $FeSe_{1-x}S_x$ for $x \lesssim 0.18$, with a resistivity power law in magnetic field of $\rho \propto H^{1.55}$, which returns to the usual H^2 power law in the tetragonal phase. The high-field transverse magnetoresistivity changes from

metallic for low x to insulating-like at larger x inside the nematic state, which may arise from the emergence of an extra hole pocket. At low temperatures Fermi liquid behaviour emerges in clean samples, depending on the sulphur composition. The upper critical fields are suppressed across the nematic end point and reveal a two-band nature of superconductivity in $FeSe_{1-x}S_x$. Inside the nematic state the upper critical fields are dominated by inter-band Cooper pairing, whereas in the tetragonal state they are governed by intra-band scattering, highlighting the differences between superconductivity inside and outside of the nematic state and suggesting a change in Cooper pairing. Other superconducting properties, such as the coherence lengths, anisotropy and gaps, also change dramatically across the nematic end point. Despite these changes and differences, the excess conductivity outside of the superconducting state shows that the superconducting fluctuations remain two-dimensional across the entire phase diagram. Resistive transitions also become far broader near the nematic end point, where the excess conductivity and Ginzburg number are also enhanced. This may suggest that superconducting fluctuations are stronger at the nematic end point.

Contents

Acknowledgements **ii**

Declaration **iv**

Publications **v**

Acronyms and parameters **vii**

Abstract **x**

1 Introduction **1**

1.1 Superconductivity: An overview 2

1.2 BCS theory 4

1.3 Ginzburg-Landau theory 8

1.4 Type-II superconductivity and the vortex lattice 10

1.5 Unconventional high-temperature superconductors 12

1.6 Iron-based superconductors 15

1.6.1 $FeSe_{1-x}S_x$ 17

1.6.2 $CaKFe_4As_4$ 20

1.7 Charge carriers in the normal state 21

1.7.1 Charge carriers in metals 22

1.7.2 Electrons in a magnetic field 23

1.7.3 Hall effect 25

1.7.4 Multi-band description 25

1.7.5 Other factors affecting normal state properties 27

2 Vortex Physics **28**

2.1 Upper critical fields 28

2.1.1 Coherence lengths 28

2.1.2 Orbital and Pauli paramagnetic effects 30

2.1.3 The WHH model . . . 30
2.1.4 Gurevich two-band model (dirty limit) . . . 32
2.1.5 Gurevich two-band model (clean limit) . . . 34
2.1.6 Nucleation at surfaces and a third critical field . . . 37
2.2 Vortices in high-temperature superconductors . . . 37
2.2.1 Bean's critical state model . . . 37
2.2.2 Dew-Hughes model . . . 38
2.2.3 Vortex pinning . . . 39
2.2.4 Flux flow . . . 40
2.3 Superconducting fluctuations . . . 41
2.3.1 Temperature dependence . . . 41
2.3.2 Magnetic field scaling . . . 43
2.3.3 Ginzburg number . . . 44

3 Experimental techniques **46**
3.1 Temperature control . . . 46
3.1.1 Flow-cryostat . . . 46
3.1.2 Physical Properties Measurement System (PPMS - Quantum Design) 47
3.1.3 Variable Temperature Inserts (VTI's) . . . 47
3.1.4 Helium-3 systems . . . 47
3.2 Generating high magnetic fields . . . 48
3.2.1 Superconducting magnets . . . 48
3.2.2 Resistive DC magnets . . . 49
3.2.3 Pulsed field magnets . . . 49
3.3 Electrical transport . . . 49
3.4 Magnetisation . . . 54
3.5 Torque magnetometry . . . 57

4 Ultrahigh critical current densities in $CaKFe_4As_4$ **59**
4.1 Introduction . . . 60
4.2 Experimental details . . . 61
4.3 Magnetic susceptibility . . . 62
4.4 Lower and upper critical fields . . . 64
4.5 Magnetic hysteresis and critical current densities . . . 67
4.6 Vortex pinning force . . . 71
4.7 The vortex phase diagram . . . 73
4.8 Summary . . . 77

5 Upper critical fields in $CaKFe_4As_4$ **78**
5.1 Introduction . . . 79
5.2 Experimental details . . . 80
5.3 Upper critical field phase diagram from transport measurements . . . 81
5.4 Single band description of the upper critical fields . . . 85
5.5 Upper critical field described using a two-band model . . . 85
5.6 Summary . . . 89
5.7 Aside: Activation energy of the vortex state . . . 90

6 The high magnetic field electronic state of $FeSe_{1-x}S_x$ **92**
6.1 Introduction . . . 93
6.2 Materials and Methods . . . 95
6.3 Transverse-field magnetoresistivity in high magnetic fields . . . 96
6.3.1 Hall Effect . . . 98
6.3.2 Transverse-field magnetoresistivity across the NEP . . . 99
6.4 Resistivity exponents in temperature at zero magnetic field . . . 102
6.5 Discussion . . . 106
6.6 Summary . . . 107

7 Upper critical fields of $FeSe_{1-x}S_x$ **109**
7.1 Introduction . . . 110
7.2 Experimental details . . . 111
7.3 Results . . . 112
7.4 Single-band WHH description of $H_{c2}(T)$ . . . 116
7.5 Describing $H_{c2}(T)$ with the two-band model . . . 117
7.6 Discussion . . . 121
7.6.1 Suppression of the upper critical fields . . . 121
7.6.2 Lifshitz transition at the NEP and the role of spin fluctuations . . . 123
7.6.3 Superconducting gap . . . 124
7.7 Summary . . . 125

8 Persistent two-dimensional superconducting fluctuations across the nematic end point in $FeSe_{1-x}S_x$ **126**
8.1 Introduction . . . 127
8.2 Experimental details . . . 130
8.3 Extracting the excess conductivity . . . 131
8.4 Temperature dependence of the excess conductivity . . . 136

8.5 Magnetic field scaling of the fluctuations 137
8.6 Ginzburg number 140
8.7 Discussion 141
8.8 Summary 145

9 Conclusions **146**

A Additional material for chapter 5 **150**
A.1 The upper critical fields using a two-band model 154

B Additional material for chapter 6 **157**

C Additional material for chapter 7 **164**
C.1 Raw data 164
C.2 Two-band model parameters 170
C.3 Modelling the Maki parameter 176

D Additional material for chapter 8 **178**

References **183**

Chapter 1

Introduction

Superconductivity has been one of the mostly lively and intensely studied fields in modern physics, particularly with the discovery of the high-temperature superconductors in 1986. These materials are of interest mainly for their practical applications and are studied in many physics, materials science and chemistry departments around the world. The main quality that makes them so desirable for practical use is zero resistivity below a characteristic critical transition temperature, T_{c}, and their ability to carry dissipationless currents, often above $\sim 10^5\,\mathrm{A/cm^2}$. They open up a range of high-current and high-field applications. Superconductors are already featured in many research magnets, as well as in modern MRI scanners and magnetic levitation technology. Most applications currently work at liquid helium temperature, $\sim 4.2\,\mathrm{K}$. High-temperature superconductors, such as members of the cuprate family, have transition temperatures that can exceed $100\,\mathrm{K}$, opening up cheaper possibilities at higher temperatures; for example, using liquid nitrogen at $\sim 77\,\mathrm{K}$. These high-temperature superconductors also generally show improved superconducting properties relative to their low-T_{c} counterparts, with higher critical fields and critical current densities - properties essential for efficient applications.

Despite the plethora of work on high-temperature superconductors, a complete theory and mechanism underpinning superconductivity still remains an open question. In recent years it has been shown likely that different high-T_{c} families may have a different underlying mechanism. This in itself gives reason to continue studying these materials from a theoretical and experimental point-of-view.

This thesis will focus on experimentally studying two superconductors from the iron-based family, $CaKFe_4As_4$ and $FeSe_{1-x}S_x$. First, the background of superconductivity, including BCS and Ginzburg-Landau theories, an an overview of the iron-based superconductors focusing on $CaKFe_4As_4$ and $FeSe_{1-x}S_x$, and a more detailed discussion of the vortex phase will be presented. Next, the main experimental techniques (magnetisation, electrical transport and torque magnetometry) used in latter chapters will be covered. This

leads on to the results chapters of this thesis. The first two of these will explore the superconducting state of $CaKFe_4As_4$, extracting the critical fields, critical current density and vortex pinning force. The second explores the upper critical field in detail. The results presented on $CaKFe_4As_4$ show that it is a clean stoichiometric superconductor with high upper critical fields and extremely large critical current densities, making it an excellent candidate for practical applications. Chapters 6-8 explore experimental results on $FeSe_{1-x}S_x$. In chapter 6 the high-magnetic field normal electronic state (outside of the superconducting state) is explored. $FeSe_{1-x}S_x$ has a nematic phase that is suppressed with sulphur substitution. The differences in the electronic behaviour inside and outside of the nematic phase are characterised. Chapter 7 analyses the evolution of the upper critical field with sulphur doping, across the nematic and tetragonal phases. Finally, chapter 8 investigates the superconducting fluctuations present above the superconducting transition temperature. The data on $FeSe_{1-x}S_x$ show strong correlations between superconductivity and the normal state inside and outside of the nematic phase.

1.1 Superconductivity: An overview

Superconductivity was discovered by Heike Kamerlingh Onnes in 1911 in mercury [1], three years after helium-4 was first liquefied. Onnes observed that the resistance of mercury, and later other metals such as lead and tin, dropped to zero at some characteristic critical temperature, T_c. Experiments have shown persistent, dissipationless, currents with no measurable decrease on time scales up to a year. This perfect conductivity is the first important attribute of superconductivity, and also perhaps the property that carries the most significance for the practical applications of this phenomenon.

In 1933 Meissner and Ochsenfeld discovered the second trademark signature of superconductivity, perfect diamagnetism [2]. They showed that a magnetic field is not just excluded from a superconductor (which is enough to explain perfect conductivity and zero resistivity), but it is expelled as a sample is cooled through T_c. This is more commonly known as the Meissner effect, where the superconductor behaves as a perfect diamagnet (with magnetic susceptibility $\chi = -1$). As a magnetic field is applied to a material in the superconducting state it develops persistent currents that oppose the field and screen the bulk of the sample, keeping the magnetic field zero inside. This implies that superconductivity will be destroyed by some characteristic critical magnetic field, H_c, which is thermodynamically related to the difference between the superconducting state and normal state free energies.

These two properties, perfect conductivity and diamagnetism, are what make superconductivity unique. These two traits were first described by the London brothers in 1935, who proposed two equations to govern the local electric and magnetic fields [3]

$$\mathbf{E} = \frac{\partial}{\partial t}(\Lambda \mathbf{J}_{\mathrm{s}}) \qquad \mathbf{B} = -\mathrm{curl}(\Lambda \mathbf{J}_{\mathrm{s}}) \tag{1.1}$$

where

$$\Lambda = \mu_0 \lambda^2 = \frac{m}{n_{\mathrm{s}} e^2}. \tag{1.2}$$

Here $\mathbf{E}$ is the electric field, $\mathbf{J}_{\mathrm{s}}$ is the current density, $\mathbf{B}$ is the magnetic field flux density, m is the (electron) mass, c is the speed of light, e is the electron charge, n_{s} is the number density of superconducting quasiparticles, λ is a characteristic length scale and Λ is a phenomenological parameter. Combining the second equation in 1.1 with Maxwell's equation $\mathrm{curl}\ \mathbf{B} = \mathbf{J}$ gives

$$\nabla^2 \mathbf{B} = \frac{\mathbf{B}}{\lambda^2}, \tag{1.3}$$

which implies the magnetic field is screened exponentially from the bulk of a sample with penetration depth λ. This is, in essence, the Meissner effect. Equation 1.2 also provides us with an upper limit as $T \to 0$ on the London penetration depth, λ_{L}, as

$$\lambda_{\mathrm{L}}^2(0) = \frac{m}{\mu_0 n e^2}, \tag{1.4}$$

where n is the density of conduction electrons.

Comparisons of the penetration depth of samples in the superconducting and normal state have consistently shown that the superconducting penetration depth λ is always larger than the London penetration depth λ_{L}. This, essentially, implies a difference in the number density of conduction electrons (n) and superconducting electrons (n_{s}). The description of the excess penetration depth was provided by Pippard with the introduction of another characteristic length scale, the coherence length, ξ_0 [4]. He argued that only electrons within $\sim k_{\mathrm{B}} T_{\mathrm{c}}$, where k_{B} is the Boltzmann constant, of the Fermi energy can play a significant role in a transition that occurs at T_{c}. These electrons have a momentum range $\Delta p \simeq k_{\mathrm{B}} T_{\mathrm{c}} / v_{\mathrm{F}}$, where v_{F} is the Fermi velocity. Combining this with the uncertainty principle ($\Delta x \geq \hbar / \Delta p$) gives an estimate for the Pippard coherence length, ξ_0, as

$$\xi_0 = a \frac{\hbar v_{\mathrm{F}}}{k_{\mathrm{B}} T_{\mathrm{c}}}, \tag{1.5}$$

where a is a constant. For elemental superconductors such as lead, tin and niobium $\xi_0 \gg \lambda_{\mathrm{L}}$. Here ξ_0 is playing a role similar to that of the mean free path in electrodynamics, and is essentially a screening parameter for the decay of the superconducting order parameter as the edge of the bulk is approached.

1.2 BCS theory

The next step in the understanding of superconductivity originates from the formation of an energy gap Δ around the Fermi level on the order of $k_{\mathrm{B}}T_{\mathrm{c}}$ between the ground state and the quasi-particle excitations. The first evidence for an energy gap in the superconducting state came from specific heat measurements which showed that the electronic specific heat, C_{es}, well below T_{c} was dominated by an exponential dependence of $C_{es} \propto T_{\mathrm{c}}e^{-bT_{\mathrm{c}}/T}$, where b is a constant and T is the temperature.

At a similar time, the first electromagnetic absorption experiments on aluminium ($T_{\mathrm{c}} \sim 1.2\,\mathrm{K}$) and lead ($T_{\mathrm{c}} \sim 7.2\,\mathrm{K}$) showed the presence of a gap at the Fermi level. Whilst the T_{c} of aluminium was too low to be able to determine an accurate gap at the time, lead was shown to have a gap of $\sim 3 - 4k_{\mathrm{B}}T_{\mathrm{c}}$. The electromagnetic experiments gave an indication of the minimum total energy, $E_g = 2\Delta$, to create (or destroy) the pair of excitations, whilst the thermal ones measure the energy $E_g/2 = \Delta$ per particle.

Shortly after this in 1957 Bardeen, Cooper and Schrieffer published their theory on superconductivity, more commonly known as BCS theory [5]. They showed that even a weak attractive interaction between electrons causes an instability in the ground state of a Fermi-sea and electrons occupying states of equal and opposite momentum and spin bind to form Cooper pairs. Such an attractive interaction can be caused in second order by electron-phonon interactions. These Cooper pairs have spatial extension $\sim \xi_0$ and constitute the charge carriers of the superconducting state.

The origins of the attractive interaction in this model come from considering electrons (or more precisely, two electrons) moving through a lattice and the Coulomb potential [6]. The physical idea is that the first electron locally polarises the medium by attracting positively charged ions towards it, creating a small positive net local charge. This positive charge then in turn attracts a second electron, and gives an effective interaction between the two electrons. If this attractive potential is stronger than the screened repulsive Coulomb interaction it gives a net positive interaction which pairs the electrons, resulting in a Cooper pair and superconductivity. Since the lattice deformation from a passing electron results from the same stiffness that describes the elasticity of a solid, it can be inferred that the characteristic vibrational phonon modes and frequencies will play a role. This gives a cutoff energy $\hbar\omega_c$ (when the attraction becomes repulsive rather than attractive) of the order of the Debye energy $\hbar\omega_D$, which characterises the phonon spectrum cutoff. The electron-phonon lattice interaction underpinning superconductivity in BCS theory was experimentally confirmed by the isotope effect, which shows that T_{c} and H_{c} vary as $M^{-1/2}$

[7, 8], where M is the atomic mass, for isotopes of the same element[1].

To write down the BCS ground state wavefunction it is necessary to introduce the creation operator ($c^\dagger_{\mathbf{k}\uparrow}$) which creates an electron of momentum $\mathbf{k}$ and spin up, and the annihilation operator ($c_{\mathbf{k}\uparrow}$) which destroys an electron in the same state. With this notation, the *singlet* ($S = 0$, $L = 0$) wavefunction is

$$|\psi_0\rangle = \sum_{k>k_\mathrm{F}} g_\mathbf{k} c^\dagger_{\mathbf{k}\uparrow} c^\dagger_{-\mathbf{k}\downarrow} |F\rangle \,, \tag{1.6}$$

where k_F is the Fermi momentum and $|F\rangle$ represents the Fermi sea with all states up to k_F filled. The particle number operator is defined by $n_{\mathbf{k}\sigma} = c^\dagger_{\mathbf{k}\sigma} c_{\mathbf{k}\sigma}$, where σ is the electron spin index. This gives 0 when acting on an unoccupied state and 1 when acting on an occupied state.

BCS theory essentially searches for a solution to the electron-phonon pairing Hamiltonian, which is given by

$$\mathcal{H} = \sum_{\mathbf{k},\sigma} \epsilon_\mathbf{k} n_{\mathbf{k}\sigma} + \sum_{\mathbf{k},\mathbf{k}'} V_{\mathbf{k}\mathbf{k}'} c^\dagger_{\mathbf{k}\uparrow} c^\dagger_{-\mathbf{k}\downarrow} c_{\mathbf{k}'\uparrow} c_{-\mathbf{k}'\downarrow}, \tag{1.7}$$

where $\epsilon_\mathbf{k}$ is an energy and $V_{\mathbf{k}\mathbf{k}'}$ is the potential. BCS then took an educated 'guess' (or ansatz) for the ground state wavefunction, which has the form

$$|\psi_G\rangle = \prod_\mathbf{k} (u_\mathbf{k} + v_\mathbf{K} c^\star_{\mathbf{k}\uparrow} c^\star_{-\mathbf{k}\downarrow}) \, |0\rangle \tag{1.8}$$

where $u_\mathbf{k}$ and $u_\mathbf{k}$ are variational parameters, $|0\rangle$ is the vacuum state and $|u_\mathbf{k}|^2 + |v_\mathbf{k}|^2 = 1$. This implies that the probability of a state with pair $(\mathbf{k}\uparrow, -\mathbf{k}\downarrow)$ being occupied is $|v_\mathbf{k}|^2$, and the probability that it is empty is $|u_\mathbf{k}|^2 = 1 - |v_\mathbf{k}|^2$. The ground state expressed as a sum can be used to give the number of Cooper pairs as $N/2$. More generally this is expressed with an arbitrary phase factor $e^{i\varphi}$ with each pair creation as

$$|\psi_\varphi\rangle = \prod_\mathbf{k} (|u_\mathbf{k}| + |v_\mathbf{k}| e^{i\varphi} c^\dagger_{\mathbf{k}\uparrow} c^\dagger_{-\mathbf{k}\downarrow}) \, |0\rangle \,, \tag{1.9}$$

which can be described with a similar sum as in equation 1.8 and projecting $|\psi_N\rangle \rightarrow e^{iN\varphi/2} |\psi_N\rangle$. This can be used to give an uncertainty relationship between phase and number in the superconducting state $\Delta N \Delta\varphi \geq 1$. Note that here for an electron in state $\mathbf{k}$ the total energy is given by $E^2_\mathbf{k} = \epsilon^2_\mathbf{k} + \Delta^2_\mathbf{k}$ where $\Delta_\mathbf{k}$ is the energy gap. This is shown in figure 1.1 **a**. The full details of the derivation and this theory can be found elsewhere [5, 9, 10] and are omitted here, where the focus will be on key results from BCS theory.

[1] References are for mercury.

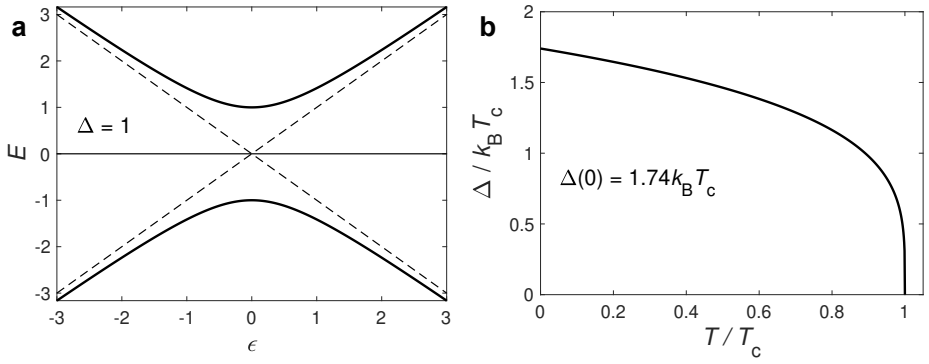


Figure 1.1: **a** the excitations of particles in the normal (dashed line) and superconducting state (solid line) relative to the Fermi energy. **b** Temperature dependence of the BCS gap.

Applying the BCS ground state wavefunction to the electron-phonon pairing Hamiltonian (equations 1.7-1.9) gives the BCS value of the gap at zero temperature

$$|\Delta(0)| = 2\hbar\omega_{\mathrm{D}} e^{-1/N(0)V}, \tag{1.10}$$

where $N(0)V$ is dimensionless, $N(0)$ is the number of electrons at $T = 0$ and V represents the pairing potential. This result implies that the typical energy scale for superconductivity is less than that of the Debye energy $\hbar\omega_{\mathrm{D}}$. At a finite temperature T the occupation of the quasiparticle state with energy $E_{\mathbf{k}}$ is given by the Fermi-Dirac distribution. Determining the expectation value gives the BCS gap equation

$$\frac{1}{N(0)V} = \int_0^{\hbar\omega_{\mathrm{D}}} \frac{1}{\sqrt{\epsilon^2 + \Delta^2}} \tanh\left(\frac{\sqrt{\epsilon^2 + \Delta^2}}{2k_{\mathrm{B}}\,T}\right) d\epsilon, \tag{1.11}$$

where $\lambda \sim N(0)V$ is the dimensionless electron-phonon coupling parameter. This can be used to determine the gap at any temperature $\Delta(T)$, below T_{c}. Taking equation 1.11 in the limit as $\Delta \to 0$ one can obtain an expression for T_{c},

$$k_{\mathrm{B}}T_{\mathrm{c}} \simeq 1.13\hbar\omega_{\mathrm{D}} e^{-1/N(0)V}. \tag{1.12}$$

Now taking the limit of equation 1.11 as $T \to 0$ the superconducting gap at zero temperature can be found as

$$\Delta(0) = 1.764 k_{\mathrm{B}} T_{\mathrm{c}}. \tag{1.13}$$

The temperature dependence of the gap is approximately described by [9]

$$\Delta(T) \simeq 1.74\Delta(0)\left(1 - \frac{T}{T_{\mathrm{c}}}\right)^{1/2}, \tag{1.14}$$

for $T \geq T_{\rm c}$, which is shown in figure 1.1 **b**. A similar expression can be found for the temperature dependence of the critical magnetic field $H_{\rm c}(T) = H_{\rm c}(0)[1-(T/T_{\rm c})^2]$. Finally, the result for the approximate temperature dependence of the penetration depth can also be derived, which is given by

$$\lambda(T) = \lambda(0)\left[1 - \left(\frac{T}{T_{\rm c}}\right)^4\right]^{-1/2}. \tag{1.15}$$

The BCS wavefunction essentially consists of an orbital part and a spin-momentum part, and must be antisymmetric under particle exchange (since we are considering Fermions). Since the spin-momentum part is antisymmetric under exchange by definition, this means that the orbital part must also be symmetric (i.e. $L = 0$, also with total spin $S = 0$). Thus, the description of superconductivity in BCS theory, whilst providing the most in-depth theoretical understanding, is limited to superconducting gaps that are singlet, s-wave and isotropic. Thorough mathematical arguments for this are presented elsewhere [5, 9]. The class of materials that this theory describes are known as *conventional* superconductors.

It is worth noting that other pairing states are available, and we are not limited to this single case. For example, a spin triplet ($S = 1$) p-wave state ($L = 1$) is possible where the spin part is now symmetric and so the orbital part must be antisymmetric. Another possibility is a d-wave state ($L = 2$) where the orbital part is again symmetric and the part is singlet ($S = 0$). These cases become important later when considering high temperature superconductors.

Thus far this overview of BCS theory has assumed the case of a pure metal, but in real systems the effects of impurity scattering are often important and affect the microscopic BCS results. Generally, impurities have the effect of making the electrodynamic response more local. Screening can be introduced with a multiplicative factor of $e^{-R/\ell}$, where R is the distance and ℓ is the mean free path in the normal state (at $T = 0$). Impurities induce more scattering and reduce the mean free path. From this, comparing to R/ξ_0, the *dirty limit* is defined as $\xi_0 \gg \ell$, and the *clean limit* as $\xi_0 \ll \ell$. In the presence of impurities, BCS theory is modified to have an effective penetration depth, $\lambda_{\rm eff}$. Using $\xi^{-1} = \xi_0^{-1} + \ell^{-1}$ gives the result

$$\lambda_{\rm eff}(T, \ell) \simeq \lambda_{\rm L}(T)\left(1 + \frac{\xi_0}{\ell}\right)^{1/2}, \tag{1.16}$$

which gives $\lambda_{\rm eff} = \lambda_{\rm L}$ in the clean limit and $\lambda_{\rm eff} > \lambda_{\rm L}$ in the dirty limit. Clearly, impurities will thus have an effect on the superconducting state, which will become important later in chapters 4-8.

1.3 Ginzburg-Landau theory

Seven years before the publication of BCS theory, in 1950, Ginzburg and Landau (GL) introduced a complex pseudo-wavefunction as an order parameter into Landau's theory on second-order transitions to describe superconducting electrons [11, 12], which is denoted by $n_s = |\psi(x)|^2$. This is a macroscopic theory of superconductivity in which the free energy of the entire system is used instead of a spectrum of local excitations. It assumes a free energy density of the form

$$f = f_{\mathrm{n0}} + \alpha|\psi|^2 + \frac{\beta}{2}|\psi|^4 + \frac{1}{2m^\star}\left|\left(\frac{\hbar}{i}\nabla - \frac{e^\star}{c}A\right)\psi\right|^2 + \frac{\mu_0 h^2}{2}, \tag{1.17}$$

where α and β are expansion coefficients, $m^\star$ is the effective mass, $e^\star$ is an effective mass, A is a vector potential and ψ is small and varies slowly in space. Here the normal state free energy is $f_{\mathrm{n0}} + \mu_0 h^2/2$, which is neglected. This free energy can be minimized, as is the standard approach in mean field theories. Using the variational principle, allowing for fields, currents or gradients with $\psi \to |\psi|e^{i\varphi}$, and expanding the minimized free energy in ψ and $\nabla\psi$ to give the differential equations

$$\frac{1}{2m^\star}\left(\frac{\hbar}{i}\nabla - \frac{e^\star}{c}\mathbf{A}\right)^2\psi + \beta|\psi|^2\psi = -\alpha(T)\psi, \tag{1.18}$$

which is analogous to the Schrödinger equation, and

$$\mathbf{J} = \frac{e^\star}{m^\star}|\psi|^2\left(\hbar\nabla\varphi - \frac{e^\star}{c}\mathbf{A}\right), \tag{1.19}$$

where **J** is the *supercurrent* density. Solutions are found here by minimising the free energy. This theory has two features that surpass the London theory. It incorporates non-linear effects in strong fields that can change the density n_s and the spatial variation of the density n_s. It is from these equation that the rest of GL theory is constructed.

The GL theory introduces a characteristic length, the *GL coherence length*,

$$\xi_{\mathrm{GL}}(T) = \frac{\hbar}{|2m^\star\alpha(T)|^{1/2}} \propto \frac{1}{(1 - T/T_{\mathrm{c}})^{1/2}} \tag{1.20}$$

which characterises the distance over which the wavefunction ψ can vary without energy increase. In a clean superconductor far below T_{c}, this is equivalent to the coherence length ξ_0 introduced earlier. However, near T_{c}, $\xi_{\mathrm{GL}}(T)$ diverges as $\sim (T - T_{\mathrm{c}})^{-1/2}$. It can be shown that the GL coherence length can be expressed as

$$\xi_{\mathrm{GL}}(T) = \frac{\Phi_0}{2\sqrt{2}\pi H_{\mathrm{c}}(T)\lambda_{\mathrm{eff}}(T)}, \tag{1.21}$$

where $\Phi_0 = h/e^\star = h/2e = 2.07 \times 10^{-15}$ Wb is the magnetic flux quantum. This provides the first relationship between the coherence length, critical field and effective penetration depth in this theory. Combining equation 1.21 with previous results and arguments from BCS theory shows the temperature dependence of the Ginzburg-Landau coherence length near T_c in the *clean* limit varies as

$$\xi_{\mathrm{GL}}(T) \simeq 0.74 \frac{\xi_0}{(1-t)^{1/2}}, \tag{1.22}$$

and in the *dirty* limit as

$$\xi_{\mathrm{GL}}(T) \simeq 0.855 \frac{(\xi_0 \ell)^{1/2}}{(1-t)^{1/2}}, \tag{1.23}$$

where $t = T/T_\mathrm{c}$ is the reduced temperature.

Another quantity introduced by GL theory is the GL parameter

$$\kappa = \frac{\lambda}{\xi}. \tag{1.24}$$

In this formalism $\xi \equiv \xi_{\mathrm{GL}}$, but here it has been left as ξ for simplicity later. κ is a dimensionless parameter and, since λ also diverges as $\sim (T - T_\mathrm{c})^{-1/2}$, is approximately independent of temperature. In the GL formalism, the parameter κ can be expressed more precisely as

$$\kappa(T) = \frac{\lambda_{\mathrm{eff}}(T)}{\xi_{\mathrm{GL}}(T)} = \frac{2\sqrt{2}\pi H_\mathrm{c}(T)\lambda_{\mathrm{eff}}^2(T)}{\Phi_0}. \tag{1.25}$$

Using the approximations $H_\mathrm{c} \propto (1-t^2)$ and $\lambda \propto (1-t^4)^{-1/2}$ shows that κ is not temperature independent, and varies as $\kappa \propto (1-t^2)^{-1}$. This however, should be finite at T_c and should not have a strong temperature dependence [9].

Classical type-I superconductors (which typically have $\lambda \sim 50\,\mathrm{nm}$ and $\xi \sim 300\,\mathrm{nm}$) have $\kappa \ll 1$. With an understanding of the parameter κ, we can now start to realize the differences between type-I and type-II superconductors, which are separated by the value of $\kappa = 1/\sqrt{2}$.

It is worth considering the surface energy, $\gamma = \mu_0 H_\mathrm{c}^2 \delta/2$, where δ is the skin depth. Qualitatively, it can be seen that γ is positive for $\kappa \ll 1$ as there is a region (of $\sim \xi - \lambda$) where the magnetic field is expelled, but the magnitude of the wavefunction is not its maximum value. The opposite is true for $\kappa \gg 1$, resulting in a negative surface energy. This becomes important later when the formation of vortices is considered.

Within the GL model, it can be shown that the critical current density, J_c of a wire is given by [9, 13]

$$J_\mathrm{c} = 2e|\psi(0)|^2 \frac{2}{3}\left(\frac{2|\alpha|}{3m^\star}\right)^{1/2} = \frac{cH_\mathrm{c}(T)}{3\sqrt{6}\pi\lambda(T)} \propto (1-t)^{3/2} \tag{1.26}$$

It is worth noting here that the GL is a mean field theory, and so neglects the effects of thermal fluctuations.

1.4 Type-II superconductivity and the vortex lattice

Superconductors have another underlying property that is essential for some of their practical applications - flux quantisation. Qualitatively, this arises from the surface energy arguments presented above, but can also be shown mathematically by considering, for example, a superconducting ring in a magnetic field, where the free energy shows a minimum at integer values of Φ_0. Cooling a superconducting ring in a magnetic field down below its T_c will cause the system to adopt one of these metastable minimums, depending on the magnitude of the applied field. A persistent current will flow around the ring to maintain a constant flux $\Phi = n\Phi_0$, essentially trapping the flux and keeping the system in the local minimum. Experiments have measured the trapped flux to occur in integer quantities of $\Phi_0 = 2.07 \times 10^{-15} = h/2e$. This is also direct evidence that $2e$ is the relevant charge for the quasiparticles of superconductivity, i.e. implying the existence of Cooper pairs.

Using a linearised form of the GL differential equation 1.18 and an appropriate gauge choice one can show the presence of a second critical field. This is defined as H_{c2}, where

$$\mu_0 H_{c2} = \frac{\Phi_0}{2\pi\xi^2}, \tag{1.27}$$

which depends only on the coherence length. This is the maximum magnetic field at which superconductivity can nucleate in the interior of a bulk sample. H_{c2} is now more commonly known as the *upper critical field*. Using ξ as the GL coherence length ξ_{GL} and substituting in equation 1.21 we arrive at

$$\mu_0 H_{c2} = \frac{\Phi_0}{2\pi\xi_{GL}^2} = \frac{4\pi\lambda^2(\mu_0 H_c)^2}{\Phi_0} = \sqrt{2}\kappa\mu_0 H_c. \tag{1.28}$$

The final form here implies that H_c and H_{c2} are only distinguishable for $\kappa > 1/\sqrt{2}$, otherwise we have $H_{c2} \leq H_c$. This provides the definition of type-I and type-II superconductivity. Type-I superconductors with $H_{c2} \leq H_c$ only have one thermodynamic critical field, H_c. Type-II superconductors with $H_{c2} > H_c$ show two thermodynamic critical fields. These are referred to as the *lower critical field*, H_{c1}, and the *upper critical field*, H_{c2}.

Type-I superconductors and type-II superconductors for $H < H_{c1}$ completely screen the magnetic field from the bulk of the material, as discussed earlier. However, type-II superconductors at magnetic fields $H_{c1} < H < H_{c2}$ show flux quantisation in the form of magnetic vortices. This was shown by Abrikosov, who found a solution to the GL equation

for type-II superconductors in a magnetic field close to H_{c2}. This predicted a periodic structure of vortices, with each vortex containing a single magnetic flux quantum, Φ_0. This is known as the *mixed state*, or *vortex state*. Magnetic vortices tend to arrange themselves into a triangular lattice to minimise the repulsion between them. The size of these vortices is defined by the coherence length ξ, which is the vortex radius. Using the temperature dependence of ξ from earlier, we can obtain an expression for the temperature dependence of H_{c2} as

$$\mu_0 H_{c2} = \frac{\Phi_0}{2\pi\xi^2_{GL}(0)}(1-t), \tag{1.29}$$

for T near T_c. Thus, measuring the gradient of H_{c2} near T_c can give an estimate of the zero temperature GL coherence length. This will be returned to later and considered in the case of anisotropic upper critical fields.

It can be shown that it becomes energetically favourable for vortices to enter the sample above the lower critical field H_{c1}, and that

$$\mu_0 H_{c1} = \frac{\Phi_0}{4\pi\lambda^2}[\ln(\kappa + 1/2)], \tag{1.30}$$

or

$$H_{c1} = \frac{H_c}{\sqrt{2}\kappa}[\ln(\kappa + 1/2)]. \tag{1.31}$$

These equations are only valid when $\kappa \gg 1/\sqrt{2}$.

Type-II superconductors have a number of interesting responses in a magnetic field. A proper analysis of this requires a calculation of the energy of a single vortex and the energy of the interaction between vortices. If a sample is first cooled in zero magnetic field from above T_c to some temperature below T_c this gives four distinguishable regimes.

1. First, a region below H_{c1} where the magnetization will be negative and linear in magnetic field, corresponding to a perfect diamagnetic state ($\chi = -1$) in the bulk of the sample.

2. Second, a region near, but just above, H_{c1} where $\Phi_0/B \gg \lambda^2$ (B is the internal magnetic field) and vortices are present separated by a distance greater than λ. In this region, the bulk of the sample is no longer perfectly diamagnetic and the magnetization starts to curve. B (and also the magnetization M) is continuous at H_{c1}, but changes initially with infinite slope. This is because once $H > H_{c1}$ and the first vortex enters the sample there is little to stop other vortices forming until they get within a distance of $\sim \lambda$ of each other.

3. Third, a region of intermediate B where $\xi^2 \ll \Phi_0/B \ll \lambda^2$ (or $H_{c1} < B \ll H_{c2}$) and many vortices are present and interacting. Here the magnitude of the magnetization starts to decrease, but remains negative.

4. Finally, there is a region near H_{c2} where $\xi^2 \simeq \Phi_0/B$ and the vortex cores are almost overlapping. This requires a more detailed treatment of the vortex core. Here the magnitude of the magnetization becomes small, before the material returns to the normal state above H_{c2}.

One of the key features of the vortex state is its irreversibility. The trapped flux inside the superconductor cannot be simply removed by decreasing the magnetic field, the vortices persist. This means that a sample can not re-enter the Meissner state. Upon decreasing the magnetic field the sign of the magnetisation should switch. The only method to effectively remove the trapped flux is to warm the sample above its transition temperature.

Experimentally this is also an important point, as superconducting magnets are often used to produce high magnetic fields. These cannot easily be warmed above their T_c and so are susceptible to trapped flux. This means that even when a superconducting solenoid is not being supplied with any current the magnetic field is not necessarily zero. One way to minimise this effect is to oscillate the current supplied to the magnet, and so also the field, positive and negative towards zero.

1.5 Unconventional high-temperature superconductors

Thus far we have discussed the theories describing conventional superconductors. This has been shown to accurately describe the behaviour of type-I materials such as lead, aluminium and tin, as well as type-II materials such as NbTi. The last of these materials has $T_c \sim 10\,\mathrm{K}$ and an upper critical field at $4.2\,\mathrm{K}$ of $\mu_0 H_{c2} \sim 10\,\mathrm{T}$. As it is relatively cheap and metallic, it is still used as the workhorse in many superconducting applications today. It is commonly used in research magnets, MRI scanners and high-field magnets on the Large Hadron Collider.

The field of superconductivity changed dramatically in 1986 with the discovery of the cuprate superconductors, with transition temperatures far exceeding those of any material previously measured. The record transition temperature in this class of materials currently stands at $\sim 140\,\mathrm{K}$ in Hg-2232, well above the boiling point of liquid nitrogen. The cuprates thus opened up new possibilities for applications at higher temperatures, such as in liquid nitrogen. Now materials such as YBCO and Bi-2212 and Bi-2232 are starting to enter into

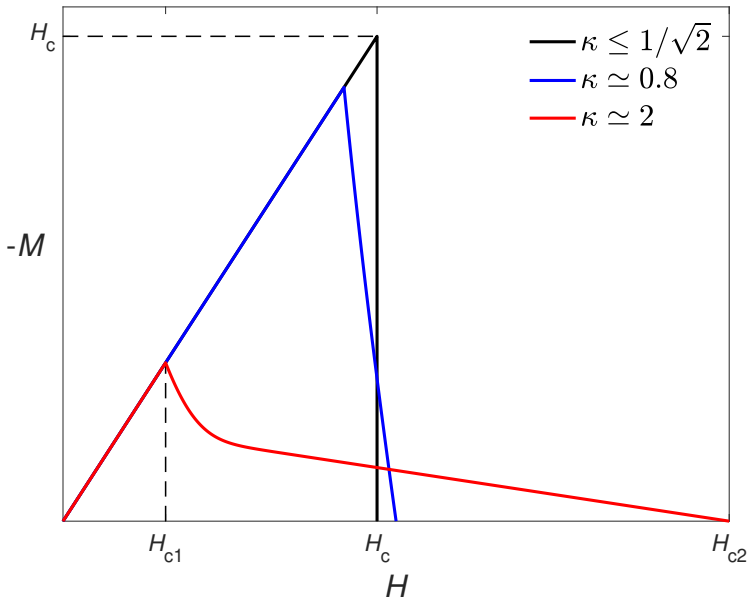


Figure 1.2: Magnetisation against magnetic field ($M(H)$) curves for an ideal type-II superconductor for different values of the order parameter κ. Here the curves have been re-scaled to H_c and factors of μ_0 have been ignored. For $\kappa \leq 1/\sqrt{2}$ (black curve) the superconductor is type$-$I exhibits a first-order transition at H_c. For $\kappa > 1/\sqrt{2}$ (blue and red curves) the superconductor is type-II and shows second-order transitions at H_{c1} and H_{c2}.

applications ($T_c \geq 90$ K). All of these materials consist of copper-oxygen, CuO_2, planes which are thought to dominate the superconducting properties.

Despite the plethora of cuprate superconductors that have been discovered and their intensive study, a theory of why they exhibit superconductivity has yet, at the time of writing, to be established. It is generally agreed that the superconductivity in these materials is d-wave and emerges from an antiferromagnetic Mott insulating ground state. The pairing mechanism however remains unclear, and the most popular theories suggest pairing of electrons through either charge density waves or spin density waves. Perhaps one of the reasons that the pairing mechanism has remained elusive is due to the number of competing electronic phases present in these materials. Despite these, it seems that the magnetic superconducting properties are well captured by the theories discussed here (BCS and GL). The layered structures of cuprate materials lead to extreme anisotropy of the superconducting state, very short coherence lengths and large fluctuation effects. The layered structure also pushes the systems towards two-dimensional behaviour that is only normally expected for de-coupled thin-films (generally thinner than the coherence length).

The parent compounds here are not superconducting, they are usually antiferromagnetic Mott insulators. Upon doping with either electrons or holes the antiferromagnetic state is suppressed and a superconducting dome emerges. On top of the competing antiferromag-

netic phase, many cuprates also exhibit a nematic state and a pseudogaped phase, the latter of which is only usually suppressed at the point at which the transition temperature shows a maximum. There are also arguments that quantum critically can be a driving force for superconductivity in these systems. A quantum critical point occurs when a phase transition is traversed at zero temperature ($0\,\mathrm{K}$) and can give rise to huge fluctuations in a given order parameter. These fluctuations have been proposed to act as a pairing mechanism between electrons to form Cooper pairs. Understanding the interplay between antiferromagnetism, the pseudogap phase, quantum criticality and superconductivity is still a very active area of research today.

The highly anisotropic nature of the crystal structure and superconductivity leads to inter-grain physics dominating the superconducting properties in polycrystalline samples. In particular, inter-grain effects can severely limit the critical current density. This is an obvious problem for practical applications, and grains need to be aligned to within $\sim 3^{\mathrm{o}}$ for proper current propagation. They also have to be processed in high-temperature, high-pressure and oxygen-rich environments to optimise their superconducting properties. Single crystals (and polycrystals) also tend to be ceramic in nature, which is not desirable for practical applications (for example, solenoid magnets need to be wound). Despite these challenges, new tapes and wires of cuprate materials show extremely promising values for upper critical fields, critical current densities and durability.

Unconventional superconductivity, i.e. superconductive pairing that is not explained by convention BCS or GL theory, does not only occur in the cuprate superconductors. Other families such as the heavy fermions, organics and iron-based superconductors are also thought to show unconventional pairing.

It is the different pairing mechanism and gap symmetry that separates these unconventional superconductors from their BCS counterparts. Within the discussions of BCS above the gap, $\Delta_{\mathbf{k}}$, was isotropic over all $\mathbf{k}$ points (due to the spherical symmetry, i.e. s-wave pairing). If a material is not isotropic, one then expects that $\Delta_{\mathbf{k}}$ will now be anisotropic and have a $\mathbf{k}$ dependence. This could arise, for example, in tetragonal systems where there is normally a different gap for $\mathbf{k}$ along the crystallographic c than for $\mathbf{k}$ along a or b. The full spherical symmetry is lacking but superconductivity has the symmetry of the underlying crystal. This is sometimes referred to as anisotropic s-wave pairing. This helps to defined the term unconventional pairing; where the symmetry of $\Delta_{\mathbf{k}}$ is *lower* than that of the crystal.

In cuprate superconductors the pairing appears to be d-wave. Anti-ferromagnetic spin fluctuations have been proposed as the microscopic pairing mechanism, which would lead to $d_{x^2-y^2}$ pairing [14]. This d-wave gap has the underlying symmetry of the orbital ($L = 2$),

and leads to nodes in its k dependence. This does not only give a anisotropic gap in these materials, but also a sign-changing order parameter, which has been shown experimentally through Josephson current measurements in a double-junction dc SQUID (Superconducting Quantum Interference Device) that combines d- and s-wave superconductors [15]. It is not only d-wave superconductors that are thought to have sign-changing order parameters. Iron-based superconductors are believed to have two superconducting s-wave gaps, which are anisotropic due to the underlying symmetry. One such scenario leads to a sign-changing order parameter between the two gaps, usually referred to as $s^{\pm}$ pairing.

1.6 Iron-based superconductors

Iron-based superconductors are a relatively new family of superconductors discovered by H. Hosono in 2008 [16, 17]. These are high-temperature unconventional superconductors, with the transition temperature T_{c} reaching $\sim 50\,\mathrm{K}$ for bulk materials in Li-1111 and Sm-FeAs(O,F) [18, 19] and reports of $\sim 65\,\mathrm{K}$ in FeSe thin films grown in $SrTiO_3$ [20, 21], and $\sim 100\,\mathrm{K}$ in monolayers of FeSe [22]. Like the cuprates, this family of superconductors has a highly anisotropic crystal structure, consisting of Fe-A layers, where the element A is typically As, Se or something similar. These are referred to as iron-chalcogenide or iron-pnictide superconductors. It is in these Fe-A layers that the superconductivity is thought to originate, similar to the CuO_2 layers of the cuprate family. It is generally believed that these materials are two-band s-wave superconductors. The reason behind Cooper pairing, like in the cuprates, is not well understood. However there are popular theories and evidence to support pairing via nematic fluctuations, spin fluctuations or phonons.

Like the cuprates, many of the parent compounds in this family do not show superconductivity and are generally anti-ferromagnetically ordered. Many also show a nematic electronic state. Depending on the compound, doping isoelectronically or with electrons/holes induces superconductivity in these materials. Doping typically suppresses the structural transition temperature for the magnetic/nematic state and superconductivity emerges, as shown in figure 1.3.

These materials are not only of interest for their scientific underpinning, but also for their use in practical applications. Unlike the cuprates, which are ceramic and brittle, iron-based superconductors are metallic or semi-metallic. This makes them far easier to use for wire and coil manufacturing than cuprate superconductors. These materials also generally have high critical current densities, as well as high upper critical fields. This makes them favourable for high-current high-field applications. The grain boundary alignment problem

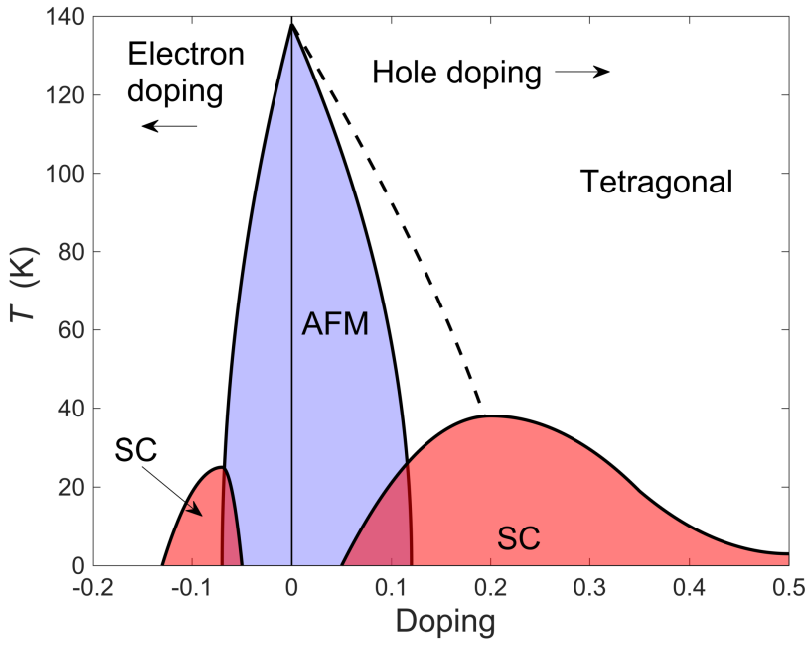


Figure 1.3: Generic temperature-doping phase diagram of an iron-based superconductor. This is based off of the Ba-122 system [23–25]. The antiferromagnetic (AFM) and superconducting (SC) phases that change/emerge upon hole and electron doping are labelled. Here doping is the number of additional electrons (negative) and holes (positive) per unit cell.

is also not as extreme as in cuprate materials, with a critical angle of only $\sim 7^{\mathrm{o}}$ for iron-based superconductors, rather than the 3^{o} for cuprates. Some iron-based superconductors, such as the Ba-122 system, are now being seriously considered for practical applications [19].

One of the major problems with these materials, particular for applications, is the amount of disorder and inhomogeneity introduced with chemical substitution. To achieve the maximum T_{c}, some materials require a $30 - 50\%$ chemical substitution, which introduces this disorder. This can be in the form of point-like defects, sheet dislocations or different substitutional phases within the same crystal. All of these can affect the superconducting properties. Some, like the point-like defects, can enhance some properties through additional vortex pinning (see section 2.2.3). However, generally large amounts of disorder push materials away from the clean limit and start to suppress superconducting properties such as the upper critical field, the critical current density and broaden transition widths. This disorder and inhomogeneity can also change properties of the normal state. This further complicates the problem of studying these materials experimentally and disentangling electronic correlations and superconductivity.

It is thus desirable to study these materials in a limit as clean as possible. This can, by

comparison, give a better understanding of the role played by disorder as well as provide a platform to better study normal state contributions and superconductivity. Thankfully, a number of iron-based superconductors exist that do not require chemical substitution in order to show bulk superconductivity, although their T_c is generally not as high. These are referred to as stoichiometric materials, where all elements appear in the chemical formula in integer form. Two of these materials, FeSe and $CaKFe_4As_4$, will be considered throughout the rest of this thesis.

1.6.1 $FeSe_{1-x}S_x$

The parent compound, FeSe, has a relatively low T_c of ~ 9 K and has the simplest structure of any iron-based (or even high-T_c) superconductor, consisting of only two elements. Unlike other iron-based superconductors it does not show any long-ranged magnetic order at ambient pressure [26], but undergoes a tetragonal to orthorhombic transition upon cooling through $T_s \sim 90$ K where a *nematic* electronic state also emerges [27–30]. This nematic state breaks the C4 rotational symmetry of the lattice. Multiple superconducting gaps have already been reported for this material [31–35], and it has been proposed to be near the BCS-BEC crossover [36, 37]. Despite the lack of long-ranged magnetic order, strong antiferromagnetic spin-fluctuations have been found in FeSe inside the nematic state [38, 39]. FeSe is thus an interesting simple system in which to study superconductivity in a stoichiometric material that has no long-ranged magnetic order. It also offers the opportunity to study the electronic properties of nematicity and antiferromagnetic spin fluctuations.

The structural transition into the nematic phase can be suppressed with chemical substitution of sulphur in $FeSe_{1-x}S_x$ and goes to zero temperature for $x \sim 0.18$ [40], as shown in Figure 1.4 [41]. The superconducting transition temperature remains similar inside the nematic state, peaking at $T_c \sim 10.5$ K for $x \sim 0.11$, but drops dramatically across the nematic end point at $x \sim 0.18$. T_c then remains relatively robust across the rest of the phase diagram to FeS ($x = 1$), where $T_c \sim 4$ K [42].

FeSe has three bands at the Fermi-level at low-temperatures, two electron bands and one hole band [43]. Upon sulphur substitution a second hole band emerges at $x \sim 0.11$ at the Z-point (in k-space) [43], where T_c is maximum. As x is increased through the nematic end point the inner hole band undergoes a Lifshitz transition [41] at the boundary between the orthorhombic and tetragonal states. The four bands, two electron and two hole, then persist across the rest of the phase diagram. As the sulphur substitution x is increased the Fermi surface becomes larger and the charge carrier density increases. However, since the substitution is isoelectronic, these materials should remain compensated (have an equal number

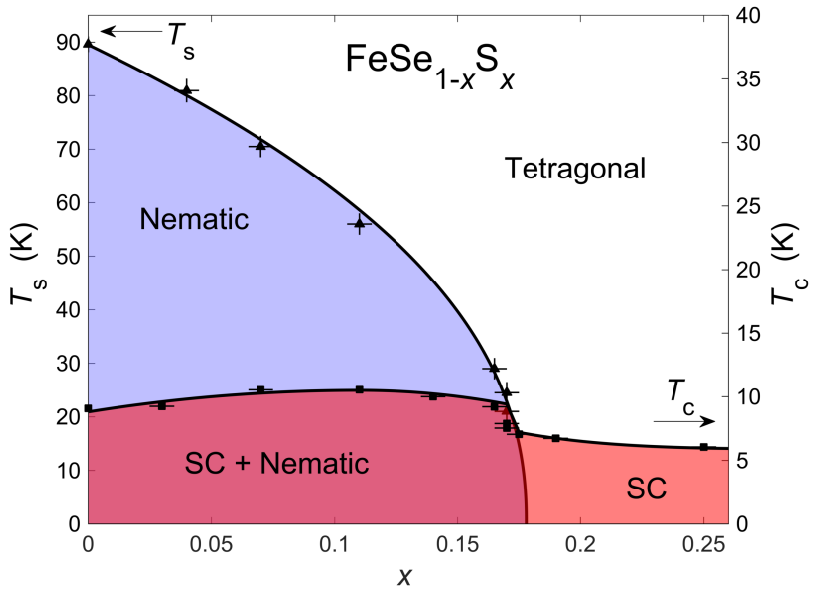


Figure 1.4: The variation of T_{s} (right axis) and T_{c} (left axis) with sulphur substitution in $FeSe_{1-x}S_x$. The tetragonal, nematic and superconducting (SC) phases are labelled.

of electrons and holes). Generally, the Fermi surface becomes more 3D with doping from FeSe to FeS.

Despite the lack of long ranged magnetic order in $FeSe_{1-x}S_x$, antiferromagnetic spin-fluctuations are present in these materials [44, 45]. The magnitude of the spin-fluctuations seem to correlated with T_{c} inside the nematic state and are strongest at low temperature, just before the superconducting transition. Across the nematic end point and into the tetragonal state the spin-fluctuations are severely suppressed [45], perhaps suggesting some link between the electron nematic order and spin-fluctuations. The spin-fluctuations are also strongest at low-temperatures for $x \sim 0.1$, where T_{c} is also at a maximum [45]. This, combined with the suppression of both T_{c} and the magnitude of the spin-fluctuations at the nematic end point perhaps suggests that these fluctuations play a key role in the superconductivity of $FeSe_{1-x}S_x$.

Under applied hydrostatic pressure in FeSe the nematic state is also suppressed [46–48]. Like with sulphur substitution, this also correlates with a drop in T_{c}. However unlike sulphur substitution, a anti-ferromagnetic state emerges at higher pressures and T_{c} increases to $\sim 27\,\mathrm{K}$ [47, 49–52]. Hydrostatic pressure on sulphur doped samples enables the nematic and magnetic states to be separated [50, 52, 53], and T_{c} shows similar behaviour to that of the parent compound [50]. This is evidence that $FeSe_{1-x}S_x$ is near magnetic order and that the superconducting transition temperature can be tuned much higher in these materials. Similarly, applying hydrostatic pressure to sulphur doped samples also suppresses

nematicity (if the compound is originally nematic), a magnetic state emerges and T_c can be enhanced [50, 54].

Superconductivity has also been extensively studied in FeSe thin films. As the thickness is decreased, the T_c is suppressed and the system seems to show a metal-insulator transition [55–57]. Thin films tend to be grown on a particular substrate, such as $SrTiO_3$, which can introduce extrinsic effects such as strain. This, for example, can change the lattice constants and so also effect the electronic properties and superconductivity. Work has also been done on FeSe thin flakes which are exfoliated from bulk single crystals and stamped onto a substrate, rather than grown. This reduces the external strain effects. The thin flakes show similar trends to the thin films. However, superconductivity is not suppressed until a much thinner limit is reached [58]. As the thickness is decreased in thin flakes superconductivity is also pushed towards a 2D limit and a Berezinskii-Kosterlitz-Thouless (BKT) transition is observed [58]. This suggests an interesting manifestation of the dimensionality of superconductivity as the thickness is decreased towards the coherence length. Perhaps the most striking result from FeSe thin films results from the electronic gating of monolayers. Here, the superconductivity can be enhanced up to $\sim 65\,\mathrm{K}$ with gating [20, 21], with some reports showing a T_c increase up to $\sim 100\,\mathrm{K}$ in monolayers of FeSe [22].

There is thus a plethora of physics to explore in $FeSe_{1-x}S_x$ alone, from competing electronic phases to hugely enhanced superconducting transition temperatures. The relatively low T_c present in bulk single crystals means that these materials are not entirely suitable for high-current or high-field applications, but they do provide a good base to study unconventional superconductivity in a clean system. Their relatively low T_c also means they have a relatively low H_{c2}, at a maximum of $\mu_0 H_{c2}(0) \sim 20\,\mathrm{T}$ at $x \sim 0.11$ when $H||c$. This means that superconductivity can be suppressed by using relatively high (but not unachievable) magnetic fields. Thus, phase diagrams, such as $H_{c2}(T)$ can be studied to the lowest temperatures and the normal electronic state can also be accessed.

This thesis presents a series of electrical transport and torque magnetometry measurements of $FeSe_{1-x}S_x$ single crystals. In chapter 6 high-field magneto transport is used to explore the electronic normal state, both at high temperatures far above superconductivity, and down to $\sim 0.3\,\mathrm{K}$ to explore the low temperature dependence of resistivity. Chapters 7 and 8 explore the superconducting state of $FeSe_{1-x}S_x$ inside the nematic state, near the nematic end point and in the tetragonal phase. Upper critical fields are studied down to $\sim 0.3\,\mathrm{K}$ in two magnetic field orientations, $H||c$ and $H||(ab)$. Upper critical fields are described well by a two-band model, and their nature changes significantly across the nematic end point. We also find the results are consistent with the emergence of an FFLO state at low temperature. Chapter 8 focuses on superconducting fluctuations extracted from

electrical transport measurements. These show persistent two-dimensional nature across the nematic end point. These studies reveal important fundamental information about the interplay of nematicity, spin-fluctuations and superconductivity in $FeSe_{1-x}S_x$.

1.6.2 $CaKFe_4As_4$

$CaKFe_4As_4$ is a stoichiometric iron-based superconductor with $T_c \sim 35\,K$. It shows no nematic or magnetic ordering at any temperature [59]. This makes it an unusual iron-based superconductor, as normally superconductivity at these temperatures only emerges from electron or hole doping a material which is normally anti-ferromagnetic. It also appears to be at, or at least near, optimal doping (maximum T_c). Studying superconductivity in this material may thus reveal information about the ingredients necessary to produce this phenomenon in a clean, metallic, stoichiometric system.

$CaKFe_4As_4$ is structurally very similar to the family of 122 iron-based superconductors, in particular it is closest to $Ba_{1-x}K_xFe_2As_2$ (Ba-122), with a reduction of symmetry from $I4/mmm$ to $P4/mmm$ [60]. $CaKFe_4As_4$ has a tetragonal structure, where Ca and K layers stack alternatively across the Fe_2As_2 layer along the c-axis [59, 61]. Fe-As bond distances are different for the As atoms above and below the Fe plane, in contrast to the 122 system that has equivalent Fe-As distances. The lowering of symmetry has significant consequences on the electronic structure of $CaKFe_4As_4$, being that of a compensated metal with a large number of electronic bands close to a nesting instability [62] as well as on its magnetic structure which forms an unusual spin-vortex crystal order by Ni or Co doping [63]. Calculations have shown that $CaKFe_4As_4$ has 8 bands at the Fermi level, 5 hole bands and 3 electron bands (see chapter 5). All of these bands are quasi-2D in nature, similar to other iron-based superconductors, but hole bands have a greater k_z dependence, making them more 3D than the electron bands.

The superconducting transition temperature T_c is suppressed with electron doping of Ni or Co [63], as shown in figure 1.5. An antiferromagnetic phase also emerges with this substitution, which overlaps with the superconducting phase. This is not entirely surprising, as $CaKFe_4As_4$ shows AFM spin-fluctuations and so is likely to be near magnetic order [64]. The magnetic state that emerges has been labelled as a 'hedgehog spin-vortex', an unusual kind of magnetic order which emerges from the slightly different underlying crystal structure [63]. As far as is known, this is the only iron-based superconductor in which this AFM order is present.

The work presented here will however focus on the stoichiometric parent compound, $CaKFe_4As_4$. This is an exceptionally clean system, with short coherence lengths and a large mean free path (see chapter 5). This system thus offers an excellent, possibly unique,

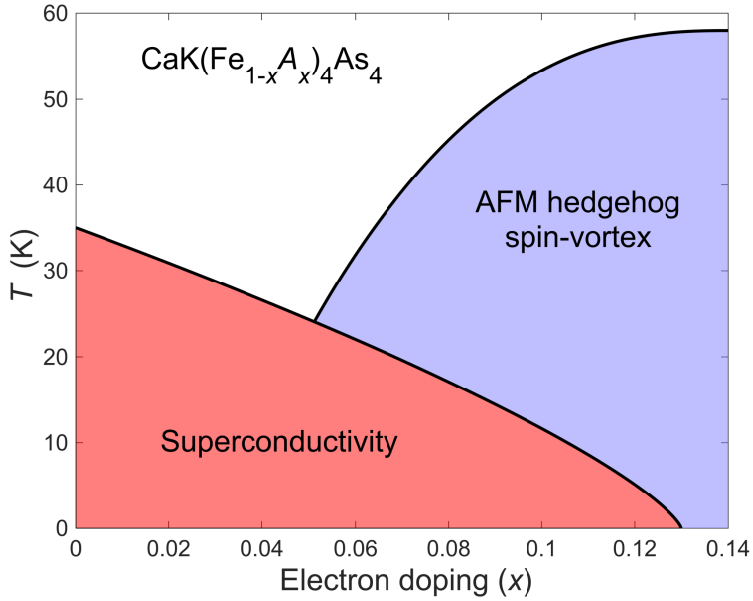


Figure 1.5: Phase diagram of temperature against electron doping for $CaK(Fe_{1-x}A_x)_4As_4$, where A is either Co or Ni and x is the number of electrons substituted onto Fe sites. Superconductivity and the antiferromagnetic (AFM) hedgehog spin-vortex phases are labelled. This was reproduced from Ref. [63].

opportunity to study superconductivity in a very clean and optimally doped system. A series of electrical transport and magnetization measurements have been performed to study the superconducting properties. The magnetization experiments in chapter 4 explore the vortex phase and critical current densities of $CaKFe_4As_4$. The pulsed magnetic field experiments in chapter 5 explore the upper critical fields in this material down to 4.2 K. Based on the results presented later in sections 4 and 5, it is argued that this material is an excellent candidate for practical applications as it has high upper critical fields and exceptionally large critical current densities - the largest of any known iron-based superconductor. These properties, along with the stoichiometry and high purity, make it an excellent candidate for high-field and high-current applications.

1.7 Charge carriers in the normal state

Studying how the charge carriers behave in the normal (non-superconducting) state can give insights into any trends, or changes that occur in the electronic structure on the approach to superconductivity. Unconventional superconductors, like ones that will be considered in this thesis, also tend to show unusual electronic phases, such as the pseudogap phase or the nematic state mentioned above. This provides the opportunity to study the properties

of these unusual phases as well, but can make untangling any contributions to superconductivity more difficult. On top of this, the iron-based superconductors that we will be considering here have multiple bands present at the Fermi level. This can again complicate the understanding of the contributions of different charge carriers. Thus, it is essential to first cover the more basic principles and the kind of behaviour we might expect to emerge before moving on to more complicated problems.

1.7.1 Charge carriers in metals

There are a number of approaches one can take to find the basic behaviour of charge carriers in a metallic lattice. The strength of interactions between (quasi)particles, amount of disorder and different temperature regimes are some of the things we will consider in this section.

The first model to describe transport properties of electrons in metals was proposed by Drude in 1900 [65], and is hence called the Drude model. This considers a sea of electrons moving in a lattice of positive ions, and assumes the microscopic behaviour of the electrons is governed by collisions with the positive ions. This assumes that there is some mean scattering time between collision, τ and that electrons travel with an average velocity. Perhaps the most important result of this theory is that it returns a form of Ohms law, $\mathbf{J} = \sigma_0 \mathbf{E}$ at zero temperature, where $\mathbf{J}$ is the current density, $\mathbf{E}$ is the electric field and

$$\sigma_0 = \frac{nq^2\tau}{m_e} = \frac{1}{\rho_0} \tag{1.32}$$

is the zero temperature conductivity, which is the inverse of the zero temperature resistivity. Here n is the electron density, q is the charge of carriers (e) and m_e is the electron mass. Using the Fermi velocity, v_{F}, the mean free path of charge carriers, ℓ, can be defined as

$$\ell = v_{\mathrm{F}}\tau. \tag{1.33}$$

This was expanded in 1928, when Arnold Sommerfeld combined the Drude model with Fermi-Dirac statistics and built the Free Electron Model [66]. The lattice is not explicitly accounted for in the Free Electron model, but a justification is provided by Bloch's theorem. For a three-dimensional electron gas, this gives the Fermi energy as

$$E_{\mathrm{F}} = \frac{\hbar^2}{2m_e}(3\pi^2 n)^{2/3}. \tag{1.34}$$

Using equation 1.32 for the scattering time, $v_{\mathrm{F}} = \sqrt{E_{\mathrm{F}}/2m_e}$ and equation 1.33 gives the mean free path in the Free Electron Model as

$$\ell = \frac{1}{\rho_0}\left(\frac{3\pi^2}{n^2}\right)^{1/3}\frac{\hbar}{e^2}, \tag{1.35}$$

giving a relationship between the mean free path and zero temperature resistivity that depends only on the electron density.

From arguments already made in previous section, we can see that finding ℓ is important in identifying whether materials are in the clean or dirty limit for superconductivity. ℓ and ρ_0 also give us information about the level, or at least the relative amount, of disorder present in a system. However, since below T_c in no applied magnetic field the resistivity of a superconductor is zero, the ρ_0 of the normal state can be difficult to extract. Methods of extracting it will be discussed later.

So far we have considered the zero temperature limit, but the temperature dependence of variables can also give information about a system. In fact, this often provides more details. The first important result considered here was predicted by *Fermi-liquid theory*, which showed at low enough temperatures the resistivity of a metal would vary as

$$\rho(T) = \rho_0 + AT^2, \tag{1.36}$$

where A is a coefficient with units K^{-2}. At higher temperatures, where thermal effects become more important, we expect *phonons* to dominate the scattering of charge carriers, which results in a *linear temperature dependence*, $\rho(T) \propto T$ (it should be noted that phonons give a $\rho(T) \propto T^5$ dependence at very low temperatures).

Materials that do not obey Fermi-liquid theory are often refereed to as *non-Fermi liquids*, or *strange metals*. We shall see later that this applies to the majority of materials that will be considered in the studies presented here. Generally, we then define the resistivity versus temperature with the equation

$$\rho(T) = \rho_0 + AT^\gamma, \tag{1.37}$$

where γ is a dimensionless temperature exponent. This can be considered even more broadly using $\gamma \to \gamma(T)$.

1.7.2 Electrons in a magnetic field

Superconductivity can be suppressed by applying a magnetic field, and so understanding the behaviour of normal electrons can be essential. Generally, scattering in a magnetic field is governed by $\omega_\mathrm{c}\tau$, where ω_c is the cyclotron frequency. Figure 1.6 illustrates the path charge carriers take in zero magnetic field (left) and in an applied magnetic field (right). In zero field, the charge carriers travel some mean free path $\ell(0)$ before a scattering event occurs. When a magnetic field is applied the electrons/holes experience a Lorentz force, $\mathbf{F} = q\mathbf{v} \times \mathbf{B}$, which bends the path of the particle (here in figure 1.6 we are assuming

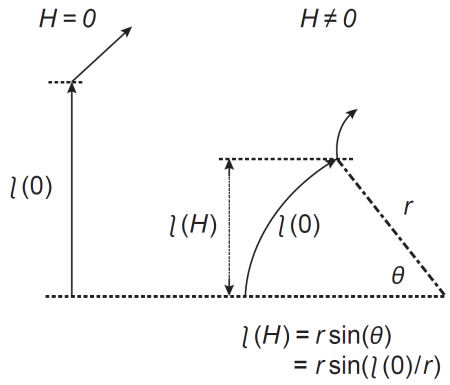


Figure 1.6: The path of charge carriers in zero magnetic field (left) and in a magnetic field (right). This assumes $M = 0$, and so $B = \mu_0 H$. Here ℓ is the mean free path and the magnetic field is perpendicular to the page (towards the reader).

that the magnetic field is perpendicular to the direction of travel at velocity $\mathbf{v}$, otherwise expressed as $\mathbf{B} \perp \mathbf{J}$). The curved path is now still $\ell(0)$, but the longitudinal distance that the charge carrier has actually travelled is $\ell(H)$, which is less than $\ell(0)$.

For a single-band metal, the change in resistivity is given by

$$\frac{\Delta\rho_{xx}}{\rho} = (\omega_c\tau)^2 = \left(\frac{eB\tau}{m}\right)^2 = \left(\frac{ne^2\tau}{m}\frac{1}{ne}\right)^2 B^2. \tag{1.38}$$

Working through the mathematics [67, 68], it can be shown that for a single-band metal the longitudinal resistivity (the resistivity in the direction of current flow) in a magnetic field should have the form

$$\rho_{xx} = \rho_{H=0} + aB^2 = \rho_{H=0} + a(\mu_0 H)^2, \tag{1.39}$$

where $\rho_{H=0}$ is the zero field resistivity (technically here we should use $\rho_{H=0} = \rho_{H=0}(T)$), B is the internal magnetic field, $\mu_0 H$ is the applied magnetic field and a is coefficient with units T^{-2}. The finally equality in this equation holds in the limit where the magnetization, M, is small. By using substitutions from equations 1.32 and 1.41, the last equality in equation 1.38 can be shown to result in a certain scaling known as Kohler's rule [67, 68], where

$$\frac{\Delta\rho_{xx}}{\rho_{H=0}} = \left(\frac{R_H}{\rho_{H=0}}\right)^2 H^2 \propto \left(\frac{H}{\rho_{H=0}}\right)^2. \tag{1.40}$$

Since for a Fermi-liquid we also have $\rho_{H=0}(T) \propto T^2$, this rule gives a single scaling curve in $\Delta\rho_{xx}/\rho_{H=0} \propto (H/\rho_{H=0})^2 \propto (H/T)^2$ which should be obeyed for Fermi-liquids with a single scattering time.

1.7.3 Hall effect

The Lorentz force on electrons does not only lead to a longitudinal contribution to the resistivity, but also a transverse one, ρ_{xy}. This is known as the *Hall effect*, R_{H}. The first important feature of the Hall effect is that it is zero in zero magnetic field, as we would expect, and for a single scattering time should result in a linear dependence in magnetic field, $\rho_{\mathrm{xy}} = R_{\mathrm{H}}B = R_{\mathrm{H}}\mu_0 H$. R_{H} is defined as the slope of the Hall effect (usually in low fields), and is described by

$$R_{\mathrm{H}} = -\frac{1}{ne}, \tag{1.41}$$

for a single band (i.e. simple metal) where n is the carrier density and e is the charge of the carriers. This has two main implications for systems with a single scattering time. First, the Hall effect can be used to find the carrier density, n, and second, the sign of the Hall effect determines whether the system consists of electrons or holes.

1.7.4 Multi-band description

Thus far, our discussion of the normal electronic state has been limited to systems with a single-band and a single scattering time, generally with elliptical Fermi surfaces. As mentioned above, iron-based superconductors are multi-band materials, often with three, four, or more bands at the Fermi level. Some of these bands may have little, or no, contribution to scattering, but we should consider the effects multiple bands have on the electrical conduction and resistivity. This is actually a rather complicated problem in iron-based superconductors, as many of the bands present are warped cylinders, rather than ellipses, making them quasi-2D in nature. They also, generally, do not have a single Fermi velocity, v_{F}, for each band. This means there can be multiple scattering times even on one of the bands, complicating the problem here further. Electrical transport in iron-based superconductors, particularly the Hall effect, is still an open theoretical field today.

However, with some sensible assumptions, we can begin to build up a more accurate description of the effect of applying a magnetic field on the resistivity. This model was first proposed in Ref. [69]. If we consider a system of elliptical Fermi surfaces, each of which have their own scattering time τ, mobility μ and carrier density n, with $H||c$ the conductivities can be expressed as

$$\sigma_{\mathrm{xx}}[H] = \mathrm{F}_{\mathrm{xx}}[H] = \sum_i \frac{|en_i\mu_i|}{1+\mu_i^2H^2} \tag{1.42}$$

and

$$\sigma_{\mathrm{xy}}[H] = \mathrm{F}_{\mathrm{xy}}[H] = \sum_i \frac{en_i\mu_i^2H}{1+\mu_i^2H^2} \tag{1.43}$$

where σ_{xx} and σ_{xy} are the conductivities of the in-plane and Hall component respectively. n_i and μ_i are the density and mobility of band i, and H is the magnetic field. For simplicity, we define the conductivity of each band as $\sigma_i = en_i\mu_i$. The conductivities here are elements of the tensor

$$\sigma = \begin{pmatrix} \sigma_{\mathrm{xx}} & \sigma_{\mathrm{xy}} \\ \sigma_{\mathrm{yx}} & \sigma_{\mathrm{yy}} \end{pmatrix}, \tag{1.44}$$

where we set $\sigma_{\mathrm{xx}} = \sigma_{\mathrm{yy}}$ and $\sigma_{\mathrm{xy}} = -\sigma_{\mathrm{yx}}$. Resistivity elements can be found by inverting this tensor, giving

$$\rho_{\mathrm{xx}} = \frac{\sigma_{\mathrm{xx}}}{\sigma_{\mathrm{xx}}^2 + \sigma_{\mathrm{xy}}^2}, \quad \rho_{\mathrm{xy}} = \frac{\sigma_{\mathrm{xy}}}{\sigma_{\mathrm{xx}}^2 + \sigma_{\mathrm{xy}}^2}, \tag{1.45}$$

for the transverse-field (resistivity in the direction of current flow with $I \perp H$) and Hall components respectively. This analysis has been performed previously on other iron-based superconductors [69] and on $FeSe_{1-x}S_x$ [48, 70–72]. Values of the mobilities and densities are found by minimising the form

$$\sum_k \left[\left(\frac{\sigma_{\mathrm{xx}}[H_k] - \mathrm{F}_{\mathrm{xx}}[H_k]}{\sigma_{\mathrm{xx}}[H_k]} \right)^2 + \left(\frac{\sigma_{\mathrm{xy}}[H_k] - \mathrm{F}_{\mathrm{xy}}[H_k]}{\sigma_{\mathrm{xy}}[H_k]} \right)^2 \right], \tag{1.46}$$

where σ_{xx} and σ_{xy} are the raw data, F_{xx} and F_{xy} are the fitted forms from equations 1.42 and 1.43, and k is the index for each magnetic field point. This form is minimised to produce fits to the experimental data. To perform this analysis, it has been assumed that each sample is perfectly compensated; *i.e.* that the total number of holes and electrons is the same, $n_{\mathrm{h}} = n_{\mathrm{e}}$, as should be true for $FeSe_{1-x}S_x$. This also means that the total number of independent variables over which fits are performed is reduced by 1. This assumption has been tested by performing uncompensated ($n_{\mathrm{h}} \neq n_{\mathrm{e}}$) two band fits where relevant, which match the compensated fits exceptionally well, returning density (and mobility) values for the hole and electron band very similar to those produced by the compensated model.

This model has a few caveats and cases in which it fails. For example, in the single-band case here $\rho_{\mathrm{xx}}(H) = 1/|en\mu|$ is constant and independent of the applied magnetic field. This result contradicts equation 1.39 above. The single band case does however return the expected Hall effect of $\rho_{\mathrm{xy}} = H/en$.

Next, we consider the two-band compensated case. Here, the transverse-field resistivity ρ_{xx} is given by

$$\frac{\Delta\rho_{\mathrm{xx}}}{\rho_{H=0}} = \frac{\sigma_1\sigma_2(\mu_1 - \mu_2)^2H^2}{(\sigma_1 + \sigma_2)^2 + (\sigma_1\mu_2 + \sigma_2\mu_1)^2H^2}, \tag{1.47}$$

where $\rho_{H=0} = 1/(\sigma_1 + \sigma_2)$ and $\Delta\rho_{\mathrm{xx}} = \rho_{\mathrm{xx}} - \rho_{H=0}$. This can be rearranged to give

$$\rho_{\mathrm{xx}} = \rho_{H=0} + \frac{1}{(\sigma_1 + \sigma_2)^3} \frac{\sigma_1\sigma_2(\mu_1 - \mu_2)^2H^2}{1 + \frac{(\sigma_1\mu_2 + \sigma_2\mu_1)^2}{(\sigma_1 + \sigma_2)^2}H^2} = \rho_{H=0} + \frac{\alpha H^2}{1 + \beta H^2}, \tag{1.48}$$

where

$$\alpha = \frac{\sigma_1\sigma_2(\mu_1 - \mu_2)^2}{(\sigma_1 + \sigma_2)^3} \quad \text{and} \quad \beta = \frac{(\sigma_1\mu_2 + \sigma_2\mu_1)^2}{(\sigma_1 + \sigma_2)^2}. \tag{1.49}$$

Thus, the two-band model can be expressed in a simple form (the last equality in equation 1.48), dependent on only three parameters. This will be used later.

1.7.5 Other factors affecting normal state properties

Iron-based superconductors show a number of competing phases, which we may expect to contribute to transport properties. Long-ranged magnetic order, the electron nematic state, antiferromagnetic spin fluctuations and nematic fluctuations are some of the phenomena that may contribute to transport properties. It is not theoretically understood how some of these states manifest in transport properties, especially in an applied magnetic field. The electronic characteristics of the nematic phase, where spin-fluctuations are also present, in $FeSe_{1-x}S_x$ is something that will be experimentally explored in a later chapter.

Transport properties within and proximal to magnetic phases have been explored in detail, where quantum criticality is thought to dominate. A quantum critical point occurs when a second order phase transition is suppressed, using a particular order parameter such as chemical substitution or physical pressure, to zero temperature. These order parameters, or tuning parameters vary, but generally charge doping, chemical pressure or applied pressure (usually hydrostatic) are used. These change the electronic structure by either doping the material or changing the lattice parameters. Near a quantum critical point, characteristic length scales tend to diverge, resulting in strong fluctuations (related to the type of order being suppressed) and giving unusual transport properties. One way in which they manifest that we can access experimentally is with different transport exponents γ, from equation 1.37 [73]. For example, as $T \to 0$ near an antiferromagnetic quantum critical point one expects $\gamma = 1$ [74]. The amount of disorder present in a system can also change the transport exponents, which has been shown previously [75].

In summary, there are many factors that can affect the transport properties of the normal state in unconventional superconductors. Understanding them is of key importance, and will form part of the discussions, particularly in chapter 6.

Chapter 2

Vortex Physics

This chapter will introduce some of the more advanced and interesting characteristics of the vortex state in type$-$II superconductors. This will include a more detailed discussion of the upper critical field(s), with a particular emphasis on how it can be modelled for a multi-band system. Next, the nature of vortices in high-temperature superconductors will be covered, from the nature of vortex pinning and flux flow to how the critical current density can be found from magnetisation data. Finally this chapter will give an overview of fluctuations that arise from superconductivity, with a focus on the conductivity above the superconducting transition temperature.

2.1 Upper critical fields

The upper critical field $\mu_0 H_{c2}$, introduced in section 1.3, is an important property of superconductivity. First, and perhaps most importantly, it defines the practical limit for applications. But there is more information about the physics of a system that can be extracted from H_{c2}. Some of this can be inferred from expressions already discussed, such as extracting the coherence length. There are a number of approaches to this that will be discussed below.

2.1.1 Coherence lengths

First, one can extract the coherence length with an application of GL theory. For a more general case here we will consider an anisotropic superconductor, governed by anisotropic upper critical fields (and two coherence lengths) when the magnetic field is applied along different high symmetry axes. In the first case, when the magnetic field is applied parallel to the crystallographic c-axis, $H||c$, the GL coherence length of Cooper pairs forming

screening orbits in the (ab)-plane can be written as

$$\xi_{ab}^{\mathrm{GL}} = \sqrt{\frac{\Phi_0}{2\pi T_{\mathrm{c}} \mu_0 \left|\frac{dH_{\mathrm{c2}}^{c}}{dT}\right|_{T_{\mathrm{c}}}}}. \tag{2.1}$$

Here $\mu_0 |dH_{\mathrm{c2}}^{c}/dT|_{T_{\mathrm{c}}}$ is the slope of H_{c2}^{c} (when $H||c$) in the limit of T near T_{c}. This is essentially derived from equation 1.21, where H_{c2} is estimated at zero temperature as $T_{\mathrm{c}}\mu_0 |dH_{\mathrm{c2}}^{c}/dT|_{T_{\mathrm{c}}}$, i.e. a linear dependence. The GL coherence length when $H||(ab)$ can be written as

$$\xi_{c}^{\mathrm{GL}} = \frac{\Phi_0}{2\pi T_{\mathrm{c}} \mu_0 \left|\frac{dH_{\mathrm{c2}}^{ab}}{dT}\right|_{T_{\mathrm{c}}} \xi_{ab}^{\mathrm{GL}}}, \tag{2.2}$$

where now $\mu_0 |dH_{\mathrm{c2}}^{ab}/dT|_{T_{\mathrm{c}}}$ is the slope of H_{c2}^{ab} (when $H||(ab)$) near T_{c}. The upper critical field when $H||(ab)$, H_{c2}^{ab}, does not depend solely on a single coherence length as it is affected by both in-plane and inter-plane screening, hence why equation 2.2 for ξ_{c}^{GL} also depends on the in-plane coherence length ξ_{ab}.

One issue with using the GL model for the anisotropic coherence lengths here is the assumed temperature dependence (the linear dependence of H_{c2} with temperature). Because of this, H_{c2} at low temperature is often overestimated and so equations 2.1 and 2.2 underestimate the coherence lengths. One modification for this is to introduce a factor of 0.69 (dirty limit) to 0.73 (clean limit) into the gradients near T_{c} (see WHH model below) to account for the general shape of H_{c2} in single-band superconductors. This, however, does not account for other effects, such as Pauli paramagnetism, that can change the upper critical field.

The most accurate way to determine the coherence lengths is to measure the upper critical field down to lowest temperatures. Then, the above equations can be modified to give

$$\xi_{ab} = \sqrt{\frac{\Phi_0}{2\pi \mu_0 H_{\mathrm{c2}}^{c}(T \to 0)}}, \tag{2.3}$$

and

$$\xi_{c} = \frac{\Phi_0}{2\pi \mu_0 H_{\mathrm{c2}}^{ab}(T \to 0)\xi_{ab}}, \tag{2.4}$$

where ξ_{ab} and ξ_{c} are the true zero temperature coherence lengths. Here $H_{\mathrm{c2}}(T \to 0)$ is the upper critical field as the temperature goes to zero (note we use $T \to 0$ as we can never *actually* measure H_{c2} at $T = 0$).

Finding coherence lengths gives us an estimate of the size of vortices in the system, and so also an appropriate length scale for certain interactions. When combined with measurements of the penetration depth λ (which can also be anisotropic), it allows a value of

the parameter κ to be estimated. Comparing coherence lengths to the mean free path ℓ also enables us to determine if the material is in the clean or dirty limit. Thus, the coherence lengths are important parameters we can extract, giving our first motivation for studying upper critical fields.

2.1.2 Orbital and Pauli paramagnetic effects

The upper critical field can be limited by a number of different factors, dependent on elements such as the Fermi surface, coherence lengths, Fermi velocities and orientation in magnetic field. For example, a conventional type-II isotropic superconductor will have the same upper critical field along all high symmetry directions, giving a single coherence length.

The first limiting case we shall consider is from orbital contributions. This essentially manifests as a saturation of the vortex lattice as the normal vortex cores start to overlap, resulting in equation 2.3. This gives the orbitally limited upper critical field, $H_{\rm orb}$, and is generally the limit of the upper critical field for type-II superconductors in the absence of other effects that suppress $H_{\rm c2}$.

One such effect is Pauli paramagnetism, or Pauli pair-breaking. Here, as the magnetic field becomes larger and approaches the Zeeman energy, one of the spins in a Cooper pair flips, breaking the quasi-particle (Cooper pair) apart. If this is at a lower field than the orbital limit, then $H_{\rm c2}$ is suppressed. This results in a rather different temperature dependence of $H_{\rm c2}$, depending on the magnitude of the paramagnetic pair-breaking contribution, as shall be explored later. The limit here is known as the Pauli field, $H_{\rm P}$, which is related to the orbital field by [76]

$$H_{\rm P}(0) = \frac{H_{\rm orb}(0)}{\sqrt{1+\alpha_{\rm M}^2}}, \tag{2.5}$$

where $\alpha_{\rm M}$ is the Maki parameter and the magnitude of the paramagnetic contribution [76]. Note in the case of $\alpha_{\rm M} = 0$ (no paramagnetic contribution), we have $H_{\rm P} = H_{\rm orb}$. The Maki parameter can also be defined by $\alpha_{\rm M} = \sqrt{2}H_{\rm orb}(0)/H_{\rm P}^{\rm BCS}(0)$, where $H_{\rm P}^{\rm BSC}$ is the BCS Pauli field [77]. Here it is also convenient to defined the BCS Pauli paramagnetic field in the week coupling limit as $\mu_0 H_{\rm P}^{\rm BCS}(0) = 1.84 T_{\rm c}$, at $T = 0$.

2.1.3 The WHH model

With the coherence lengths above we have started to discuss the upper critical field in its two extreme limits, near $T_{\rm c}$ and as $T \to 0$. Here we will start to consider the full temperature dependence of $H_{\rm c2}$ and describing it in a single-band model. The first upper

critical field model we will consider was developed by Werthamer, Helfand and Hohenberg, and is known as the WHH model [78]. This is used to describe single-band superconductors in the dirty limit ($\ell \ll \xi$). It includes paramagnetic limiting effects as well as contributions to the upper critical field from spin-orbit scattering. Here the upper critical field is described by

$$\ln\left(\frac{1}{t}\right) = \sum_{\nu=-\infty}^{\infty}\left\{\frac{1}{|2\nu+1|} - \left[|2\nu-1| + \frac{\bar{h}}{t} + \frac{(\alpha\bar{h})^2}{|2\nu+1| + (\bar{h}+\lambda_{\mathrm{SO}})/t},\right]^{-1}\right\} \quad (2.6)$$

where ν is the summing index (other parameters are defined below). This equation can be cast into a more convenient form, removing the summation, to give

$$\ln\left(\frac{1}{t}\right) = \left(\frac{1}{2} + \frac{i\lambda_{\mathrm{SO}}}{4\gamma}\right)\psi\left(\frac{1}{2} + \frac{\bar{h} + \frac{1}{2}\lambda_{\mathrm{SO}} + i\gamma}{2t}\right) + \left(\frac{1}{2} - \frac{i\lambda_{\mathrm{SO}}}{4\gamma}\right)\psi\left(\frac{1}{2} + \frac{\bar{h} + \frac{1}{2}\lambda_{\mathrm{SO}} - i\gamma}{2t}\right) - \psi\left(\frac{1}{2}\right), \quad (2.7)$$

where $t = T/T_{\mathrm{c}}$ is the reduced temperature, $\bar{h}$ is the reduced magnetic field, λ_{SO} is the spin-orbit scattering term, $\gamma = [(\alpha_{\mathrm{M}}\bar{h})^2 - (\lambda_{\mathrm{SO}}/2)^2]$, α_{M} is the Maki parameter and ψ is the di-gamma function. The reduced magnetic field is given by $\bar{h} = (4/\pi^2)H_{\mathrm{c2}}/|-dH_{\mathrm{c2}}/dt|_{t=1}$ where $|dH_{\mathrm{c2}}/dt|_{t=1}$ is the magnitude of the slope of the upper critical field near T_{c}. Here, as in equation 2.5, the Maki parameter represents the Pauli paramagnetic effects which (generally) suppress H_{c2}. It is a dimensionless variable, and in the WHH model described by

$$\alpha = \frac{3}{2m^{\star}v_{\mathrm{F}}\tau}, \quad (2.8)$$

where $m^{\star}$ is the effective mass, v_{F} is the Fermi velocity and τ is the total scattering rate. The spin-orbit scattering term λ_{SO} has the effect of enhancing H_{c2}, but should only be considered when $\alpha_{\mathrm{M}} \neq 0$. It is described by

$$\lambda_{\mathrm{SO}} = \frac{1}{3\pi T_{\mathrm{c}}\tau_2}, \quad (2.9)$$

where τ_2 is the spin-orbit scattering time. Note $\tau^{-1} = \tau_1^{-1} + \tau_2^{-1}$ and τ_1 is the mean scattering time from orbital effects. Examples of the WHH model with different parameters are shown in figure 2.1. Here $h^{\star}$ is plotted against the reduced temperature T/T_{c}, where $h^{\star} = (\pi^2/4)\bar{h}$.

In the absence of paramagnetic effects and spin-orbit scattering ($\alpha_{\mathrm{M}} = 0$ and $\lambda_{\mathrm{SO}} = 0$), the zero temperature value of H_{c2} can be predicted in this model as

$$\mu_0 H_{\mathrm{c2}} = -0.69 T_{\mathrm{c}}\mu_0\left(\frac{dH_{\mathrm{c2}}}{dT}\right)_{T_{\mathrm{c}}}. \quad (2.10)$$

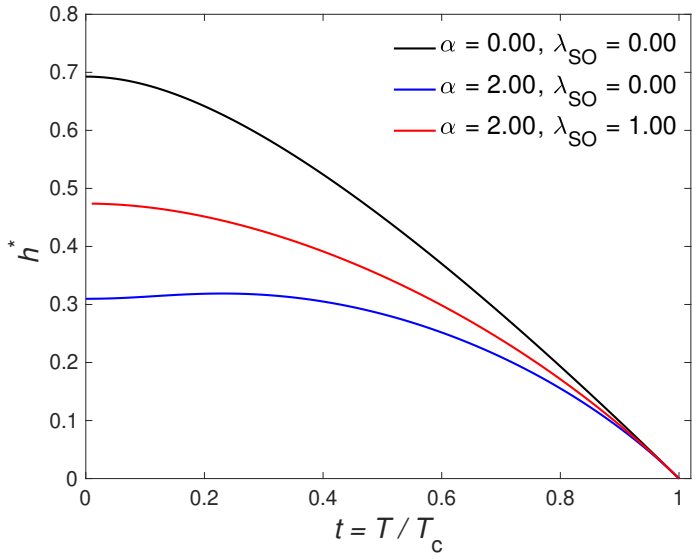


Figure 2.1: $h^\star$ against reduced temperature for three examples of the WHH model, using the parameters as labelled.

This is the same as the orbitally limited critical field, $H_{\rm orb}$, discussed above. In the clean limit, the prefactor is replaced by -0.73.

This model has been shown to work well for many different superconductors, from conventional s-wave type-II materials to unconventional d-wave systems. It has also been shown to describe the temperature dependence of H_{c2} for a number of iron-based superconductors.

2.1.4 Gurevich two-band model (dirty limit)

Iron-based superconductors are multi-band systems and have been shown in a number of experiments to have multiple superconducting gaps, usually manifesting on different bands. Because of this the temperature dependence of a number of their parameters, such the superfluid density ($\rho_{\rm s}$) and the penetration depth λ, cannot be describe in a single-band model. This has lead to the development of a number of multi-band theories of superconductivity to describe the evolution of these parameters. This is the case for the upper critical field which, as we will see below, can change significantly in a multi-band model. Here, we will consider two different two-band models of the upper critical field, both developed by A. Gurevich.

The first model we are going to cover is the two-band model in the *dirty limit* [79]. This model is constructed from the Usadel theory [80] and considers two elliptical Fermi-

surfaces. In this model, the upper critical field is described by

$$a_1[\ln t + U(h)] + a_2[\ln t + U(\eta h)] + a_0[\ln t + U(h)][\ln t + U(\eta h)] = 0, \qquad (2.11)$$

where $t = T/T_c$ is the reduced temperature, $h = H_{c2}D_1/2\Phi_0 T$ is the reduced magnetic field, $\eta = D_2/D_1$ and D_i is the diffusivity of band i. Here the prefactors are defined as $a_0 = 2w/\lambda_0$, $a_1 = 1+\lambda_-/\lambda_0$ and $a_2 = 1-\lambda_-/\lambda_0$, and $\lambda_\pm = \lambda_{11} \pm \lambda_{22}$, $w = \lambda_{11}\lambda_{22} - \lambda_{12}\lambda_{21}$ and $\lambda_0 = (\lambda_-^2 + 4\lambda_{12}\lambda_{21})^{1/2}$. Here λ_{ij} represents a coupling constant between bands i and j, and as the cross-terms λ_{12} and λ_{21} only appear together we set $\lambda_{21} = \lambda_{12}$ for simplicity. The function $U(x)$ is defined as $U(x) = \psi(x + 1/2) - \psi(1/2)$ where ψ is again the digamma function. Note that this model does not include paramagnetic effects or spin-orbit scattering, unlike the WHH model above. For $\eta = 1$ this reduces down to $\ln(t)+U(h) = 0$, which is equivalent to the WHH model in the dirty limit with no paramagnetic effects or spin-orbit scattering [79]. Examples of equation 2.11 in different limits are shown in figure 2.2.

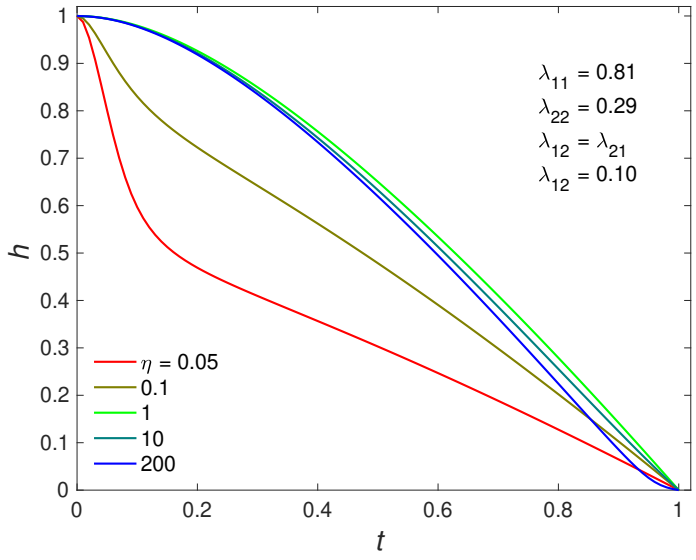


Figure 2.2: Reduced magnetic field, h, against reduced temperature, t, for examples of the Gurevich two-band model in the dirty limit, described by equation 2.11 for various values of η. These curves have been produced using the band coupling parameters $\lambda_{11} = 0.81$, $\lambda_{22} = 0.29$ and $\lambda_{12} = \lambda_{21} = 0.1$ (typical values for dirty two-band superconductors, such as MgB_2).

This model has been shown to work well for certain systems, particularly if they are in the dirty limit. Perhaps the best known example is MgB_2. For the case of $\eta = 1$ (equal band diffusivities) equation 2.11 has the solution $\ln(t) + U(h) = 0$, which is the case for a single-band dirty superconductor [78].

2.1.5 Gurevich two-band model (clean limit)

We will find that the systems presented in the studies below are all in the *clean limit*. This gives motivation to consider another model developed by A. Gurevich [81]. This model incorporates two ellipsoidal bands in the *clean limit*, includes paramagnetic and inter-band effects, and is based off of Eliashberg theory. The upper critical field is governed by the equation

$$a_1[\ln t + U_1] + a_2[\ln t + U_2] + [\ln t + U_1][\ln t + U_2] = 0, \tag{2.12}$$

where $a_1 = (\lambda_0 + \lambda_-)/2w$, $a_2 = (\lambda_0 - \lambda_-)/2w$, $\lambda_\pm = \lambda_{11} \pm \lambda_{22}$, $w = \lambda_{11}\lambda_{22} - \lambda_{12}\lambda_{21}$ and $\lambda_0 = (\lambda_-^2 + 4\lambda_{12}\lambda_{21})^{1/2}$. Here λ_{ij} represents a coupling constant between bands i and j, and as the cross-terms λ_{12} and λ_{21} only appear together we set $\lambda_{21} = \lambda_{12}$ for simplicity. U is defined as $U = U(t, h, \alpha, q, \eta, s)$ where

$$U = 2e^{q^2 s}\mathrm{Re}\sum_{n=0}^{\infty}\int_{q\sqrt{s}}^{\infty} du e^{-u^2}\left(\frac{u}{n+1/2} - \frac{t}{\sqrt{h\eta}}\tan^{-1}\left[\frac{u\sqrt{h\eta}}{t(n+1/2) + i\alpha h}\right]\right). \tag{2.13}$$

The U functions are defined as $U_1 = U(t, h, \alpha, q, 1, 1)$ and $U_2 = U(t, h, \alpha, q, \eta, s)$ and the variables b, α, q, η and s are defined as

$$\begin{aligned} h &= \frac{\hbar^2 v_1^2 H}{8\pi\phi_0 k_\mathrm{B}^2 T_\mathrm{c}^2}, \quad \alpha = \frac{4\mu\phi_0 k_\mathrm{B} T_\mathrm{c}}{\hbar^2 v_1^2}, \\ q^2 &= \frac{Q_z^2\phi_0\epsilon_1}{2\pi H}, \quad \eta = \frac{v_2^2}{v_1^2}, \quad s = \frac{\epsilon_2}{\epsilon_1}. \end{aligned} \tag{2.14}$$

v_i is the Fermi velocity of band i, H is the magnetic field, Q_z is the magnitude of the Fulde-Ferrell-Larkin-Ovchinnikov (FFLO) modulation and ϵ_i is proportional to the effective mass of band i.

This model goes further than the dirty limit two-band description of the upper critical field in a number of ways. First, as mentioned above, it includes paramagnetic limiting effects. These can be extended further by defining a different α for each band, i.e. α_1 and α_2. The band coupling constants, λ_{11}, λ_{22} and $\lambda_{12} = \lambda_{21}$, also allow for different kinds of scattering/pairing. λ_{11} and λ_{22} describe the *intra-band* pairing (i.e. on the same band) for the two respective bands, while λ_{12} and λ_{21} describe *inter-band* pairing between the two bands. Note that the inter-band parameters only ever appear as the product $\lambda_{12}\lambda_{21}$, and so one can set $\lambda_{12} = \lambda_{21}$ for simplicity as they are indistinguishable (this also reduces the parameter space by 1, making computations of this model easier and faster). From the different band coupling constants, we can then define some limits on the type of superconductivity they emerge from. In the limit where $\lambda_{11}\lambda_{22} \gg \lambda_{12}\lambda_{21}$ the system is dominated by *intra-band* pairing. This could, for example, place a system in the s^{++} pairing limit.

However, when $\lambda_{11}\lambda_{22} \ll \lambda_{12}\lambda_{21}$, the system is now dominated by *inter-band* effects, and so can show predominate $s^{\pm}$ pairing. This is also discussed by A. Gurevich elsewhere [81]. Note that true $s^{\pm}$ pairing symmetry requires that the involved band coupling constants are negative, i.e $\lambda_{12} < 0$ and $\lambda_{21} < 0$. However, since λ_{12} and λ_{21} only ever appear as the product $\lambda_{12}\lambda_{21}$ it is difficult to infer pairing symmetry from these band coupling parameters alone. To do this (and compare between different regimes) it is thus necessary to have information about the underlying symmetry of the superconducting order parameter. For example, many iron-based superconductors have been shown to have a sign-changing order parameter and dominant $s^{\pm}$ pairing. Extracting these parameters from experimentally measured $\mu_0 H_{c2}(T)$ curves can give an indication of the type of underlying symmetry of superconductivity and establish if the system is dominated by intra-band or inter-band effects.

Finally, this model includes the manifestation of an FFLO state in the upper critical field, which is characterised by the magnitude of Q_z. This is a theoretically predicted state that exists in certain superconductors at low temperatures and in very high magnetic fields [82–84]. Perhaps the best example of this is in $CeCoIn_5$ [85, 86]. If a singlet BCS superconductor (opposite spins and $\mathbf{k} = 0$) is subjected to a magnetic field spin pair breaking will not occur until the energy of the magnetic field exceeds the Zeeman energy (becomes greater than the Fermi energy) of the system, flipping one of the spins and breaking the Cooper pair. In a normal metal, the same principle can lead to a spin-split Fermi surface, with the different states having different momentums. The above theories showed that Cooper pairing in high-fields can occur across these spin-split Fermi surface sheets, leading to a singlet pair with $\mathbf{k} \neq 0$. This pair with finite momentum leads to a spatially modulated order parameter with wavevector $\mathbf{q}$. This state occurs from a first order transition inside of the superconducting state, and leads to an enhanced upper critical field at low temperatures. This is often how it is experimentally searched for, with measurements including electrical transport, torque magnetometry and heat capacity. For this to occur, it is obvious that Pauli pair-breaking must be strong in the system. Systems with shallow bands, small Fermi energies and/or large effective masses are the most likely candidates for the emergence of an FFLO state. Because of this, conventional superconductors are unlikely to show an FFLO state, and it is searched for in more exotic superconductors such as organics, heavy fermion and iron-based compounds. Generally, systems also have to be clean for an FFLO state to emerge.

The effects of varying different parameters in different limits in this model are shown in figure 2.3. This is designed to give a flavour of the different kind of curve shapes that can be produced in different limits, and where (if at all) an FFLO state is likely to manifest.

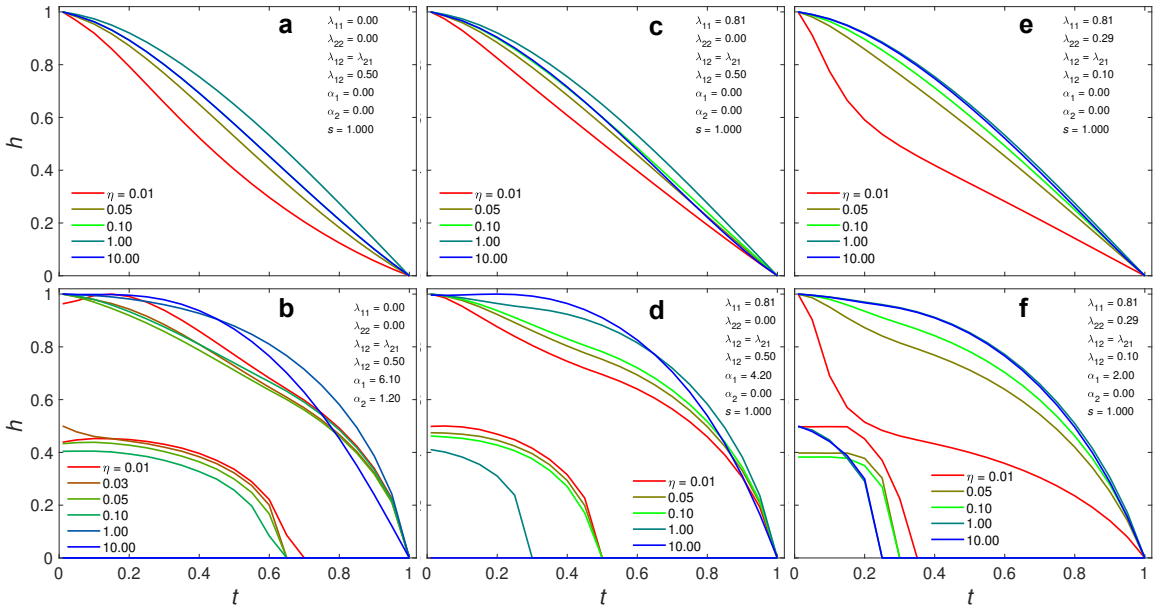


Figure 2.3: h against reduced temperature for a number of different parametrisations of equations 2.12-2.14. Each panel shows how $h(t)$ varies for different values of η while the other parameters stay fixed. The parameters listed in each panel correspond to $s^{\pm}$ pairing in **a** and **b** with $\lambda_{11} = \lambda_{22} = 0$, $\lambda_{12} = \lambda_{21} = 0.5$, $s^{\pm}$ pairing in **c** and **d** with $\lambda_{11} = \lambda_{22} = 0.81$, $\lambda_{12} = \lambda_{21} = 0.5$, and s^{++} pairing in **e** and **f** with $\lambda_{11} = 0.81$, $\lambda_{22} = 0.29$ and $\lambda_{12} = \lambda_{21} = 0.1$. For panels **b**, **d** and **f** the lower curves (left corners) represent the magnitude of the FFLO modulation, $Q/(2Q(0))$. Note that $s = 1$ in all panels.

It is clear that a variety of different shapes can be produced. This model has been used on previously on many iron-based superconductors, generally in the $s^{\pm}$ pairing limit [61, 81, 87–90].

It is also worth noting that a single-band version of this model exists, including the paramagnetic effects and the FFLO Q_z modulation. This is given by

$$\ln(t) + U = 0, \tag{2.15}$$

where $U = U_1$ from above. The other parameters (h, α and q) are defined the same as above. In this single-band model it can be shown that the critical paramagnetic pair-breaking value for an FFLO state to emerge on a elliptical Fermi surface is $\alpha_c \sim 1.8$ [81].

This critical value, α_c is more difficult to define in the two-band model as the parameter space is far larger, and there is a strong dependence on η. Certain limits have been calculated theoretically. For example, the formation of the FFLO state in a system with a cylindrical Fermi surface requires a large Zeeman energy and a critical Maki's parameter of $\alpha_c = 4.76$ [91], whilst a three-dimensional Fermi surface gives $\alpha_c = 1.8$ [92]. Generally, the systems considered here have quasi-2D Fermi surfaces, and so we may expect values

between these two for a FFLO state to emerge. However, these values do not take into account inter-band effects, which could dramatically change α_c. Generally, a larger value of α (above α_c) gives a greater magnitude of Q_z to the FFLO modulation, which in turn causes an increased enhancement in the upper critical field at low temperatures.

2.1.6 Nucleation at surfaces and a third critical field

Real superconductors have a finite size, and so surface effects and behaviour at surfaces should be considered. It has been shown that superconductivity can nucleate at a metal-insulator interface (such as the boundary of a typical sample) in a parallel magnetic field [93]. This leads to a *third critical field*, H_{c3}, which can be higher than the upper critical field, H_{c2}, by a factor of ~ 1.695. For fields between H_{c2} and H_{c3} it can be shown that there is a superconducting surface layer of thickness $\sim \xi(T)$ in directions *parallel* to the applied magnetic field where superconductivity can nucleate and persist. Note that this only happens in directions *parallel* to the applied magnetic field, and not in directions *normal* to the applied magnetic field.

This can give a layer at magnetic fields above H_{c2}, but lower than H_{c3}, that can support a supercurrent and so can have zero resistivity. Hence, this can be an important consideration when measuring the upper critical field using electrical transport measurements.

2.2 Vortices in high-temperature superconductors

One of the key properties of high-temperature superconductors is the vortex lattice. This is the phenomenon that enables some of their most interesting applications that rely on flux-locking (or pinning) of the vortices, such as magnetic quantum levitation. There are properties of vortices that make different materials suitable for different applications, and so studying the vortex state is important. Some of these that we will discuss are vortex pinning, flux creep and thermally activated flux flow. These can be considerably different in unconventional superconductors, particularly where impurities and grain boundaries can have a significant effect on superconductivity.

2.2.1 Bean's critical state model

The irreversible magnetisation of the vortex state can be used to find the critical current density. This comes from the *critical state* model, which relies on strong enough vortex pinning to prevent any considerable motion of vortex lines. Essentially, this then implies

that the diamagnetic signal produced by the sample in an applied magnetic field is proportional to the strength of the screening currents isolating the vortices. This in turn gives information about the maximum current that the superconductor can support in an applied field. This was developed further by C. P. Bean into *Bean's critical state model*, which describes the relationship between the magnetization and critical current density for different sample geometries [94]. For the cuboidal geometry, this is given by

$$J_{\mathrm{c}}(H) = \frac{2\Delta M(H)}{a(1 - \frac{a}{3b})}, \tag{2.16}$$

where $\Delta M = M_{\mathrm{up}} - M_{\mathrm{down}}$ is in units of $\mathrm{A/cm}$. Here M_{up} and M_{down} are the magnetizations when the magnetic field is increasing and decreasing respectively. The magnetization is calculated as $M = m/V$ where m is the magnetic moment and $V = abc$ is the sample volume, where a, b and c are the length, width and thickness of the sample in units of cm. Note that in equation 2.16 $b > a$.

A similar expression can be produced for the cylindrical geometry,

$$J_{\mathrm{c}}(H) = \frac{3\Delta M(H)}{2r}, \tag{2.17}$$

where r is the radius of the cylinder, and now $M = m/V_{\mathrm{cyl}}$ where $V_{\mathrm{cyl}} = \pi r^2 h$ where h is the height of the cylinder.

2.2.2 Dew-Hughes model

The critical state model, including the work by Bean, was extended to find a theory of the pinning force of vortices in superconductors [95]. In an applied magnetic field the screening currents of a vortex will be perpendicular to the direction of the field in that vortex, giving a Lorentz force. This gives a pinning force density of $F_{\mathrm{P}} = \mu_0 H \times J_{\mathrm{c}}$ (when $H \perp J_{\mathrm{c}}$). In the Dew-Hughes model, if a dominant vortex pinning mechanism exists over a certain temperature range, the normalized vortex pinning force density $f_{\mathrm{P}}(H) = F_{\mathrm{P}}(H)/F_{\mathrm{P}}^{\mathrm{max}}$ at different temperatures should collapse into one curve. Here $F_{\mathrm{P}}^{\mathrm{max}}$ is the maximum of the pinning force density as a function of the applied magnetic field, $\mu_0 H$. This results in a scaling law, which is described by

$$f_{\mathrm{P}}(h) = h^p (1 - h)^q, \tag{2.18}$$

where $h = H/H_{\mathrm{irr}}$ is the reduced magnetic field and H_{irr} is the irreversibility field. Here the exponents p and q are dimensionless, greater than zero and their values depend on the origin of the pinning mechanism. This equation gives two points at which $f_{\mathrm{P}}(h) = 0$ -

when $h = 0$ and when $h = 1$. It is worth noting that this is not defined for $H > H_{\rm irr}$, where the vortices are de-pinned. We now define $h_{\rm max}$ as the reduced magnetic field at which the maximum pinning force density, $f_{\rm P}^{\rm max}$ occurs. Taking the derivative of equation 2.18 with respect to h gives

$$\frac{df_{\rm P}(h)}{dh} = h^{p-1}(1-h)^{q-1}(p - h(p+q)). \tag{2.19}$$

At $(h_{\rm max}, f_{\rm P}^{\rm max})$ we have $df_{\rm P}/dh = 0$, which results in a relationship between $h_{\rm max}$, p and q

$$h_{\rm max} = \frac{p}{p+q}, \tag{2.20}$$

which can be used to help characterise the type of flux pinning, and predict $h_{\rm max}$ for different pinning mechanisms. We note that the derivative is also zero at $h = 0$ and $h = 1$.

2.2.3 Vortex pinning

Vortex pinning in high-$T_{\rm c}$ superconductors is a complex problem which still involves a large amount of research. In these materials, vortex dynamics are not just governed by the repulsion between vortices (as in the Abrikosov flux lattice), but tend to be pinned at different locations within the compound. Vortices are generally pinned at locations where the superconducting order parameter is suppressed. At these points, it is more difficult for Cooper pairs to persist and so it becomes more energetically favourable for them to be occupied by vortices in a magnetic field. Different types of *pinning centres* occur in different samples, and here we will cover an overview of the main types, their properties and their experimental signatures.

Vortex pinning is influenced by a number of factors including the superconducting nature of the pinning centre; the size and spacing of pinning centre compared to the penetration depth λ; the size of the pinning centres compared to the flux-lattice spacing (and so also the coherence length ξ); and the rigidity of flux-lines.

The different nature of pinning centres gives rise to two different types - $\delta\kappa$-pinning (or $\delta T_{\rm c}$-pinning) where the order parameter is slightly suppressed, which can lead to local variations in $T_{\rm c}$, and *normal-pinning* on non-superconducting particles, which could be metallic, insulating, magnetic or just voids. The size of the pinning microstructure can determine if magnetic pinning can be dominant. The size of the pinning centres (relative to the vortex size) determines the dimensionality of the pinning - i.e. if it is volume (bulk), surface, or point-like. For example, flux-lines only interact with the surface of volume pins, and the force is limited by the projection of the surface in the direction of the Lorentz force. These are generally large precipitates in the structure, and usually have all dimensions far larger than ξ. Surface pins have only one dimension smaller than ξ, which is usually

perpendicular (or near-perpendicular) to the flux-line. In contrast point-like pins are smaller than ξ in all directions, and so are essentially completely screened from the bulk by the vortex. A smaller rigidity of the vortex lattice can lead to a less uniform flux-line structure and an increased elasticity of the vortex lattice, which is usually characterised by a glassy state. These different qualities lead to different vortex behaviour, and different exponents in equation 2.18. This in turn gives different values for $h_{\max}$ in equation 2.20. A full table of this is given in Ref. [95] (page 6), but here we will quote a few of the final results that will be necessary in chapter 4.

1. Point-like $\delta\kappa$-pinning: $h_{\max} \sim 0.67$
2. Point-like normal-pinning: $h_{\max} \sim 0.33$
3. Surface $\delta\kappa$-pinning: $h_{\max} \sim 0.6$
4. Surface normal-pinning: $h_{\max} \sim 0.2$
5. Volume $\delta\kappa$-pinning: $h_{\max} \sim 0.5$

Vortices in high-T_{c} superconductors can also be pinned on multiple sites (sometimes even of different nature), which can complicate this problem and affect the $h_{\max}$ values.

2.2.4 Flux flow

At finite temperatures, thermal energy can allow a vortex to overcome its local pinning force and jump between pinning centres. This usually has to be driven by an external force, such as an applied current or a change in the magnetic field. This can lead to small resistive voltages and the flux dynamics changing slowly over time. This is referred to as *flux creep*, and usually has a larger effect on a vortex glass state.

A theory that describes flux creep was developed by P. Anderson and Y. Kim [96, 97]. This describes the collective motion of bundles of flux lines, as the repulsive interaction between flux-lines is typically large when compared to the inter-line distance. This theory gives a characteristic decay time for persistent currents of up to $\sim 10^{390}$ years in high-T_{c} superconductors.

Inside the superconducting state, the relaxation of the vortex lattice is perhaps the easiest method of measuring flux creep, using the decay of the magnetization at constant field and temperature as a function of time. Another method is using the thermally activated flux flow (TAFF) which can be seen in the resistive broadening of superconducting transitions. Models suggest that the resistivity in this region can be described as [98–100]

$$\rho = \rho_{0,f} e^{-U_0/k_{\mathrm{B}}T}, \tag{2.21}$$

where $\rho_{0,f}$ is a characteristic resistivity of the flux flow and $U_0 = J_c BVL$ is the activation energy of the vortex state. Here B is the internal magnetic field, V is the volume of a flux bundle and L is the characteristic hopping distance of flux-lines. The activation energy is proportional to the vortex pinning force density ($J_c B$), and so this can be used to compare between different materials. Equation 2.21 can be re-arranged to give

$$\ln(\rho) - \ln(\rho_{0,f}) = -\frac{U_0}{k_B T}. \tag{2.22}$$

Linear fits to Arrhenius plots of $\ln(\rho)$ against $1/T$ will give a linear region with a gradient of $-U_0/k_B$. We also note that fits to temperature sweeps at different magnetic fields should have a common intercept in $\ln(\rho)$ against $1/T$, which should be near T_c (or T_{on} in resistive transport).

2.3 Superconducting fluctuations

The Ginzburg-Landau theory presented above focuses on finding the minimum of the free energy. In reality, thermal effects above $T = 0$ allow for spatial variations of the order parameter $\psi(r)$ for energies up to $\sim k_B T$. These superconducting fluctuations (SCF's) can have effects on the properties of superconductivity below T_c. Here however, we are going to focus on superconducting fluctuations above T_c, which can reveal information about the intrinsic nature of superconductivity. Above T_c, thermodynamic fluctuations can give rise to superconducting effects essentially as $\langle \psi^2 \rangle \neq 0$, despite $\langle \psi \rangle^2 = 0$ [9, 101, 102]. Thermal fluctuations on the order parameter from $\psi \rightarrow \psi + \delta\psi$ raising the free energy by $\sim k_B T$ have a probability of $e^{-F/k_B T}$, meaning they are fairly common. Above T_c the fluctuations are of largest amplitude when they are confined to small regions, increase local pockets by energy $\sim k_B T$. It can be shown that these fluctuations are present in 0, 1, 2 and 3 dimensions [9, 101–104].

2.3.1 Temperature dependence

The argument for fluctuations in 1 or more dimensions treats a macroscopic sample as particles whose size is limited by the coherence length, ξ. For example, since $|\alpha| = \hbar^2/2m^\star\xi^2$ this leads to a diamagnetic susceptibility of the bulk above T_c proportional to $k_B T\xi(T)/\Phi_0^2$ in three dimensions. In reality, these also have a magnetic field dependence, and can be different for 2D systems [9]. SCF's can also have a profound effect on the conductivity above T_c. We might expect the contribution of the fluctuations to the conductivity to be of

the form

$$\sigma_{\rm SCF} = \frac{(2e)^2}{m^\star} \sum_{\mathbf{k}} \frac{\langle |\psi_{\mathbf{k}}|^2 \rangle \, \tau_{\mathbf{k}}}{2}. \tag{2.23}$$

The temperature dependence of $\sigma_{\rm SCF}$ is found to be $(T - T_{\rm c})^{-(4-d)/2}$, where $d = 1, 2, 3$ is the number of dimensions.

In three dimensions the result can be found by averaging over a sphere (with a radius of the coherence length), using the density of states as $4\pi k^2 dk/(2\pi)^3$ and integrating to give

$$\sigma_{\rm SCF}^{\rm 3D} = \frac{e^2}{32\hbar\xi(0)}, \left(\frac{T}{T - T_{\rm c}} \right)^{1/2} \tag{2.24}$$

where the substitution $\xi(T) = \xi(0)[T/(T - T_{\rm c})]^{1/2}$ has been used. This is typically smaller than the normal state conductivity (σ in equation 1.32) by a factor of $\sim 1/(k_{\rm F}^2 \ell \xi(0)) \sim 10^{-5}$, which can make it difficult to distinguish experimentally.

The two dimensional case assumes a layer (or film) thickness d. Here the density of states becomes $2\pi k dk/(2\pi)^2$ and the result becomes [103]

$$\sigma_{\rm SCF}^{\rm 2D} = \frac{e^2}{16\hbar d} \left(\frac{T}{T - T_{\rm c}} \right), \tag{2.25}$$

which depends only on the layer thickness d and the transition temperature $T_{\rm c}$. The contribution to the conductivity in the 2D case is $\sim 10^2$ times larger than in the 3D case. Errors in the calculation of the 2D SCF conductivity are considerable. For $d \leq \xi$, it can be shown that the 2D result is accurate to $\sim 10\%$. However, in the limit of $d \gg \xi$ it can be shown that the 3D result can be recovered with a factor of $d/2\xi$ [9]. This may imply that thin films undergo a 2D to 3D crossover as T is increased further above $T_{\rm c}$, since ξ is temperature dependent.

The final case we will consider for completeness is the 1D limit in a thin wire with cross-sectional area $A \ll \xi^2$. The density of states in this case becomes $dk/2\pi A$, and the conductivity of the SCF's is given by

$$\sigma_{\rm SCF}^{\rm 1D} = \frac{\pi e^2 \xi(0)}{16\hbar A} \left(\frac{T}{T - T_{\rm c}} \right)^{3/2} \tag{2.26}$$

Using $A \simeq (a\xi)^2$, where a is a numerical factor < 1, can give a range of conductivity values at T near $T_{\rm c}$.

Thus, the temperature dependence of the conductivities with different dimensionality will give different power law curves. This is most obvious when plotting $\sigma_{\rm SCF}$ against $\epsilon = \ln(T/T_{\rm c})$ on a log-log scale, which will give straight lines with a gradient of the

exponent. For the 3D and 2D case, the values of ξ and d can be used to give the respective theoretical curves. These are often referred to as Aslamasov-Larkin (AL) superconducting fluctuations.

The above arguments mean that the natural length scale associated with SCF's is the coherence length ξ. Thus, at magnetic fields greater than H_{c2} the fluctuations should be suppressed as the limit on the particle size is exceeded. This may mean that we expected fluctuations to scale to $H_{c2}(0)$.

Here it becomes important to discuss how σ_{SCF} is extracted. To do this, one must first find the normal state conductivity, σ. In zero, magnetic field, this is simply defined as $\sigma = 1/\rho$, and the SCF contribution can be found by subtracting the normal state conductivity

$$\sigma_{\mathrm{SCF}} = \sigma - \sigma_{\mathrm{n}} = \rho^{-1} - \rho_{\mathrm{n}}^{-1} \tag{2.27}$$

where σ is the measured conductivity and σ_{n} is the normal state conductivity. However, the temperature dependence of the resistivity of unconventional superconductors is not well understood, and so the zero-field method is not ideal. A better method is to suppress the SCF's using a magnetic field and recover the normal state resistivity in high fields. In a magnetic field we consider the contribution of SCF's to the in-plane transverse conductivity, σ_{xx}. In order to calculate this properly from the resistivity, one has to first find the inverse of the conductivity tensor (see section 1.7). Usually the Hall resistivity ρ_{xy} is small compared to ρ_{xx} and so has little contribution. From this, the SCF's conductivity as a function of both temperature and magnetic field can be extracted. This of course does rely on a suitable model for the normal state resistivity.

2.3.2 Magnetic field scaling

Given the method of extracting the SCF contribution to the conductivity presented above, it seems sensible to next consider the effect that a magnetic field has on the SCF's. There are two different cases to consider, $H > H_{c2}(0)$ and $H \leq H_{c2}(0)$. For the case of $H > H_{c2}(0)$ in the low temperature limit ($T < T_{\mathrm{c}}$) the magnetic field passes the coherence length of the material and it can be shown that the change in conductivity is

$$\delta\sigma = -\frac{2e^2}{3\pi^2} \ln\left(\frac{1}{\tilde{h}}\right), \tag{2.28}$$

where $\tilde{h} = (H - H_{c2})/H_{c2}(T)$. This can actually *reduce* the conductivity, and so *enhance* the resistivity, at high fields and low temperatures. Hence, superconducting fluctuations can

be responsible for anomalous magneto-transport at low temperatures. At magnetic fields below the upper critical field, $H \leq H_{c2}(0)$, the change in conductivity is given by

$$\delta\sigma = \frac{3e^2}{2\gamma_E \pi^2} \frac{T_{c(0)}}{T - T_c(H)}, \tag{2.29}$$

where γ_E is a constant. Here $T_c(H)$ is the evolution of the transition temperature in a magnetic field, i.e. the equivalent of $H_{c2}(T)$.

This can be extended to included the dimensionality of the fluctuations, similar to earlier. The equations that describe the magnetic field scaling of superconducting fluctuations are [105–108]

$$\sigma^{2D}_{SCF}(H) = \left(\frac{T}{H}\right)^{1/2} F_{2D}\left(A\frac{T - T_c(H)}{(TH)^{1/2}}\right), \tag{2.30}$$

$$\sigma^{3D}_{SCF}(H) = \left(\frac{T^2}{H}\right)^{1/3} F_{3D}\left(B\frac{T - T_c(H)}{(TH)^{2/3}}\right), \tag{2.31}$$

for 2D and 3D fluctuations respectively. Here A and B are constants appropriate to the material. $T_c(H)$ is found from the upper critical field curves, $H_{c2}(T)$. For large positive values of x (that will be considered here) the above functions scale as $F_{2D}(x) \sim x^{-1}$ and $F_{3D}(x) \sim x^{-1/2}$ [105]. The arguments of the scaling functions are another representation of the critical region in a magnetic field. We note that this formulation only considers the effect of the Aslamazov-Larkin term [103], which near T_c generally dominates other contributions such as the Maki-Thompson term [109, 110] and Zeeman effects, due to the large phase relaxation rate [109–112]. Other formalisations of magneto-conductivity also exist, such as in Ref. [110]. 3D magnetic field scaling has been shown to work on fluctuations in cuprate superconductors previously [106, 113].

Thus, using equations 2.30 and 2.31 one can attempt magnetic field and temperature scaling of the SCFs for different dimensionality. This can reveal further information about the nature of the fluctuations, and so of the underlying superconductivity.

2.3.3 Ginzburg number

A parameter that can be used to compare other properties of a superconductor to the fluctuations is the Ginzburg number, Gi, which represents the magnitude of the fluctuations. This is given by [114]

$$Gi = \frac{1}{2}\left(\frac{k_B T_c}{\mu_0^2 H_c^2(0)\epsilon(0)\xi^3(0)}\right)^2, \tag{2.32}$$

where $\mu_0 H_c = \mu_0 H_{c2}/(\sqrt{2}\kappa)$ is the thermodynamic critical field, ξ is the coherence length and the anisotropy parameter $\epsilon = \sqrt{m^\star_{ab}/m^\star_c} = H^c_{c2}/H^{ab}_{c2}$. Here H^c_{c2} and H^{ab}_{c2} are the upper critical fields when $H||c$ and $H||(ab)$ respectively. Equation 2.32 can be re-arranged and cast into SI units to give

$$Gi = 1.7 \times 10^{-11} \frac{T_c^2 \kappa^4}{\mu_0 H_{c2}(0) \epsilon^2(0)}. \tag{2.33}$$

Typically high-temperature cuprate superconductors have $Gi \sim 10^{-3}$, whilst iron-based materials tend to have slightly larger values of $Gi \sim 10^{-2} - 10^{-3}$.

Chapter 3

Experimental techniques

This chapter will introduce the experimental methods used throughout this thesis. The main techniques used have been electrical transport, magnetisation and torque magnetometry to measure single crystals of iron-based superconductors.

3.1 Temperature control

Samples have been measured in a number of different systems in order to achieve stable and reliable temperatures in different ranges. Chiefly, the two types of systems used have been helium-4 variable temperature inserts and helium-3 systems.

Temperatures were measured using the standard 4-point resistance method of either a cernox or RuO_2, depending on the system. These were calibrated before use, and the conversion from resistance to temperature was usually done using a Lakeshore temperature controller.

3.1.1 Flow-cryostat

Sample screening and temperature dependence for electrical transport in zero magnetic field was usually done using a ^{4}He flow cryostat. This system relied on generating a pressure gradient to pull helium-4 from a dewar into a vacuum chamber containing the samples. The entire setup was cooled as the helium is drawn through the system. Cooling was done as slowly as possible to ensure there is no rapid contraction and damage to the samples or to any contacts. However, warming data is usually considered to be more reliable as the chamber warmed over several hours.

3.1.2 Physical Properties Measurement System (PPMS - Quantum Design)

Experiments in magnetic fields up to $16\,\mathrm{T}$ have been performed in a Quantum Design $16\,\mathrm{T}$ Physical Properties Measurement System (PPMS) [115]. For temperature control, this system has many similarities to the flow cryostat, but also has a network of heaters. Using a balance between the helium flow, pumping strength and heat load the temperature could be stabilised down to $1.8\,\mathrm{K}$ in normal operation for several hours at a time. This variable temperature insert (VTI) sits inside a $16\,\mathrm{T}$ superconducting $\mathrm{Nb_3Sn}$ solenoid capable of both positive and negative polarity, giving a field range of $-16\,\mathrm{T}$ to $16\,\mathrm{T}$. This superconducting magnet has a persistent mode, which means that the magnetic field can be held at a particular value. This system was used for electrical transport, magnetisation and torque measurements.

3.1.3 Variable Temperature Inserts (VTI's)

Other VTI systems have been used to stabilise temperatures at high-field facilities, mainly at the HFML in Nijmegen and LNCMI in Toulouse. Helium-4 systems at these facilities work in a similar way as described above, utilising a balance of the flow of helium-4 and the current put through a heater in a PID system. To achieve temperatures below the boiling point of helium-4, $4.2\,\mathrm{K}$, the liquid helium-4 was pumped. This removes the higher energy (temperature) particles and reduces the temperature of the liquid. Using this method, temperatures as low as $\sim 1.4\,\mathrm{K}$ were achieved.

3.1.4 Helium-3 systems

To achieve temperatures below $1.4\,\mathrm{K}$, different systems have to be used. One method is to use helium-3. These systems have a helium-4 $1\,\mathrm{K}$ pot in which helium-4 is condensed and pumped down to $\sim 1.4\,\mathrm{K}$. The helium-3 is then passed through a coil which is thermally linked to the $1\,\mathrm{K}$ pot, which causes the helium-3 (which has a boiling point of $3.19\,\mathrm{K}$ at atmospheric pressure) to start condensing into a second chamber, the helium-3 pot. The liquid helium-3 was then pumped on, using either a standard pump or a sorb at a higher temperature, to remove the higher energy helium-3. This can achieve temperatures as low as $\sim 0.25\,\mathrm{K}$. This technique was used to achieve data at the lowest temperatures, of $\sim 0.3\,\mathrm{K}$, that will be presented in this thesis.

Data from three different helium-3 systems will be presented here. The first is a quantum design helium-3 insert which is designed to work with a PPMS [116]. This achieved a base temperature of $\sim 0.41(1)\,\mathrm{K}$. The other two systems were used at the HMFL Nijmegen,

which achieved a base temperature of $\sim 0.33(1)$ K, and at the NHMFL Tallahassee Florida, which achieved a base temperature of $\sim 0.40(4)$ K.

It is worth noting here that the temperature estimates for data from Tallahassee have larger errors as the temperature was usually measured with the outer superconducting magnet at a constant field of 11 T. The types of thermometers used to measure the temperature (cernox and RuO_2) have magnetoresistance, and so values in magnetic field have to be extrapolated back to zero-field. This generally becomes more of a problem at lower temperatures as generally magnetoresistance increases as temperature decreases.

3.2 Generating high magnetic fields

As most of the data that will be presented here were taken in magnetic fields it is important to discuss how these fields were generated. Three principal types of solenoid have been used - superconducting, resistive and pulsed field.

3.2.1 Superconducting magnets

The superconducting magnets used were made of either NbTi or $\mathrm{Nb_3Sn}$, and were kept below their T_c using liquid helium-4 (at 4.2 K). Generally these magnets have to be ramped relatively slowly, when compared with resistive magnets (and definitely when compared to pulsed field magnets), and do not achieve as high magnetic fields as large resistive magnets, as they are limited by the upper critical fields and critical current densities of the superconducting material. The advantages of using superconducting magnets centre around their zero resistance property. This means ramping the magnet uses less energy, and they can be held at constant field, usually using a persistent switch, using minimal (in theory zero) extra energy. Most of these magnets are also capable of changing the field polarity (generating positive and negative fields)[1].

Because of the natural hysteresis of type-II superconductors these magnets can be unreliable (often not at the reported field) at low fields, typically below ~ 10 mT for the superconducting magnets used in this thesis. This can prove to be problematic when measuring magnetisation on type-II superconductors that have small lower critical fields. However, this problem can be avoided by oscillating the magnet down to zero field. This was typically done in steps, using a smaller field sweep rate at lower fields. Using this method remanent magnetic fields less than ~ 0.1 mT were achieved. This was tested and confirmed using a standard palladium reference sample[2].

[1] This is largely dependent on the power supply.

[2] The magnetic susceptibility of palladium is well known as a function of both temperature (paramagnetic)

3.2.2 Resistive DC magnets

Large resistive magnets have been used at the HMFL in Nijmegen and NHMFL in Tallahassee. These consist of sequentially connected rings of copper, through which large currents are passed, and are generally cooled using high-pressured water. Pure resistive magnets used at the HMFL have been used to produce magnetic fields up to $38\,\mathrm{T}$. In Tallahassee, a resistive magnet combined with a superconducting outset solenoid was used to produce magnetic fields up to $45\,\mathrm{T}$. Generally, the larger $45\,\mathrm{T}$ magnet was only used for positive fields, as the superconducting outset takes several hours to ramp. The purely resistive $38\,\mathrm{T}$ magnet was used for both positive and negative fields. This makes it particularly useful in studies concerning electrical transport measurements for determining electronic behaviour, which require positive and negative fields to (anti)symmetrise the data and extract the ρ_{xx} and ρ_{xy} contributions to the resistivity. Experiments presented in this thesis in magnetic fields up to $45\,\mathrm{T}$ at the NHFML in Tallahassee were performed by P. Reiss and A. Coldea.

3.2.3 Pulsed field magnets

Magnetic fields above $45\,\mathrm{T}$ were produced using pulsed field solenoids. These are tightly wound solenoids of copper, and large DC currents are passed through them in a very short time, typically $\sim 30\,\mathrm{ms}$. A typical field trace up to $88\,\mathrm{T}$ is shown in figure 3.1. These magnets were again used for positive and negative magnetic fields. Data presented here were taken on two different magnets, one capable of $70\,\mathrm{T}$ and another capable of $90\,\mathrm{T}$. The $90\,\mathrm{T}$ magnet consists of two different coils, an outer coil and an inner coil. The outer coil is fired first with a slower pulse that reaches $\sim 30\,\mathrm{T}$, and the inner coil is fired during this pulse so that the field peak from both coils coincides. This is what gives the trace in figure 3.1 its characteristic time dependence.

3.3 Electrical transport

Electrical transport measurements have been performed using both 4-point and 5-point (Hall) configuration on single crystals of $\mathrm{FeSe}_{1-x}\mathrm{S}_x$ and $\mathrm{CaKFe_4As_4}$. The crystals are cuboidal platelets (and tetragonal at room temperature, however $\mathrm{FeSe}_{1-x}\mathrm{S}_x$ crystals become orthorhombic in the nematic phase, see section 1.6.1), making faces easy to identify

and magnetic field (linear in field). The sample itself is cylindrical, and so its demagnetisation factor is also easy to calculate. Hence, the magnetic moment of the palladium sample can easily be converted susceptibility, and so one can calculate the magnetic field that the sample was in. The tests were performed using field sweeps at a constant temperature of $300\,\mathrm{K}$ and measuring the remanent moment of the sample (and so also the remanent magnetic field) using different sweep rates and stages of oscillating the field back to zero.

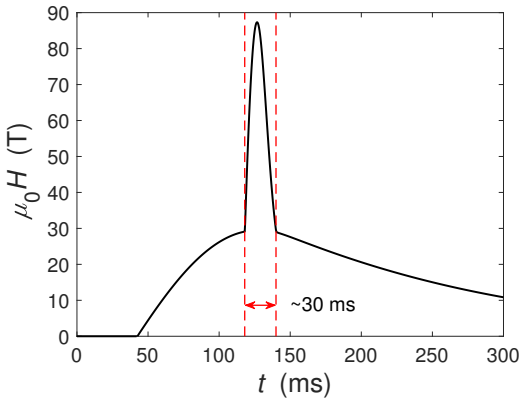


Figure 3.1: An example of a magnetic field pulse up to $\sim 88\,\mathrm{T}$ as a function of time. This was done on a $90\,\mathrm{T}$ magnet, which consists of two concentric copper coils. The outside coil is fired first with a longer pulse, and the inside coil is fired over a short period of $\sim 30\,\mathrm{ms}$ whilst the outside coil is at maximum field, which is what gives this plot its profile.

for electrical contacts. Typical sample lengths were between $1\,\mathrm{mm}$ and $200\,\mu\mathrm{m}$[3], and typical thicknesses were between $5\,\mu\mathrm{m}$ and $\sim 50\,\mu\mathrm{m}$[4]. Reliable contacts were made to samples mounted on small quartz pieces using indium solder and either gold or platinum wires, giving resistance values between any two contacts less than $1\,\Omega$. Gold and platinum wires were fixed to the quartz piece away from the sample using DuPont 4929 silver epoxy (cured at room temperature) to reduce vibrations. An example of a sample used for 5-point resistivity measurements is shown in figure 3.2. Generally low frequencies $< 35\,\mathrm{Hz}$ were used, apart from in pulsed field measurements, where frequencies in the range $20 - 100\,\mathrm{kHz}$ are necessary[5].

Resistivity was measured in a number of different locations. Measurements done in a Quantum Design Physical Properties Measurement System (PPMS) were either taken using the electrical transport option (ETO) [117] or using a SR830 Lock-in Amplifier. If the Lock-in Amplifier method was used, stable currents were usually supplied using a Keithley 6221. The Keithley plus Lock-in method was also used at high-field facilities[6]. Usually when this was done the sample voltage was passed through a $\times 100$ gain transformer or pre-amplifier to improve the signal-to-noise ratio and increase the signal to a more easily

[3]For these smaller samples, the tip of the soldering iron is of comparable size to the sample. Putting reliable contacts on any samples smaller than this is beyond my level of skill.

[4]The $CaKFe_4As_4$ samples were usually thinner, in the $5 - 10\,\mu\mathrm{m}$ range, and the $FeSe_{1-x}S_x$ samples ranged in thickness from $\sim 15 - 50\,\mu\mathrm{m}$.

[5]The resistance can actually have a frequency dependence at these high frequencies. If multiple samples are being measured it is also important to pick these frequencies carefully to avoid cross-talk between different signals.

[6]At the HFML Nijmegen and NHFML Tallahassee.

measurable value. Low currents between 1 and 5 mA were used to avoid local heating[7].

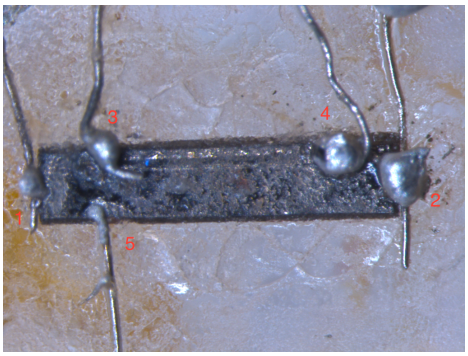


Figure 3.2: An example of a sample that has been prepared for a 5-point measurement. The current is applied through contacts 1 and 2. The voltage V_{xx} is measured across contacts 3 and 4, and the Hall voltage V_{xy} is measured across 3 and 5. A 4-point measurement looks similar, but without the contact labelled 5.

Reliable data from electrical transport is achieved by changing external parameters, such as temperature and magnetic field, slowly. At low temperatures, data as a function of temperature were taken with sweep rates no larger than 1 K/min. For determining temperature resistivity exponents in chapter 6 sweep rates as low as 0.3 K/min were used. Magnetic field sweep rates using superconducting magnets were typically 300 mT/min[8], and 2 T/min using resistive DC magnets.

Electrical transport has been used to probe a number of properties. Resistivity can show phase transitions as well as giving information about the electronic structure and scattering. Effects such as superconductivity and metal-insulator transitions are unmistakable in electrical transport and structural, magnetic and charge ordering transitions also change the electronic structure or scattering processes, causing a change of gradient and resistive anomalies.

At high temperatures the resistivity is dominated by phonon scattering, usually leading to a linear resistivity [118]. As the temperature is reduced the thermal vibrations of the lattice are reduced and the resistivity becomes proportional to T^2 [68, 118], as discussed in section 1.7. At very low temperatures the resistivity will be dominated by impurities, leading to a constant temperature independent resistivity. Therefore, the residual resistivity ratio, RRR, can be defined as $\rho(300\,\mathrm{K})/\rho(0\,\mathrm{K})$ in zero magnetic field. Generally, the larger the RRR value the lower the impurity level. The RRR is thus a good method of screening

[7]The indium solder used has a superconducting transition temperature of $T_c \sim 3.4$ K, which also helps to reduce the local heating of samples below this temperature.

[8]With the exception of measurements of the lower critical field in chapter 4, where sweep rates of 0.2 mT/s were used since the lower critical field of high-temperature superconductors is usually very small - often only a few mT.

and comparing the quality of samples. Finding the RRR is however slightly problematic for superconductors, where at low temperatures below $T_{\rm c}$ the resistivity is zero, $\rho = 0$. One can always extrapolate the low temperature resistivity from the $\rho(T)$ dependence above $T_{\rm c}$, but as is shown in chapter 6 the characteristic can change significantly below $T_{\rm c}$. To account for this, RRR is re-defined slightly here as $\rho(300\,{\rm K})/\rho(\,T_{\rm on}+1\,{\rm K})$ (see later in this section for a definition of $T_{\rm on}$), which still enables a reliable comparison between different samples.

To find details about the electronic structure in a magnetic field it is essential to explicitly extract the in-plane transverse and Hall resistivities when the magnetic field is parallel to the c-axis of the crystal, $H||c$. Magnetic fields cause a Lorentz force on charge carriers and bend their path, thus resulting in extra scattering and an increased resistivity. This model yields the classical $\rho \propto H^2$ Fermi-liquid behaviour of the transverse magnetoresistance, $\rho_{\rm xx}$ for metals discussed in section 1.7.2. The Lorentz force also gives rise to the transverse Hall resistivity, $\rho_{\rm xy}$. The Hall resistivity will change sign if the sign of the magnetic field is changed[9], which means it can be extracted if measurements are done in both positive and negative magnetic fields. Assuming some resistance $R(H)$ is measured, where $\mu_0 H$ is the magnetic field, the different components can be found by symmetrising and anti-symmetrising the resistance data,

$$R_{\rm xx} = \frac{R(H^+) + R(H^-)}{2}, \qquad R_{\rm xy} = \frac{R(H^+) - R(H^-)}{2}, \tag{3.1}$$

where H^+ and H^- denote positive and negative magnetic fields, respectively. An example of this is shown in figure 3.3. The different resistivity components are then found using the sample dimensions and contact layout as $\rho_{\rm xx} = R_{\rm xx}A/L$ and $\rho_{\rm xy} = R_{\rm xy}t_{\rm S}$, where A is the cross-sectional area, L is the length between the in-plane voltage taps and $t_{\rm S}$ is the thickness of the sample.

Different transitions, such as structural and superconducting, were observed in resistivity data, and so it is important to define how transition temperatures were extracted.

The structural/nematic transition that is observed in the $FeSe_{1-x}S_x$ series appears as a kink in the resistivity as a function of temperature. This gives rise to a local minimum in the derivative, $d\rho/dT$. This minimum is centred on the structural transition temperature, defined as $T_{\rm s}$. To accurately extract this value for different samples the regions either side of the minimum were fitted with linear fits, and the intercept of these fits is defined as $T_{\rm s}$[10],

[9] Sometimes referred to as changing the magnetic field polarity.

[10] One could use the local minimum as the definition of the structural transition. However, this is much more sensitive to noise in the experiment and in the derivative. Using linear fits either side of the transition proved to be much more reliable (regardless of where the data was taken), and so this method was used for data analysis.

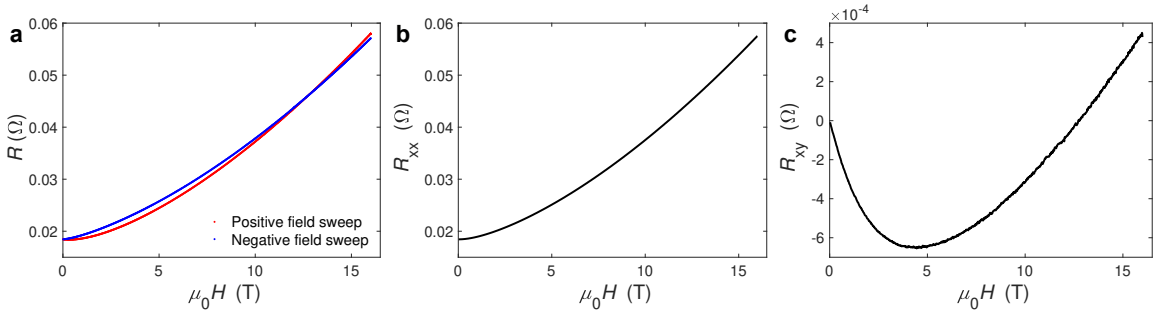


Figure 3.3: **Symmetrizing electrical transport data.** **a** Resistance against applied magnetic field for positive (red) and negative (blue) fields at constant temperature. **b** The symmetrized component of resistance, R_{xx}, against magnetic field. **c** The anti-symmetrized component of resistance, R_{xy}, against magnetic field. The components are calculated using equation 3.1.

as shown in figure 3.4**a**. All data showing a structural transition were passed through the same algorithm to reliably find T_{s}.

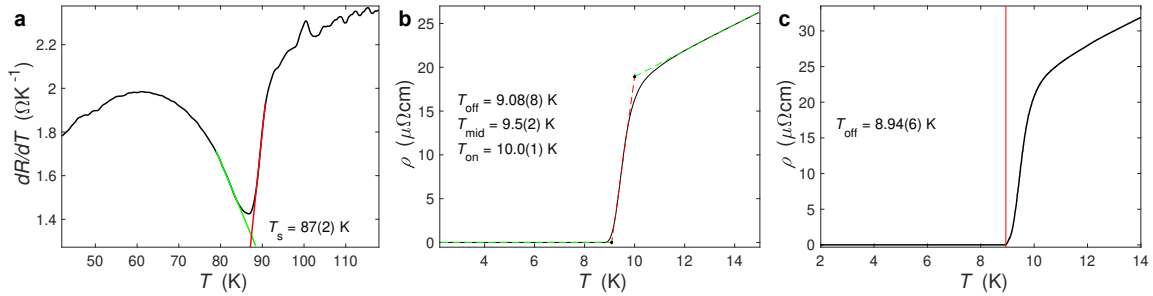


Figure 3.4: **a** The derivative of zero-field resistance data with respect to temperature, dR/dT, as a function of temperature. This derivative has been taken in the vicinity of the nematic transition for a sample of FeSe. The red and green lines are linear fits just above and below the transition, and their intercept is defined as T_{s}. **b** Resistivity against temperature showing a superconducting transition. The dashed red line is a linear fit to the transition region, and the dashed green lines are linear fits to the superconducting state ($\rho = 0$) and normal state. The intercepts are defined as the offset critical temperature, T_{off}, and onset critical temperature T_{on}. The midpoint T_{mid} is the peak in $d\rho/dT$. **c** The same data as in **b**, with the $T_{\mathrm{off}} = T_{\mathrm{c},0}$ critical temperature extracted through deviation from the low-temperature superconducting state.

A transition into the superconducting state is marked by a drop to zero resistivity, an example of which is shown in figure 3.4**b**-**c**. Three values were extracted from this data. The first was the midpoint, T_{mid}, which was defined as the peak in $d\rho/dT$. From the derivative, a region below the transition was found where the derivative is zero and above the transition (in the normal state) where the derivative returns to an approximately constant value.

Linear fits were performed around the midpoint, as well as above and below the transition. The lower intercept of the fits is defined as the offset critical temperature, $T_{\rm off}$, and the higher intercept as the onset critical temperature, $T_{\rm on}$. These are shown in figure 3.4**b**. Generally, the offset temperature $T_{\rm off}$ was found to be far closer to the bulk thermodynamic transition. For this reason $T_{\rm c}$ from resistivity data was defined as the offset temperature, unless otherwise specified.

Upper critical fields, $\mu_0 H_{\rm c2}$, from resistivity were also found using the same method, where the values become $\mu_0 H_{\rm off}$, $\mu_0 H_{\rm mid}$ and $\mu_0 H_{\rm on}$ for the offset, midpoint and onset critical fields respectively. For the same reason as with superconducting transition in $\rho(T)$ data, $\mu_0 H_{\rm c2}$ was defined as the offset critical field, $\mu_0 H_{\rm off}$, in $\rho(\mu_0 H)$ data.

Another method has also been used to identify offset critical values. From the data in the superconducting state (where $\rho = 0$) the noise level was found. When the resistivity increased to, typically, 1σ of the noise level $T_{\rm c,0}$ was defined, where the sample leaves the superconducting state. This can be compared to the $T_{\rm off}$ and always gave good agreement. An example is shown in figure 3.4**c**. The same method was used for $H_{\rm c2}$ extraction in magnetic fields, as a comparison.

All critical temperatures and fields were extracted using the same algorithm(s) to ensure reliable and consistent data analysis.

3.4 Magnetisation

Magnetisation measurements presented here were all performed in a 16 T Quantum Design PPMS using a Vibrating Sample Magnetometer (VSM). Samples were mounted on a quartz sample holder using small amounts of GE varnish for minimum magnetic background. The basic principle of a VSM is that a changing magnetic flux will induce a voltage in a pickup coil (Lenz's law) [119]. Here, the changing flux will be provided by a sample with a magnetic moment. The voltage induced in the coil is given by

$$V_{\rm coil} = \frac{\partial \phi}{\partial t} = \left(\frac{\partial \phi}{\partial z}\right)\left(\frac{\partial z}{\partial t}\right), \tag{3.2}$$

where ϕ is the magnetic flux, t is time and z is the samples vertical position with respect to the coil centre. The magnetic moment of the sample, m, is then given by

$$m = \frac{V_{\rm coil}}{2\pi f C A_z \sin(2\pi f t)}, \tag{3.3}$$

where f is the oscillation frequency, C is a coupling constant related to the coil dimensions and A_z is the vertical oscillation amplitude [120]. The frequency used here was always 40 Hz and the typical oscillation amplitude was 2 mm.

To find an accurate magnetic moment it is important that the whole sample leaves the coil centre at the peak(s) of its oscillation. For samples with a z length greater than $2\,\mathrm{mm}$ a larger oscillation amplitude was used, which was found by checking the moment for saturation as a function of the oscillation amplitude. All single crystals here had z length less than $2\,\mathrm{mm}$, and so this check was only important for larger powder/polycrystalline samples.

All superconducting samples were centred at base temperature ($2\,\mathrm{K}$) in a small magnetic field, typically $5\,\mathrm{mT}$, so the sample was in the Meissner state. This ensured a large signal for centring and a reliable position in the coil centre.

Finding the magnetic susceptibility, χ, required an accurate value of the demagnetisation factor, N. The demagnetisation factor was calculated using the sample dimensions as described in [121–123], and generally gives an error of $\Delta N \sim 2\%$. The magnetic susceptibility is defined as

$$\chi = \frac{\chi_{\mathrm{obs}}}{1 - N\chi_{\mathrm{obs}}}, \tag{3.4}$$

where $\chi_{\mathrm{obs}} = M/\mu_0 H$ is the observed susceptibility, M is the magnetic moment per unit volume and $\mu_0 H$ is the applied magnetic field [124].

Finding accurate values of χ was important, particularly when considering the superconducting volume fraction of samples. In the Meissner state the magnetic field is completely expelled from the superconductor, resulting in $\chi = -1$. Any susceptibilities that deviate from this indicate that only part of the sample is in the superconducting state.

Magnetisation was used to extract various superconducting properties. Temperature sweeps in a constant low magnetic field (typically $1 - 10\,\mathrm{mT}$) can be used to find the bulk T_{c}, as shown in figure 3.5**a**. Here T_{c} was defined as the onset of the transition, where the sample leaves the normal state. This can be easily extracted using the derivative, $\partial\chi/\partial T$. $\mu_0 H_{\mathrm{c2}}$ points are found in the same way using higher magnetic fields.

Magnetisation hysteresis loops at constant temperature, $M(H)$ where $M = m/V$ and V is the sample volume, were used to extract the irreversibility field, $\mu_0 H_{\mathrm{irr}}$. The irreversibility field was identified as the point at which the hysteresis loop closes, as shown in figure 3.5 **c**.

$M(H)$ data were also be used to extract the lower critical field, $\mu_0 H_{\mathrm{c1}}$. For this, sweeps to smaller fields were necessary, typically $100\,\mathrm{mT}$ at a rate of $0.1\,\mathrm{mT/s}$. $\mu_0 H_{\mathrm{c1}}$ marks the transition from the Meissner state into the vortex state for type-II superconductors. In the Meissner state $\chi = -1$ and a linear response of $M(H)$ is obtained. Thus, $\mu_0 H_{\mathrm{c1}}$ was found when $M(H)$ deviated from linear behaviour, as shown in figure 3.5**b**.

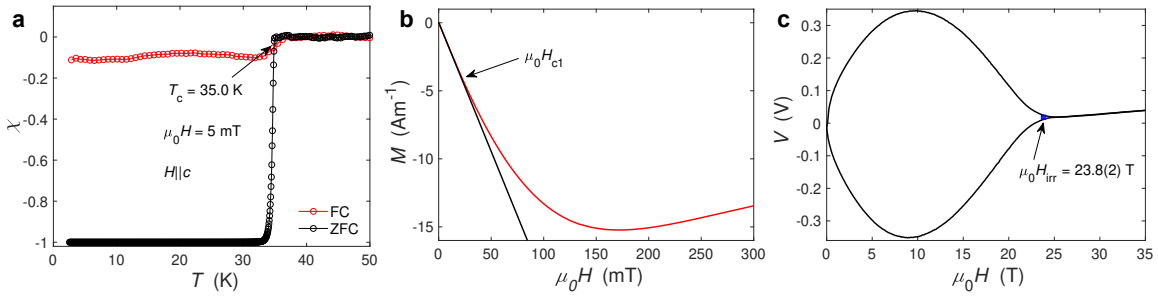


Figure 3.5: **Extracting values from magnetisation.** **a** Magnetic susceptibility, χ, as a function of temperature. The black and red curves represent zero-field cooled (ZFC) and field cooled (FC) data respectively. The susceptibility is determined from experimental data, using the calculated demagnetisation factor for the sample of $N \sim 0.99$ (see section 4.3). T_c is defined as the point at which the ZFC data becomes diamagnetic. **b** Magnetisation against applied magnetic field. The red curve represents the data and the black line is a linear fit to the low-field regime. $\mu_0 H_{c1}$ is defined as the point at which the data deviates from the linear dependence. **c** Voltage against applied magnetic field. $\mu_0 H_{irr}$ is defined as the point at which the hysteresis loop closes. Note that **c** is actually torque magnetometry data, but the same algorithm was used to identify $\mu_0 H_{irr}$ from magnetisation and torque data.

Four (or five) quadrant $M(H)$ loops can be used to calculate the critical current density, J_c, of superconductors in the vortex state using the extended version of Bean's critical state model [94]. For cuboidal samples the critical current density is given by

$$J_c = \frac{2\Delta M}{a(1 - \frac{a}{3b})}, \tag{3.5}$$

where $\Delta M = |M_{up} - M_{down}|$ is the change in magnetisation per unit volume in $\mathrm{A/cm}$, and a and b are sample dimensions in the plane perpendicular to the applied magnetic field with $a > b$. For cylindrical samples the critical current density is given by

$$J_c = \frac{3\Delta M}{2r}, \tag{3.6}$$

where r is the radius of the cylinder and the magnetic field is applied along the length of the cylinder. The sweep rate used for these measurements typically was $3 - 5$ mT/s, depending on the maximum target field[11]. The Meissner state was always observed in the first quadrant of these measurements, as expected. To accurately determine the critical current density in small positive fields it was then necessary to ramp the magnet to a small positive field again, usually 1 T, to close a complete hysteresis loop of the vortex phase (as the original

[11] For magnetic fields above 12 T in the 16 T PPMS a slower sweep rate of 3 mT/s has to be used. A slower sweep rate also has to be used when changing the magnet polarity. Both of these are important considerations for complete four or five quadrant $M(H)$ loops.

loop over this part would have been in the Meissner state). $J_c(H)$ curves were calculated for both positive and negative fields, which were then compared to check for consistency.

For all magnetisation measurements the magnetic field was first oscillated to zero at a temperature above the samples T_c to remove any trapped flux or remnant field. The sample was then zero field cooled to the desired temperature before any data were taken. The superconducting magnet in the PPMS was tested for remnant fields using a palladium reference sample. It was found that the best way to zero the magnet was to oscillate down from $1\,\mathrm{T}$ in stages, using a progressively smaller sweep rate. Using this method remnant fields $< 0.1\,\mathrm{mT}$ were achieved.

3.5 Torque magnetometry

Torque measurements presented here were performed using a $16\,\mathrm{T}$ PPMS as well as a $38\,\mathrm{T}$ resistive DC magnet in Nijmegen. In a magnetic field the torque is given

$$\tau = \mathbf{M} \times \mathbf{B}, \tag{3.7}$$

where M is the magnetisation of a sample and B is the magnetic field. Thus, torque is not a direct measurement of magnetisation, but rather the component of magnetisation perpendicular to the applied magnetic field. It is essentially a measure of the magnetic anisotropy of a sample. For a pure system with no anisotropy the moment will align with the magnetic field, and so the torque of the sample will be zero. This also means that the torque is zero when it is applied along a high-symmetry axis. For this reason, it has been necessary to slightly miss-align samples with the magnetic field.

The torque measurements conducted here were performed with piezoresistive cantilevers, specifically the Seiko PRC-400 self-sensing micro-cantilever chip. This utilizes a $400\,\mu$m 'active' cantilever on which a sample is mounted (using a small amount of vacuum grease) alongside a 'dummy' lever. These levers are attached to the chip with piezoresistive arms, the resistance of which depends on the torque experienced by the lever. Thus, the two arms will have different resistance values based on the sample mounted at the end of the 'active' lever. These leavers form two of the resistive parts of a Wheatstone bridge, the other components being a fixed resistor and a variable resistor. Whilst the variable resistor is kept at a fixed value, the change in voltage dropped across the bridge depends only on the difference in the resistance of the two cantilevers, and thus only on the deflection of the 'active' cantilever relative to the 'passive' one, which is proportional to the torque of the sample (for small angles, usually $< 1^{\mathrm{o}}$). The changes in voltage can be very small, and so

the variable resistor is adjusted before each measurement (field sweep) such that the voltage across the Wheatstone bridge is zero. This allows for a higher voltage sensitivity. The levers have a typical resistance of $\sim 500\,\Omega$. Small currents of $\sim 70\,\mu$A, supplied by either a Keithley 6221 or a Stanford SR830 lock-in, were used to minimise heating effects whilst maintaining a strong signal. Voltages across the bridge were measured using an SR830 with the signal amplified $\times 100$ using a transformer. Large torque can break the cantilever, and so samples were kept to a reasonable size of $\sim 150\,\mu\text{m}\times 150\,\mu\text{m}\times 50\,\mu\text{m}$.

Note that for larger deflections, $> 1^{\text{o}}$, the magnetisation of the sample will start to change significantly. This results in the relationship between torque and voltage becoming non-linear. This can become particularly problematic for measurements of the upper critical field or the irreversibility field near $H||(ab)$, where they have a large angular dependence. The sample dimensions above should ensure that the deflection stays small, below 1^{o}, and so data will always be in the regime where $\tau \propto V$. The exact relationship also depends on the characteristics of each cantilever. Calibrating each lever is not straightforward, and so torque will be presented in volts (or millivolts), which proves sufficient for the purposes of this method here.

These measurements have been used solely here to identify the irreversibility field, $\mu_0 H_{\text{irr}}$, of type-II superconductors from magnetic field sweeps. As discussed above, the sign of the magnetisation changes with the magnetic field direction, which also introduces a hysteresis into the torque signal while the sample is superconducting. The point at which this hysteresis closes is thus defined as $\mu_0 H_{\text{irr}}$, as in figure 3.5**c**. Samples are (usually) paramagnetic outside of the superconducting state, and so the magnetisation is linear in field. This means one can expect the torque in the normal state to have a $\tau \sim H^2$ dependence.

Chapter 4

Ultrahigh critical current densities in the stoichiometric iron-based superconductor $CaKFe_4As_4$

As the main trend throughout this thesis is superconductivity, this first experimental chapter will begin by analysing the bulk superconducting properties of a particular iron-based superconductor, $CaKFe_4As_4$. This chapter will cover the experimental mapping of the lower critical fields, upper critical fields, irreversibility fields and the critical current density through magnetisation studies. From these results a vortex phase diagram is constructed. The critical current density has also been used to find the vortex pinning force density, the magnetic field dependence of which provides details of the nature of pinning centres.

This chapter focuses on the superconducting properties and the critical current density of $CaKFe_4As_4$ in both single crystals and polycrystalline samples. The results here were found using magnetization measurements in magnetic fields up to 16 T. $CaKFe_4As_4$ exhibits an ultra-high critical current density of $J_c \sim 10^7$ A/cm^2 at 5 K, when the magnetic field is perpendicular to the conducting (ab)-plane (parallel to the c-axis). J_c is then enhanced further by a factor 10 in single crystals when the magnetic field is parallel with the (ab)-plane at 5 K, but is also significantly suppressed by the presence of grain boundaries in powder samples. Here the lower critical fields, $\mu_0 H_{c1}$, and the upper critical fields, $\mu_0 H_{c2}$, of single crystals and a powder sample have been extracted from magnetisation measurements for a single crystal in two magnetic field orientations, $H||c$ and $H||(ab)$, and for a pressed powder sample. These are used to build a vortex phase diagram for the single crystal and a polycrystalline sample. A second magnetization peak is present in the magnetic hysteresis loops of single crystals when $H||c$, which implies that vortex dynamics change significantly with temperature and magnetic field. The flux pinning force density is extremely large, and the pinning parameters suggest the existence of surface and point core

pinning of vortices. These results suggest that $CaKFe_4As_4$, with such large critical current densities and very high upper critical fields, is an exciting new candidate for practical applications.

This chapter will first recap important properties of iron-based superconductors. It will then cover varies aspects about superconductivity that can be extracted from various magnetisation measurements for $CaKFe_4As_4$. This includes the lower critical field, $\mu_0 H_{c1}$, from low field magnetisation against magnetic field data, $M(H)$, at constant field and the upper critical field, $\mu_0 H_{c2}$ from magnetisation against temperature at constant applied field. Next, the irreversibility field, $\mu_0 H_{irr}$, and the critical current density are extracted from four and five quadrant $M(H)$ hysteresis loops up to $16\,\mathrm{T}$. These large hysteresis loops also show a second magnetisation peak, indicating a vortex glass transition. From the magnetic field transitions, the vortex phase diagram when $H||c$ is constructed. The vortex pinning force is calculated using the critical current density and the applied magnetic field. Finally, the wider implications of these results are discussed, and $CaKFe_4As_4$ is compared to other iron-based superconductors. The results in this chapter begin to establish $CaKFe_4As_4$ as a good candidate for practical applications.

4.1 Introduction

Many of the properties of iron-based superconductors make them attractive for applications. They are more metallic than other superconductors, have relatively high superconducting transition temperatures, high upper critical fields, good grain boundary connectivity and, generally, large critical current densities [125–128]. The last of these properties, the critical current density J_c, is of utmost importance, particularly for high-field applications [129, 130]. Generally a high J_c exceeding $10^5\,\mathrm{A/cm^2}$ even at high magnetic fields above $10\,\mathrm{T}$ is found in many optimally-doped iron-based superconductors [129].

Critical currents in superconductors are generally limited by the superconducting volume fraction, the vortex pinning strength and flux motion. Different types of pinning determine the properties of a vortex lattice, including formation of vortex glass phase with elastic or plastic creep, vortex melting, vortex liquid phases and ordered-to-disordered phase transitions [98, 131]. Different pinning mechanisms tend to dominate in different systems. For example, polycrystalline or pressed powder samples will usually be strongly influenced by the effects of surface pinning on grain boundaries. As the vortex motion and flux pinning is affected by disorder and inhomogeneities in superconductors, it is important to understand what happens in a stoichiometric and clean high-T_c superconductor, such as $CaKFe_4As_4$.

4.2 Experimental details

Single crystals of $CaKFe_4As_4$ samples were grown by the FeAs self-flux method and the pressed powder sample was synthesized using a solid state reaction method, as detailed elsewhere [59, 61, 132]. The single crystals were cuboidal, whereas the pressed powder sample was cylindrical. Magnetic measurements were carried out using the VSM (Vibrating Sample Magnetometer) option of a Quantum Design Physical Property Measurement System with the magnetic fields up to 16 T. The magnetic isotherms were performed up to 16 T with a magnetic field ramping rate of $3\,\mathrm{mTs}^{-1}$ at several temperatures ranging from 2 K up to 40 K. All the hysteresis loops at constant temperatures, $M(H)$, and temperature dependent magnetization in constant magnetic field, $M(T)$, were performed after cooling the sample in zero magnetic field from above T_c. The magnetic field was always oscillated to zero above T_c to minimise and remnant magnetic field before cooling for measurements.

Magnetic susceptibility data, $\chi(T)$ has been corrected for demagnetization effects [122, 133]. For an applied external field H_a, the internal field $H_\mathrm{i} = H_\mathrm{a} - N_\mathrm{eff}M$, where N_eff is the effective demagnetization factor. χ is found from $\chi = \chi_\mathrm{obs}/(1 - N_\mathrm{eff}\chi_\mathrm{obs})$, where $\chi_\mathrm{obs} = M/\mu_0 H_\mathrm{a}$ and $M = m/V$, where m is the magnetic moment and V is the sample volume. The effective demagnetization factor of this single crystal is estimated as $N_\mathrm{eff} = 0.995$ when $H||c$ by assuming perfect diamagnetism inside the superconducting state ($\chi = -1$), which is very similar to the calculated demagnetization factor for this orientation of $N = 0.994$ [122, 133]. When $H||(ab)$ the value of $N_\mathrm{eff} = 0.70$, which is extracted from zero-field cooled data assuming that in this orientation the sample is again perfectly diamagnetic. $N_\mathrm{eff} = 0.41$ for the cylindrical polycrystalline sample is extracted both from calculations and experiment [122, 133].

Lower critical fields, $\mu_0 H_\mathrm{c1}$, were extracted from $M(H)$ loops up to 0.5 T using a slow magnetic field sweep rate of $0.2\,\mathrm{mTs}^{-1}$ at each temperature. The deviation point of $M(H)$ curves from linear behaviour gives the magnetic field of first flux penetration, $\mu_0 H^\star_\mathrm{c1}$. The upper critical fields, $\mu_0 H_\mathrm{c2}$, were extracted from the temperature dependence of magnetization at different constant magnetic field up to 16 T. The upper critical fields $\mu_0 H_\mathrm{c2}$ (or in this case, 'T_c2') are defined as the point at which $M(T)$ curves deviate from the high-temperature (paramagnetic) behaviour. The irreversibility fields, $\mu_0 H_\mathrm{irr}$, are defined as the point at which the magnetization loops close and no longer show the characteristic irreversible behaviour of the superconducting state. Irreversibility fields have been found using $\Delta M(H)$ and the point at which the critical current density $J_\mathrm{c}(H)$ (see section 4.5 later in this chapter) returns to the background value. This was done for both positive and negative magnetic fields in order to estimate errors.

From $M(H)$ loops the critical current density, $J_c(H)$, was extracted using Bean's extended critical state model (see section 2.2.1 for more details) [94]. For a cuboidal crystal, the magnetic field dependence of J_c (in units of A/cm^2) is given by equation 2.16, $J_c = 2\Delta M/[a(1 - a/3b)]$ (for $a < b$), where $\Delta M = M_{up} - M_{dn}$, and M_{up} and M_{dn} are the magnetization while magnetic fields are increasing and decreasing respectively. The sample dimensions a and b are entered in units of cm. The magnetization ΔM is expressed in units of A/cm and is obtained from the magnetic moment divided by the sample volume, $M = m/V$ where $V = a \times b \times c$. Here, a and b are in-plane sample dimensions perpendicular to the applied magnetic field and c is sample dimension parallel to the applied magnetic field. In this chapter, a single crystal of $CaKFe_4As_4$ has been measured with the dimensions $(a, b, c) = (1.09, 1.365, 0.0025)$ mm when $H||c$ and $(a, b, c) = (0.0025, 1.09, 1.365)$ mm when $H||(ab)$. The thickness of the single crystal was evaluated using Gaussian fits to intensities from optical images across the length and width of the sample. To estimate J_c of the cylindrical pressed powder sample the expression $J_c = 3\Delta M/d$ was used (equation 2.17), where $V = 2\pi(d/2)^2 l$, $d = 5.03$ mm and $l = 4.08$ mm are the volume, diameter and length of the cylinder, respectively [94]. Again, ΔM is in units of A/cm and all sample dimensions are in units of cm. The average grain size for the powder sample is $\sim 1.7(7)\,\mu$m. The vortex pinning force density can be estimated from $F_P = J_c \times \mu_0 H$ [95].

4.3 Magnetic susceptibility

$\chi(T)$ from zero-field-cooled (ZFC) and field-cooled (FC) magnetization measurements in low magnetic fields for the single crystal when $H||c$ and $H||(ab)$ and for the powder sample are shown in figures 4.1 **a**-**c**. A perfect diamagnetic state is reached at low temperatures for all measured samples in all magnetic field orientations, which implies the existence of the Meissner state in an ideal superconductor. The critical temperature, $T_c = 35$ K is defined here as the bifurcation point between ZFC and FC data. The superconducting transition is very sharp for the single crystal ($\Delta T_c \sim 1$ K) suggesting a high quality of this single crystal, as has also been established by X-ray scattering and resistivity data (see figure A.2**a** in appendix A and the supplementary material in Ref. [134]). The powder sample also shows perfect diamagnetism at low temperatures, but it has a much broader, and possibly two-step (the derivative of the ZFC data, $d\chi/dT$, shows two peaks), transition with a width of $\Delta T_c \sim 12$ K. This is likely due to pinning on grain boundaries and grain size effects, as seen in other powdered iron-based superconductors [135]. No secondary phases were identified in the powder sample from X-ray studies (see the supplementary

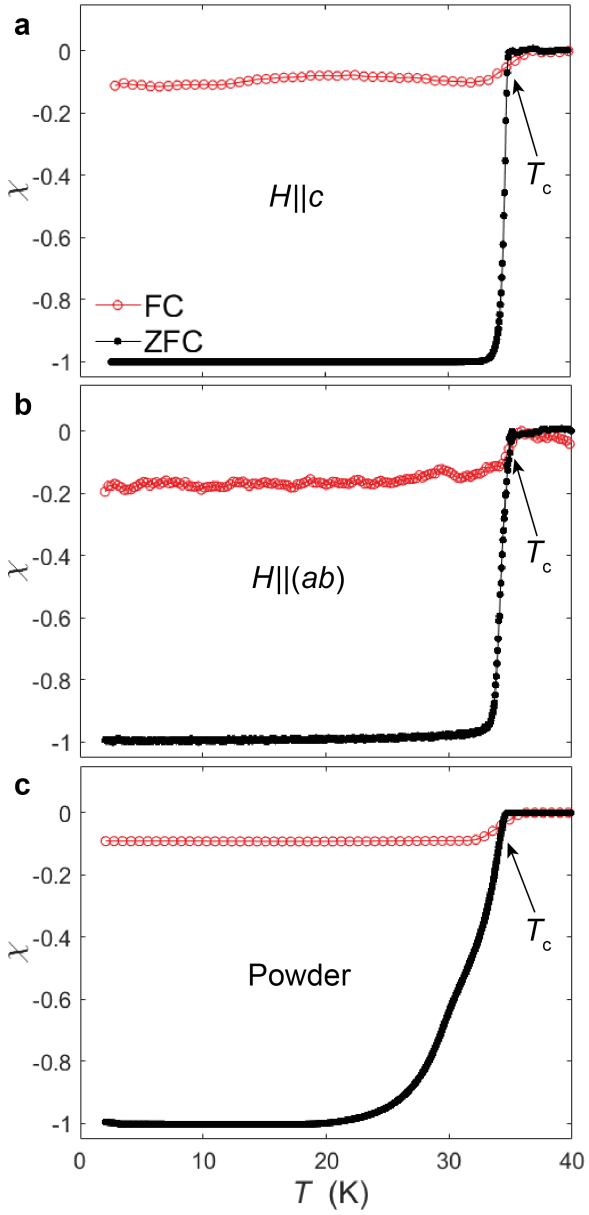


Figure 4.1: Temperature dependence of magnetic susceptibility, χ, deduced from zero-field cooled (black) and field-cooled (red) magnetization measurements for the single crystal when **a** $H||c$ and **b** $H||(ab)$ in an applied magnetic field of $5\,\mathrm{mT}$ as well as **c** the powder sample in $2\,\mathrm{mT}$. The arrows indicate the positions of the onset values of the critical temperature, $T_\mathrm{c} = 35\,\mathrm{K}$. It should be noted here that the T_c from $\chi(T)$ agrees well with the T_c value from resistivity (see figure 5.1 in chapter 5 and figure A.2**a** in appendix A).

material in Ref. [134]). The small diamagnetic signal in the FC data reflects the strong nature of pinning in the samples and the permanent trapped fluxed.

4.4 Lower and upper critical fields

The temperature dependence of the lower critical field was determined using low-field magnetic hysteresis measurements, as shown in figure 4.2 **a**-**c** for $H||c$, $H||(ab)$ and the pressed powder sample respectively. The negative and linear dependence of magnetization with magnetic field is a signature of the Meissner state, up to $\mu_0 H_{c1}(T)$, above which magnetic flux starts to penetrate the bulk and vortices begin to form. The temperature dependence of the extracted lower critical field for the single crystal and the powder sample is shown in figure 4.2 **d**. The lower critical field for $H||(ab)$ is larger than that for $H||c$. The $\mu_0 H^{\star}_{c1}(T)$ values for the pressed powder sample were extracted by fitting a linear dependence to the magnetization above the anomaly (deviation from negative linear behaviour, before the signal returns to the expected behaviour for the Meissner state), which is likely caused by grain boundaries effects, different phases or disconnected polycrystals in different magnetic field orientations (each establishing their own screening currents). The latter of these causes seems unlikely as perfect diamagnetism, $\chi = -1$, was established for the powder sample earlier (see figure 4.1**c**), and one would expect a superconducting volume fraction significantly less than 1 if each grain had their own screening currents, rather than universal screening currents for the whole sample. The lower critical field for the powder lies in between the two magnetic field orientations of the single crystal, as could be expected from powder averaging effects. The lower critical field points for the powder sample have a very weak temperature dependence below $\sim 10\,\mathrm{K}$, consistent with μSR results [136].

Upper critical fields, $\mu_0 H_{c2}$, have been determined from ZFC magnetization as a function of temperature (from $5 - 40\,\mathrm{K}$) for different constant magnetic fields up to $16\,\mathrm{T}$ for the single crystal and the powder sample, shown in figure 4.2**f**-**h**, as labelled. The upper critical fields as a function of temperature near T_c is defined by the point at which magnetization starts to deviate from the high-temperature paramagnetic value. Just below the critical transition temperature into the superconducting state, a small jump in the temperature dependence of the magnetization occurs for both the single crystal and the powder sample, which is more pronounced as the field increases. This effect is unexplained, but may be caused by flux jumps or other properties of a vortex glass state. This could also be caused by other magnetic properties, but while this system shows AFM spin fluctuations [137], it lacks any long-ranged magnetic order [59, 61, 137, 138]. For this reason, it is probable that these small jumps are not related to other forms of magnetic order.

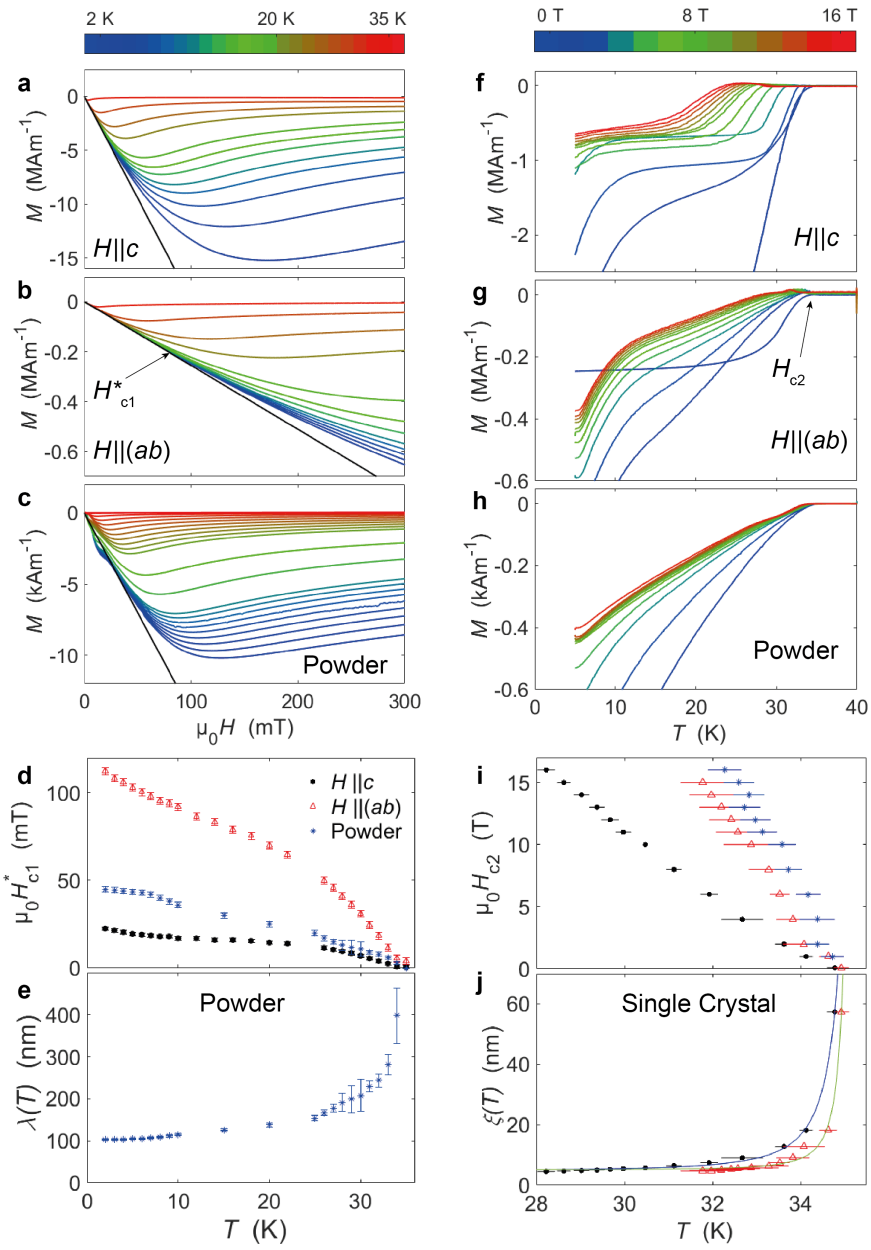


Figure 4.2: Magnetization, M, versus magnetic field at constant temperatures for the single crystal when **a** $H||c$ and **b** $H||(ab)$ as well as for **c** the powder sample of $CaKFe_4As_4$. The arrow in **b** shows the point of deviation of magnetization from linear dependence in the Meissner state, defined as the first penetration field $\mu_0 H^{\star}_{c1}$. Temperatures in **a**-**c** are indicated by the top left colour bar. **d** The temperature dependence of the lower critical field $\mu_0 H^{\star}_{c1}$ measured for the single crystal in two orientations in magnetic field as well as the powder sample. **e** The penetration depth, λ, for the powder sample as a function of temperature. **f**-**g** The temperature dependence of magnetization in different magnetic fields up to 16 T for the single crystal in two orientations and **h** for the powder sample. Applied magnetic fields in **f**-**h** are indicated by the top right colour bar. **i** The upper critical field $\mu_0 H_{c2}$ versus temperature for the single crystal and the powder sample. **j** Coherence lengths, ξ_{ab} and ξ_c, for the single crystal of $CaKFe_4As_4$ near T_c.

Figure 4.2**i** shows the upper critical field phase diagram near T_c of $CaKFe_4As_4$ extracted from magnetization studies. The temperature dependence of the upper critical field has a large slope near T_c, indicating a very high value of $\mu_0 H_{c2}(T = 0)$. To estimate the upper critical field in the zero temperature limit, $\mu_0 H_{c2}(T = 0)$, the Werthamer-Helfand-Hohenberg (WHH) formula close to T_c is used [78],

$$\mu_0 H_{c2}(0) = -0.69 T_c \left(\frac{d\mu_0 H_{c2}}{dT} \right)_{T_c}, \tag{4.1}$$

where there are no Pauli paramagnetic effects. The slope of upper critical field, $(d\mu_0 H_{c2}/dT)$, is $2.6(1)\,\mathrm{TK}^{-1}$ for $H||c$ and $5.7(7)\,\mathrm{TK}^{-1}$ for $H||(ab)$ for the single crystal, and $10.1(5)\,\mathrm{TK}^{-1}$ for the powder sample. Using $T_c = 35\,\mathrm{K}$, gives $\mu_0 H_{c2}(T = 0) \sim 62\,\mathrm{T}$ when $H||c$ and a much larger value of $135\,\mathrm{T}$ when $H||(ab)$. The powder sample shows a significantly larger upper critical field predicted from the WHH model at $T = 0$ of $241\,\mathrm{T}$, a factor of ~ 4 larger than for $H||c$ in the single crystal. The larger upper critical fields in the pressed powder could imply the presence of additional pinning centres compared to the single crystals, for example, arising from grain boundaries. It is however more likely that the upper critical field for powder will be limited at lower temperatures and higher magnetic fields, perhaps by Pauli paramagnetic effects. Further experiments would be required to establish this. The slope of the upper critical fields from resistivity data measured in high magnetic fields (see chapter 5) gives slightly larger slopes near T_c but also show significant deviation from single-band behaviour. This is discussed in chapter 5 later in more detail, but this implies that the predictions of $\mu_0 H_{c2}(T = 0)$ from the slopes here may be unreliable.

The Pauli limit for a single band is reached when the condensation energy is overcome by the Zeeman energy, defined as $\mu_0 H_p/T_c = 1.84\ \mathrm{TK}^{-1}$ in the case of singlet pairing and weak spin-orbit coupling [76, 139]. Using $\mu_0 H_{c2}(T = 0)$, the corresponding value of $\mu_0 H_{c2}(0)/T_c$ is $\sim 1.8\,\mathrm{TK}^{-1}$ for $H||c$, increasing to $3.9\,\mathrm{TK}^{-1}$ when $H||(ab)$ and $6.9\,\mathrm{TK}^{-1}$ for the powder sample. This would imply that $CaKFe_4As_4$ may be Pauli limited when $H||c$, but lower temperature data at higher magnetic fields would be needed to clarify this (as is done in chapter 5 later).

In order to estimate the superconducting coherence lengths, ξ, the Ginzburg-Landau (GL) approach and equations 1.20-1.21 are used. The coherence lengths as a function of temperature near T_c are shown in figure 4.2**j**. Coherence lengths from the WHH zero temperature extrapolation of the upper critical fields, $\mu_0 H_{c2}(T = 0)$, are found to be $\xi_{ab} = 1.9(1)\,\mathrm{nm}$, $\xi_c = 0.87(8)\,\mathrm{nm}$ for the single crystal, and $\xi = 0.97(8)\,\mathrm{nm}$ for the powder sample. The extracted mean free path for single crystals is $\ell = 26.6\,\mathrm{nm}$, calculated from the extrapolated normal state resistivity at zero temperature of $\rho_0 \sim 9.4(2)\,\mu\Omega\mathrm{cm}$, which

is presented in more detail in chapter 5 and figure 5.1 (and using carrier concentration reported in Ref. [61]). This suggests that single crystals of $CaKFe_4As_4$ lie well within the clean limit, where $\xi(0) \ll \ell$.

The lower critical field values extracted in figure 4.2**d** were used to calculate the London penetration depth as a function of temperature, $\lambda(T)$, for the powder sample. In order to estimate $\lambda(T)$, demagnetization effects are corrected for (as detailed earlier using N_{eff}=0.41) and an estimate for the value of the Ginzburg-Landau order parameter of $\kappa \sim 88$ is used. This gives a low temperature London penetration depth $\lambda(0) = 104(6)$ nm, as shown in figure 4.2**e**, which is similar to the value of 133 nm, extracted from previous studies using literature values for single crystals [140]. Muon relaxation studies estimate the penetration depth as 209 nm for a single crystal [141] and 286 nm for a powder sample [136], which are larger than reported in this chapter.

4.5 Magnetic hysteresis and critical current densities

Figure 4.3**a**-**c** show the $M(H)$ loops at constant temperatures between 2 to 35 K in magnetic fields up to 16 T for the single crystal when $H||c$ and $H||(ab)$, and for the powder sample respectively. The hysteresis areas decreases with increasing temperature. The symmetrical shape of $M(H)$ loops imply the existence of flux pinning centres, suggesting that the magnetization is dominated by bulk pinning rather than surface and geometrical barriers [95]. The $M(H)$ loops for the powder are less symmetric, which may suggest that surface pinning is present in this sample [95]. The magnetic hysteresis loop in figure 4.3**b** when $H||(ab)$ displays a dip near zero magnetic field which may be caused by the highly inhomogeneous field distribution in the vortex state in this orientation [142], the anisotropy of J_c [143] or self-field effects in this orientation.

A second magnetization peak (SMP) is present for the single crystal when $H||c$, as shown in figure 4.3**a**. With decreasing temperature, the peak moves to higher magnetic fields beyond the maximum applied magnetic field of 16 T. In the region between the valley (local minimum at fields below the location of the SMP) and the peak the width of the irreversible magnetization, ΔM, in figure 4.3**a** extends with increasing magnetic field, showing a clear fishtail effect. This effect has been observed in other superconducting single crystals, such as cuprates [144, 145], Nb_3Sn [146], MgB_2 [147] and iron-based superconductors, such as BaK122 [148] and LiFeAs [149]. Although its origin is not fully explained, the fishtail effect is strongly dependent on the sample orientation in externally applied magnetic field, and it is usually not present when $H||(ab)$. Importantly, the width of the $M(H)$ loops for $H||(ab)$ is much larger than of the loops for $H||c$ (larger irreversibility

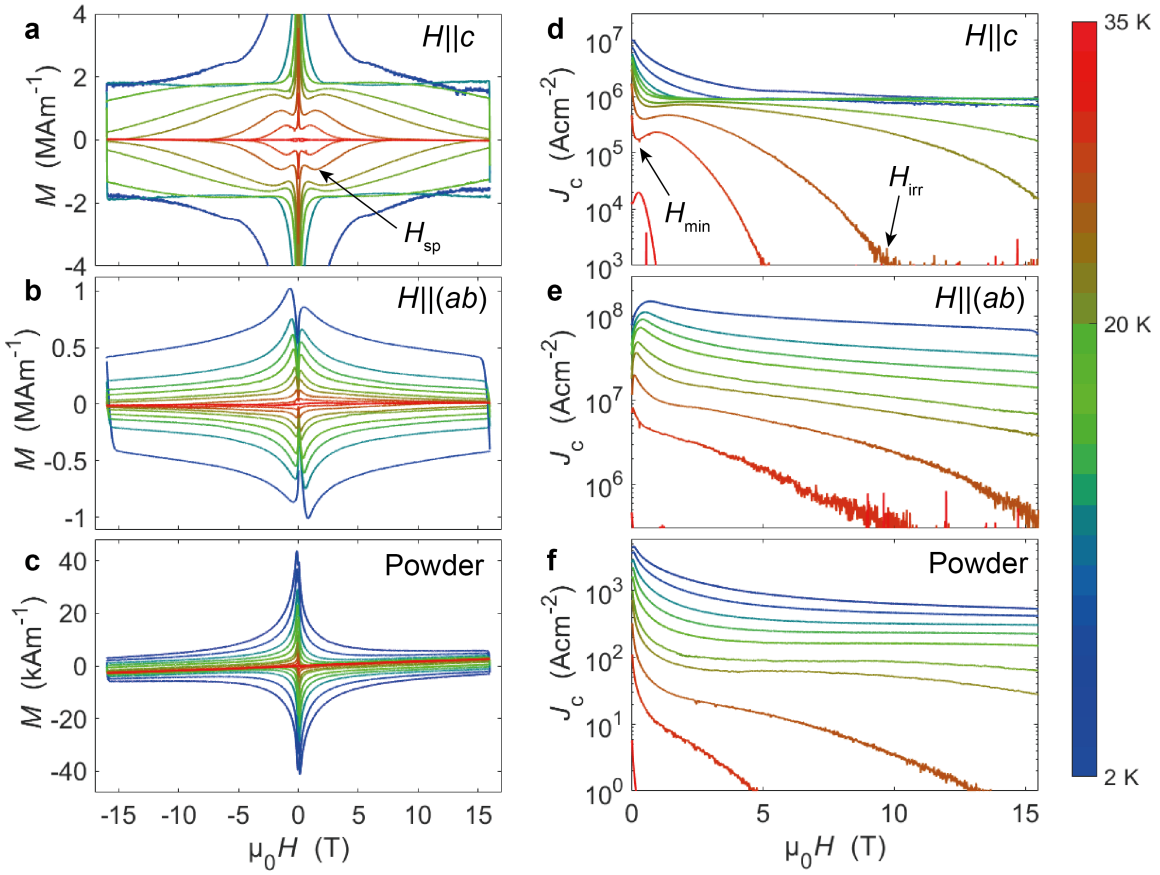


Figure 4.3: The isothermal magnetization loops, $M(H)$, for the single crystal in two orientations with **a** $H||c$ and **b** $H||(ab)$ and **c** the powder sample of $CaKFe_4As_4$. The critical current density, J_c, calculated from $M(H)$ using the Bean model [94], plotted as a function of magnetic field at constant temperatures for the single crystal when **d** $H||c$ and **e** $H||(ab)$, and **f** the powder sample, respectively. The arrows indicate the positions of the second magnetisation peak, $\mu_0 H_{\rm sp}$, in **a**, and the irreversibility field, $\mu_0 H_{\rm irr}$, and local minimum in magnetisation (and critical current density) inside the superconducting state, $\mu_0 H_{\rm min}$, in **d**.

field when $H||(ab)$) or the powder sample (figure 4.3**c**), implying that the pinning mechanisms are anisotropic and strongly affected by the granularity. Similar effects caused by anisotropy of flux pinning were observed in other iron-based superconductors, such as Fe(Se,Te) [150] and SmFeAs(O,F) [151].

According to the extended Bean model [94], the critical current density, J_c, can be determined from the magnetisation hysteresis loop width, ΔM (see sections 2.2.1 and 4.2). As the critical current remains rather constant with the change of magnetic field for the low temperature magnetization isotherms, the extended Bean's model gives a good estimation of the critical current density in this case. Other models that take into account the field variation of the critical current density and the vortex dynamics were also developed by Kim *et. al.* in Ref. [152] and Kim, Anderson *et. al.* in Ref. [97].

Figure 4.3**d**-**f** show the field dependence of the critical current density, $J_c(H)$, at constant temperatures obtained for the single crystal for different orientations in magnetic field and the powder sample, as labelled. The value of J_c for $H||c$ is extremely high, on the order of 10^7 A/cm^2, and is enhanced again by almost an order of magnitude for the $H||(ab)$ magnetic field orientation. However, the powder sample has a J_c which is at least three orders of magnitude lower than that of the single crystal, but similar to other polycrystalline iron-based superconductors [129, 130]. The low J_c of the powder sample is not particularly surprising as it is significantly affected by extrinsic factors, such as grain morphology, surface roughness, inter-grain voids, interfaces and other surface affects [129]. These extrinsic factors could be improved by optimising the synthesis process. For example, this could be done by using a ball-milling process, re-sintering and optimising the temperature and length of the preparation process. An optimisation of the superconducting properties when preparing polycrystalline and pressed powders has since been done in Ref. [153].

Figure 4.3**d**-**e** shows that J_c in $CaKFe_4As_4$ is robust up to $16\,$T, dropping by only a factor of ~ 2.5 between 1 and $16\,$T for $H||(ab)$ ($\sim 1.9(2) \times 10^8$ to $\sim 0.7(2) \times 10^8$ A/cm^2). To further emphasise this important aspect, $J_c(T)$ is plotted for the single crystal and the powder sample with respect to temperature for different magnetic fields of 0 and $15\,$T, as shown in figure 4.4 **a** and **b**, respectively. These are the highest J_c values obtained for any iron-based superconductor, to the authors best knowledge. These critical current density values suggest strong vortex pinning, establishing this stoichiometric high-T_c compound as a potential candidate for practical applications. The critical current density remains large over a wide temperature range, even with increasing magnetic field up to $15\,$T. The critical current density for $CaKFe_4As_4$ when $H||c$ is compared to other superconductors in figures 4.4**a** ($0\,$T) and 4.4**b** ($16\,$T). It is clear that $CaKFe_4As_4$ performs extremely well, with an ultra-high self-field $J_c \sim 10^7$ A/cm^2 for $H||c$ which remains robust up to $\sim 31\,$K

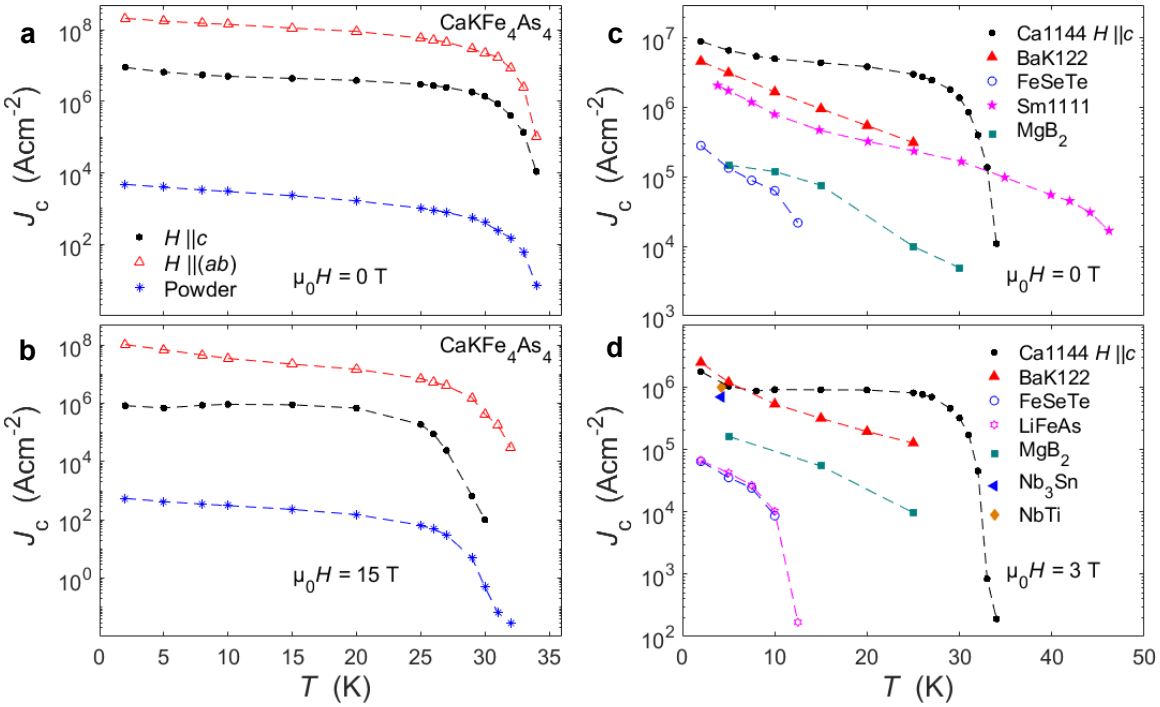


Figure 4.4: The temperature dependence of J_c, extrapolated at **a** $\mu_0 H = 0\,\mathrm{T}$ and **b** $\mu_0 H = 15\,\mathrm{T}$ for the single crystal in the two field orientations and of the powder sample of $CaKFe_4As_4$. Comparison between the temperature dependence of J_c in single crystals of $CaKFe_4As_4$ with those reported for different iron-based superconductors (SmFeAs(O,F) [151], (Ba,K)Fe_2As_2 [148], Fe(Se,Te) [150] and LiFeAs [149]) and commonly used superconductors (MgB_2 [154–156], Nb_3Sn [156] and NbTi [157]) in magnetic fields of **c** 0 T and **d** 3 T for $H||c$.

in 3 T (up to a value of 10^6 A/cm^2). To further confirm these large J_c values, additional crystals have been measured, which show very similar values to those presented here (see published work and SM in Ref. [134]). A slight decrease in J_c is noticed as the thickness of the sample increases from $\sim 2\,\mu$m towards $15\,\mu$m (see Table SM1 in Ref. [134]). These high J_c values of this stoichiometric clean superconductor close to an optimum doping is surprising, as one would expect a high density of defects to achieve stronger effective pinning and larger critical currents.

4.6 Vortex pinning force

In order to understand the nature of flux pinning, the temperature and field dependencies of the vortex pinning force density, $F_P = \mu_0 H \times J_c$, when $H \perp J_c$ is calculated (see section 2). According to the Dew-Hughes model [95], if a dominant vortex pinning mechanism exists in certain temperature range, the normalised vortex pinning force density $f_P = F_P/F_P^{max}$ at different temperatures should collapse into a single curve, as shown in figure 4.5**a**. Here, F_P^{max} is the maximum pinning force density. The resulting scaling law is given by $f_P(h) = h^p(1-h)^q$ (equation 2.18). The parameters p, q and h_{max} (the reduced field at which the pinning force is maximum) are related by equation 2.20. The indices p and q are two parameters whose values depend on the origin of pinning mechanism and $h = H/H_{irr}$ is the reduced field, where the irreversibility field $\mu_0 H_{irr}$ is estimated as the magnetic field at which $J_c(H)$ reaches the background noise value, as defined in figure 4.3 **a**.

Figures 4.5**a**-**b** shows $f_P(h)$ of $CaKFe_4As_4$ at different temperatures for the single crystal when $H||c$ and the powder sample respectively. As the irreversibility field exceeds the accessible magnetic field of 16 T at temperatures below $\sim$ 28 K, only data closed to T_c are presented ($T \geq 29$ K). The calculated maximum pinning force density (F_P^{max}) at 30 K reaches a value of 9.58 GN/m^3 for the single crystal and is severely reduced to only 0.0007 GN/m^3 for the powder sample. $f_P(h)$ collapse onto on a single curve with a $h_{max} \sim 0.28$ for the single crystal in figure 4.5**a**, indicating that a dominant pinning mechanism exists within this temperature range. For the powder sample the peaks in $f_P(h)$ are much broader and h_{max} has more variation with temperature. This is likely due to its granular nature, however the h_{max} value is close to that of the single crystal. The fitting parameters to the $f_P(h)$ give $p = 1.4(1)$, $q = 3.7(3)$ and $h_{max} \sim 0.28$ for the single crystal when $H||c$, and $p = 1.0(1)$, $q = 2.1(1)$ and $h_{max} \sim 0.33$ for the powder sample. In the Dew-Hughes model for pinning mechanism, a value of $h_{max} \sim 0.2$ corresponds to surface pinning for normal centre of core interaction, while $h_{max} \sim 0.33$ corresponds to point core pinning, also known as small size normal pinning [95] ($\delta\kappa$ or δT_c flux pinning, as defined

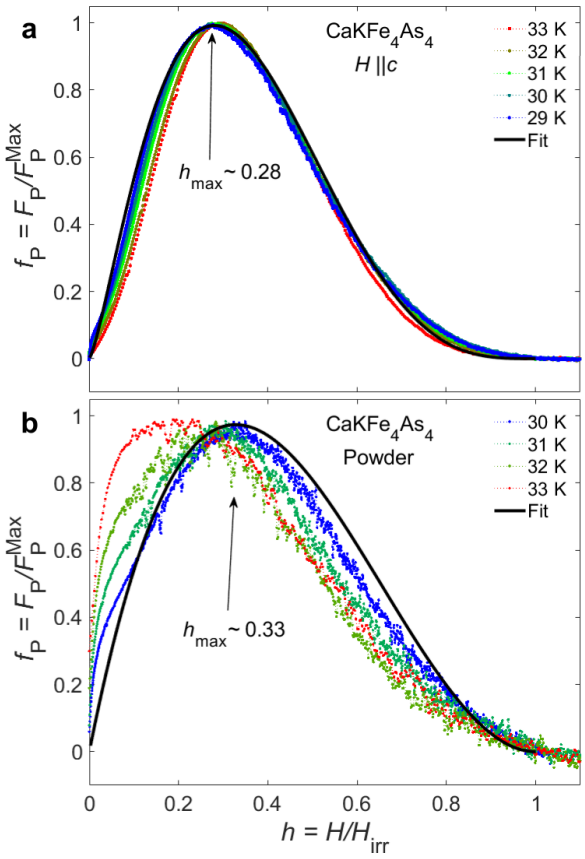


Figure 4.5: The scaled normalized pinning force density against reduced field, $f_{\rm P}(h)$, for different temperatures for **a** the single crystal when $H||c$ and **b** powder sample of $CaKFe_4As_4$. The solid black lines represent the model based on the scaling form $f_{\rm P}(h) = h^p(1-h)^q$. The peak in $f_{\rm P}$ occurs at $h_{\rm max} \sim 0.28$ for the single crystal in **a** and $h_{\rm max} \sim 0.33$ for the powder in **b**.

in section 2.2.3). Thus, $h_{\max} \sim 0.28 - 0.33$, observed for $CaKFe_4As_4$ suggests that vortex pinning is caused by a mixture of the surface and strong point core pinning of vortices, similar to the Fe(Se,Te) systems [158].

The obtained values of exponents p and q in $CaKFe_4As_4$ (listed in Table SM2 in Ref. [134]) also support the idea that not a single model can describe the flux pinning mechanism [95] and that flux creep may have a significant influence on vortex pinning, as would be expected for a vortex glass state. However, similar values of p and q have been reported for other unconventional superconductors, such as $FeTe_{0.6}Se_{0.4}$ ($h_{\max} = 0.28$) and $YBa_2Cu_3O_7$ ($h_{\max} = 0.33$) [158–160]. In the 122 iron-based superconductors, the pinning mechanism depends on the doping level and dopant type, but generally $h_{\max}$ tends to increase with increasing doping level [161]. The highest J_c is achieved when $h_{\max} \sim 0.40 - 0.45$ for the optimally-doped compounds [161]. Single crystal of $Ba_{0.6}K_{0.4}Fe_2As_2$ shows only small-size normal pinning ($h_{\max} = 0.33$) [95], whereas the values obtained for $BaFe_{1.8}Co_{0.2}As_2$ single crystals ($h_{\max} = 0.4$, $p = 1.67$, $q = 2$) [161] are correlated to a dense vortex pinning nano-structure, likely due to the inhomogeneous distribution of cobalt ions. This implies that a high J_c can also be caused by a dense vortex pinning nano-structure. Violation of the scaling behaviour in the underdoped and overdoped 122 iron-based superconductors, like in the powder sample here, implies the existence of multiple pinning sources [161]. Stoichiometric $CaKFe_4As_4$ single crystals show superconducting behaviour equivalent to an optimally-doped superconductor [161], but in the absence of inhomogeneities introduced by chemical substitution. This scaling analysis implies that the proximity to a optimally-doping regime and that a mixture of pinning mechanisms might be responsible for the high critical current densities in $CaKFe_4As_4$.

4.7 The vortex phase diagram

Based on these magnetization studies, the vortex phase diagrams of $CaKFe_4As_4$ have been constructed for the single crystal when $H||c$ and the powder sample, as shown in figure 4.6**a**-**b**. There are five different characteristic fields separating different regions of the $H - T$ vortex phase diagram. The local minimum in magnetisation inside the superconducting state, $\mu_0 H_{\min}$, and the second magnetisation peak, $\mu_0 H_{\rm sp}$, are the magnetic fields located at the valley point and the SMP, as defined in $J_c(H)$ plots in figure 4.3**d**. The irreversibility field, $\mu_0 H_{\rm irr}$, is defined in figure 4.3**d** and the lower and upper critical fields have been discussed in detail previously (in section 4.4) and are shown in figure 4.2. In the powder sample, there is no second magnetization peak. The irreversibility is very close to the upper critical field in the single crystal, which is a very important feature for $CaKFe_4As_4$

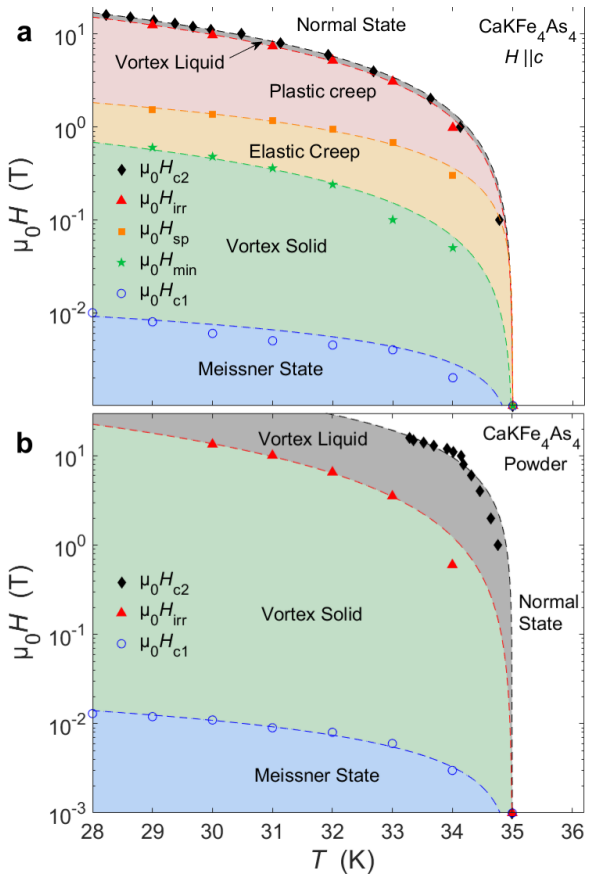


Figure 4.6: The vortex phase diagram of **a** the single crystal when $H||c$ and **b** powder sample of $CaKFe_4As_4$. The different magnetic fields separating different regions in the vortex phase diagram are defined in figures 4.2 and 4.3. The dashed lines are fits using the empirical expression $H(T) = H(0)(1 - T/T_c)^n$ and represent the separation of different vortex phases.

to be useful for applications, as the irreversibility line demarcates the field at which vortex flow is unpinned and magnetic irreversibility sets in. The powder sample has upper critical fields a factor of 4 larger than in single crystals when $H||c$ and the vortex liquid state is significantly further extended. This suggests that grain boundaries increase the density of pinning centres to give rise to larger upper critical fields, whereas the poor grain connectivity in powder is detrimental to supporting large critical currents, as they are significantly reduced.

Different regimes of vortex dynamics [162, 163], marked elastic creep and plastic creep, separated and by the $\mu_0 H_{\rm sp}$ line are shown in the phase diagram in figure 4.6**a**. In general, the vortex nature is determined by the competition between the elastic energy of the vortex lattice, the pinning energy and thermal energy [161]. The second magnetization peak effect is commonly associated with an ordered-to-disordered vortex phase transition, which occurs at $\mu_0 H_{\rm min}$ when the pinning energy exceeds the elastic energy [133]. The motion of the vortices is governed by the elastic force in the elastic and plastic creep regions, and the second magnetisation peak at $\mu_0 H_{\rm sp}$ corresponds to the threshold field of the elastic-plastic crossover. In the plastic creep region, as the magnetic field increases the vortex lattice softens and vortices are pinned more easily, resulting in an increase in the critical current density. As the magnetic field increases the pinning force and thermal energy affect the vortices significantly and the vortices can more easily move from one pinning centre to another in the vortex liquid state, which is at magnetic fields above the irreversibility field. In the case where the pinning energy does not exceed the elastic energy the SMP disappears, owing to the absence of an order-disorder transition, as in the case of powder sample in figure 4.6**b**. Here it is worth noting that the absence of a SMP in the powder sample could be caused by a number of other factors, such as a larger variety of pinning mechanisms (for example, surface pinning) which changes the dynamics.

The vortex phase diagram of the $CaKFe_4As_4$ single crystal is very similar to that reported for the (Ba,K)Fe_2As_2 single crystal [148], with $\mu_0 H_{\rm min}$ having almost the same value but the 122 compounds exhibiting a larger $\mu_0 H_{\rm sp}$ and irreversibility field. The temperature dependence of the different characteristic fields in figure 4.6**a** can be modelled using the empirical expression

$$H(T) = H(0)\left(1 - \frac{T}{T_{\rm c}}\right)^n, \tag{4.2}$$

with n varying between $1.3(1)$ and $0.6(1)$. The obtained n value corresponding to the $\mu_0 H_{\rm min}(T)$ curve is $n = 1.2(1)$, similar to values reported for other iron-based superconductors [149, 164], whereas the $\mu_0 H_{\rm sp}(T)$ and its corresponding exponent of $n = 0.83(6)$

is much smaller than those found in other systems [148, 149, 164]. Furthermore, the vortex phase diagram of $CaKFe_4As_4$, bounded by the temperature dependence of the irreversibility field, shows a high exponent value of $n = 1.3(1)$, which cannot be understood within the framework of conventional superconductivity.

$CaKFe_4As_4$ is a stoichiometric clean superconductor exhibiting very high critical current values, rather unexpected, as a high density of point-like defects is usually necessary to achieve such high values of J_c. However, recent Scanning Tunnelling Microscopy (STM) studies find a disordered vortex lattice up to $8\,$T, with the vortices pinned at the locations where the superconducting order parameter is strongly suppressed due to pair breaking, and the vortex core size decreases with increasing field [165]. The low-temperature vortex core size determined by STM is $\sim 1.3\,$nm, in reasonable agreement with the values of the coherence lengths estimated from the upper critical fields presented in this chapter of $\sim 1.9\,$nm when $H||c$, demonstrating the importance of point-like pinning in this material. Furthermore, the surface topography measured by STM exhibits steps on the surface due to structural defects, surface reconstruction and small stripes, which as possible sources of surface pinning. Other types of two-dimensional surface pinning may be influenced by the anisotropic layered structure and stacking faults that may occur between Fe-As layers along the c-axis.

The observed high critical current density values are likely to be generated by intrinsic effects due to the ionic size variation that may occur in the crystallographic structure and the two-dimensional surface defects in $CaKFe_4As_4$. This structure has relevant differences compared to a 122 system, due to the absence of a glide plane and the positions of the Fe-As layers generating different Fe-As distances and two distinct As sites (rather than a single site symmetry in 122 systems). The reduced symmetry and distinct As sites or switching of C and K (which could again give a further 2 different As sites) sites could make small structural defects more likely. The small structural defects can cause mean free path fluctuation induced pinning, which is an effective way to enhance the critical current density [166]. Furthermore, close to the optimal doping, as in the case of $CaKFe_4As_4$, the vortex core energy of the flux lines can be enhanced [167]. Thus, the high vortex core energy and the strength of the intrinsic de-pairing effect could be key factors responsible for the extremely high J_c value in this compound. Generally, an intrinsically high depairing critical density (see chapter 5 for a calculation of the depairing current density in $CaKFe_4As_4$) is significantly reduced due to the presence of extrinsic effects, such as weak links and grain mismatch, as for the powder sample of $CaKFe_4As_4$.

4.8 Summary

In summary, in this chapter the critical current densities and the vortex phase diagram of the optimally-doped stoichiometric clean superconductor $CaKFe_4As_4$, both in single crystal and powder form has been investigated. This material exhibits extremely large J_c values up to 10^7 A/cm^2 when $H||c$ at low temperatures, which is the highest value for a iron-based superconductor. The critical current density for both in-plane and out-plane orientations has a very weak temperature dependence in the temperature range up to ~ 25 K. The large magnetization hysteresis loops suggest strong flux pinning. The fish-tail effect is present for $H||c$, similar to other optimally-doped 122 superconducting single crystals, but this effect is missing when $H||(ab)$ and for the powder sample. The flux pinning force density suggest the existence of surface and the strong point-like core pinning of the vortices in the high-temperature regime. The extremely-high critical current density of $CaKFe_4As_4$ suggests that the vortex core energy is enhanced in this optimally doped superconductor and the reduced symmetry of Fe-As bonds could play an important role in pinning. Furthermore, in the powder sample the critical current densities are significantly reduced, likely due to the weak grain connectivity, as often found in other iron-based superconductors. The ultra-high critical current densities and the vortex phase diagram of $CaKFe_4As_4$ place this clean stoichiometric high-T_c superconductor as a realistic contender for practical applications.

Chapter 5

Upper critical fields in the stoichiometric iron-based superconductor $CaKFe_4As_4$

In this chapter further details of the superconducting state of $CaKFe_4As_4$ are explored using pulsed magnetic fields up to $90\,\mathrm{T}$ in order to find the upper critical fields, $\mu_0 H_{c2}$. In order to gain a better understanding of the superconducting properties of $CaKFe_4As_4$, $\mu_0 H_{c2}(T)$ has been measured for two magnetic field orientations, $H||c$ and $H||(ab)$, using electrical transport. Previous work on the upper critical fields in $CaKFe_4As_4$ in magnetic fields up to $60\,\mathrm{T}$ could not reach the low temperature region [61], but these experimental studies provide a complete $\mu_0 H_{c2}(T)$ phase diagram down to $4.2\,\mathrm{K}$. This allows for the modelling of the entire temperature dependence of the upper critical field. The upper critical fields of $CaKFe_4As_4$ are highly isotropic at $4.2\,\mathrm{K}$ and has exceptionally large upper critical fields of $\mu_0 H_{c2}(4.2\,\mathrm{K}) \sim 85\,\mathrm{T}$. From the upper critical fields the low temperature coherence lengths are established as $1.83(3)\,\mathrm{nm}$ and $1.87(6)\,\mathrm{nm}$. Extrapolating the field sweeps to $H = 0$ gives a T^2 resistivity dependence and the zero-temperature resistivity is found to be $\rho_0 = 9.4\,\mu\Omega\mathrm{cm}$, giving a mean free path of $\ell = 26.6\,\mathrm{nm}$. This places $CaKFe_4As_4$ in the clean limit ($\ell \gg \xi$). A two-band model describes the temperature dependence of $\mu_0 H_{c2}$ for both orientations and the band coupling parameters indicate the presence of different pairing channels. At low temperatures, $\mu_0 H_{c2}(T)$ does not saturate (as would be expected for a single-band superconductor) but shows an upturn, consistent with the emergence of an FFLO state in $CaKFe_4As_4$ below $\sim 14\,\mathrm{K}$. The large and isotropic upper critical fields of $CaKFe_4As_4$, combined with its stoichiometry, extremely large critical current density and high-T_c, make it an excellent candidate for practical applications.

This chapter will first recap important properties of upper critical fields in superconductors and what might be expected in iron-based materials. Next, the methods of extracting the upper critical fields from pulsed magnetic field transport data are discussed, along with the extraction of important parameters from the upper critical fields (such as the coherence

lengths) and it is shown that $\mu_0 H_{c2}(T)$ cannot be described using single band models of the upper critical field for either orientation. This leads on to describing the temperature dependence of the upper critical field using a two-band model in the clean limit, as described in section 2.1.5. The implications of the parameters of the two-band model are discussed, with an emphasis on the manifestation of a FFLO state at low temperatures. Finally, the results on $CaKFe_4As_4$ are linked together and summarised, and it is established that this material is an excellent candidate for practical applications.

5.1 Introduction

The upper critical field is an important attribute of superconductors that sets one of their constraints for practical applications. It depends on the interplay between different pairing gaps and symmetry and can shed light on the nature of superconductivity, as mentioned in section 2.1. Furthermore, the temperature dependence of the upper critical field can also provide evidence for the presence of the Fulde-Ferrell-Larkin-Ovchinnikov (FFLO) state [81, 91] in which the order parameter varies in space. The iron-based superconductors have unusually large upper critical fields that reveal exotic effects caused by the interplay of orbital and paramagnetic pair-breaking in multi-band superconductors with unconventional pairing symmetry [87]. They also provide the right conditions for the FFLO state to emerge, in clean samples, due to the presence of shallow bands [62] and large Pauli paramagnetic effects [81].

$CaKFe_4As_4$ is a clean and stoichiometric superconductor with a relatively high T_c of $35\,\mathrm{K}$ and it belongs to a new family of 1144 iron-based superconductors [59]. This system lacks long-ranged magnetic order or a nematic electronic state at low temperatures [59, 61, 64, 137, 168–170] but upon doping with Ni or Co a hedgehog magnetic structure is stabilized [169, 171, 172]. This electron doping also suppresses T_c, suggesting that $CaKFe_4As_4$ is optimally doped, or at least near optimal doping. $CaKFe_4As_4$ has an exceptionally large critical current density due to the strong point-like defects caused by local structural site effects as well as surface pinning [134, 173, 174]. Due to reduced symmetry compared with the 122 family of iron-based superconductors, $CaKFe_4As_4$ is predicted to have up to ten different bands (figures 5.1**e** and A.1). However, angle resolved photoemission spectroscopy (ARPES) detects a Fermi surface composed of three hole pockets and two electron pockets [62, 141]. The superconducting gaps are nearly isotropic and different for each of the Fermi surface sheets [62]. The presence of electron and holes sheets supports a spin resonance corresponding to the (π, π) nesting wave vector detected by neutron diffraction [64] and promotes a $s^{\pm}$ superconducting pairing symmetry in $CaKFe_4As_4$. This

system is an ideal model for understanding the effect of pairing on the upper critical field in optimally doped iron-based superconductors, as it is far cleaner than other optimally doped materials. It is an ideal comparison for an optimally doped 122 system, such as $BaFe_2As_2$.

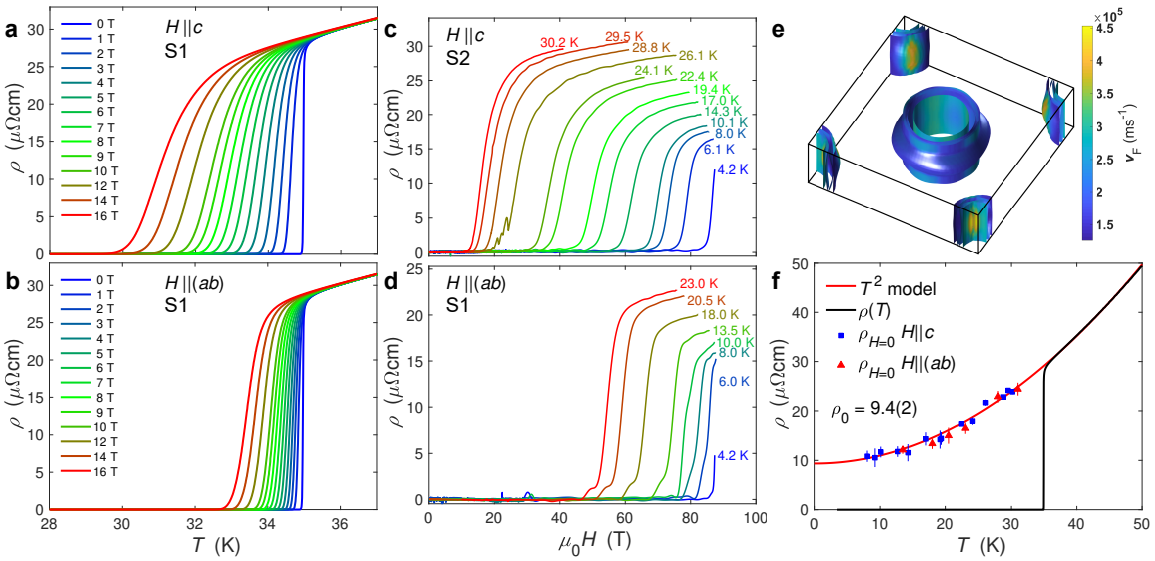


Figure 5.1: Resistivity versus temperature for $CaKFe_4As_4$ (S1) at different constant magnetic fields for **a** $H||c$ and **b** $H||(ab)$. Resistivity versus magnetic field at constant temperatures measured concomitantly in pulsed fields up $90\,\mathrm{T}$, for **c** $H||c$ (S2) and **b** $H||(ab)$ (S1). **e** Fermi surface of $CaKFe_4As_4$ using experimental lattice parameters (as detailed in Fig. A.1). The colours reflect the variation of the Fermi velocity. **f** Resistivity against temperature for sample S1 together with the zero-field extrapolated values from high fields shown in **c** and **d** (see also figure. A.2**d**). The zero-temperature resistivity ρ_0 is estimated as $9.4(2)\,\mu\Omega\mathrm{cm}$ using a Fermi-liquid T^2 behaviour (red line in **f**).

5.2 Experimental details

Single crystals of $CaKFe_4As_4$ were grown in the Ames Laboratory, as discussed elsewhere [59, 132]. Robust electrical contacts were achieved used indium solder, giving contact resistances less than $0.5\,\Omega$. Samples were measured using the standard 4- and 5-point ac lock-in techniques and a current of $1\,\mathrm{mA}$ for low field measurements ($\leq 16\mathrm{T}$) and $5\,\mathrm{mA}$ for pulsed field measurements. Several high quality single crystals have been investigated, with large residual resistivity ratios ~ 14.5 ($RRR = \rho(300\mathrm{K})/\rho(36\mathrm{K})$), small residual resistivity, $\rho_0 \sim 9.4\,\mu\Omega\mathrm{cm}$, and sharp superconducting transitions, $\Delta T_\mathrm{c} \sim 0.1\,\mathrm{K}$ (see figure. 5.1**f** and A.2**c**). Temperature sweeps were performed in Oxford up to $16\,\mathrm{T}$ in a Quantum Design PPMS in constant dc magnetic fields and for different magnetic field orientations ($H||c$ and $H||(ab)$). Pulsed magnetic field measurements were performed at LNCMI Toulouse up to

$90\,\mathrm{T}$ at constant temperatures below $35\,\mathrm{K}$ for both field orientations. Magnetic fields up to $90\,\mathrm{T}$ were produced by using current pulses through two different solenoid coils. An example of the magnetic field produced as a function of time in shown in figure 3.1.

5.3 Upper critical field phase diagram from transport measurements

Figure 5.1 shows resistivity against temperature for different fixed magnetic fields for orientations of the sample in relation to the applied magnetic field. As the magnetic field increases the superconducting transition becomes broader in temperature. When $H||c$ it is suppressed by $5\,\mathrm{K}$ in $16\,\mathrm{T}$ (figure. 5.1**a**), as compared with the $H||(ab)$ case for the zero resistivity offset shifts down by only $2\,\mathrm{K}$ in $16\,\mathrm{T}$ (figure. 5.1**b**). This implies that the orbital contributions are less effective in suppressing superconductivity for the $H||(ab)$ orientation. These data are used to extract the upper critical field near T_c, defined as the offset field, as shown in figures. 3.4, A.2**a** and A.2**b**. In order to completely suppress superconductivity in $CaKFe_4As_4$ pulsed magnetic fields up to $90\,\mathrm{T}$ have been used. Resistivity data against magnetic fields up to $90\,\mathrm{T}$ measured at fixed temperature are shown in figure. 5.1**c** and 5.1**d** for the two different magnetic field orientations. Despite the strong disparity in the degree of suppression of superconductivity between the two field directions close to T_c, at the lowest measurable temperature of $4.2\,\mathrm{K}$ the normal state is reached at a similar field of $\sim 85\,\mathrm{T}$ for both orientations.

Based on these experimental data, the complete upper critical field phase diagram of $CaKFe_4As_4$ has been constructed down to $4.2\,\mathrm{K}$ as shown in figure. 5.2**a** for the two field orientations. These results are in good agreement with previous studies up to $60\,\mathrm{T}$ for both offset and onset critical fields [61] (see figure A.4**a** and **b**) and reveal extremely large upper critical fields, reaching almost $\sim 3T_\mathrm{c}$ at the lowest temperatures. These values are above the Pauli paramagnetic limit, $\sim 1.84T_\mathrm{c}$, estimated to be $\sim 65\,\mathrm{T}$ for a single-band superconductor with a transition temperature of $35\,\mathrm{K}$. The anisotropy of the upper critical field, defined as the ratio of the upper critical field for different orientations, $\Gamma(T) = H_{\mathrm{c}2}^{ab}(T)/H_{\mathrm{c}2}^{c}(T)$, drops dramatically with decreasing temperature from ~ 4 to 1 between T_c and $4.2\,\mathrm{K}$, as shown in figure 5.2**b**. Interestingly, the upper critical fields for the two orientations cross at $T \sim 4.2\,\mathrm{K}$, leading to isotropic superconducting behaviour in the low temperature limit. This phenomenon has been found in optimally doped iron-based superconductors, such as $FeSe_{0.5}Te_{0.5}$ [175, 176] and (Ba,K)Fe_2As_2 [177]. This behaviour reflects the large Pauli paramagnetic effects in iron-based superconductors and the influence of Fermi surface details on limiting the orbital effects [177]. The Fermi surface of $CaKFe_4As_4$ has significant

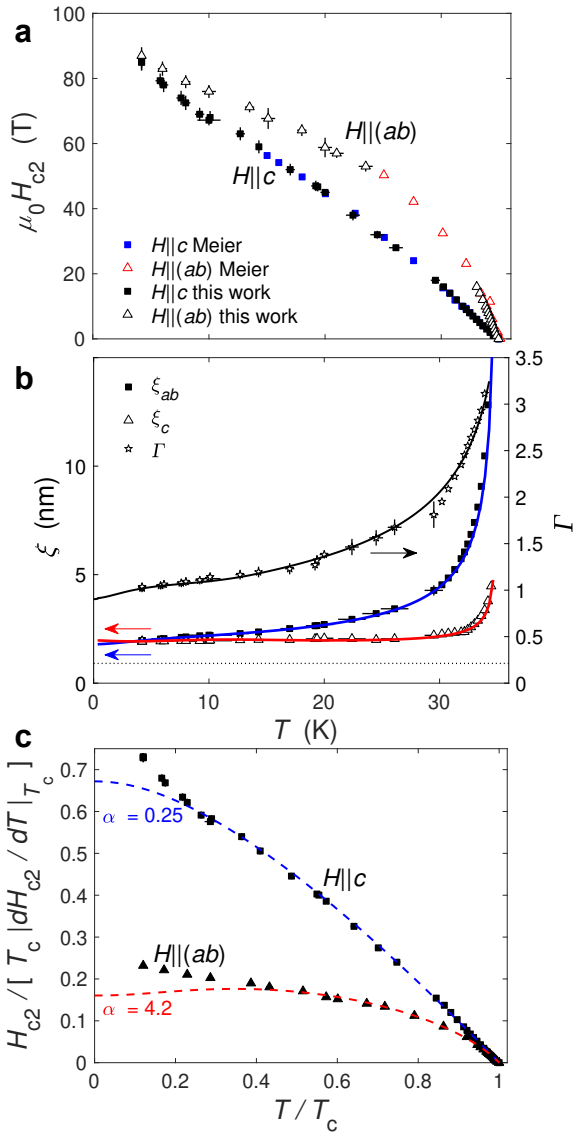


Figure 5.2: **a** Upper critical fields as a function of temperature in $CaKFe_4As_4$ when $H||c$ (solid squares) and $H||(ab)$ (open triangles), together with previous reported data measured up to $60\,\mathrm{T}$ from Ref. [61]. **b** The temperature dependence of coherence length extracted close to T_c, as described in the SM. The $H_{c2}(T = 0)$ value were used to find the zero-temperature coherence lengths. The horizontal dashed line represents the 3D-2D crossover when coherence length $\sim c/\sqrt{2}$. The anisotropy $\Gamma = H_{c2}^{ab}/H_{c2}^{c}$ on the right axis approaches $\Gamma = 1$ at $\sim 4.2\,\mathrm{K}$. Solid lines are guide to the eye. **c** Upper critical fields for $H||c$ (black squares) and $H||(ab)$ (black triangles) scaled by the superconducting transition temperature, T_c, and the slope near T_c from the WHH model against reduced temperature T/T_c. The dashed blue and red lines are fits to the WHH model for $H||c$ and $H||(ab)$ using different values of α. Deviation from the WHH model occurs at low temperatures for both field orientations.

warping for the outer electron and hole band that can potentially allow circulating currents out of plane (see figure A.1**d**). Furthermore, the calculated anisotropy of the penetration depth based on plasma frequencies (as in Ref. [178]) is Γ_λ=$\lambda_c/\lambda_{ab} \sim 4.5$, (see figure A.1) similar to the measured anisotropy close to T_c (figure 5.2**b**), suggesting that the Fermi surface details play an important role in understanding its superconducting properties.

Having experimentally determined the upper critical fields for different orientations in magnetic field, the associated coherence lengths are extracted in different temperature regimes (see the sections 2.1.1 and A). In the vicinity of T_c, the Ginzburg-Landau coherence lengths, shown in figure 5.2**b**, are $\xi_{ab}^{GL} = 1.66(4)$ nm and $\xi_c^{GL} = 0.53(2)$ nm for $CaKFe_4As_4$, similar to previously reported values [61]. In the low temperature limit, the coherence lengths are $\xi_{ab} = 1.83(3)$ nm and $\xi_c = 1.87(6)$ nm, as extracted in figure A.3 in Appendix A. This demonstrates the presence of an isotropic superconducting state at lowest temperature in $CaKFe_4As_4$. The coherence lengths approach the 3D to 2D crossover close to $c/\sqrt{2} \sim 0.911$ nm, as shown in figure 5.2**b** [59, 138]). The low temperature extracted coherence lengths from upper critical fields presented here are larger than ~ 0.7 nm reported from STM measurements, which probe locally the vortex lattice rather than an overall averaged effect [165]. The small coherence lengths of $CaKFe_4As_4$ are compatible with the large upper critical fields, consistent with small Fermi velocities and the high T_c value of $CaKFe_4As_4$ ($\xi \sim \hbar v_F/(2\pi k_B T_c)$ [81]). Using the extrapolated zero-temperature normal state resistivity $\rho_0 \sim 9.4(2)\,\mu\Omega$cm in figure 5.1**f** and carrier concentrations from Ref. [61], the mean free path is estimated to be $\ell = 26.6(7)$ nm. Since the mean free path due to elastic scattering from impurities is far larger than the coherence length, $\xi(0) \ll \ell$, $CaKFe_4As_4$ can be described as being in the clean limit. Resistivity data in figure 5.1**f** show also a sharp superconducting transition, indicating a high quality single crystal. Furthermore, the extrapolated high-field resistivity at low temperatures (see figure A.1**d**) displays a T^2 dependence, indicative of a Fermi-liquid behaviour that extends up to ~ 55 K. This further reinforces the claim that these single crystals are clean.

Another important property of superconductors that can be determined is the intrinsic amount of current (i.e. energy) that is needed to break apart a Cooper pair. This is found by considering the energy associated with a Cooper pair in BCS and Ginzburg-Landau theories and is usually referred to as the depairing current density, J_d. This has a temperature and magnetic field dependence which is given by [9]

$$J_d(T,H) = \frac{2}{3\mu_0\lambda^2(T)}\sqrt{\frac{\mu_0(H_{c2}^2(T) - H^2)^{1/2}\Phi_0}{6\pi}}, \tag{5.1}$$

where λ is the superconducting penetration depth and Φ_0 is the magnetic flux quantum. At zero temperature and field, this gives

$$J_{\mathrm{d}}(0,0) = \frac{2}{3\mu_0\lambda^2(0)}\sqrt{\frac{\mu_0 H_{\mathrm{c2}}(0)\Phi_0}{6\pi}}. \tag{5.2}$$

Substituting in $\mu_0 H_{\mathrm{c2}} = \Phi_0/2\pi\xi$ this can be rearranged to give

$$J_{\mathrm{d}}(0,0) = \frac{\Phi_0}{3\sqrt{3}\pi\mu_0}\frac{1}{\lambda^2(0)\xi(0)}. \tag{5.3}$$

This is the *ideal* intrinsic limit on a superconductor, or the maximum value of the critical current that is expected. It does not take into account other effects such as vortex dynamics, grain boundaries and pinning forces that can also limit the critical current density (these limiting factors are what give the *critical* current density, J_{c}, which is presented for $CaKFe_4As_4$ in chapter 4).

Previous magnetisation results in chapter 4 give $\mu_0 H_{\mathrm{c1}} = 22(1)\,\mathrm{mT}$ when $H||c$ at low temperature which, combined with the upper critical field results here, give $\kappa \sim 99(2)$ and $\lambda = 183(6)\,\mathrm{nm}$. Using this and $\xi = 1.86\,\mathrm{nm}$ gives $J_{\mathrm{d}} = 1.61(9) \times 10^8\,\mathrm{A/cm^2}$ when $H||c$, one of the largest among iron-based superconductors. This supports the extremely large critical current densities, reported previously for $CaKFe_4As_4$ in chapter 4 and Ref. [134].

As mentioned in section 2.1.6 it can be important to consider the nucleation of superconductivity at surfaces when measuring the upper critical field. The nucleation of superconductivity at a metal-insulator interface can enhance the upper critical field by $H_{\mathrm{c3}} \sim 1.695 H_{\mathrm{c2}}$ [93]. This can occur in a layer of thickness $\sim \xi$ in directions *parallel* to the applied magnetic field. The volume of this surface state has to be able to carry the applied current in order for this state to exist. This effect could become important at low temperatures, where there are upturns in the temperature dependence of the upper critical fields. Using the critical current density of $\sim 2 \times 10^7\,\mathrm{A/cm^2}$ measured in chapter 4, the coherence length of $\xi_{ab} \sim 1.8\,\mathrm{nm}$ and the sample height of $\sim 10\,\mu\mathrm{m}$, gives an edge current carrying capacity of $\sim 0.36\,\mathrm{mA}$ at $\sim 4.2\,\mathrm{K}$. The applied current used during pulsed field experiments was $5\,\mathrm{mA}$, which well exceeds the current carrying capacity of any surface layer that might exist by more than a factor of 10. It is also worth noting here that the above value for the critical current density is at zero applied magnetic field. In reality as the magnetic field is increased the critical current density drops, and so the the current carrying capacity should also decrease. Hence, the above value is actually an *over estimate* of the current density that a surface layer could carry. At these high fields above $80\,\mathrm{T}$ the real value will be far lower, and so the applied current will well exceed that of a current carrying surface layer. For this reason, surface nucleation of superconductivity can ignored

and the so the transitions here can be confidently assigned to the upper critical field, $\mu_0 H_{c2}$ (and not a surface third critical field $\mu_0 H_{c3}$).

5.4 Single band description of the upper critical fields

In order to assess the role of orbital and Pauli paramagnetic effects on the upper critical field of $CaKFe_4As_4$ the temperature dependence of the upper critical field is first described using the three-dimensional Werthamer-Helfand-Hohenberg (WHH) model [78], with the inclusion of spin paramagnetism effects. The slope close to T_c ($\mu_0 H'_{c2} = -|d\mu_0 H_{c2}/dT|_{T=T_c}$) is used to estimate the zero-temperature orbital upper critical field and $\mu_0 H_{c2}^{orb} = 0.73\mu_0 H'_{c2}$ for the clean limit ($0.69\mu_0 H'_{c2}$ in the dirty limit) for a single-band weak-coupling superconductor with an ellipsoidal Fermi surface [179]. The orbital pair breaking dominates the temperature dependence for $H||c$ down to 10 K, below which it deviates, as shown in figure 5.2**c**. However, when the magnetic field is aligned along the conducting (ab)-plane, a Pauli pair breaking contribution has to be included which reduces the orbital-limited critical field by $\mu_0 H_P = \mu_0 H_{c2}^{orb}/\sqrt{1+\alpha^2}$, where α is the Maki parameter, as discussed in section 2.1. The extracted Maki parameter α is small where the orbital effects dominate ($\alpha \sim 0.25$ for $H||c$), but it becomes significant reaching $\alpha = 4.2$ for $H||(ab)$ (see figure 5.2**c**). This value is close to that of $FeSe_{0.4}Te_{0.6}$ single crystals where $\alpha \sim 5.5$ suggesting that the upper critical field is dominated by Pauli paramagnetic effects [180]. Strong paramagnetic effects are an important signature of optimally doped iron-based superconductors [88, 89, 181–183]. For a clean isotropic single-band, the Maki parameter is given by $\alpha = \pi^2 \Delta m^\star/(4E_F m_e)$. The values of the measured superconducting gap Δ varies between $2.4 - 13$ meV whereas the Fermi energies vary significantly for different bands, being smallest for the inner hole band, α (~ 3 meV) and the shallow electron band δ (~ 10 meV) [62, 141]. The band structure calculation predicts four electron pockets centred at the M-point, as shown in figure A.1. Experimentally, only one electron pocket can be resolved from ARPES measurements due to a significant intrinsic linewidth and the fact that the bottom of these bands is located very close to Fermi level [62]. Thus, the presence of the shallow bands, together with the small Fermi energies E_F and large superconducting gap Δ create conditions for large α and strong Pauli pair-breaking.

5.5 Upper critical field described using a two-band model

In order to describe the complete temperature dependence of the upper critical field for $CaKFe_4As_4$, including the upturn below ~ 10 K for both orientations, a two-band model

in the clean limit is considered, as detailed in Ref. [81] and in section 2.1.5. This model accounts for the presence of two different bands, with inter-band scattering ($\lambda_{11}, \lambda_{22}$) and intra-band effects ($\lambda_{12}, \lambda_{21}$), includes paramagnetic effects and allows for the presence of an FFLO inhomogeneous state at high-fields and low temperatures [81]. An FFLO state is characterized by a real-space modulation of the superconducting order parameter either in amplitude or phase such that the system energy is minimized under the constraints of a large Zeeman energy and superconducting condensation energy [91]. As the FFLO wave vector, Q, appears spontaneously below a certain temperature, T_{FFLO}, the spinodal instability line in $\mu_0 H_{c2}(T)$ at a finite Q acquires the characteristic upturn [81].

In most iron-based superconductors, the pairing is expected to be mediated by spin-fluctuations, leading to a sign changing $s^{\pm}$ order parameter. In this case, upper critical fields are generally described by dominant inter-band coupling parameters with $\lambda_{11} = \lambda_{22} = 0$ and $\lambda_{12} = \lambda_{21} \sim 0.5$ ($\lambda_{11}\lambda_{22} \ll \lambda_{12}\lambda_{21}$) [61, 87–90] (also see chapter 7). Furthermore, in these multi-band systems orbital fluctuations can dominate the pairing interactions in certain conditions favouring a gap with equal sign on each pocket, resulting in the s^{++} pairing [184] ($\lambda_{11}\lambda_{22} \gg \lambda_{12}\lambda_{21}$).

To model the upper critical fields for both field orientations, different input parameters from previous experiments on $CaKFe_4As_4$ are considered. For example, the ratio between the extreme velocities of the Fermi surfaces is taken from ARPES experiments [141] and it gives a starting value of $\eta_c \sim 0.02$, which is the squared velocity ratio between the two bands (see equations 2.12-2.14 in section 2.1.5). Upper critical field simulations have a strong sensitivity to η values, as shown in figure 2.3 and it can change for different field orientations due to differences in the in-plane velocities on the Fermi surface (see figure 5.1**e** and A.1). It is assumed that $s = 1$ (defined in section 2.1.5) for both field orientations and the starting values of the Maki parameters are those from the single band models of the upper critical fields in figure 5.2**c**.

Firstly, the upper critical field data are simulated for $CaKFe_4As_4$ using parameters corresponding to the $s^{\pm}$ case (dashed lines figures 5.3**a** and 5.3**b**), which provide a reasonable representation of the observed temperature dependence for both orientations. However, it is found that $\mu_0 H_{c2}(T)$ is best described using $\lambda_{11} = 0.81$, $\lambda_{22} = 0.29$ and $\lambda_{12} = \lambda_{21} = 0.1$ (solid lines in figures 5.3**a** and 5.3**b**), which is consistent with s^{++} pairing. For the later model, the constrained Fermi velocities are $v_1 \sim 380(20)\,\mathrm{meV\AA}$ and $v_2 \sim 54(4)\,\mathrm{meV\AA}$ when $H||c$, and $v_1 \sim 195(20)\,\mathrm{meV\AA}$ and $v_2 \sim 41(4)\,\mathrm{meV\AA}$ when $H||(ab)$ (see Table 5.5). The values of v_2 are similar in both orientations, indicative of a strongly warped sheet (see figure A.1). On the other hand, v_1 is larger for $H||c$ and is close to $\sim 360\,\mathrm{meV\AA}$, reported for the α hole band from ARPES measurements [141]. The band coupling constants,

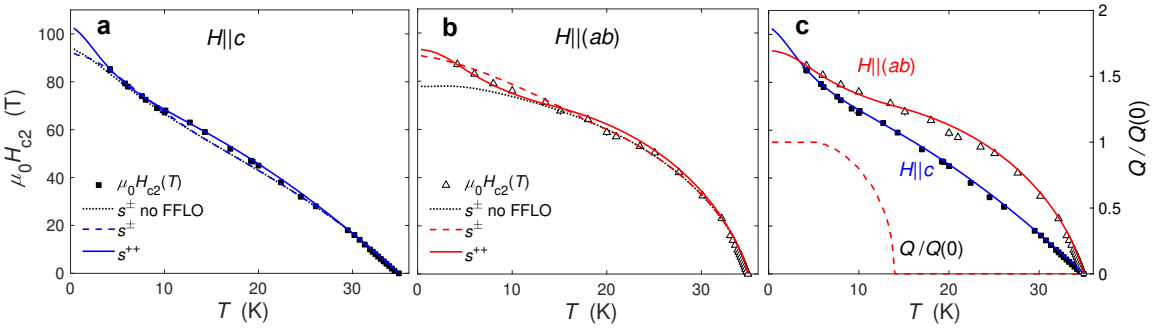


Figure 5.3: Upper critical fields for **a** $H||c$ (solid squares) and **b** and **c** $H||(ab)$ (open triangles) described by the two-band model. The dotted lines correspond to $s^{\pm}$ pairing ($\lambda_{11} = \lambda_{22} = 0$, $\lambda_{12} = \lambda_{21} \sim 0.5$, $\alpha_1 = 0.95$, $\alpha_2 = 0$ for $H||c$ and $\alpha_1 = 3.1$ and $\alpha_2 = 0.7$ for $H||(ab)$). Solid lines represent s^{++} pairing ($\lambda_{11} = 0.81$, $\lambda_{22} = 0.29$ and $\lambda_{12} = \lambda_{21} = 0.1$, $\alpha_1 = 0.5$ for $H||c$ and $\alpha_1 = 3.2$, $\alpha_2 = 0$ for $H||(ab)$). The values of η vary between ~ 0.02 in **a** and ~ 0.04 in **b**. **c** The temperature dependence of the upper critical field including the emergence of the FFLO state for the two different pairing symmetries with the same parameters as in **b**. The lower dashed and red line represents the scaled FFLO $Q/Q(0)$ modulation for $H||(ab)$ for the respective pairing (right-axis).

$\lambda_{i,j}$ that describe the data suggest that the inter-band scattering due to spin-fluctuations is smaller than the intra-band effects which seem to dominate in $CaKFe_4As_4$. These intra-band effects can occur in the presence of strong orbital fluctuations [184]. For s^{++} pairing to overcome $s^{\pm}$ pairing it normally requires the presence of strong disorder which leads to similar superconducting gaps on different Fermi surfaces [185]. Furthermore, the band coupling constants for the s^{++} case resemble those for MgB_2, which can be described as a two-band superconductor in the dirty limit [186]. However, $CaKFe_4As_4$ is in the clean limit suggesting that disorder effects are negligible, or at least very small. Thus, based on the band coupling parameters, it can be concluded that orbital fluctuations may dominate the Cooper pairing in this materials, rather than the spin fluctuations (like in other iron-based superconductors).

When the magnetic field lies along the conducting planes, $H||(ab)$, the low temperature upturn of the upper critical field in figure 5.3**b** cannot be fully captured by only considering the two-band model with large Pauli paramagnetic effects, $\alpha \sim 3.2$. The formation of the FFLO state in a system with a cylindrical Fermi surface requires a large Zeeman energy and a critical Maki's parameter of $\alpha_c = 4.76$ [91], compared to $\alpha_c = 1.8$ [92] for a three-dimensional Fermi surface. $CaKFe_4As_4$ has a complex Fermi surface with two-dimensional cylindrical and highly warped sheets, which together with a large value of α creates the necessary conditions for the emergence of an FFLO state [81]. A FFLO state can be realized in very clean materials with weak scattering of quasiparticles, and it generally

	$\mu_0 H_{\rm off}$				$\mu_0 H_{\rm on}$			
	$s^{\pm}$		s^{++}		$s^{\pm}$		s^{++}	
	$H\|\|c$	$H\|\|(ab)$	$H\|\|c$	$H\|\|(ab)$	$H\|\|c$	$H\|\|(ab)$	$H\|\|c$	$H\|\|(ab)$
λ_{11}	0	0	0.81	0.81	0	0	0.81	0.81
λ_{22}	0	0	0.29	0.29	0	0	0.29	0.29
λ_{12}	0.5	0.5	0.1	0.1	0.5	0.5	0.1	0.1
α_1	0.95	3.1	0.5	3.2	1.5	4.2	1.0	3.5
α_2	0	0.7	0	0	0	0	0	0
v_1 (meVÅ)	510(20)	253(20)	380(20)	195(20)	400(20)	215(20)	312(20)	181(20)
v_2 (meVÅ)	40(4)	51(5)	54(4)	41(4)	36(3)	43(4)	44(4)	38(4)
η	~ 0.006	~ 0.04	~ 0.02	~ 0.04	~ 0.008	~ 0.04	~ 0.02	~ 0.045

Table 5.1: The different parameters used for the simulations of the upper critical field using a two-band model and considering different pairing symmetries and magnetic field orientations in $CaKFe_4As_4$.

manifests as change in slope in the upper critical field at low temperatures [81]. In order to describe the upper critical field data of $CaKFe_4As_4$ over the entire temperature range, a FFLO state needs to be stabilized below $T_{\rm FFLO} \sim 14\,$K, as shown in Fig. 5.3**c**. Possible contenders to support such an effect are the shallow electron Fermi surface pocket, δ, in the zone corner which is very close to the Fermi level ($\sim 10\,$meV) as well as the inner hole band α ($\sim 3\,$meV), as detected by ARPES measurements [62].

The temperature dependence of the upper critical field data in $CaKFe_4As_4$ implies that the intra-band scattering is likely to dominate the inter-band scattering, the latter of which is being promoted by spin fluctuations. In the presence of spin-orbit coupling the orbital fluctuations can lead to s^{++} pairing, as suggested as a possibility for LiFeAs [187]. Usually s^{++} pairing results in far lower critical fields than $s^{\pm}$ pairing [81], so these results for $CaKFe_4As_4$ are somewhat unusual as $\mu_0 H_{\rm c2}$ is almost $3T_{\rm c}$ at the lowest temperature. The presence of several scattering channels in a multi-band system like $CaKFe_4As_4$ can increase the upper critical field to a much greater extent than in single gap superconductors, caused by the relative weight of different scattering channels. $CaKFe_4As_4$ theoretically has up to six large cylindrical hole bands, (with the equivalent of 50% hole doping in a 122 iron-based superconductor) providing a large density of states (see figures 5.1**e** and A.1, and Ref. [141]) and it can also promote intra-band scattering driven by orbital or electron-phonon couplings. On the other hand, the shallow bands in $CaKFe_4As_4$ are more likely to be involved in the stabilization of the FFLO state. Thus, the temperature dependence of the upper critical fields in $CaKFe_4As_4$ can reflect the behaviour of two dominant superconducting gaps that reside on different sheets of the cylindrical Fermi surface, possibly one on a large hole band and another one on a shallow, small band.

5.6 Summary

In summary, the upper critical fields of $CaKFe_4As_4$ have been experimentally studied in magnetic fields up to $90\,\mathrm{T}$ and down to $4.2\,\mathrm{K}$, providing a complete phase diagram for this stoichiometric superconductor. The anisotropy decreases dramatically with temperature, the system becoming essentially isotropic near $4\,\mathrm{K}$. Upper critical fields are extremely large in this system, reaching close to $\sim 3T_\mathrm{c}$ at the lowest temperature, well above the expectation based on conventional single-band superconductivity. Instead, the temperature dependence of the upper critical field can be described using by a two-band model in the clean limit. The band coupling constants suggest a dominant orbital pairing over spin fluctuation pairing in $CaKFe_4As_4$. Furthermore, for magnetic fields aligned in the conducting plane and due to large Pauli paramagnetic effects, the temperature dependence of the upper critical field is consistent with the emergence of an FFLO state at low temperatures. The low temperature coherence lengths are $\xi_{ab} = 1.83(3)\,\mathrm{nm}$ and $\xi_c = 1.87(6)\,\mathrm{nm}$. Using $\xi_{ab} = 1.83\,\mathrm{nm}$ and the lower critical field when $H||c$ in chapter 4 the depairing current density was found as $J_\mathrm{d} = 1.61(9) \times 10^8\,\mathrm{A/cm^2}$, one of the highest among iron-based superconductors. The large and isotropic upper critical fields in $CaKFe_4As_4$ at low temperature, combined with its stoichiometry and high critical current density, make it an ideal candidate for practical applications.

5.7 Aside: Activation energy of the vortex state

Equations 2.21-2.22 in section 2.2.4 describe the resistivity in the vortex liquid state, just above the superconducting transition. These describe the thermally activated flux flow, and can be used to extract the activation energy of the vortex state. Figures 5.4**a** and 5.4**b** show Arrhenius plots of the natural logarithm of resistivity against $1/T$ at constant magnetic fields for $H||c$ and $H||(ab)$ respectively. Black lines show linear fits to each temperature sweep. These fits all have a common intercept, which is very similar to the onset temperature of superconductivity, $T_{\rm on}$, as expected. Gradients of linear fits thus give us the activation energy, $U_0/k_{\rm B}$, which is shown in Figure 5.4**c** against the applied magnetic field. Here activation energy values for optimally K doped Ba-122 and Bi2212 extracted from Refs. [99, 188] are also shown for comparison. The activation energy for $CaKFe_4As_4$ is larger than for both other systems shown, as well as for other iron-based superconductors [51]. The activation energy of the vortex liquid state is proportional to the vortex pinning energy, and so also pinning force. The large activation energy observed here implies a large pinning force is present inside the superconducting state. This large pinning force supports previous observations of extremely high critical current densities of $CaKFe_4As_4$ presented in chapter 4 and Ref. [134]. It has been suggested that an FFLO modulation with a wavelength comparable to the lattice constant could enhance the pinning force [189, 190]. This is because the order parameter varies sinusoidal, and so more vortices can pass through a particular pinning centre than in the uniform superconducting state. However, since the pinning forces extracted here are well below the fields necessary for the FFLO to manifest and the length scale associated with the FFLO state is unknown, one can not reliably comment on whether the FFLO state could be a cause of the large pinning forces in $CaKFe_4As_4$. To establish this, one would have to study the pinning force and vortex dynamics in more detail at magnetic fields where the FFLO state manifests, above $\sim 75\,\mathrm{T}$ at low temperatures.

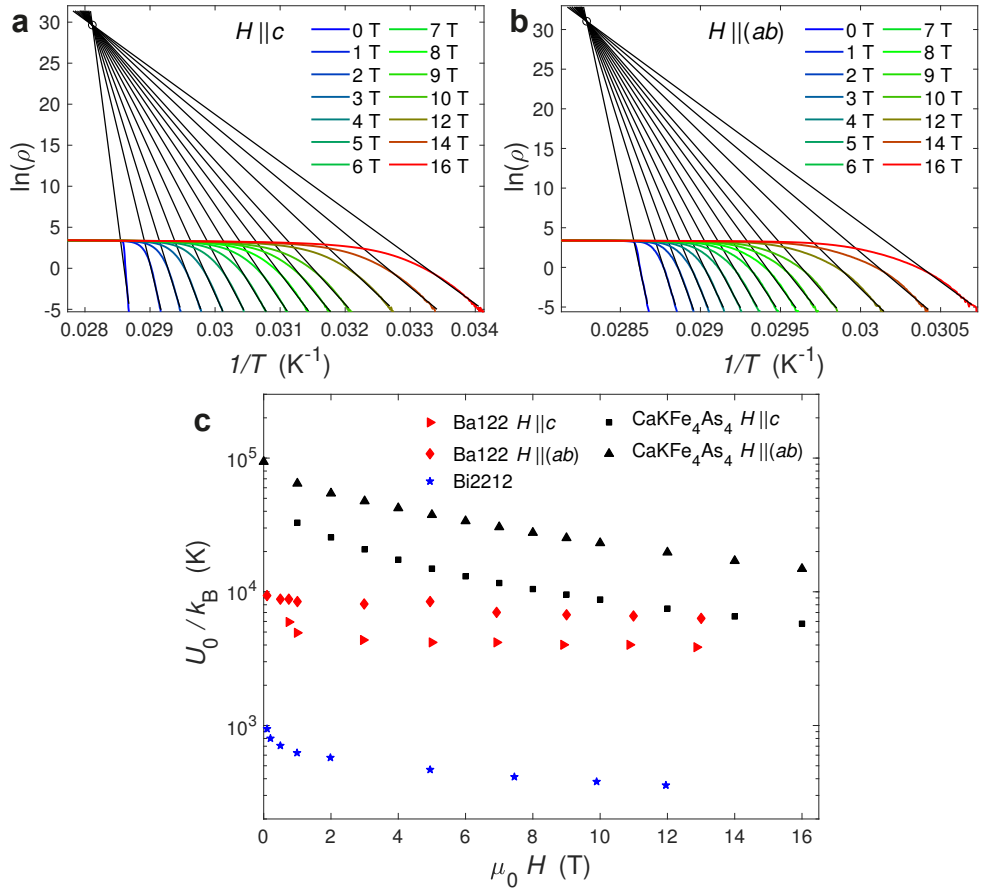


Figure 5.4: **Activation energy in CaKFe$_4$As$_4$. a** and **b** the natural logarithm of resistivity against the inverse of temperature (using the same data as in figures 5.1**a** 5.1**b**) for $H||c$ and $H||(ab)$ respectively. The regions over which the linear fits were performed were identified by finding the exponential regions in $\rho(T)$ and $d\rho(T)/dT$. **c** the activation energy of the vortex liquid state as a function of the applied magnetic field. Data is shown here for $H||c$ and $H||(ab)$, as well as for K doped Ba-112 and Bi-2212 from Refs. [99, 188] for comparison.

Chapter 6

The high magnetic field electronic state of $FeSe_{1-x}S_x$

In this chapter the normal electronic state of $FeSe_{1-x}S_x$ is studied across the nematic transition using magnetotransport studies in high magnetic fields up to $69\,$T. The nematic state exhibits non-Fermi-liquid behaviour with an unusual transverse-field magnetoresistivity ($\sim H^{1.55}$), reflecting an unconventional scattering mechanism. Outside the nematic phase, resistivity is dominated by a $\sim T^{1.5}$ dependence, similar to studies under pressure [54]. The transverse-field magnetoresistivity is very large inside the nematic phase, when compared to the tetragonal state. As a function of temperature the high-field ($34\,$T) magnetoresistivity has a peak at $T \sim 14\,$K for FeSe, which increases upon x substitution. For $x \gtrsim 0.1$ this changes and the low temperature high-field resistivity becomes insulating like, until it returns to more conventional behaviour in the tetragonal state. Inside the nematic phase at low temperatures the resistivity is linear, followed by Fermi-liquid behaviour upon further cooling for certain x and impurity levels. The data presented in this chapter reveal the anomalous transport of the nematic state due to the subtle changes in the electronic structure and/or scattering, which are also influenced by impurity levels.

This chapter will first recap iron-based superconductors, the $FeSe_{1-x}S_x$ system and why one might wish to understand the normal electronic state of unconventional superconductors, particularly at low temperatures where it is most difficult to access experimentally. Data will then be presented on the in-plane transverse-field magnetoresistivity (with $H||c$), with a particular focus on the evolution of its temperature dependence and the Hall effect with x substitution. The magnetic field dependence of the transverse-field magnetoresistivity is then considered, covering a range of scaling that fails in this system and presenting a different mathematical argument to describe the magnetoresistivity. A similar approach is then taken to describing the temperature dependence of the resistivity in zero magnetic field. The final set of data discussed is the longitudinal-field magnetoresistivity

(with $H||(ab)$), which is used to extract the low-temperature electronic behaviour below T_c. Finally, the implications of these results are discussed, focusing on changes across the phase diagram with x substitution, any changes in the Fermi surface that these may correlate with and links this may have to superconductivity in FeSe$_{1-x}$S$_x$.

6.1 Introduction

A key to understanding unconventional superconductivity in iron-based superconductors may lie in the changes of their electronic structure at low temperature. This can be explored through a number of different measurement techniques, all of which have their own positives and limitations. For example, Angle Resolved Photo Emission Spectroscopy (ARPES) measurements probe the band structure but are limited in temperature and can only be used in zero magnetic field. Quantum oscillations, that also depend on the Fermi surface, can be probed by a number of experimental techniques but usually only present at very low temperatures in iron-based superconductors, require (usually very) high magnetic fields and only appear in the normal state. Using resistivity measurements in magnetic fields can probe Fermi surfaces and determine the quasi-particle masses from these quantum oscillations, which is of particular interest in the proximity of quantum critical points [43, 191, 192]. The critical fluctuations associated with quantum critical points have emerged as a candidate for superconducting pairing in unconventional systems. One proposition centres around nematic fluctuations [184, 193–195]. However, the presence of other competing electronic phase, such as long-ranged magnetic order or spin fluctuations, can obscure the importance of nematic fluctuations. Hence a system which has fewer competing states is desirable, such as FeSe$_{1-x}$S$_x$. In unconventional superconductors, close to an antiferromagnetic critical point, an unusual scaling between a linear resistivity in temperature and magnetic fields has been found previously [196, 197]. Magnetic fields can also induce metal-to-insulator transitions, as in hole-doped cuprates, where superconductivity emerges from an exotic electronic ground state [192]. Ideally these studies are performed to very low temperatures to unravel any quantum effects as the temperature goes to zero. This becomes a problem with optimally doped iron-based superconductors where T_c and $\mu_0 H_{c2}$ are high, making the low temperature normal electronic state experimentally inaccessible.

FeSe is an ideal candidate among the iron-based superconductors to study electronic structure, scattering and correlations down to low temperatures. FeSe is a unique bulk superconductor with $T_c \sim 9$ K which displays a variety of complex and competing electronic phases [27]. FeSe is a bad metal at room temperature and it enters a nematic electronic state below $T_s \sim 87$ K. This nematic phase is characterized by multi-band shifts driven by orbital

ordering that lead to Fermi surface distortions [27, 28]. Furthermore, the electronic ground state is that of a strongly correlated system and the quasiparticle masses display orbital-dependent enhancements [28, 29]. FeSe shows no long-range magnetic order at ambient pressure, but antiferromagnetic spin fluctuations are present at high energies over a large temperature range [26, 45]. Below $T_{\rm s}$, the spin-lattice relaxation rate from NMR experiments is enhanced as it captures the low-energy tail of the stripe spin fluctuations [37, 38]. Recent μSR studies also suggest the close proximity of FeSe to a magnetic quantum critical point, since the muon relaxation rate shows unusual temperature dependence inside the nematic state [198]. These changes in the electronic structure and magnetic fluctuations of FeSe can have profound implications on its transport and superconducting properties. STM reveals a highly anisotropic superconducting gap driven by orbital-selective Cooper pairing [33]. Due to the the presence of the small inner bands, whose Fermi energies are comparable to the superconducting gap, FeSe was placed inside the BCS-BEC crossover regime [36]. In large magnetic fields, when the Zeeman energy is comparable to the gap and Fermi energies, a highly-polarized superconducting state may occur [36].

An ideal route to untangling the roles played by different competing interactions on nematicity and superconductivity is provided by the isoelectronic substitution of selenium by sulphur ions in FeSe$_{1-x}$S$_x$ [40]. This tuning parameter suppresses nematicity and leads to changes in the electronic structure, similar to the temperature effects, with the Fermi surface becoming isotropic in the tetragonal phase and the electronic correlations becoming weaker [27, 40, 41, 43]. As nematicity is suppressed, it creates ideal conditions to explore a potential nematic end point [199], in the absence of long-ranged magnetic order. The superconducting dome extends outside the nematic state but anisotropic pairing remains robust [32] and a different superconducting state was suggested to be stabilized in the tetragonal phase [31].

Thus, FeSe$_{1-x}$S$_x$ provides an ideal system to study the low temperature electronic behaviour of an iron-based superconductor, in this case across a nematic phase transition. The relatively low $T_{\rm c}$ and $\mu_0 H_{\rm c2}$ of this system mean the normal state, above superconductivity, is experimentally accessible in relatively high magnetic fields down to very low temperatures, unlike other iron-based superconductors. As FeSe$_{1-x}$S$_x$ shows no long-ranged magnetic order and so any differences between this system and other iron-based superconductors could be attributed to either the lack of magnetism or the electronic nematic state. FeSe$_{1-x}$S$_x$ also offers the opportunity to study any effects that nematic order may have on electronic properties.

6.2 Materials and Methods

Single crystals of $FeSe_{1-x}S_x$ were grown by the $KCl/AlCl_3$ chemical vapour transport method [200]. The composition for samples from the same batch were checked using EDX (Energy Dispersive X-ray spectroscopy), as reported previously in Ref. [43]. The structural transition at T_s also provides useful information about the expected x value, as shown in figure 6.1. More than 30 samples were screened for high magnetic field studies to test their properties. Residual resistivity ratios, $RRR = \rho(300\,\mathrm{K})/\rho(T_{on} + 1\,\mathrm{K})$, vary from 15-44, as shown in figure 6.1**c**. There is a small variation within the same batch due to the inhomogeneous distribution of sulphur, which generally becomes more prominent with increasing x (see figures 6.1 and B.5). It is estimated that the nematic end point is located close to $x \sim 0.175(5)$ (see figures 6.1). Note that in Refs. [201, 202] the nominal sulphur concentration, x_{nom}, is up to $\sim$25% more than the real x (see also Refs. [43, 45, 199]).

In-plane transport measurements with $I||(ab)$ (transverse-field, with the current parallel to the (ab)-plane and the magnetic field perpendicular to it, or $H||c$) were performed in a variable temperature cryostat in dc fields up to $38\,\mathrm{T}$ at HFML, Nijmegen and up to $\sim 70\,\mathrm{T}$ at LNCMI, Toulouse with the magnetic field applied along the c-axis (transverse-field magnetoresistivity) and along the (ab) conducting plane (longitudinal-field magnetoresistivity, with both current and field parallel to the (ab)-plane) at constant temperatures. Low-field measurements were performed in a $16\,\mathrm{T}$ Quantum Design PPMS. The transverse-field resistivity ρ_{xx} and Hall ρ_{xy} components were measured using a low-frequency five-probe technique and were separated by (anti)symmetrizing data measured in positive and negative magnetic fields (for transverse-field magnetoresistivity). Good electrical contacts were achieved using In soldering along the long edge of the single crystals and electrical currents lower than $3\,\mathrm{mA}$ were used to avoid heating.

The complete suppression of the structural transition occurs at $x_c \sim 0.175(5)$ as shown in figure 6.1, which agrees with previous reports [43, 199]. This value however differs from that reported in Ref. [201], where the nominal concentrations have been used. For example, in Ref. [201] $x_{nom} = 0.16$ has $T_s \sim 51\,\mathrm{K}$, which would correspond to $x \sim 0.13$, based on the phase diagram here and previous reports [43, 199]. The two $x \sim 0.17$ and the $x \sim 0.18$ samples come from the same batch and their differences reflect the sulphur variation and the degree of disorder ($x \sim 0.18$ is cleaner with an $RRR \sim 24$, compared with ~ 16 for the two $x \sim 0.17$ samples). For the $x \sim 0.18$ sample the derivative evolves more gradually, without a well-defined structural transition when compared to the other sulphur substitutions, and so it is likely that this sample is the closest to the nematic end point, just inside the nematic state.

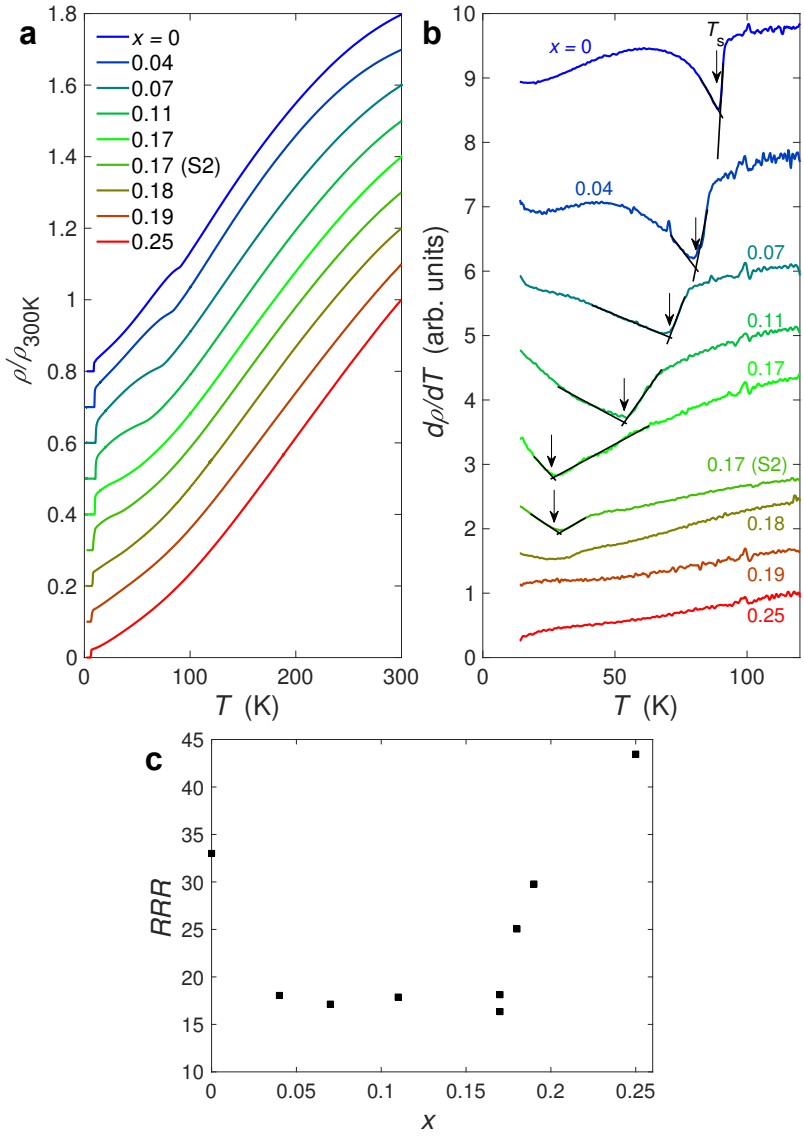


Figure 6.1: **Temperature dependence of the resistivity of FeSe$_{1-x}$S$_x$. a** Resistivity, normalised to the 300 K value, against temperature for different sulphur concentrations. **b** The first derivative of the resistivity with respect to temperature for the same data. The location of the structural transition, T_s is defined by the intercept of the linear fits on either side of the transition, as indicated by arrows. In **a** and **b** the curves for different sulphur concentrations have been offset for clarity. **c** The residual resistivity ratio (defined as the ratio between the room temperature and the onset of superconductivity resistivity), RRR, as a function of x.

6.3 Transverse-field magnetoresistivity in high magnetic fields

Figure 6.2**a**-**e** show the transverse-field magnetoresistivity, $\rho_{xx}(H)$, of different single crystals of FeSe$_{1-x}$S$_x$ up to 35 T at various fixed temperatures inside the nematic phase, and

up to 69 T for $x \sim 0.25$ in the tetragonal phase. From these constant temperature runs, the magnetoresistivity at fixed fields is extracted for each composition x, as shown in figures 6.2**f-j**. These reveal several striking features.

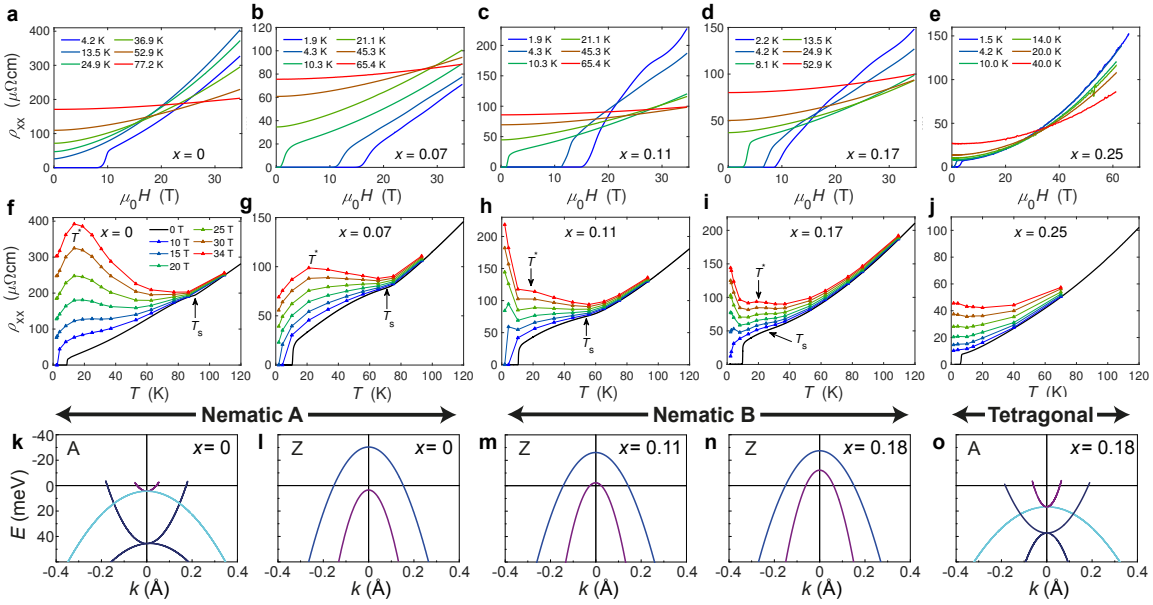


Figure 6.2: **Transverse-field magnetoresistivity for FeSe$_{1-x}$S$_x$. a-e** Field-dependent in-plane resistivity at different constant temperatures for different compositions, x, inside and outside the nematic phase. The magnetic field is applied along the c-axis, perpendicular to the in-plane electrical current. A strong magnetoresistivity develops inside the nematic phase. **f-j** Resistivity against temperature in zero field (solid line) and at fixed magnetic fields (symbols), as extracted from the top panels for different x. The peak in magnetoresistivity is indicated by T^* and the nematic phase emerges at T_s. **k-o** Schematic band dispersion at low temperatures at two high symmetry points at the top of the Brillouin zone, Z and A, for different x (based on ARPES data reported in Refs. [27, 28, 40, 41]). The horizontal lines represent the location of distinct regions in the magnetotransport behaviour called nematic A ($x = 0, 0.07$), nematic B ($x = 0.11, 0.17$) and the tetragonal phase for $x \gtrsim 0.18$. In the tetragonal phase, the compensated semi-metal is formed of two electron and two-hole like bands. Deep inside the nematic phase the inner hole band and inner electron bands are brought to the vicinity of the Fermi level.

Firstly, the magnetoresistivity increases significantly once a system enters the nematic state below T_s, and its magnitude varies depending on the concentration x, being largest for FeSe ($x = 0$), just above T_c at ~ 14 K. Secondly, in the vicinity of T_c in magnetic fields much larger than the upper critical field, the magnetoresistivity shows an unusual temperature dependence that varies strongly with x across the phase diagram, as shown in figure 6.2**f-g**. The resistivity slope in 34 T, $d\rho_{xx}(34\,\mathrm{T})/dT$, of FeSe changes sign at a crossover temperature, $T^\star \sim 14$ K, as shown in figure 6.2**f** (and also in the colour plot of

the slope in figure 6.7**d**). With increasing sulphur substitution from FeSe towards $x \sim 0.07$ (defined as the nematic A region), the position of $T^\star$ shifts to a slightly higher temperature of ~ 20 K, and the peak in magnetoresistivity is much smaller than for FeSe. For higher sulphur concentrations, approaching the nematic phase boundary, ($x \sim 0.11-0.17$, defined as the nematic B region), there is a small peak at $T^\star$. However, the slope of the resistivity in 34 T at low temperatures becomes negative and is strongly enhanced, different from the nematic A phase (see figures 6.2**h**, 6.2**i** and 6.7**d**). Lastly, in the tetragonal phase, the magnetoresistivity shows conventional behaviour and increases quadratically in magnetic fields (figures 6.2**e** and 6.2**j**).

The unusual downturn of resistivity in high fields below $T^\star$ inside the nematic A phase was previously assigned to large superconducting fluctuations in FeSe in magnetic fields up to 16 T [37, 38]. This behaviour remains robust in magnetic fields at least a factor of 2 higher than the upper critical field (~ 16 T for $H||c$ [37], also see chapter 7). Furthermore, it also manifests in $x \sim 0.07$ inside the nematic A phase but it disappears for higher $x \gtrsim 0.1$. As T_c and the upper critical field inside the nematic phase for different x remain close to that of FeSe [43], the changes in the resistivity slope in high magnetic fields are likely driven by field-induced effects that influence scattering and/or the electronic structure. The additional hole pocket emerging at $x \sim 0.1$ (figure 6.2**m**) [40, 41, 43] could well be responsible for the dramatic changes in the low-temperature magnetoresistivity found here.

6.3.1 Hall Effect

The Hall coefficient, $R_\mathrm{H} = \rho_\mathrm{xy}/\mu_0 H$, extrapolated in the low-field limit (below 1 T) for $FeSe_{1-x}S_x$ has an unusual temperature dependence, as shown in figure 6.3**b**. For a two-band uncompensated metal, the sign (and magnitude) of the Hall coefficient depends on the difference between the hole and electron mobilities [70]. In the tetragonal phase (above T_s for samples with a nematic transition) and for $x \gtrsim 0.18$, R_H is close to zero (figure 6.3**b**), as expected for a two-band compensated metal. At low-temperature and low field (~ 1 T) in the nematic A phase the R_H is negative, suggesting that transport is dominated by an additional highly mobile electron band [40, 203]. It becomes positive at all temperatures inside the nematic B phase, dominated by a hole-like band (figure 6.3**a**). This could again be caused by the additional hole pocket emerging at $x \sim 0.1$. It is worth mentioning that inside the nematic B phase the quantum oscillations are dominated by a low-frequency pocket with light-mass that disappears at the nematic end point [43]. The behaviour of R_H could be linked to the disappearance of a small (quasi) 3D hole pocket centre at the Z-point in FeSe below T_s and its re-emergence in the nematic B phase with x substitution near $x \sim 0.1$, as found in ARPES studies [40] and shown in figure 6.2**m**. Interestingly, the

subtle (or perhaps not so subtle) changes in the electronic structure in $FeSe_{1-x}S_x$ seem to correlate with the different features observed both in magnetoresistivity (figures 6.2**f**-**i**) and in the magnitude of the Hall coefficient, $|R_{\rm H}|$, that also shows a maximum near $T^\star$ (figure 6.3**b**). The Hall component of FeSe in increasing magnetic field is unusual, changing sign and showing highly non-linear behaviour [40]. A magnetic field can induce changes in scattering and/or field-induced Fermi-surface effects in the limit when the cyclotron energy is close to the Zeeman energy. The smallest inner bands of $FeSe_{1-x}S_x$ shift in energy as a function of composition x (and temperature [43]), as shown in figure 6.2**k**-**o**. Furthermore, the Hall effect in iron-based superconductors can be affected by the spin fluctuations that induce mixing of the electron and hole currents [204].

6.3.2 Transverse-field magnetoresistivity across the NEP

Next, the transverse-field magnetoresistivity across the phase diagram and near the NEP of $FeSe_{1-x}S_x$ will be analysed and discussed. At low temperatures inside the nematic phase, the transverse-field magnetoresistivity is dominated by quantum oscillations [43], making it difficult to quantify the field dependence of the normal state. A near-linear magnetoresistivity is detected at low temperatures for $x \sim 0.07$ in figure 6.2**b** and for a dirty sample (with low $RRR \sim 8.5$) in figure B.6. The quasi-linear field magnetoresistivity at low temperature can arise from squeezed trajectories of carriers in semi-classically large magnetic fields in the case of small Fermi surfaces ($\omega_c\tau \gg 1$) [67, 205]. Another explanation for the almost linear magnetoresistivity is the presence of mobility fluctuations caused by spatial inhomogeneities, as found in low-carrier systems [205–207].

Classical magnetoresistivity in systems with a single dominant scattering time is expected to follow a H^2 dependence [67]. This results in Kohler's rule[68], which is violated in $FeSe_{1-x}S_x$ (see figures 6.4**a**-**c**), suggesting that the magnetoresistivity is not dominated by a single scattering time. Magnetoresistivity is however quadratic in magnetic fields up to $69\,$T in the tetragonal phase (see figures 6.2**e**, B.1**e** and B.1**f**), but not inside the nematic phase. $FeSe_{1-x}S_x$ are compensated multi-band systems [27] where the high-field magnetoresistivity is expected to be large and dependent on the various scattering times of different electron and hole bands. Magnetoresistivity in these cases has a more complicated form (see sections 1.7.2 and 1.7.4 for examples), and so instead simpler scaling laws have been sought to reveal any underlying behaviour, in particular near any critical points [196, 197]. For example, in $BaFe_2(As_{1-x}P_x)$ for $x \sim 0.33$ at the antiferromagnetic critical point, a universal $H - T$ scaling was empirically found between the linear resistivity in temperature and magnetic field [196]. Here a similar scaling of $\Delta\rho_{\rm xx}/\rho_{H=0}$ against $\mu_0 H/T$ is shown in figures 6.5**d**-**f** for certain samples. There is clearly no scaling for $x = 0$ and

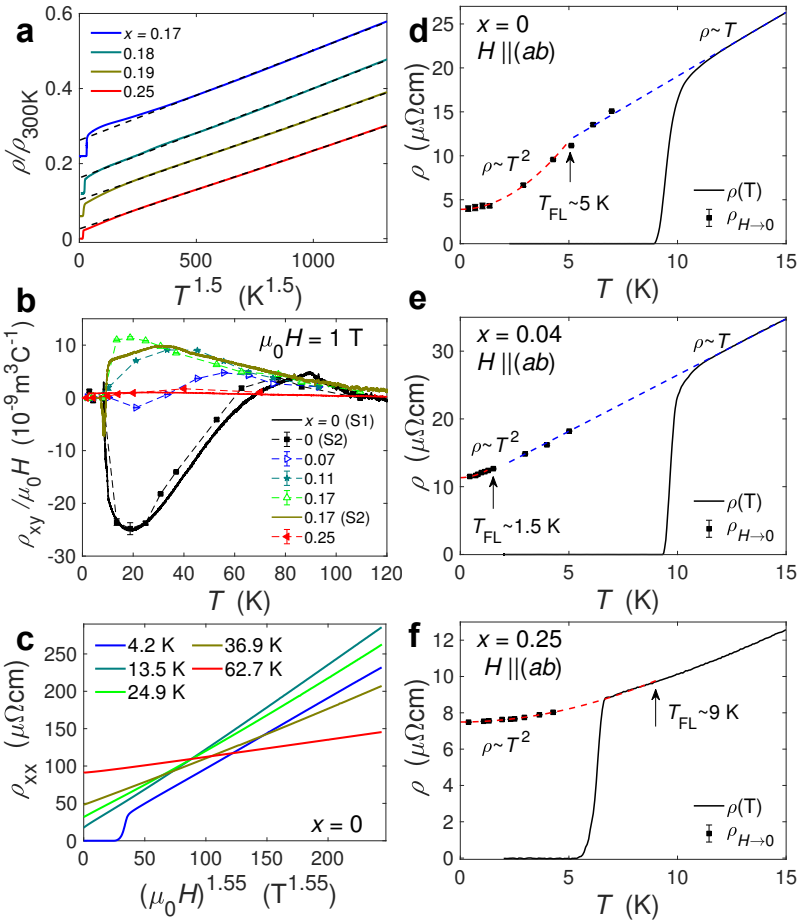


Figure 6.3: **Normal electronic state of FeSe$_{1-x}$S$_x$.** **a** Temperature dependence of resistivity against $T^{1.5}$ over a large temperature region, just outside the nematic phase. **b** Hall effect coefficient in low magnetic fields (1 T) indicating the change in sign and the dominance of different carriers across the nematic phase. **c** Transverse-field symmetrized resistivity versus $H^{1.55}$ for FeSe inside the nematic phase at constant temperatures. **d-f** The low-temperature resistivity for $x = 0$, 0.04 and 0.25 respectively. The solid lines are the zero-field resistivity data. Solid circles represent the zero-field extrapolated values of ρ_{xx} when $H||(ab)$ plane. The dashed red lines represent fits to a Fermi-liquid behaviour found below T_{FL}, as indicated by arrows. Dashed blue lines are linear fits to the linear part of the resistivity.

0.25. However, in Ref. [202] for a particularly dirty sample of $x_{\mathrm{nom}} = 0.18$ with $RRR \sim 5$ and weak magnetoresistivity (a factor ~ 100 smaller than the $x \sim 0.17$ sample(s) presented in this chapter) H/T scaling was proposed, suggesting that disorder may play an important role in this type of scaling in FeSe$_{1-x}$S$_x$. Near the nematic end point of FeSe$_{1-x}$S$_x$, at $x \sim 0.17$, the $H - T$ dependence collapses onto a single curve, as shown in figure 6.4**e** for a $x \sim 0.17$ sample. Despite this, the energy scaling of magnetoresistivity used to described the antiferromagnetic critical point in Ref. [196] is not obeyed in the vicinity of the nematic

end point in $FeSe_{1-x}S_x$, as shown in figures 6.4**g-i**. This attempted energy scaling has the form

$$\Gamma = \alpha k_B T \sqrt{1 + \left(\frac{\beta}{\alpha}\right)^2 \left(\frac{\mu_B \mu_0 H}{k_B T}\right)^2}, \tag{6.1}$$

using $\alpha = 1$ and $\beta = 1$. Other reasonable values of α and β have also been attempted, but also show no scaling. The violation of this scaling suggests that temperature and magnetic fields have different energy dependencies in $FeSe_{1-x}S_x$. This could be due to additional effects from, for example, the nemato-elastic coupling [208] and/or the effect of impurities. For example, a dirty sample of $FeSe_{1-x}S_x$ close to $x_{nom} \sim 0.18$ was recently suggested to obey $H - T$ scaling [202] (as discussed above in this paragraph), suggesting that disorder does play a role.

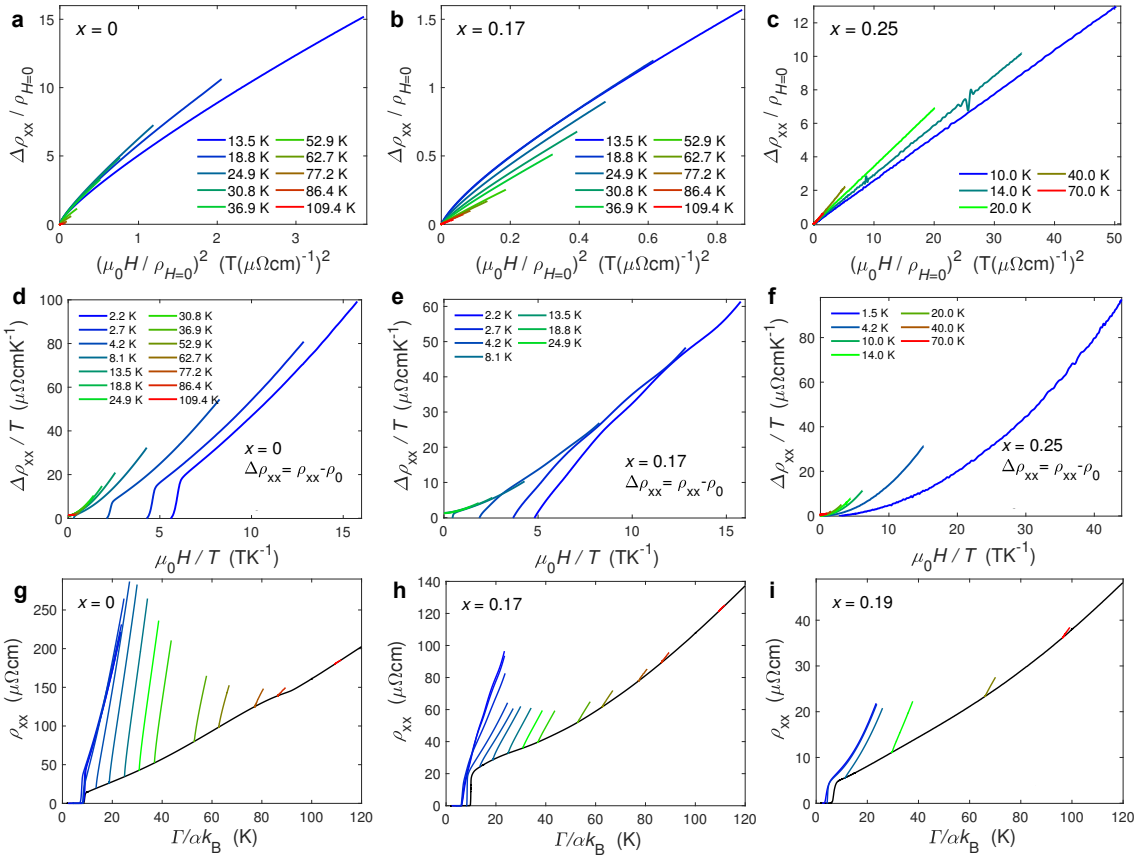


Figure 6.4: **The magnetoresistivity scaling in $FeSe_{1-x}S_x$.** **a-c** Kohler's plots, $\Delta\rho_{xx}(\mu_0 H)/\rho_{xx}(H=0) \propto (\mu_0 H/\rho_{xx}(H=0))^2$, where $\Delta\rho_{xx} = \rho_{xx} - \rho_{xx}(H=0)$ for $x = 0, 0.17$ and 0.25, respectively. **d-f** $H - T$ scaling of $\Delta\rho_{xx}/\rho_0 \sim \mu_0 H/T$, where $\Delta\rho_{xx} = \rho_{xx} - \rho_0$ and ρ_0 is the zero-temperature zero-field resistivity. **g-i** Energy scaling of resistivity as Γ, where $\Gamma = \alpha k_B T\sqrt{1 + (\beta/\alpha)^2(\mu_B\mu_0 H/(k_B T))^2}$ using $\alpha = 1$ and $\beta = 1$, for $x = 0, 0.17$ and 0.19 respectively.

For reasons described above, a different approach to model the magnetoresistivity data in the nematic state of $FeSe_{1-x}S_x$ is proposed, using a power law in magnetic fields given by

$$\rho_{xx}(H) = \rho_{xx}(H = 0) + b(\mu_0 H)^{\delta}. \tag{6.2}$$

Taking the derivative with respect to magnetic field gives

$$\frac{d\rho_{xx}(\mu_0 H)}{d(\mu_0 H)} = b\delta(\mu_0 H)^{\delta-1}, \tag{6.3}$$

plots of which are shown in figures 6.5**a**, 6.5**d** and 6.5**g**. Taking the natural logarithm gives

$$\ln\left(\frac{d\rho_{xx}}{d(\mu_0 H)}\right) = \ln(b) + \ln(\delta) + (\delta - 1)\ln(\mu_0 H). \tag{6.4}$$

Using this, the magnetic field exponent δ can be extracted from the gradient of plots of $\ln(d\rho_{xx}/dH)$ against $\ln(\mu_0 H)$, as shown in figures 6.5**b**, 6.5**e** and 6.5**h**. Figures 6.5**c**, 6.5**f** and 6.5**i** show the variation of the exponent for certain samples (inside the nematic phase) as a function of magnetic field using the above method. The exponent was found using a moving average field window of 1 T. These findings clearly show the evolution of the magnetic field exponent from $\delta \sim 1.55$ inside the nematic state towards $\delta \sim 2$ outside of the nematic state. All the magnetoresistivity data inside the nematic phase can be described by a unique exponent $\delta \sim 1.55(5)$ over a large field window ($\sim 5 - 35$ T), as shown by the colour plot in figure 6.7**c**, as well as in figures 6.3**c** and B.1**a**-**d**. Furthermore, this gives $\delta \sim 2$ for samples in the tetragonal phase (see figure 6.7**c**). Inside the nematic phase, the Fermi surface of $FeSe_{1-x}S_x$ distorts anisotropically [27, 28] and an unusual type of scattering could become operational due to presence of hot and cold spots along certain directions [209].

6.4 Resistivity exponents in temperature at zero magnetic field

A similar approach as in equation 6.2 can be employed to determine the variation of resistivity exponents with temperature, now using

$$\rho = \rho_0 + AT^{\gamma}, \tag{6.5}$$

where γ is the temperature exponent and ρ_0 is the resistivity at $T = 0$. However, the above approach that has been used here for magnetic field sweeps on the temperature dependence

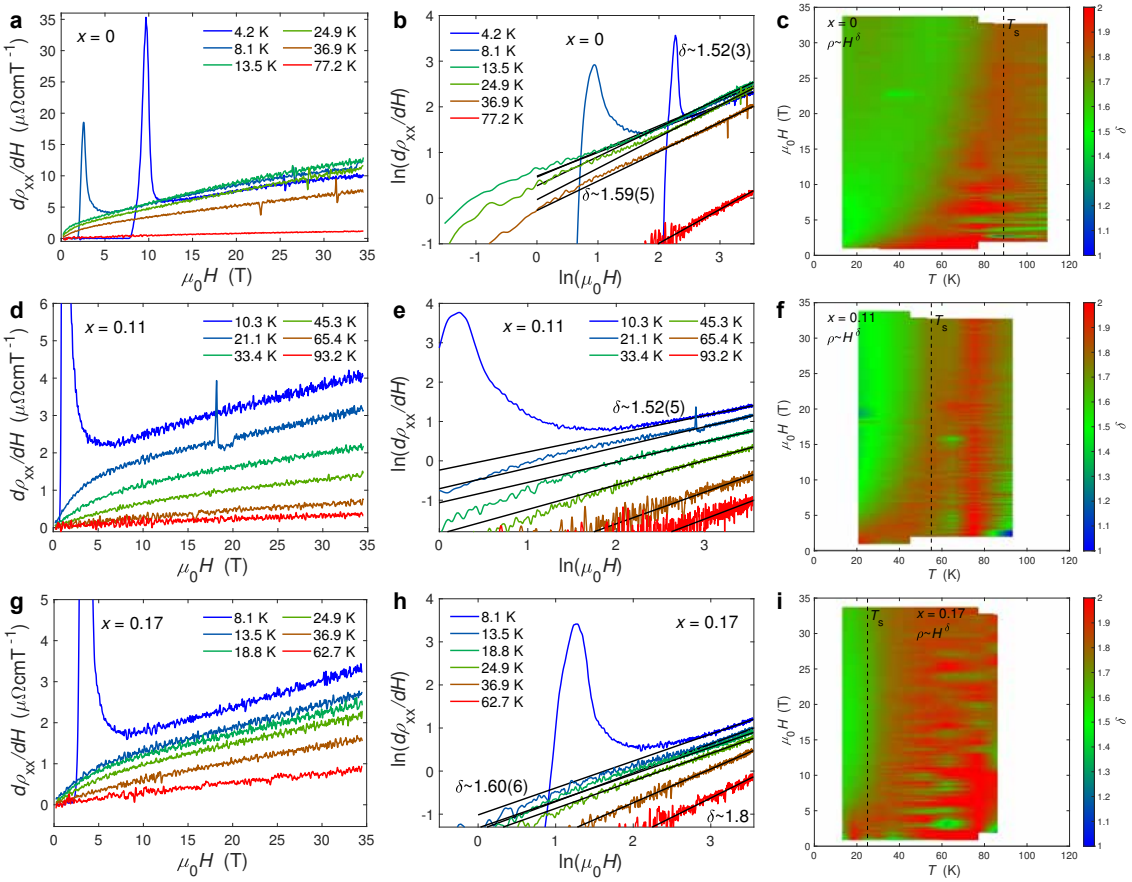


Figure 6.5: **Extraction of the magnetic field exponent δ, from the relationship $\rho_{xx} = \rho_{H\to 0} + bH^{\delta}$, for $FeSe_{1-x}S_x$. a**,**d**,**g** Derivative of the symmetrized transverse-field resistivity with respect to the applied magnetic field for $x = 0, 0.11$ and 0.17, respectively. **b**,**e**,**h** Natural logarithm of the derivative against the natural logarithm of magnetic field for the same data in **a**,**d**,**g**. Here linear fits to the high-field region allow the extraction of the magnetic field exponent from the gradient, which is $\delta - 1$. **c**,**f**,**i** Colour plots of δ in the temperature-magnetic field plane, extracted above the superconducting transition temperature using the relationship $d\ln(\rho_{xx} - \rho_{xx}(H=0))/d(\ln(\mu_0 H)) = \delta$. Consistent values of δ were obtained from linear fits over small regions using $\ln(\rho_{xx} - \rho_{xx}(H=0)) = \ln(b) + \delta\ln(\mu_0 H)$.

gives relatively noisy results, and so accurate exponent determination is difficult. Instead, a different approach is employed. Rearranging equation 6.5 and taking the logarithm gives

$$\ln(\rho - \rho_0) = \ln(A) + \gamma\ln(T) \tag{6.6}$$

Taking the derivative with respect to $\ln(T)$ and rearranging again gives

$$\gamma = \frac{d\ln(\rho - \rho_0)}{d\ln(T)}, \tag{6.7}$$

from which the exponent γ can be extracted. For this it is first necessary to establish ρ_0 for each sample from low temperature magnetic field sweeps with $H||(ab)$, as detailed later in

this chapter. The results of this approach are shown in figure 6.6. As an aside, the nematic transition temperature is clearly visible here as minimum in $\gamma(T)$.

Note that this approach is also slightly flawed. Different scattering mechanisms and underlying physics could result in different ρ_0 values. For example, in the $x = 0.25$ sample T^2 Fermi-liquid behaviour is observed at low temperature (see later) and so a ρ_0 value from this is used. However, the exponent at higher temperatures tends to $\gamma \sim 1.5$ over a large temperature range. The choice of ρ_0 in this case means that the exponent is actually predicted to be slightly larger in this region. Even with this criticism, this is currently the best model for accurately finding how the temperature exponent evolves.

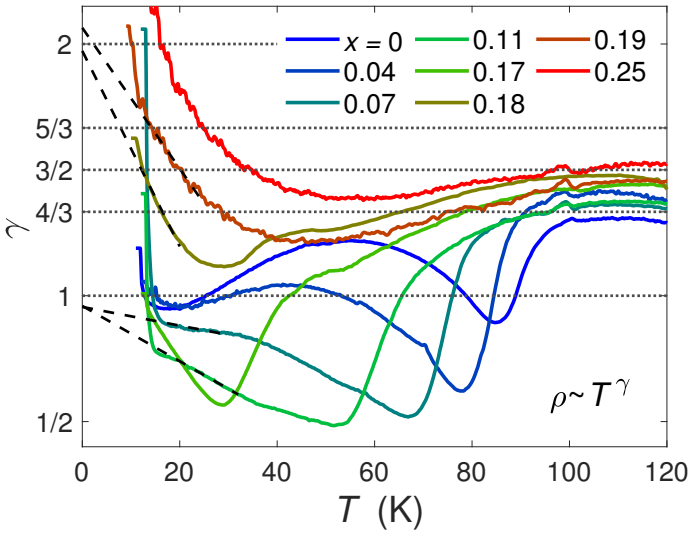


Figure 6.6: **The temperature dependence of the exponent γ from $\rho = \rho_0 + AT^\gamma$ for $FeSe_{1-x}S_x$.** The γ exponent is estimated from $\gamma = d\ln(\rho - \rho_0)/d\ln(T)$ for various sulphur concentrations. The ρ_0 values are the zero-field zero-temperature resistivity extracted from figures B.2, B.3 and B.4. The curves shown here were used to generate the colour plots in figures 6.7**a** and 6.7**b**. Dashed black lines show possible extrapolations of the exponent towards the zero temperature limit. The horizontal lines indicate different possible exponents predicted by theory in the vicinity of a critical point [209–211]. The γ exponent depends on the value of ρ_0, which was extracted at the lowest temperature from longitudinal-field magnetoresistivity in figure B.2.

Figure 6.7**a** shows a colour plot of the exponent γ, which is close to 1 at low temperatures inside the nematic phase (a value of γ=1.1(2) was previously reported in the nematic state for FeSe [212]). It becomes sub-linear close to the nematic phase boundary, indicating a significant deviation from Fermi-liquid behaviour. Outside the nematic phase a $T^{1.5}$ dependence of resistivity describes the data well over a large temperature range, up to 120 K (see figures 6.3**a** and 6.7**a**). This is in agreement with previous studies of $FeSe_{1-x}S_x$ under pressure [54]. Using the high-magnetic field data below T_c, the low-temperature

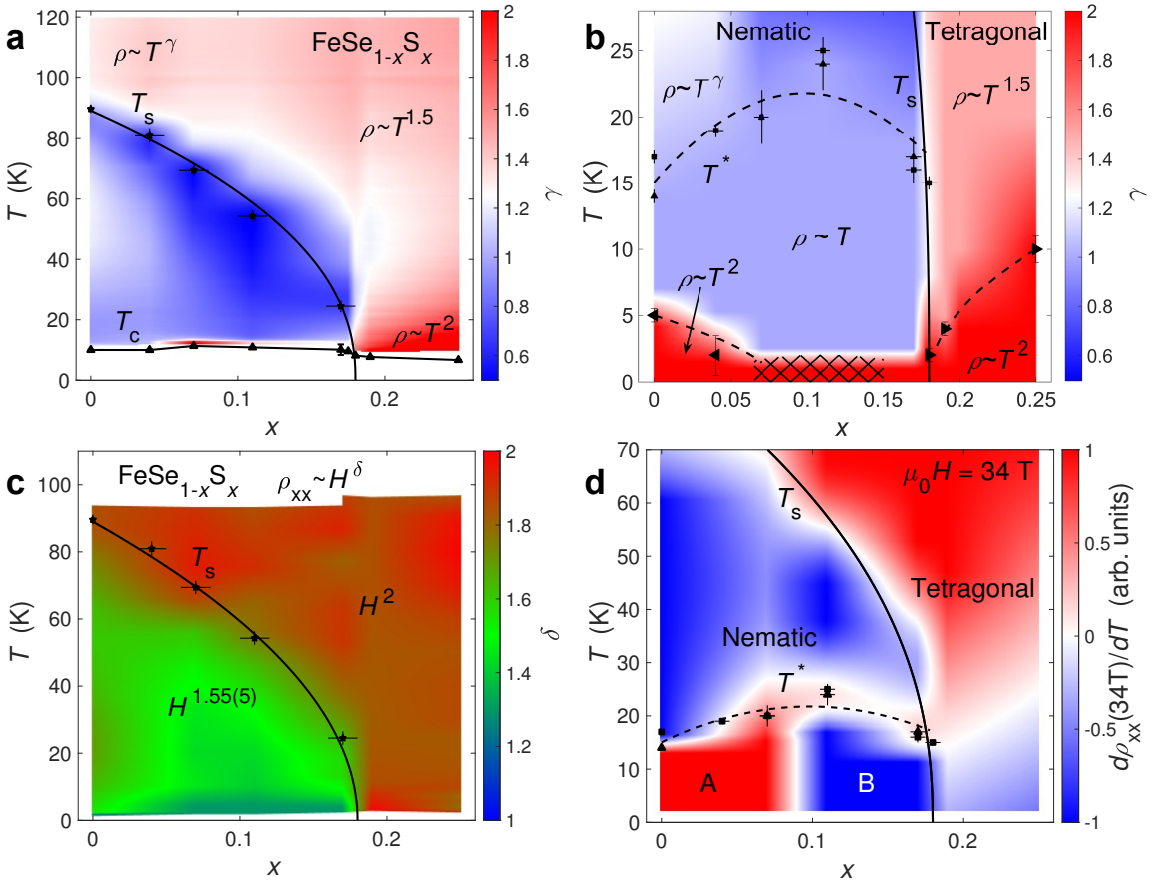


Figure 6.7: **Phase diagrams of the resistivity exponents and high-field transport in FeSe$_{1-x}$S$_x$. a** The colour plot of the temperature exponent, γ, extracted from zero-field resistivity data, as shown in figure 6.6. **b** The low-temperature resistivity exponent below T^*, extrapolated from high magnetic fields as shown in figures B.2-B.4, indicating the non-Fermi liquid behaviour of the nematic phase. Fermi liquid behaviour recovers below T_{FL} for the x compositions with lowest disorder both inside the nematic phase and in the tetragonal phase. **c** The temperature dependence of field exponent δ, showing a dominant $\sim H^{1.55}$ power law inside the nematic phase (based on figure 6.5). **d** The colour plot of the slope of resistivity in 34 T between the nematic A and B phases. Solid squares represent T_{s} and solid triangles T_{c}. T^* indicated by stars represents the peak in magnetoresistivity and the maximum in $|R_{\mathrm{H}}|$. Solid lines indicate the nematic and superconducting phase boundaries and the dashed lines are guides to the eye. The hashed region at low temperatures in **b** has not yet been accessed experimentally.

resistivity is extracted in the absence of superconductivity, $\rho_{H\to 0}(T)$. Figures 6.3**d-f** show resistivity against temperature for different values of x, together with the extrapolated high-field points, using longitudinal-field magnetoresistivity when $H||(ab)$ plane, shown in figure B.2 (also see figure B.3 for the temperature dependence of $\rho_{H\to 0}$). Transverse-field magnetoresistivity data is also used to extract the zero-field resistivity, using the estab-

lished power law $H^{1.55}$, as shown in figure B.4. From both measurements, strong evidence for a linear resistivity in the low temperature regime is found, below $T^\star$, inside the nematic phase. Linear resistivity was also detected from the $35\,\mathrm{T}$ temperature dependence of the longitudinal-field magnetoresistivity in Ref. [201]. However, it was assumed to occur near the *nematic critical point* defined as $x_{\mathrm{nom}} \sim 0.16$, which corresponds to $x \sim 0.13$ in the phase diagrams here (as the resistivity derivative in Ref. [201] shows a $T_{\mathrm{s}} \sim 51\,\mathrm{K}$). At low temperatures, it is observed that Fermi-liquid behaviour recovers in the tetragonal phase (as in Refs. [201, 213]) and inside the nematic phase, below T_{FL} (see figures 6.3**d**-**f** and 6.7**b**). This is strongly dependent on composition and impurity level, even in the vicinity of the nematic end point (see figures B.5 and B.6). T_{FL} is highest for the samples with the largest residual resistivity ratio, and is generally only found for $RRR > 16$. Theoretical models suggest that the temperature exponent, γ, in vicinity of critical points is highly dependent on the presence of *cold spots* on different Fermi surface sheets, due to the symmetry of the nematic order parameter [209, 211]. On the other hand, near a antiferromagnetic critical point in the presence of spin fluctuations the impurity level also affects the temperature exponent [75]. Furthermore, the scale at which the crossover to Fermi liquid behaviour occurs at T_{FL} in nematic critical systems could depend on the strength of the coupling to the lattice [208].

6.5 Discussion

An overall representation of the resistivity slope $d\rho_{\mathrm{xx}}(34\mathrm{T})/dT$ in $34\,\mathrm{T}$ for $FeSe_{1-x}S_x$ as a function of temperature is shown in the phase diagram in figure 6.7**d**. The low-temperature manifestation of electrical transport in the nematic A and B phases is clearly different below $T^\star$. In order to identify possible sources of scattering responsible for these changes, the role of spin fluctuations is considered. Recent NMR data found that low frequency antiferromagnetic spin fluctuations are present inside the nematic phase of $FeSe_{1-x}S_x$, being strongest around $x \sim 0.1$ [45]. In FeSe, spin fluctuations are rather anisotropic [45, 214] and strongly field-dependent below $15\,\mathrm{K}$ [38]. Interestingly, the spin-fluctuations relaxation rate is enhanced below $T^\star$ [38], suggesting a correlation between spin-dependent scattering, the high-field magnetoresistivity and the low-temperature transport inside the nematic state. High-magnetic fields are expected to align magnetic spins and could affect the energy dispersion of low-energy spin excitations and spin-dependent scattering in magnetic fields. In FeSe, the spin-relaxation rate in different magnetic fields up to $19\,\mathrm{T}$ deviates at $T^\star$ [38] but it remains relatively constant in $19\,\mathrm{T}$ at low temperatures. This may suggest the variation in magnetoresistivity in high magnetic fields at low temperatures in $FeSe_{1-x}S_x$ is

more sensitive to the changes in the electronic behaviour rather than to the low frequency spin fluctuations across the nematic phase.

The low-temperature regime below $T^\star$ displays linear resistivity, which is a potential manifestation of scattering induced by critical spin-fluctuations in clean systems [75]. μSR studies place FeSe near an itinerant antiferromagnetic quantum critical point at very low temperatures [198] and low frequency spin-fluctuations are only found inside the nematic state [38, 45]. On the other hand, approaching the nematic end point in $FeSe_{1-x}S_x$ it is found that the resistivity is not linear in temperature but is dominated by a $T^{1.5}$ dependence. This is in contrast to the linear resistivity found near an antiferromagnetic critical point in $BaFe_2(As_{1-x}P_x)$ [212]. Theoretically, $\gamma = 3/2$ could describe the resistivity caused by strong antiferromagnetic critical fluctuations in the dirty limit [75, 215]. However, with increasing x in $FeSe_{1-x}S_x$ the spin fluctuations are suppressed and a Lifshitz transition was detected at the nematic end point [43]. At the nematic end point the divergent fluctuations for different Fermi surfaces could display unusual power laws in resistivity, as discussed in Refs. [209–211]. To assess the critical behaviour, it is worth emphasizing that the effective masses associated with the outer hole bands do not show any divergence close to the nematic end point $x \sim 0.18$ [43]. This agrees with the variation of the $A^{1/2}$ coefficient (see figure B.7) and previous studies under pressure [54], suggesting the critical nematic fluctuations could be quenched by the coupling to the lattice along certain directions in $FeSe_{1-x}S_x$.

The striking difference in magnetotransport behaviour between the nematic and tetragonal phase in $FeSe_{1-x}S_x$ can have significant implications on what kind of superconductivity is stabilized inside and outside the nematic phase as different pairing channels may be dominant in different regions, as found experimentally [31, 32]. Linear resistivity found at low temperatures inside the nematic state is present in the region where spin-fluctuations are strongest. Furthermore, the absence of an enhancement in superconductivity (such as in T_c for example) at the nematic end point in $FeSe_{1-x}S_x$ is supported by the lack of divergent critical fluctuations, found both with chemical pressure [43] and applied pressure [54]. This can be a direct manifestation of the quenching of critical fluctuations by the interaction with the lattice [208].

6.6 Summary

In conclusion, the evolution of the low-temperature magnetotransport behaviour at high-magnetic fields up to $69\,\mathrm{T}$ has been studied in $FeSe_{1-x}S_x$. The nematic state has non-Fermi liquid behaviour and displays unconventional power laws in magnetic field, with $\rho_{xx} \propto$

$H^{1.55}$, reflecting the dominant anomalous scattering inside the nematic phase. In high magnetic fields, well-above the upper critical fields, the transverse-field magnetoresistivity shows a change in slope as a function of temperature that reflects the changes in the low frequency spin-fluctuations and/or the electronic structure. This evolves with increasing x, and becomes insulating like for $x \gtrsim 0.1$ (where an extra hole pocket emerges at the Fermi level) inside the nematic phase. In zero-field above the superconducting transition, the resistivity shows a dominant $T^{1.5}$ temperature dependence outside of the nematic phase. In the low-temperature limit, a high magnetic field suppresses superconductivity and reveals an extended linear resistivity in temperature followed by a Fermi-liquid like dependence, highly dependent on the composition and impurity level. This study reveals the anomalous transport behaviour of the nematic state, strikingly different from the tetragonal phase, that influences how superconductivity may be stabilised in different phases.

Chapter 7

Upper critical fields of $FeSe_{1-x}S_x$

In the previous chapter the normal state properties of $FeSe_{1-x}S_x$ have been experimentally mapped using electrical transport down to low temperatures. The attention of this chapter will turn to the superconducting state and the evolution of the upper critical fields across the phase diagram of $FeSe_{1-x}S_x$. It will focus in particular on changes across the nematic end point to assess any effects the nematic state may have on superconductivity. Such changes can also be linked to properties of the normal state that we have analysed in the previous chapter.

In this chapter the upper critical fields are experimentally investigated as a function of temperature down to $\sim 0.33\,\mathrm{K}$ for sulphur concentrations across the entire nematic phase and nematic end point, $0 \leq x \leq 0.25$. Measurements have been performed for two magnetic field orientations, with the field parallel to the crystallographic c-axis, $H||c$, and parallel to the (ab)-plane, $H||(ab)$, in magnetic fields up to $45\,\mathrm{T}$ using both electrical transport and magnetic torque measurements. The upper critical field shows multi-band behaviour across the entire phase diagram. Inside the nematic phase when $H||c$, H_{c2} shows strikingly linear behaviour down to the lowest experimental temperatures and appears to be limited by Pauli paramagnetic effects. Across the nematic end point the ratio H_{c2}/T_c is dramatically suppressed for both orientations and the multi-band nature changes significantly. The width of the superconducting transitions is largest near the nematic end point, which may be due to an increase in the superconducting fluctuations present here. The anisotropy of the upper critical field increases dramatically across the nematic end point, signifying a change in the nature of superconductivity and the dominance of a quasi two dimensional band. The coherence length ξ_{ab} increases across the nematic transition, while ξ_c remains relatively constant. When $H||(ab)$ the upper critical field shows an upturn at low temperatures inside the nematic state. A two-band model of the upper critical field describes the data well, and using this model the changes in superconductivity across the entire phase diagram are mapped. The upturn of H_{c2} below $\sim 2\,\mathrm{K}$ when $H||(ab)$ deep

inside the nematic state ($0 \leq x < 0.11$) is consistent with the manifestation of a Fulde-Ferrel-Larkin-Ovchinnikov (FFLO) state [81, 91]. Finally, the changes of the parameters in the two-band model suggest there may be a change in the dominant pairing from $s^{\pm}$ to s^{++} across the NEP.

This chapter will first recap some of the important information regarding upper critical fields in superconductors (for more details see section 2.1) and why $FeSe_{1-x}S_x$ is an ideal candidate for these studies. Some additional experimental details will then be covered, before the data is presented. The discussion will begin with certain parameters such as the coherence lengths and anisotropy before moving on to a single band description of the upper critical fields in $FeSe_{1-x}S_x$ using the WHH model (see section 2.1.3) and, more importantly, why it fails. $H_{c2}(T)$ is then described using the two-band model in section 2.1.5, which works well across the x phase diagram and in both magnetic field orientations. The bulk of the discussion in this chapter will cover the evolution of the parameters in this model with x substitution, their relevance for superconductivity, links to other superconducting parameters and the extraction of the superconducting gap(s).

7.1 Introduction

The upper critical fields of unconventional superconductors often display unique behaviour that cannot be described by BCS physics and offer an insight into the nature of superconductivity. The upper critical field, $\mu_0 H_{c2}$, gives access to important parameters for superconductivity such as the coherence length, ξ, and the anisotropy. Analysing upper critical fields also gives access to other factors that may limit them, such as orbital, Zeeman and paramagnetic effects. Upper critical fields in iron-based superconductors are usually extremely large and generally have multi-band character, manifesting from the complex Fermi-surfaces and multiple superconducting gaps present in these materials. Understanding the contribution that different bands have towards superconductivity requires detailed analysis of $H_{c2}(T)$, especially at low temperatures where the behaviour can deviate significantly from conventional models, such as the WHH model. Studying the evolution of $H_{c2}(T)$ towards low temperatures can be challenging in many unconventional superconductors, including iron-based superconductors, where H_{c2} can exceed $100\,\mathrm{T}$ and so it is difficult to access this regime experimentally. Iron-based superconductors also provide the right conditions for the Fulde-Ferrell-Larkin-Ovchinnikov (FFLO) state to develop in clean materials due to the presence of shallow bands and large Pauli paramagnetic effects [81, 91].

FeSe offers a platform on which to study upper critical fields down to the lowest temperature in an unconventional iron-based superconductor as it has a relatively low superconducting transition temperature, T_c, of ~ 9 K, and so has an experimentally accessible upper critical field (~ 25 T at the lowest temperatures). Multiple superconducting gaps have already been reported for this material [31, 32, 34, 35, 216], and it has been proposed to be near the BCS-BEC crossover [36, 37]. It exhibits an unusual nematic electronic state after an orthorombic-tetragonal structural transition at $T_s \sim 90$ K without long-ranged magnetic order [26–30]. The structural transition can be suppressed using isoelectronic sulphur substitution in FeSe$_{1-x}$S$_x$ [40], and goes to $T = 0$ at $x \sim 0.175$, which is defined as the nematic end point (NEP). Superconductivity remains robust across the nematic end point, but it has been suggested that there are changes in the nature of superconductivity here [31, 32]. T_c has a maximum of ~ 10.5 K at $x \sim 0.11$, shows a sharp drop at the nematic end point but remains almost constant across to FeS ($x = 1$), where $T_c \sim 4$ K [42]. Thus, due to the relatively low T_c of these materials, the upper critical field should be experimentally accessible across the entire doping range down to $T = 0$. These materials offer a unique opportunity to study the behaviour of unconventional superconductivity in the iron based family down to the lowest temperatures in the absence of long-ranged magnetic order across a nematic phase boundary.

7.2 Experimental details

Single crystals of FeSe$_{1-x}$S$_x$ were grown by the KCl/AlCl$_3$ chemical vapour transport method [200]. The composition for samples from the same batch were checked using EDX as reported previously in Ref. [43]. The structural transition at T_s also provides useful information about the expected x value, as shown in figure A.2. The nematic end point is located at $x \sim 0.175(5)$. Electrical transport samples were measured using the low-frequency 4- or 5-point contact method. Low resistance contacts ($< 1\,\Omega$) were made using indium solder to reduce heating at low temperatures. Typically a current of 1 mA was used. Quantum oscillations are observed when $H||c$ (see figures C.1-C.7 in Appendix C), indicating high-quality single crystals. Torque measurements were performed using two cantilevers, one with a sample and one without, across a quarter bridge, as described in section 3.5. Small AC currents $< 100\,\mu$A at low frequency were applied, and the voltage across this bridge was measured. This voltage is proportional to the torque of the sample, which is related to the magnetisation $V \propto \tau = M \times \mu_0 H$. Low magnetic field measurements up to 16 T were performed using a Quantum Design Physical Properties Measurements System (PPMS). Both field sweeps at fixed temperature and temperature sweeps in constant field were used

to build critical field phase diagrams. High field measurements were performed at the HFML Nijmegen up to 38 T and NHFML Tallahassee up to 45 T at temperatures down to $\sim$ 0.33 K. At high field facilities upper critical fields were identified from magnetic field sweeps at constant temperature.

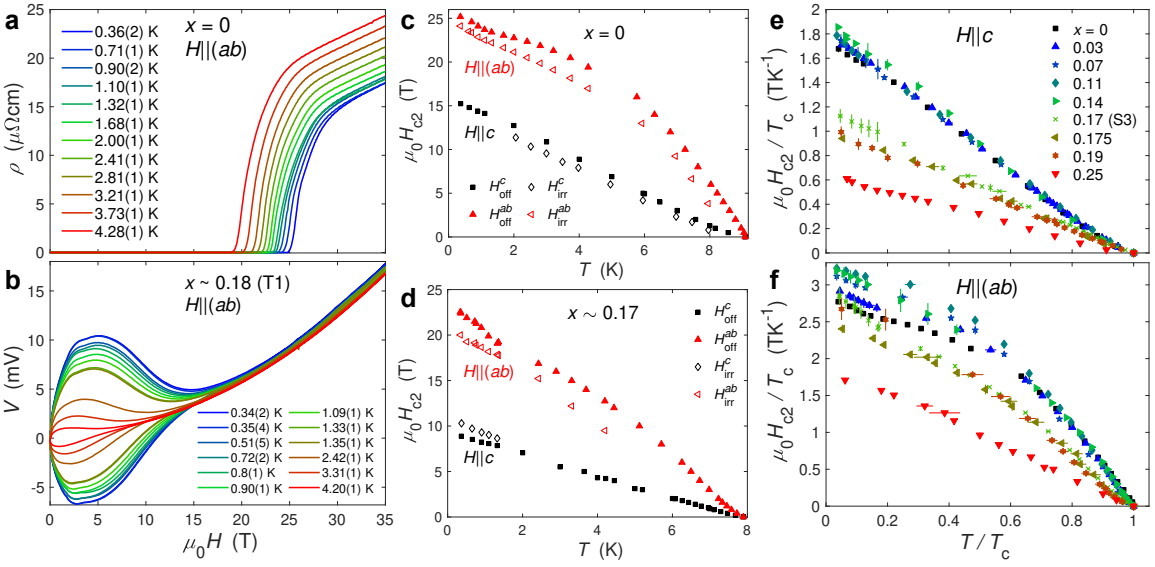


Figure 7.1: **Raw data and upper critical fields in $FeSe_{1-x}S_x$. a** Resistivity against magnetic field at different temperatures for $x = 0$ with $H||(ab)$. **b** Voltage (proportional to torque in arbitrary units) against magnetic field at different temperatures for $x \sim 0.18$ when $H||(ab)$. **c** and **d** Upper critical fields, $\mu_0 H_{c2}$ (defined from the offset criterion in figure 3.4, $H_{\rm off}$), against temperature in both field orientations for samples with $x = 0$ and $x \sim 0.17$, respectively. $\mu_0 H_{c2}$ is shown in closed symbols, and $\mu_0 H_{\rm irr}$ with open symbols. **e** and **f** The upper critical field in reduced units of $\mu_0 H_{c2}/T_c$ against T/T_c for $H||c$ and $H||(ab)$, respectively.

7.3 Results

Two different techniques have been used to extract the upper critical fields, resistivity and torque magnetometry. An example of resistivity against magnetic field (for $x = 0$) is shown in figure 7.1**a**. Here, the superconducting state is characterised by zero resistivity. Figure 7.1**b** shows an example of torque data against magnetic field (for $x \sim 0.18$, near the NEP). Since torque is proportional to the magnetisation, the sample is superconducting while the data shows hysteresis. More examples of raw data for resistivity against magnetic field are shown in figures C.1-C.7, and torque against magnetic field in figures C.8-C.10 (see Appendix C).

The upper critical field is extracted from resistivity using two methods. The first method involves fitting the transition with three linear fits (as shown in figure 3.4**b**) and extracting $\mu_0 H_{\rm off}$, $\mu_0 H_{\rm mid}$ and $\mu_0 H_{\rm on}$ from the intercepts and midpoint (peak in the derivative $d\rho/dH$). The second method uses noise analysis at low-field, and $\mu_0 H_{\rm c2,0}$ is defined as the point at which the signal increases to 1σ above the noise level, as shown in figure 3.4**c**. We find that $H_{\rm off}$ and $H_{\rm c2,0}$ agree well, and are used as the definition of $H_{\rm c2}$ from electrical transport throughout the rest of this chapter. Examples of the temperature dependence of the upper critical field, $H_{\rm c2}(T)$, are shown in figures 7.1**c** and 7.1**d**. For $x = 0$ (figure 7.1**c**) $H_{\rm off}$ and $H_{\rm irr}$ are shown (see figure 3.5**c** for an example of $H_{\rm irr}$ extraction from torque data and figures C.8, C.9 and C.10 for raw data). The general trends and features present here are consistent between the two measurement techniques. Inside the nematic phase with $H||c$ note that $H_{\rm c2}$ ($H_{\rm c2}^{c}$) in figure 7.1**c** is near linear down to the lowest temperatures. There is an upturn of $H_{\rm c2}$ at low temperatures when $H||(ab)$ ($H_{\rm c2}^{ab}$) inside the nematic phase.

Near the NEP in figures C.3-C.6 the resistive transitions become broader and the normal state at high-fields is more difficult to define, especially when $H||c$ where large quantum oscillations are present. When $H||(ab)$ the transitions are very broad (reaching $\sim 15\,\mathrm{T}$ at low temperature for $x \sim 0.175$, compared to $\sim 2\,\mathrm{T}$ for $x = 0$ and $\sim 4\,\mathrm{T}$ for $x = 0.25$ at the same temperature), and despite the lower $T_{\rm c}$ in this part of the phase diagram ($\sim 7 - 8.5\,\mathrm{K}$) the normal state is not completely reached at low temperatures and magnetic fields above $35\,\mathrm{T}$. For this reason, only $H_{\rm off}$ and $H_{\rm c2,0}$ can be defined near the NEP in figure 7.1**d**, along with $H_{\rm irr}$ from torque measurements. Again, we find good agreement between the two measurement techniques for this sulphur composition.

The upper critical field in reduced units of $\mu_0 H_{\rm c2}/T_{\rm c}$ against $T/T_{\rm c}$ for $H||c$ is shown in figure 7.1**e**. The reduced units are used to better compare between different x values. All samples inside the nematic state collapse onto a single straight line and intercepts $(T/T_{\rm c}) = 0$ at $\sim 1.84\,\mathrm{TK}^{-1}$, which is the Pauli paramagnetic limit for a single band [77]. This may imply that the upper critical field inside the nematic state is Pauli limited for $H||c$. As x increases towards and across the nematic end point the upper critical field is then systematically suppressed, dropping well below the Pauli limit for $x \sim 0.25$. The shape of the curves also change across the transition, becoming non-linear.

The upper critical field in reduced units for $H||(ab)$, shown in figure 7.1**f**, displays similar behaviour for all samples deep inside the nematic state, but does not scale in $\mu_0 H_{\rm c2}/T_{\rm c}$ as when $H||c$. All samples inside the nematic state do however show an upturn in $H_{\rm c2}$ when $H||(ab)$ at low temperature, which seems to be most pronounced near the nematic end point. As x increases across the nematic end point the upper critical field is again systematically suppressed when $H||(ab)$, similar to when $H||c$. The shape of the $H_{\rm c2}(T)$ for

$H||(ab)$ curves near T_c changes near and across the nematic end point, going from linear for $x \leq 0.11$ towards concave curvature across the nematic transition, and then back to near linear again for $x \sim 0.25$. The reason for this can be understood using a two-band model in the clean limit, and will be discussed later.

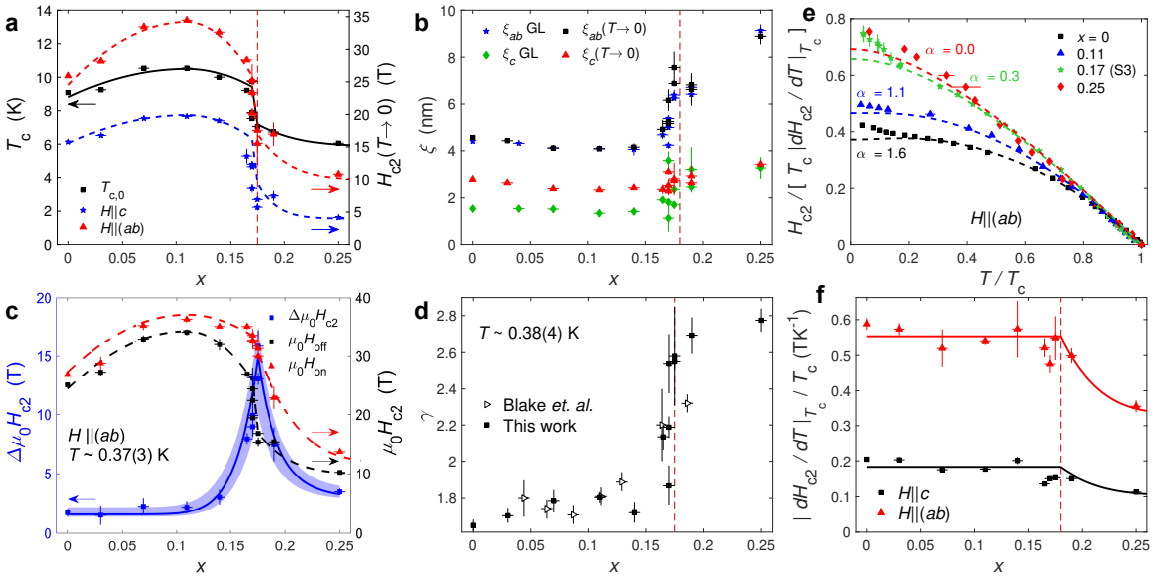


Figure 7.2: **Upper critical field parameters in $FeSe_{1-x}S_x$.** **a** Superconducting transition temperature T_c (black, left-axis) and the upper critical field as temperature goes to 0 K, $\mu_0 H_{c2}(T \to 0)$ for $H||c$ (right-axis, blue) and $H||(ab)$ (right-axis, red) against sulphur concentration, x. **b** Coherence lengths extracted from the Ginzburg-Landau model near T_c and from $\mu_0 H_{c2}(T \to 0)$ against x. **c** The offset (right-axis, black) and onset (right-axis, red) critical fields and the transition width $\mu_0 \Delta H_{c2} = \mu_0(H_{on} - H_{off})$ (left-axis, blue) versus x at the lowest temperatures. **d** Upper critical field anisotropy γ against sulphur concentration at the lowest temperatures. Vertical dashed lines show the nematic end point. **e** H_{c2} scaled using the slope near T_c and T_c, $H_{c2}/[T_c|dH_{c2}/dT|_{T_c}]$, against the reduced temperature, T/T_c for a selection of sulphur substitutions. The dashed lines show WHH model fits to the data with no spin-orbit scattering using the Maki parameters, α, as labelled. **f** Slope of the upper critical field near T_c divided by T_c, $|dH_{c2}/dT|_{T_c}/T_c$, as a function of x for the two field orientations. This is proportional to the superconducting gap, Δ.

The evolution of T_c, $\mu_0 H_{c2}^c(T \to 0)$ and $\mu_0 H_{c2}^{ab}(T \to 0)$ with sulphur concentration x is shown in figure 7.2**a**. The upper critical fields correlated well with T_c, and all three parameters show a sharp drop at the nematic end point, again suggesting changes in the nature of superconductivity inside and outside of the nematic phase.

In figure 7.2**b** we map the superconducting coherence lengths from both the GL approach and $\mu_0 H_{c2}(T \to 0)$ using data from both magnetic field orientations and equations 2.1-2.4. ξ_{ab}^{GL} and ξ_{ab} match well due to the linear and near-linear behaviour of $H_{c2}^c(T)$,

whereas ξ_c^{GL} and ξ_c deviate because of the curvature of $H_{\mathrm{c2}}^{ab}(T)$, as expected. The coherence lengths reported here for FeSe are in good agreement with previous transport results [217, 218] and STM measurements [216]. As the upper critical field has been measured down to low temperatures, ξ_{ab} and ξ_c are more reliable values than ξ_{ab}^{GL} and ξ_c^{GL}. ξ_{ab} is enhanced across the nematic end point, whilst ξ_c seems to remain relatively constant. Comparing the coherence lengths to the mean free path (ℓ, calculated and shown in figure 7.3) places all of the samples measured here in the clean limit ($\ell \gg \xi$).

The offset and onset critical fields from transport at the lowest temperature when $H||(ab)$ as a function of x are shown in figure 7.2**c**, along with the superconducting transition width, $\Delta\mu_0 H_{\mathrm{c2}}^{ab}$. The transition width is clearly dramatically enhanced near the nematic end point. We propose two cases for this. Firstly, this could be caused by enhanced superconducting phase or amplitude fluctuations [102], which would allow superconducting 'puddles' to persist to higher magnetic fields, thus broadening the superconducting to normal state transitions in electrical transport. These enhanced superconducting fluctuations could be linked to the enhanced nematic fluctuations previously reported near the NEP [199]. Second, the broader transitions here could be caused by compostion variation or sample inhomogeneity. As the changes in this region of the phase diagram are very sharp with changing x even a small change of ~ 0.005 would have far more dramatic effects than in all other parts of the phase diagram. However, if a systematic evolution of the onset critical field (H_{on}) is considered, we note that the composition variation would have to range from $\sim 0.11-0.19$. This large variation does not agree with the observed T_{s} (see figure A.2**b**) or previous EDX results [43], which suggest that the compositional variation is much smaller than this. For this reason, the increase in $\Delta\mu_0 H_{\mathrm{c2}}^{ab}$ at the NEP is likely due to an enhancement in the superconducting fluctuations. Previous work has shown that nematic fluctuations are enhanced at the NEP [199], which may be linked to the broader transitions and enhanced superconducting fluctuations we report here.

Note, as mentioned above, that the onset fields near the NEP are more difficult to define because of the broad transitions and field range (38 T). It is likely that the onset fields have been underestimated near the NEP, and so $\Delta\mu_0 H_{\mathrm{c2}}^{ab}$ has also been underestimated.

The anisotropy of the superconducting state, defined as $\gamma = H_{\mathrm{c2}}^{ab}(T \to 0)/H_{\mathrm{c2}}^{c}(T \to 0)$, is shown as a function of x in figure 7.2**d**. Inside the nematic state γ seems to follow T_{c}, but increases across the NEP and continues to slowly increase further outside of the nematic state. This again suggests an abrupt change in superconductivity across the NEP. We note that the anisotropy likely continues to increase up to $x = 1$ (at FeS), where a value of $\gamma \sim 6$ has been reported [42].

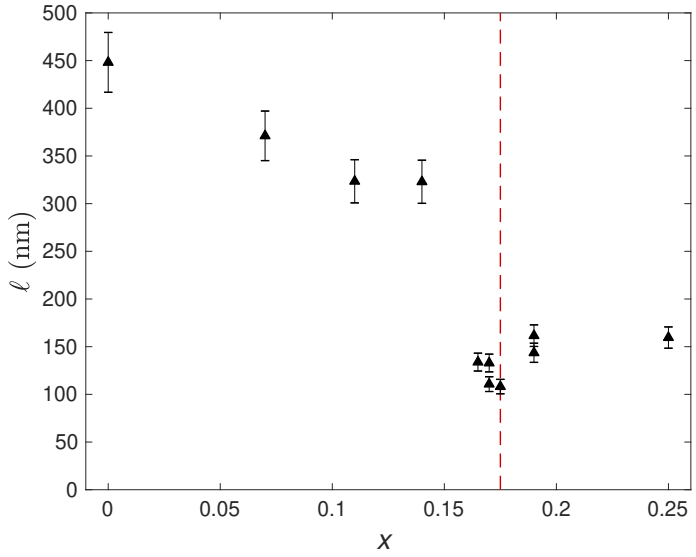


Figure 7.3: **Mean free path path in FeSe$_{1-x}$S$_x$.** The mean free path, ℓ as a function of sulphur concentration. This has been calculated using the equation $\ell = (3\pi^2/n^2)^{1/3}\hbar/(e^2\rho_0)$ where n is the charge carrier density and ρ_0 is the zero temperature resistivity, as we found previously in Ref. [219]. The mean free path we find here is far larger than the coherence length across the entire phase diagram, places all samples in the clean limit ($\ell \gg \xi$).

7.4 Single-band WHH description of $H_{c2}(T)$

In order to describe the temperature dependence of H_{c2} the single-band WHH model [78] in the absence of spin-orbit scattering terms is first considered. Fits are performed near T_c using this model in both magnetic fields orientations.

The upper critical fields when $H||c$ are linear down to lowest temperatures, and so are not captured by this model (which always flattens off at low temperatures, see figure 2.1), apart from close to T_c (where the WHH model is linear). However, the data when $H||(ab)$ can be captured relatively well using this model down to $\sim 0.3T_c$. This is shown in figure 7.2**e**, where the upper critical field scaled to T_c and the slope near T_c, $H_{c2}/[T_c|dH_{c2}/dT|_{T_c}]$, is plotted against the reduced temperature, T/T_c, for a selection of x substitutions. All samples require a different Maki parameter to describe the data near T_c. This model works well inside the nematic A phase at high temperatures, near T_c, but clearly fails at low temperatures where there is an upturn in H_{c2} and the dependence is near linear in the tetragonal state. Note that it also fails near T_c near the NEP, where there is concave curvature that can not be captured by the WHH model.

The slope in the WHH model is given by

$$\left|\frac{d(\mu_0 H_{c2})}{dT}\right|_{T_c} = \frac{1}{2e}\frac{6\pi T_c}{v_F^2 \tau}, \tag{7.1}$$

where v_{F} is the Fermi velocity, τ is the scattering time and $|dH_{c2}/dT|_{T_c}$ is defined as the slope near T_c. The upper critical field is proportional to the slope near T_c, and from either the BCS Pauli limit or the Clogston formula [76] this is also proportional to the superconducting gap, Δ. This implies that the reduced slope, divided through by T_c, is proportional to the superconducting gap, $|dH_{c2}/dT|_{T_c}/T_c \propto \Delta/T_c$ (note this also means that $\Delta/T_c \propto 1/v_F^2$). Figure 7.2**f** shows $|dH_{c2}/dT|_{T_c}/T_c$ as a function of x for the two magnetic field orientations. The reduced slope implies that the magnitude of the gap remains relatively constant inside the nematic state (for both field orientations), and drops across the NEP and into the tetragonal state. This has very similar trend to results for the gap reported previously from STM measurements, which also drop across the NEP [31]. This single-band analysis implies that the upper critical field in FeSe$_{1-x}$S$_x$ may be dominated by a single-band, but the overall nature of $H_{c2}(T)$ is not captured by any single-band model.

7.5 Describing $H_{c2}(T)$ with the two-band model

The previous section demonstrates that single-band models fail to describe the temperature dependence of the upper critical fields of FeSe$_{1-x}$S$_x$, especially at low temperatures, for all samples in both magnetic field orientations. However, the temperature dependence of upper critical fields can be modelled using a more complex two-band model in the clean limit, as detailed in Ref. [81] and section 2.1.5. This model accounts for the presence of two different bands, with inter-band scattering ($\lambda_{11}, \lambda_{22}$) and intra-band effects ($\lambda_{12}, \lambda_{21}$) and includes paramagnetic effects and allows for the presence of an FFLO inhomogeneous state at high-fields and low temperatures [81]. An FFLO state is characterized by a real-space modulation of the superconducting order parameter either in amplitude or phase such that the system energy is minimized under the constraints of a large Zeeman energy and superconducting condensation energy [91]. As the FFLO wave vector Q appears spontaneously below a certain temperature, T_{FFLO}, the instability line in $H_{c2}(T)$ at a finite Q acquires the characteristic upturn [81].

For other iron-based superconductors $s^{\pm}$ pairing is well established and so one can use the inter-band pairing limit, generally mediated by spin fluctuations, where $\lambda_{11}\lambda_{22} \ll \lambda_{12}\lambda_{21}$, as done in other iron-based compounds [61, 88–90]. First, it is necessary to eliminate the scenario of different superconducting gaps opening at different temperatures, which could significantly affect the evolution of $H_{c2}(T)$ (and would require a different model). Gaps opening at different temperatures is usually a sign of different types of superconducting phases (i.e. different symmetry). Heat capacity studies of FeSe$_{1-x}$S$_x$ show only one jump at T_c and no other jumps inside the superconducting state [32, 220]. This

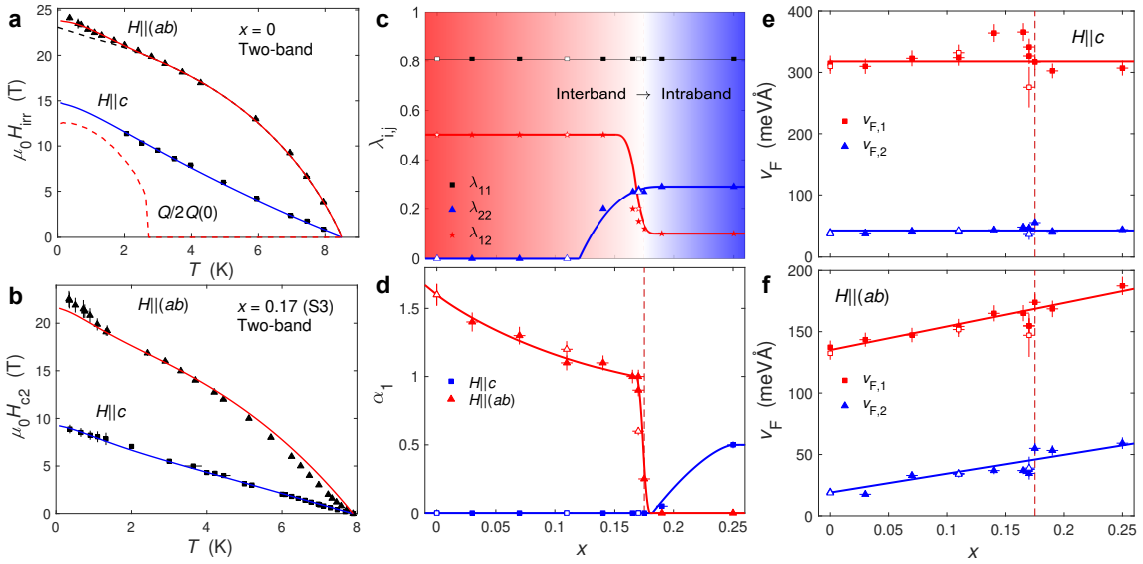


Figure 7.4: **Two-band model of the upper critical field for $FeSe_{1-x}S_x$.** **a** and **b** $H_{c2}(T)$ for both $H||c$ and $H||(ab)$ with two-band fits for $x = 0$ and $x \sim 0.17$. **c** Band coupling constants λ_{ij} from two-band fits for $H||(ab)$ across the phase diagram for $FeSe_{1-x}S_x$. **d** Two-band parameter α_1 across the phase diagram for $H||c$ (blue) and $H||(ab)$ (red). **e** and **f** Fermi velocities from the two-band model as a function of x for $H||c$ and $H||(ab)$ respectively. Here red represents the dominant band (band 1) and blue the second band. Solid lines are guides to the eye.

implies that all gaps open at a single thermodynamic transition at T_c, and therefore only H_{c2} models with a single superconducting transition temperature need be considered.

The approach taken for initial parameters in this model is the same as in chapter 5 section 5.5, but for each x substitution. To begin the two-band upper critical field description FeSe will first be considered. The starting value for α_1 of ~ 1.6 is used from the single-band model above, and a value of $\eta \sim 0.02$ is estimated from Fermi velocity ratios. $\alpha_2 = 0$ is set for these calculations, consistent with Pauli paramagnetic effects only on the dominant band. Examples of models produced for FeSe in different limits are shown in figure C.11, where it is determined that the inter-band pairing limit with a dominant band ($\lambda_{11} = 0.81$, $\lambda_{22} = 0$ and $\lambda_{12} = \lambda_{21} = 0.5$) best describe $H_{c2}(T)$.

Examples of two-band fits for $x = 0$ and $x \sim 0.17$ are shown in figures 7.4**a** and 7.4**b** respectively. Models for all samples are shown in figure C.12. For FeSe when $H||c$ the data can be described by $\lambda_{11} = 0.81$, $\lambda_{22} = 0$, $\lambda_{12} = \lambda_{21} = 0.5$, $\alpha_1 = \alpha_2 = 0$ and $\eta \sim 0.014$, where no FFLO modulation is present. This value of η is consistent with the ratio of Fermi velocities previously reported for the β and δ bands [40, 41]. When $H||(ab)$ the upper critical field is best described by $\lambda_{11} = 0.81$, $\lambda_{22} = 0$, $\lambda_{12} = \lambda_{21} = 0.5$, $\alpha_1 = 1.6$, $\alpha_2 = 0$ and $\eta = 0.04$, where an FFLO modulation is present below $\sim 0.3T_c$.

The variation of the band coupling constants $\lambda_{i,j}$ for $H||(ab)$ with x is shown in figure 7.4**c**. While λ_{11} remains constant, the second band coupling constant λ_{22} increases after $x \sim 0.11$, where the second inner hole pocket emerges [43], and increases to a constant value outside of the nematic state. The inter-band coupling λ_{12} decreases across the nematic phase transition. The behaviour when $H||c$ is similar and is shown in figure C.14.

Figure 7.4**d** shows the evolution of α_1 (the Maki parameter, or paramagnetic contribution) for both $H||c$ and $H||(ab)$. Paramagnetic contributions (α) change dramatically across the NEP for both field orientations. When $H||c$, $\alpha_1 = \alpha_2 = 0$ inside the nematic state and increases slightly outside. The low values of α here imply that paramagnetic contributions to the upper critical field are small. For $H||(ab)$, α_1 decreases from ~ 1.6 to ~ 1 inside the nematic phase before dropping to 0 across the NEP.

From the two-band model values for the Fermi velocities across the phase diagram have been evaluated, and are shown in figures 7.4**e** for $H||c$, 7.4**f** for $H||(ab)$ and C.15 (which also compares the Fermi velocities predicted from $H_{c2}(T \to 0)$ and ξ using equation 1.5). For FeSe the dominant band (1) when $H||c$ has $v_1 \sim 350\,\mathrm{meV\AA}$, which is remarkably similar to the value of $\sim 360\,\mathrm{meV\AA}$ reported for the β band from ARPES experiments [40, 41]. When $H||(ab)$ we find $v_1 \sim 140\,\mathrm{meV\AA}$, which is similar to that of the δ band reported from ARPES [40, 41] and very similar to the value of the β and γ orbits of $\sim 130\,\mathrm{meV\AA}$ from quantum oscillations [70]. When $H||c$, the Fermi velocity of the dominant band, v_1, evolves similar to T_c, with a slight drop at the NEP, while v_2 remains relatively constant. However with $H||(ab)$ both v_1 and v_2 evolve linearly, with no dramatic changes or jumps at the NEP. The different values for each magnetic field orientation suggests that the upper critical field is governed by different bands in each orientation.

A summary of all of the parameters for the two-band upper critical field model for $H||c$ and $H||(ab)$ is shown in tables 7.1 and 7.2 respectively, and figure C.14.

To describe the upturn of H_{c2} with $H||(ab)$ at low temperatures inside the nematic A state it is necessary to invoke the presence of an FFLO state [92]. The formation of an FFLO state in a system with a single cylindrical Fermi surface requires a large Zeeman energy and a critical Maki parameter of $\alpha_c = 4.76$ [91], compared to $\alpha_c = 1.8$ for a three-dimensional Fermi surface [81]. These critical values of α_c will be different in multi-band systems. $FeSe_{1-x}S_x$ has a complex Fermi surface with two-dimensional cylindrical, highly warped sheets and small Fermi energies (shallow bands). Together, with relatively large values of α (~ 1.6), this could create the conditions for the emergence of an FFLO state [81]. An FFLO state can be realized in very clean materials with weak scattering of quasiparticles and it generally manifests as change in slope of the upper critical field at low temperatures [81]. The two-band model analysis show that a robust FFLO state with large

Table 7.1: Two-band parameters for different sulphur substitutions, x, for $H||c$. The additions of T1 to the x value indicate samples measured using torque.

x	λ_{11}	λ_{22}	λ_{12}	α_1	α_2	v_1 (meVÅ)	v_2 (meVÅ)	η
0	0.81	0	0.5	0	0	315(14)	39(4)	~ 0.01
0 (T1)	0.81	0	0.5	0	0	310(14)	38(3)	~ 0.01
0.03	0.81	0	0.5	0	0	314(14)	40(4)	~ 0.01
0.07	0.81	0	0.5	0	0	323(15)	42(4)	~ 0.01
0.11	0.81	0	0.5	0	0	324(15)	42(4)	~ 0.01
0.11 (T1)	0.81	0	0.5	0	0	332(16)	43(4)	~ 0.012
0.14	0.81	0.2	0.5	0	0	364(15)	43(4)	~ 0.014
0.165	0.81	0.25	0.1	0	0	367(15)	48(4)	~ 0.01
0.17 (S2)	0.81	0.25	0.1	0	0	341(14)	45(4)	~ 0.01
0.17 (S3)	0.81	0.15	0.3	0	0	327(13)	46(4)	~ 0.015
0.17 (T1)	0.81	0.25	0.2	0	0	276(33)	37(7)	~ 0.03
0.175	0.81	0.27	0.1	0	0	317(13)	54(5)	~ 0.03
0.19	0.81	0.27	0.1	0.1	0	303(12)	41(3)	~ 0.018
0.25	0.81	0.29	0.1	0.5	0	307(12)	43(4)	~ 0.02

Table 7.2: Two-band parameters for different sulphur substitutions, x, for $H||(ab)$. The additions of T1 to the x value indicate samples measured using torque.

x	λ_{11}	λ_{22}	λ_{12}	α_1	α_2	v_1 (meVÅ)	v_2 (meVÅ)	η
0	0.81	0	0.5	1.6	0	137(6)	19(2)	~ 0.02
0 (T1)	0.81	0	0.5	1.6	0	132(6)	19(2)	~ 0.02
0.03	0.81	0	0.5	1.4	0	143(6)	18(2)	~ 0.01
0.07	0.81	0	0.5	1.3	0	147(6)	33(3)	~ 0.05
0.11	0.81	0	0.5	1.1	0	154(6)	34(3)	~ 0.05
0.11 (T1)	0.81	0	0.5	1.2	0	152(6)	34(3)	~ 0.05
0.14	0.81	0.2	0.5	1.1	0	165(7)	37(3)	~ 0.05
0.165	0.81	0.25	0.1	1.0	0	166(7)	37(3)	~ 0.01
0.17 (S2)	0.81	0.25	0.1	1.0	0	155(6)	38(3)	~ 0.03
0.17 (S3)	0.81	0.15	0.3	0.8	0	156(6)	35(3)	~ 0.01
0.17 (T1)	0.81	0.25	0.2	0.6	0	147(17)	39(8)	~ 0.1
0.175	0.81	0.27	0.1	0.3	0	174(7)	55(4)	~ 0.2
0.19	0.81	0.27	0.1	0	0	169(7)	53(4)	~ 0.1
0.25	0.81	0.29	0.1	0	0	187(8)	59(5)	~ 0.1

Q emerges in FeSe with $H||(ab)$, where α_1 is largest. An FFLO state has been reported recently from upper critical field studies of FeSe in Ref. [221] from resistivity and heat capacity studies at a similar temperature (~ 2.5 K) to the results reported here. Here both T_{FFLO} and Q_{max} are largest, and decrease with increasing x up to $x \sim 0.11$, where the FFLO modulation vanishes, corresponding to a critical value of $\alpha_1 \sim 1.1$. Figure 7.5**a** shows the temperature at which the FFLO state emerges, T_{FFLO}, as a function of x, and the colour corresponds to the magnitude of the FFLO Q modulation in the FFLO state. The FFLO modulation only exists in the nematic A region, before the second inner hole-band emerges. This also correlates with changes in the electronic behaviour between the nematic A and nematic B phases observed in chapter 6 and Ref. [219]. A spin-polarized/split Fermi surface in a magnetic field would provide the necessary conditions for the FFLO state to appear [81]. An FFLO state is most likely to occur on a band close to the Fermi level, of which there are a number of candidates in FeSe$_{1-x}$S$_x$. The state could emerge on either the hole (α) pocket, or the electron bands, all of which have small Fermi energies and are close to the Fermi level (< 10 meV at 10 K) [28, 40].

7.6 Discussion

This section will cover the implications of the results and analysis presented thus far in this chapter. In particular, it will focus on the changes that occur with sulphur substitution in FeSe$_{1-x}$S$_x$, the implications that this has for superconductivity and changes in the electronic structure that could drive the changes observed in the upper critical fields.

7.6.1 Suppression of the upper critical fields

Through the NEP the shape of the $H_{\mathrm{c2}}(T)$ curves change. When $H||c$ the curves become less linear and a small upturn at low temperatures starts to emerge, particularly in the tetragonal state for $x = 0.25$. The low temperature upturn with $H||c$ can be described by increasing λ_{22} and decreasing λ_{12} across the NEP. This essentially corresponds to 'turning on' intra-band interactions on the second band and reducing the inter-band coupling between the two bands. When $H||(ab)$ there is less convex curvature near T_{c}, corresponding to a smaller Maki parameter, and the low temperature upturn appears to increase. The same evolution of the λ_{ij} parameters describes the $H||(ab)$ evolution of the upper critical field with increasing x, with $\alpha_{1,ab}$ also decreasing towards zero. This captures the low temperature upturn when $H||(ab)$ as well, and no FFLO modulation is necessary (as is expected as $\alpha \to 0$).

It is worth noting that the two-band model used here fails to describe some of the data from $x \sim 0.14 - 0.18$ with $H||(ab)$ where the curvature changes both near T_c and again at lower temperatures. Near T_c and inside the nematic A phase the curvature of $H_{c2}(T)$ is convex (like for all simulations of the WHH model in figure 2.1). For $x \sim 0.14 - 0.18$ and $H||(ab)$ the curvature near T_c changes and becomes concave (such as the $\eta = 10$ case in figure 2.3**c** and the $\eta = 200$ case in figure 2.2). However, the $H_{c2}^{ab}(T)$ data $x \sim 0.14 - 0.18$ also show an upturn at low temperatures, which cannot be accounted for using these high η values. Thus, different values of η can be used to describe the data either near T_c, or in the low temperature regime, but not both. In this chapter the two-band fitting focuses on capturing the low temperature data. Capturing the changes of curvature in $H_{c2}^{ab}(T)$ both near T_c and at low temperature for $x \sim 0.14 - 0.18$ is a possible focus for future work. It is likely to require a three-band model of the upper critical field in the clean limit which includes paramagnetic effects, which is beyond the scope of the work presented here (and, to the best knowledge of the author, is not available in literature).

Outside of the nematic phase the shape of $H_{c2}(T)$ changes for both field orientations, and it cannot be described in the inter-band pairing limit. For $x \sim 0.25$ the temperature dependence of the upper critical field is best described by $\lambda_{11} = 0.81$, $\lambda_{22} = 0.29$ and $\lambda_{12} = \lambda_{21} = 0.1$ for both field orientations, similar to MgB_2 [186]. For $H||c$ we find $\alpha_1 \sim 0.5$ and $\eta \sim 0.025$, and for $H||(ab)$ $\alpha_1 = 0$ and $\eta \sim 0.1$, with the absence of an FFLO modulation in both orientations. These parameters are consistent with s^{++} Cooper pairing symmetry.

It has been shown that the upper critical field should be lower for s^{++} than $s^{\pm}$ pairing (if all other parameters are fixed) [81], which is consistent with the reduction in H_{c2}/T_c observed across the nematic end point. It should be noted that from the band coupling parameters presented here, one can only establish if inter-band or intra-band coupling dominates, although a two-band intra-band case strongly infers s^{++} pairing. However, neutron scattering data on FeSe indicates a spin-fluctuation mediated sign changing pairing symmetry, $s^{\pm}$, over orbital fluctuation mediated non-sign changing symmetry [44]. At the other end of the phase diagram, for FeS ($x = 1$) the pairing symmetry is less clear but appears to be dominated by an anisotropic s-wave gap [222]. Hence, the data presented here are consistent with the pairing symmetry changing from $s^{\pm}$ to s^{++} across the nematic end point. This is also in agreement with previous STM results [31], where they observed a suppression of the superconducting gap across the NEP. This change in pairing across the nematic end point could then account for the changes observed in other superconductivity parameters, such as the anisotropy, T_c and the coherence lengths.

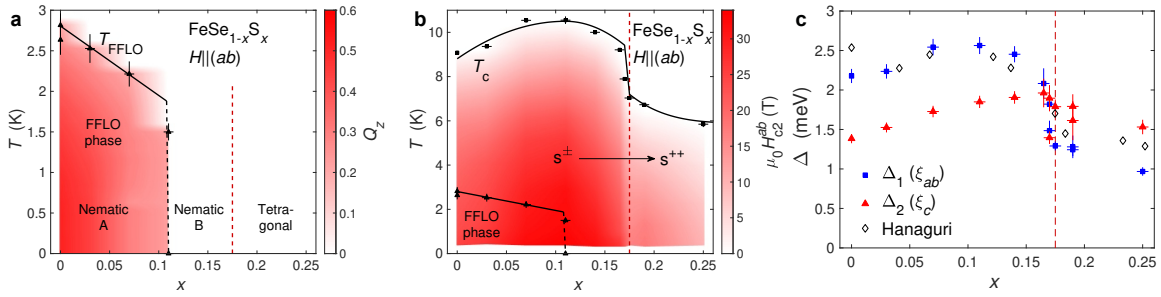


Figure 7.5: **Superconductivity phase diagrams for FeSe$_{1-x}$S$_x$. a** Temperature against x doping phase diagram, where colour shows the magnitude of the FFLO Q vector when $H||(ab)$. The transition temperature of the FFLO state, T_{FFLO} is shown as black squares, and black lines are guides to the eye. **b** Temperature against x phase diagram of superconductivity in FeSe$_{1-x}$S$_x$. The colour represents the magnitude of H_{c2} when $H||(ab)$. Black squares represent T_{c} and black triangles are T_{FFLO}. **c** Superconducting gaps, Δ, as a function of sulphur concentration. The gaps are calculated from the two different coherence lengths and Fermi velocities from the two-band model. Results from Ref. [31] are also included. Black lines are guides to the eye, and the red dashed lines in all panels represents the nematic end point at $x \sim 0.175$.

Furthermore, it is worth noting that the single-band model (in the clean limit) which includes the FFLO modulation cannot account for the shape of $H_{\mathrm{c2}}(T)$ in either orientation for any samples [81, 181]. For $H||(ab)$, where the low temperature upturn is observed in FeSe, the value of α needed to describe the $H^{ab}_{\mathrm{c2}}(T)$ data near T_{c} for FeSe is ~ 1.6, which is below the critical value for a single elliptical Fermi sheet of $\alpha_{\mathrm{c}} \sim 1.8$ [81], above which the FFLO state would start to emerge. Thus, the single-band model cannot capture the low-temperature up-turn.

Figure 7.5**b** summarises the findings from the upper critical fields in FeSe$_{1-x}$S$_x$. Colour indicates the magnitude of H_{c2} when $H||(ab)$, and T_{c} and T_{FFLO} are shown. From this, it is clear that H_{c2} is suppressed across the NEP and the nature of superconductivity inside the nematic state is different to that of the tetragonal state. The evolution of the magnitude of H_{c2} is strikingly similar to magnitude of low frequency spin fluctuations reported from nuclear magnetic resonance (NMR) studies [45], which will be discussed in more detail in section 7.6.2.

7.6.2 Lifshitz transition at the NEP and the role of spin fluctuations

The deviation of H_{c2} from the single-band model is most pronounced near the NEP, especially for $H||(ab)$. However, the upturn at low temperatures here cannot be described using an FFLO modulation (in either a two-band or a single-band model) as the paramagnetic effects are not sufficiently strong. Instead, here the upturn can be described with the variation

of the parameter η and the Fermi velocities (see figures C.14**d** and C.15). The changes here could be linked to the Lifshitz transition reported at the NEP previously [41, 43], which could cause extreme changes in the Fermi velocities (since $v_{\mathrm{F}} \propto dE_{\mathrm{F}}/dk_{\mathrm{F}}$ [68, 118]).

The Lifshitz transition in FeSe$_{1-x}$S$_x$ occurs when the hole band splits at Γ point [41, 43]. This could mean the loss of the inter-band pairing between the δ hole band and one of the electron pockets. This could account for the changes in the λ_{ij} parameters, as well as the changes in η, that are observed in the two-band analysis and the suppression of H_{c2}.

Low frequency anti-ferromagnetic spin fluctuations are present inside the nematic state and their magnitude is severely reduced across the NEP [44, 45, 223]. The magnitude of the spin fluctuations correlate well with T_{c} and $H_{\mathrm{c}2}$ in both orientations. The Q vector associated with spin fluctuations between different bands (electron and hole) could provide the coupling necessary for inter-band pairing in this system. The reduction in the spin fluctuations across the NEP (and in the tetragonal phase) could therefore account for the suppression of H_{c2} and the change in pairing from $s^{\pm}$ to s^{++} across the NEP. It is worth noting that high frequency spin fluctuations have been detected in FeSe outside of the nematic state [39], but it appears to be the low frequency spin fluctuations that contribute to superconductivity.

7.6.3 Superconducting gap

In a clean system with large Fermi velocities the superconducting gap is given by

$$\Delta = \frac{1.76\hbar v_{\mathrm{F}}}{2\pi\xi} \tag{7.2}$$

where v_{F} is the Fermi velocity and ξ is the coherence length. From this two superconducting gaps are calculated using $\Delta_1 = \hbar v_{1,c}/(\pi\xi_{ab})$ and $\Delta_2 = \hbar v_{1,ab}/(\pi\xi_c)$ where $v_{1,c}$ and $v_{1,ab}$ are the velocities from the dominant band in the two-band model presented in this chapter for $H||c$ and $H||(ab)$, respectively. The results of this, along with the gap reported in Ref. [31], are shown as a function of x in figure 7.5 **c**. The values for Δ_1 are in good agreement with those in Ref. [31] inside the nematic phase, and show a drop across the NEP. The values Δ_1 and Δ_2 reported here for FeSe are very similar to those of $2.3\,$meV and $1.5\,$meV reported previously in Ref. [216]. The second gap Δ_2 seems to be largest near the NEP, but remains relatively constant when compared to Δ_1. The first gap, Δ_1, follows the same evolution as T_{c} and the magnitude of $H_{\mathrm{c}2}(0)$ in both field orientations. This provides further evidence for the change in the nature of superconductivity across the NEP. The agreement with previous results supports the validity of the results and arguments presented here.

7.7 Summary

In this chapter the upper critical fields of FeSe$_{1-x}$S$_x$ have been mapped for $0 \leq x \leq 0.25$ in two magnetic field orientations, $H||c$ and $H||(ab)$, using electrical transport and torque magnetometry. $H_{c2}(T)$ for $H||c$ is surprisingly linear, which is unusual for superconductors. For $H||(ab)$ there is an up-turn in $H_{c2}(T)$ at low temperatures inside the nematic state. A two-band model of the upper critical field in the clean limit is necessary to describe the evolution of $H_{c2}(T)$ for all x substitutions. The up-turn of $H_{c2}(T)$ for $H||(ab)$ is consistent with the manifestation of an FFLO state for $x \leq 0.11$, inside the nematic A phase. The upper critical fields are suppressed across the NEP and there is a change from $s^{\pm}$ to s^{++} Cooper pairing, which is supported by the change in the two-band model parameters. The superconducting transition temperature, coherence lengths and anisotropy also change dramatically through the NEP, giving further evidence of changes in the nature of superconductivity across this transition. The larger T_c and H_{c2} correlate with stronger spin-fluctuations (measured using NMR [45]). The band coupling constants from the two-band analysis show that inter-band coupling is strong inside the nematic state, which could be moderated by the spin-fluctuations. The reduction of the spin-fluctuations outside of the nematic state drives the system to a s^{++} state where H_{c2}/T_c is suppressed. Finally, an enhancement of the width of the superconducting transition is observed in electrical transport near the NEP, which could be attributed to an increase in superconducting fluctuations.

Chapter 8

Persistent two-dimensional superconducting fluctuations across the nematic end point in $FeSe_{1-x}S_x$

In this final chapter the role of fluctuations of the superconducting state above the transition temperature, T_c, will be assessed across the phase diagram of $FeSe_{1-x}S_x$. Four samples of $FeSe_{1-x}S_x$ with different sulphur substitutions, $x = 0.03$, 0.165, 0.17 and 0.25, are studied in detail by extracting the in-plane transverse-field magnetoresistance from electrical transport in narrow temperature intervals, just above the superconducting transition. Multiple single crystals were screened using the temperature dependence of their resistivity in zero field, and the highest quality ones used, with the largest residual resistivity ratios, small ρ_0 and sharp superconducting transitions. Field sweeps have been performed in small intervals above the superconducting transition. Both two-band and $\rho \propto H^{\delta}$ (as established in chapter 6) models are used to fit the high-field region, which has previously been established to describe the in-plane magnetic field ($H||c$) data well (see chapter 6 and Ref. [219]). From the difference between these models and the resistivity data the excess conductivity has been extracted, which is assigned to superconducting fluctuations above T_c. The fluctuations can be described by the two-dimensional AL formula both inside and outside of the nematic phase, and seem to both show fluctuations up to $\sim 2.4T_c$. At the NEP and near T_c the magnitude of the fluctuating conductivity increases above the 2D limit. The enhanced SCF's here may be linked to the strong nematic fluctuations at the NEP [199]. Finally, the conductivity of the SCF's can be scaled in both temperature and magnetic field onto a single 2D curve for all sulphur substitutions tested, providing further evidence for the persistence of 2D fluctuations in $FeSe_{1-x}S_x$ over a large temperature and magnetic field range and the entire phase diagram.

This chapter will begin by recapping the important details of superconducting fluctuations from section 2.3, where they arise and why one might expect to find them in FeSe. Different methods of extracting any excess conductivity that may arise from superconducting fluctuations will then be covered, and which models apply in different parts of the phase diagram of $FeSe_{1-x}S_x$. Next, the dimensionality of the superconducting fluctuations will be assessed with both magnetic field and temperature. Finally, the broader implications of these findings on $FeSe_{1-x}S_x$ will be discussed, with a particular emphasis on the inferences that can be made about superconductivity and linking the results in this chapter to those on the upper critical fields in $FeSe_{1-x}S_x$ in chapter 7.

8.1 Introduction

Fluctuations of the superconducting state originate from thermal effects that cause spatial variations of the superconducting order parameter, ψ. This essentially means that even above T_c, $\langle\psi^2\rangle \neq 0$, which arises from Gaussian amplitude fluctuations. The physical origin of this is Cooper pairs forming above the bulk transition temperature, sometimes referred to as preformed Cooper pairs. These effects are not long-ranged above T_c and the scattering time of the preformed Cooper pairs is very small, generally much shorter than the scattering time of the material (τ). It has also been shown that phase fluctuations of the superconducting order parameter (which is complex in nature) in low carrier density, and also low superfluid density, can significantly enhance any superconducting fluctuations present [224]. Superconducting fluctuations above T_c can affect a number of parameters. For example, they cause diamagnetism above the transition temperature (where materials are usually either paramagnetic or antiferromagnetic) and changes in the heat capacity. However, this chapter will focus on another property that is changed by superconducting fluctuations, the excess conductivity.

Any superconducting fluctuations present can provide significant details about the superconducting state, such as the dimensionality and important length scales. The manifestation of superconducting fluctuations as excess conductivity is covered in more detail in section 2.3. The fluctuations also provide a link between the superconducting state and the normal state, of which a good understanding is necessary to extract them (which will be covered in more detail later in this chapter in section 8.3). Superconducting fluctuations near T_c can influence the tailing and broadening of resistive transitions. Thus, by assessing the impact of superconducting fluctuations, one can unravel further details about broadening of transitions with both temperature and magnetic field, for example, near the nematic end point in $FeSe_{1-x}S_x$.

The origin of certain characteristics of superconductivity in the iron-based superconductors, such as large and anisotropic upper critical fields (compared to their T_c values), still remain elusive. There are apparent changes in the electrical resistivity, conductivity and other thermodynamic properties at temperatures above the superconducting transition temperature, T_c. The large upper critical fields, high anisotropy and short coherence lengths in these systems can enhance the effect of superconducting fluctuations, even above T_c. These have been extensively studied in many cuprate superconductors, where the fluctuations are generally found to be 3-dimensional (3D) and only persist to temperatures just above T_c [106, 112, 113, 225], usually $\sim 1.1T_c$. It has been proposed that preformed Cooper pairs in cuprate superconductors may even be responsible for the anomalous resistivity in the 'pseudogap' phase[1] [226–228].

Superconducting fluctuations (SCF's) have been studied to a lesser extent in iron-based superconductors, but were observed previously [229] and have been used to describe an excess of conductivity at low temperatures, just above the superconducting state. These fluctuations are caused by Cooper pairing above T_c, but where the scattering time is very short and the mean path length of a pair is less than that of a single Fermi wave vector. This means these preformed Cooper pairs should cause an excess conductivity, but the resistivity will still be finite and greater than zero [102].

An iron-based superconductor one might consider studying for fluctuation effects is FeSe. Details about FeSe and $FeSe_{1-x}S_x$ are covered in section 1.6.1 and previous chapters. The nature of superconducting fluctuations in FeSe has been consider previously, to a certain extent. First, FeSe has been proposed to be near a BCS-BEC (Bose-Einstein Condensate) crossover [36, 228, 230]. BCS is characterised by weakly coupled fermions pair-condensing to form a condensate wavefunction, while in a BEC the attraction is so strong the pairs condense and give a pseudo-particle which is bosonic. The physics of this crossover is described by two length scales, the coherence length or average pair size, ξ_{pair}, and the mean inter-particle distance, $1/k_F$, where k_F is the Fermi wavevector. The pair size is large in the BCS regime which leads to $k_F\xi_{\text{pair}} \gg 1$, while the inter-particle distance is very small for a BEC which gives $k_F\xi_{\text{pair}} \ll 1$. This leads to a natural BCS-BEC crossover regime characterised by $\xi_{\text{pair}} \sim 1$. This crossover can also be characterised using the superconducting gap and the Fermi energy (E_F), where one then expects $\Delta/E_F \sim 1$

[1]The origin of the pseudogap phase in cuprates is still a widely debated topic. Different origins have been proposed including charge density wave order and proximity to magnetism (and even antiferromagnetic critical points). It is unlikely that superconducting fluctuations are the cause of the pseudogap phase as the transition temperature associated with it is significantly higher than T_c and far above the $\sim 1.1T_c$ reported for the extend of superconducting fluctuations. However, the fluctuations would influence the conductivity and resistivity, making the pseudogap in the cuprates more difficult to disentangle.

[228]. For FeSe in the previous chapter superconducting gaps of $\Delta_1 = 2.2(1)$ meV and $\Delta_2 = 1.4(1)$ meV were established, similar to $\Delta_1 \sim 2.3$ meV and $\Delta_2 \sim 1.4$ meV [216], and $\Delta \sim 2.5$ [31] reported previously from STM experiments. Fermi energies of ~ 3 meV and ~ 10 meV have been reported on the hole and electron bands respectively [36, 40, 43], which leads to a range of the ratio Δ/E_{F} between ~ 0.15 and ~ 0.8. This latter value (for the Fermi energy of the hole band and the larger gap, which is likely to open on the hole band, established by comparing velocities from the studies of the upper critical fields in chapter 7 and ARPES experiments) places FeSe in the BCS-BEC crossover regime[2]. In this regime it is expected that strong fluctuations of the superconducting state will be present.

There have already been a number of studies that probe superconducting fluctuations in FeSe. Ref. [37] explores the regime around T_{c} using diamagnetism and NMR. This study shows a strong diamagnetic signal in high-magnetic fields above T_{c} and an enhancement of $\Delta(1/T_1T)$ (after the background has been subtracted) from NMR, both up to temperatures of ~ 20 K (or $\sim 2.2T_{\mathrm{c}}$) and consistent with superconducting fluctuations. They assign this regime below ~ 20 K to preformed Cooper pairs. Refs. [36] and [37] also observe a peak in the temperature dependence of the magnetoresistance at ~ 14 K for FeSe in magnetic fields up to 16 T, and the downturn below ~ 14 K they attribute to superconducting fluctuations. This is at the same temperature as was observed in chapter 6 (see figure 6.2), but since the peak persists up to 34 T (well above H_{c2} for $H||c$) it is unlikely that the downturn is due to superconducting fluctuations. Nuclear magnetic resonance (NMR) experiments also detect an anomalous signal in the selenium relaxation rate $1/T_1T$ below ~ 15 K at zero-field for FeSe [38] (also at a similar temperature to the peak in magnetoresistance). The temperature of this decreases with applied field, and the authors assign it to superconducting fluctuations in a pseudogap phase of FeSe. Another study using torque magnetometry (which is proportional to the magnetisation, and so probes the diamagnetic response) also detect enhanced diamagnetism in field above T_{c}, although in a regime closer to T_{c} [231]. In this study they however observe that the onset temperature of fluctuations increases with applied field, which seems counterintuitive. Ref. [231] also extract an excess conductivity in the vicinity of T_{c} for FeSe in zero field from a linear fit to the resistivity, but given the complexity of scattering discussed in chapter 6, this is not a reliable method. The single crystals used in Ref. [231] are also of lower quality than the ones that will be presented later in this chapter, with a low $RRR \sim 13$ (compared with the ~ 30 in chapter 6). Nonetheless, there is literature suggesting that magnetisation, torque and NMR all show signals of superconducting fluctuations in FeSe.

[2]Or, at least one of its bands.

The work in this chapter will not only look at FeSe (in fact, the lowest sulphur concentration that will be presented is $x = 0.03$ in $FeSe_{1-x}S_x$), so it is worth considering what one might expect upon isoelectronic sulphur substitution. T_c remains relatively constant inside the nematic phase of $FeSe_{1-x}S_x$, with a small increase around $x \sim 0.1$, drops sharply at the NEP and continues decreasing further into the tetragonal phase. The upper critical field in the zero temperature limit, $\mu_0 H_{c2}(T \to 0)$, (and also $\mu_0 H_{c2}(T \sim T_c)$, the upper critical field near T_c) also shows a similar x dependence. The larger superconducting gap behaves similar to T_c, while the second gap remains relatively constant (see chapter 7 figure 7.5**c**). Generally, the coherence length(s) increase with further x substitution (see chapter 7 figure 7.2**b**). This coincides with the density of states (i.e. number of charge carriers) and the Fermi energy E_F of each band increasing with x substitution, which means that the ratio Δ/E_F decreases away from ~ 0.8 (for FeSe) with increasing x. Thus, the system is expected to move away from the BCS-BEC crossover regime with sulphur substitution, which could reduce the magnitude of any superconducting fluctuations. Sulphur substitution decreases the lattice parameters and makes the Fermi surface of $FeSe_{1-x}S_x$ more three-dimensional (the cylinders warp more, giving a greater z dependence), which may be expected to manifest in the fluctuations as well. However, in chapter 7 figure 7.2**d** the superconducting anisotropy (γ) increases across the NEP, suggesting that superconductivity becomes more two-dimensional. Studying the variation of any superconducting fluctuations across the NEP may then help to unravel this problem. This may also highlight any further differences in superconductivity in the nematic and tetragonal states.

8.2 Experimental details

In-plane electrical measurements were performed in a Quantum Design PPMS in DC magnetic fields up to 16 T. High quality samples with large residual resistivity ratios (RRR) and sharp superconducting transitions were used (see figure 8.1). Magnetic fields were always applied parallel to the c-axis, $H||c$. Resistivity was measured using the low-frequency five-probe technique with $I \perp c$ and the ρ_{xx} and ρ_{xy} contributions were obtained by (anti)symmetrising the data taken in positive and negative magnetic fields. Good electrical contacts ($< 1\,\Omega$) were achieved with indium solder. To avoid heating electrical currents ≤ 1 mA were used. To assure a homogeneous current flow in the samples, current leads were attached to the side faces of the samples. The sulphur concentrations of these samples has been established in a previous study [43], and the nematic transition temperature, T_s, is also used as an indication of concentration inside the nematic state. Note that the $x \sim 0.17$

single crystal presented in this chapter is the same sample as $x \sim 0.17(\mathrm{S3})$ presented in chapter 7.

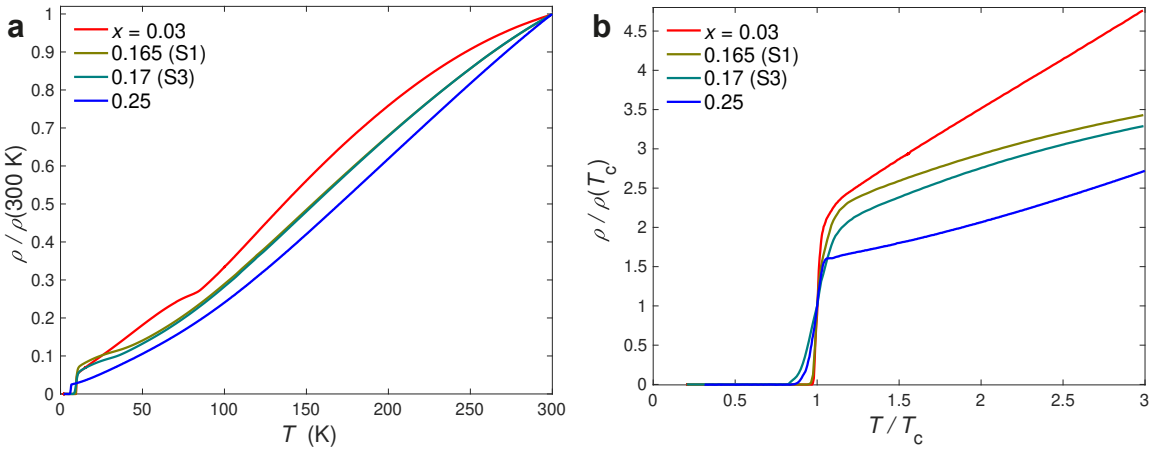


Figure 8.1: **Scaled resistivity against temperature for $FeSe_{1-x}S_x$. a** Resistivity scaled to the room temperature value (300 K) against temperature for $x = 0.03$, 0.165, $0.17(\mathrm{S3})$ and 0.25. **b** Resistivity against temperature, both scaled to their respective values at T_c. Here T_c is defined as the peak in the derivative $d\rho/dT$ (the same as the midpoint definition presented in chapter 3, Experimental Methods, in figure 3.4**b**).

8.3 Extracting the excess conductivity

Figure 8.1**a** shows the resistivity, scaled to the room temperature value (at 300 K), for the four single crystals that will be the focus of experiments in this chapter. The large RRR ($\sim 17 - 44$) indicates the high quality of the single crystals. Figure 8.1**b** shows the resistivity scaled to it's value at T_c against the reduced temperature, T/T_c for the four single crystals. Here, and throughout this chapter, T_c is defined as the midpoint of the transition, see section 3.3 and figure 3.4. This shows the sharp and smooth transitions into the superconducting state. The reduced temperature scale in figure 8.1**b** is the approximate range over which one might expect to find superconducting fluctuations. A simple approach (which has been done before in Ref. [231] for example) to fitting the temperature dependence of the resistivity is to use a function such as $\rho = \rho_0 + AT^\gamma$ (like in chapter 6), and extract the excess conductivity by subtracting the resistivity data from this expression. However, in $FeSe_{1-x}S_x$ there is not a well established model of the normal state (as explored in chapter 6) and the scattering seems to be more complicated than simple models assume. This makes extracting any excess conductivity alone a poor approach. It is also worth noting that, because of the variation in the exponent γ reported in chapter 6 with both temperature and x, the magnitude of any superconducting fluctuations will be dependent

on the temperature interval chosen to fit, giving results that will not be consistent between different x substitutions.

Instead, a different approach is used. Any superconducting fluctuations that arise from amplitude fluctuations of the order parameter (see section 2.3) will be suppressed in a magnetic field. Thus, performing magnetic field sweeps at constant temperature will suppress any superconducting fluctuations and the high-field regime can be fitted with a model that describes the normal state magnetoresistivity. Symmetrized transverse-field resistivity ρ_{xx} against applied magnetic field (for $H||c$) at constant temperature is shown for different single crystals of $FeSe_{1-x}S_x$, with $0.03 \leq x \leq 0.25$, in figure 8.2**a**-**d**, as labelled. Magnetoresistivity data has been taken in small temperature intervals above the superconducting transition for each single crystal, which then give a fine scale for analysing any changes that occur as a function of temperature.

Next, it is important to establish a model of the normal state magnetoresistivity at high fields from which superconducting fluctuations can be extracted. Thankfully, this was a large focus of chapter 6 where a good understanding of the magnetoresistivity was established. This work determined that a single-band H^2 model cannot describe the magnetoresistivity inside the nematic phase. Instead, two different models are used here for each single crystal to fit the high-field part of the magnetoresistivity (a 2 T window was used for all data, from $14 - 16$ T). First, the in-plane transverse-field resistivity data, $\rho_{xx}(H)$, is described using the two-band form in equations 1.47-1.48. This model has been derived previously and has been used on other superconductors, including cuprate and iron-based materials, including FeSe [229, 232]. For this approach the normal state resistivity is denoted as ρ_{2BF}, and it is used for all single crystals of $FeSe_{1-x}S_x$ in this study. Second, the in-plane transverse-field resistivity is described using the form $\rho_{xx}(H) = \rho_{H=0} + A(\mu_0 H)^{\delta}$ and the high-field exponents established in chapter 6. This exact exponent used varies slightly between different x compositions, depending on which part of the phase diagram they are in. For $x = 0.03$ the exponent of $\delta = 1.55$ is used, which dominates inside the nematic phase. For $x = 0.165$ and $x = 0.17$, near the NEP, δ is left as a fitting parameter since these samples have a T_s near the regime that superconducting fluctuations may be present, and so the exponent will evolve with temperature. For each field sweep at different temperatures, the exponent δ is first evaluated using the log-log approach described in section 6.3.2 in the high-field limit. For $x = 0.25$ an exponent of $\delta = 2$ (magnetoresistivity that is quadratic in magnetic field) is used, characteristic of the tetragonal phase of $FeSe_{1-x}S_x$ (see figure 6.7**c**). For this variable exponent approach the normal state resistivity is denoted as ρ_{δ}.

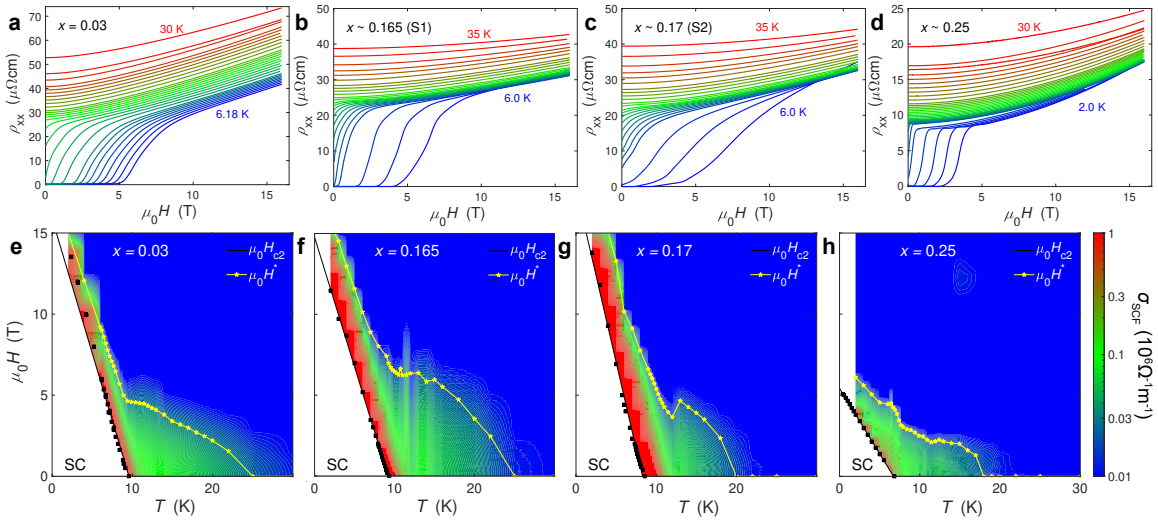


Figure 8.2: **a**-**d** symmetrized resistivity against magnetic field at constant temperature for samples with $x = 0.03$, ~ 0.165, ~ 0.17 and 0.25 respectively. The colour of different curves represent the temperature, as labelled in each panel. **e**-**h** temperature-field phase diagrams of the SCF's for samples with $x = 0.03$, 0.165, 0.17 and 0.25 respectively. The magnitude of the SCF's are shown on the colour scales. The black points and line represent the upper critical field when $H||c$. Yellow stars show the point at which the magnitude of the SCF's become small (close to zero, $\sim 2 \times 10^3\,\Omega^{-1}\mathrm{m}^{-1}$ for all samples). This can be interpreted as the boundary of the fluctuating phase.

Using these models of the normal state the excess conductivity can be extracted. This is done using a parallel resistor model, or two-fluid model using the equation

$$\Delta\sigma = \rho_{\mathrm{xx}}^{-1} - \rho_{\mathrm{n}}^{-1}, \tag{8.1}$$

where ρ_{xx} is the raw data in figures 8.2**a**-**d** and ρ_{n} is the normal state resistivity, either ρ_{2BF} or ρ_δ, depending on which model has been used. This excess conductivity is assigned to superconducting fluctuations, and hence unite $\sigma_{\mathrm{SCF}} = \Delta\sigma$.

Before discussing the excess conductivity and superconducting fluctuations in great detail, it is first worth commenting on the two models of the normal state used for each single crystal. The evolution of the exponent δ for the two samples near the nematic end point is shown in figures D.2**a** and D.2**b** for $x \sim 0.165$ and $x \sim 0.17$ respectively. δ decreases for both samples with decreasing temperature, characteristic of x compositions just inside the nematic phase (see figure 6.7**c**). This suggests that both of these samples lie just inside the nematic phase, which agrees with the T_{s} extraction from $\rho(T)$ in zero field for each sample (giving $T_{\mathrm{s}} \sim 30\,\mathrm{K}$ and $T_{\mathrm{s}} \sim 24\,\mathrm{K}$ for $x \sim 0.165$ and $x \sim 0.17$ respectively). It is worth noting that the two-band model collapses back to a H^2 dependence for $\beta = 0$. Thus for $x = 0.25$ when fitting with the two-band model one might expect that $\beta \to 0$,

as the magnetoresistivity is quadratic with field. This is what is found from the two-band analysis for $x = 0.25$, $\beta \sim 0$ for all temperatures.

Figure 8.2**e**-**h** shows the excess conductivity in the temperature-field plane on a logarithmic colour scale for $x = 0.03$, ~ 0.165, ~ 0.17 and 0.25 respectively. For these figure panels the excess conductivity has been calculated using the two-band model as the normal state, ρ_{2BF}, for all x compositions. Note that using ρ_δ as the normal state gives very similar results. The temperature and magnetic field range has been kept the same for all samples to give a better comparison of the extent of the excess conductivity with increasing x substitution in $FeSe_{1-x}S_x$. The excess conductivity is assigned to superconducting fluctuations, and is displayed on a logarithmic scale to better represent the data. The $H_{c2}(T)$ (upper critical field) line shown for each sample is taken at the offset of the transition from temperature sweeps at constant field and magnetic field sweeps at constant temperature (see chapter 7 for more details). Red regions of these plots are where the resistivity drops sharply approaching the superconducting state, and the data is dominated by vortex liquid phase in magnetic field. The regime of excess conductivity is clearly linked to the superconducting state, and decreases as the temperature is increased away from T_{c} for all samples. The $\mu_0 H^*$ points are defined as the point at which the magnitude of $\sigma_{\mathrm{SCF}}(H)$ becomes near zero, taken as 2% of the 2D value at each respective temperature (see later) for all x substitutions. This is also essentially 2% of the zero field value for the excess conductivity as a function of the magnetic field at each temperature while $T \lesssim 2.4T_{\mathrm{c}}$. This can be interpreted as the boundary of the superconducting fluctuations in the temperature-field plane. A persistent region of fluctuations is present for all samples, ranging up to $\sim 2.4T_{\mathrm{c}}$. The extent of the fluctuations in temperature and field and the $\mu_0 H^\star$ points seems to have a dome-like shape for all single crystals, which, perhaps strangely, does not collapse to $H_{\mathrm{c2}}(0)$ as $T \to 0$. If the superconducting fluctuations were governed by the length scale ξ, one might expect them to collapse here. Reasons why they do not persist to H_{c2} at low temperatures, below T_{c} will be discussed in more detail later. Interestingly, the field range of the fluctuations for both samples with $x = 0.03$ and 0.25 (figures. 8.2**e** and 8.2**h**) are similar, with both ranging up to $\sim 5\,\mathrm{T}$ near T_{c}. Near the NEP the SCF's persist up to higher magnetic fields of $\sim 8\,\mathrm{T}$ near T_{c} in both samples (figures. 8.2**f** and 8.2**g**), suggesting that the superconducting fluctuations may be enhanced near the NEP, where the nematic fluctuations are also strongest [199].

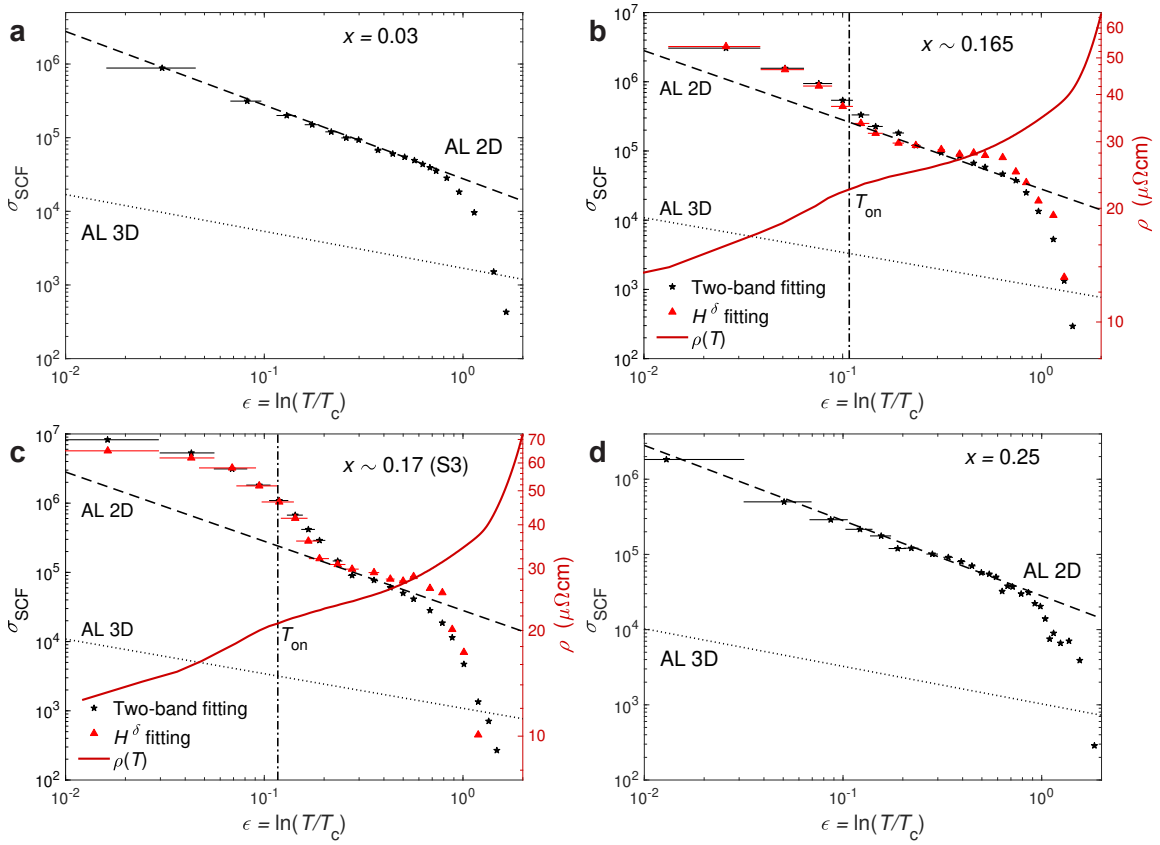


Figure 8.3: **a**-**d** The excess conductivity, assigned to superconducting fluctuations, in zero magnetic field against reduced temperature, T/T_c, for different single crystals of $FeSe_{1-x}S_x$ with $x = 0.03$, 0.165, 0.17 and 0.25 respectively. **b** and **c** The excess conductivity extracted from both two-band and H^δ fitting (black and red points, respectively) on the left axis. The right axis of these panels shows the resistivity as a function of reduced temperature and the onset temperature for superconductivity, T_{on} is labelled, defined as the kink (downturn) in the resistivity. Expected lines for 2D (dashed and black lines) and 3D (dotted black lines) Asalamov-Larkin behaviour are shown. The samples deep inside the nematic phase (**a** $x = 0.03$) and outside the nematic phase (**d** $x = 0.25$) match the 2D behaviour very well, up to $\sim 2.3T_c$. The $x \sim 0.17$ samples also show 2D behaviour at higher temperature, again up to $\sim 2.3T_c$, but have an enhanced conductivity exceeding the 2D behaviour at lower temperatures.

Table 8.1: Parameters used for different sulphur substitutions, x, to describe the 2D and 3D temperature dependence of the excess conductivity due to superconducting fluctuations, described by equations 2.25 and 2.24 respectively.

x	T_c (K)	ξ (nm)	d (nm)
0.03	9.6	4.5	0.5471
0.165	9.5	6.0	0.5405
0.17	9.0	6.2	0.5403
0.25	6.3	7.4	0.5364

8.4 Temperature dependence of the excess conductivity

To better understand the nature of the excess conductivity its temperature dependence in zero magnetic field is considered. Equations 2.25 and 2.24 in section 2.3 describe the temperature dependence of the excess conductivity due to Aslamasov-Larkin (AL) superconducting amplitude fluctuations in two-dimensions (2D) and three-dimensions (3D) respectively. These equations show that for amplitude fluctuations the conductivity should be linear in $\epsilon = \ln(T/T_c)$, but have quite different magnitudes for the 2D and 3D cases. Figures 8.3**a**-**d** show σ_{SCF} in zero magnetic field against $\epsilon = \ln(T/T_c)$ for the four different x substitutions (on the left axis for **b** and **c**). Figures 8.3**b**-**c** show the excess conductivity against the logarithm of reduced temperature extracted from both the two-band fits and H^δ fitting (left-axis), as well as the resistivity against reduced temperature (right-axis). Each panel has the expected temperature dependence of 2D and 3D superconducting fluctuations, and table 8.1 summaries the parameters used for each single crystal to generate the 2D and 3D curves. The coherence lengths used here have been found from the upper critical field near $T = 0$ K when $H||c$.

The expected 3D AL lines lie well beneath the σ_{SCF} found for all sulphur substitutions until temperatures well above T_c. The temperature dependence of the SCF's for both the $x = 0.03$ and $x = 0.25$ samples (figures 8.3**a** and 8.3**d**) are described by 2D AL superconducting fluctuations from T_c up to $\sim 2.4T_c$. The $x = 0.165$ and $x = 0.17$ samples are also described by the AL 2D up to $\sim 2.4T_c$, but are enhanced above the 2D curve at low temperature, below $\sim 0.1T_c$ (figures 8.3**b** and 8.3**c**). The collapse of excess conductivity onto the 2D curve supports the hypothesis that it is caused by fluctuations of the superconducting order parameter above T_c. This persistent 2D behaviour across the phase diagram implies that the preformed Cooper pairs are localised into sheets, likely the Fe(Se/S) layers found within these compounds.

The enhancement of the excess conductivity above the 2D line in figures 8.3**b** and 8.3**c** (left-axis) starts to occur close to the kink in the resistivity above T_c (right-axis), near the onset temperature of the resistive transition, T_{on}. This is the case for both the $x \sim 0.165$ and $x \sim 0.17$ samples, although for the former the enhancement of the excess conductivity is slightly closer to T_{on}.

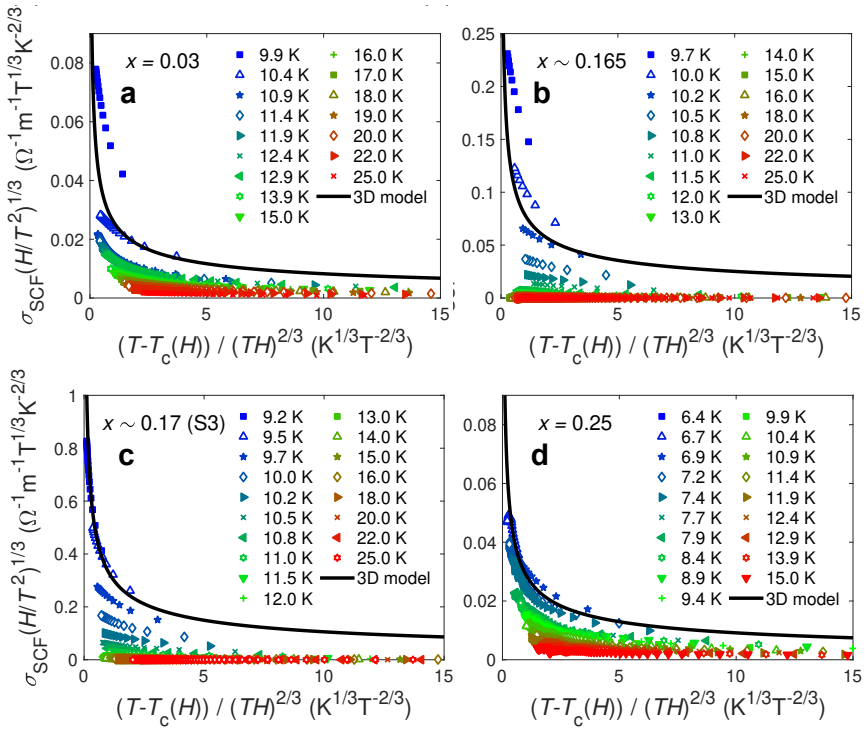


Figure 8.4: **Scaling (or lack there of) of the excess conductivity in magnetic fields using the 3D law. a-d** 3D magnetic field scaling of the excess conductivity (σ_{SCF}) for each respective sample. The colours in these panels represent the temperature. Black lines are 3D models using an exponent of x^{α} where $x = [(T - T_c(H))/(TH)^{2/3}]^{\alpha}$ and $\alpha = -1/2$, given by equation 2.31.

8.5 Magnetic field scaling of the fluctuations

Thus far the zero field temperature dependence of the excess conductivity has been discussed, but, as the excess conductivity has been extracted from the magnetoresistivity, the magnetic field effects can also be explored. One might expect the superconducting fluctuations to respond similar to bulk superconductivity in a magnetic field. The magnetic field will induce additional pair breaking, reducing the mean scattering time of Cooper pairs and so reduce the contribution of fluctuations to the conductivity. Other properties are

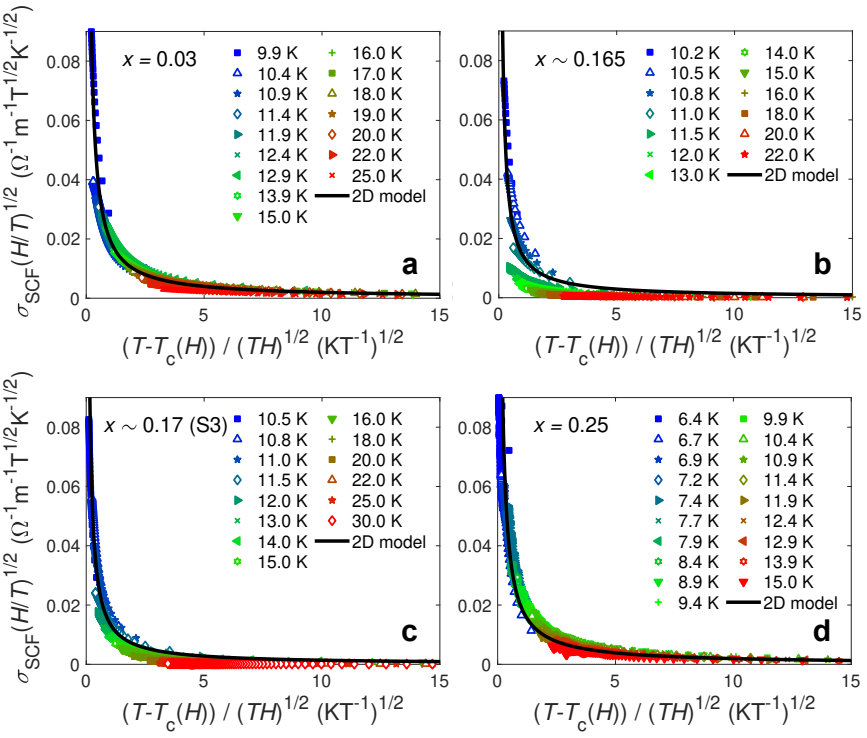


Figure 8.5: **2D magnetic field scaling of the superconducting fluctuations for each sample of $FeSe_{1-x}S_x$. a-d** 2D magnetic field scaling of the excess conductivity from superconducting fluctuations for each different sulphur composition of $FeSe_{1-x}S_x$, as labelled. The colour represents temperature, T. The solid black line is a 2D model of the data described by equation 2.30, using an exponent of x^{α} where $x = [(T - T_c(H))/(TH)^{1/2}]^{\alpha}$ and $\alpha = -1$.

affected differently in magnetic fields. For example, the diamagnetism exhibited by superconducting fluctuations is actually enhanced above T_c since $\chi \propto [T_c(H)/(T - T_c(H))]^{1/2}$ and $M \propto \chi H$ (up to a certain point, after which $T_{c2}(H)$ begins to dominate) [9, 102]. However, here only the conductivity arising from superconducting fluctuations is assessed, which does decrease with increasing magnetic fields. The exact form of the field dependence of the excess conductivity from fluctuations depends on the dimensionality of the system.

Equations that describe the magnetic field scaling of the excess conductivity from superconducting fluctuations for 2D and 3D systems are given in section 2.3.2 by equations 2.30 and 2.31 respectively [105–108]. The arguments of the scaling functions (F_{2D} and F_{3D}) are another representation of the critical region in a magnetic field. Note that this formulation only considers the effect of the Aslamazov-Larkin term [233], which near T_c generally dominates compared to other contributions such as the Maki-Thompson term [109, 110] and Zeeman effects, due to the large phase relaxation rate [109–112]. Other formalisations

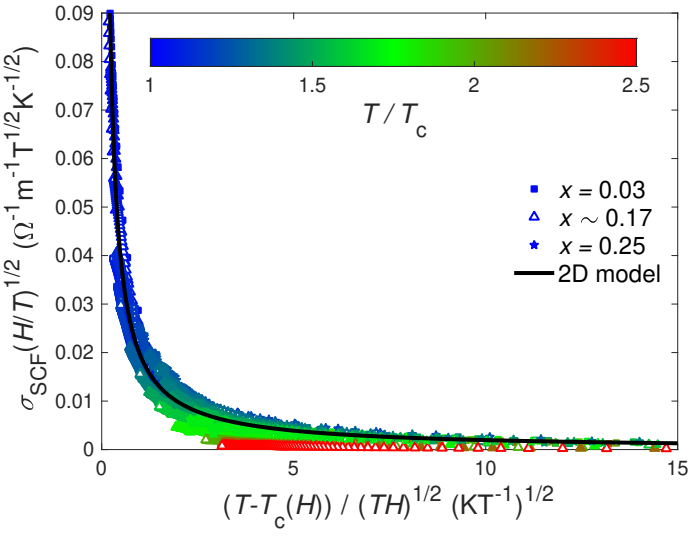


Figure 8.6: 2D magnetic field scaling of the superconducting fluctuations for different single crystals of FeSe$_{1-x}$S$_x$. The colour represents the reduced temperature, T/T_c. Black lines are 2D models using an exponent of x^α where $x = [(T - T_c(H))/(TH)^{1/2}]^\alpha$ and $\alpha = -1$.

of magnetoconductivity also exist [110]. 3D magnetic field scaling has been shown to work for superconducting fluctuations in cuprate superconductors previously [106, 113].

Here, both 3D and 2D magnetic field scaling of the excess conductivity is attempted, as shown in figures 8.4 and 8.5 respectively. Each different x compositions are shown in individual panels. Strictly speaking, for figures 8.4, 8.5 and 8.6 (as well as equations 2.30-2.31) $T_c(H)$ here is actually $T_{c2}(H)$, defined from the upper critical fields when $H||c$ for each sample in chapter 7. The exact definition $T_c(H)$ used is from the two-band model of the upper critical field in the clean limit for each sample. The 3D scaling in figure 8.4 clearly fails for all x substitutions. However, the excess conductivity as a function of magnetic field collapses onto a single curve given by the 2D scaling law in equation 2.30 for all samples, as shown in figure 8.5. Note that for $x \sim 0.165$ in figure 8.5 at intermediate temperatures the 2D scaling is not obeyed as well as in all other samples, but is still significantly better than the 3D scaling for this sample. Upper critical fields when $H||c$ are close to linear in FeSe$_{1-x}$S$_x$, as shown in chapter 7. To test the robustness of this magnetic field scaling, a linear dependence of $T_c(H)$ has also been used. This also shows 2D scaling in magnetic field and temperature for all samples but is not shown here as it is very similar to figure 8.5.

Figure 8.6 shows the excess conductivity scaled with the 2D model in equation 2.30 for all samples onto a single curve (i.e. using the same coefficient). Here the colour indicates the reduced temperature, T/T_c, and black lines are generated using equation 2.30.

Figure D.1 also shows an example of scaling using an exponent of $\alpha = -1$, which characterises 2D fluctuations in conductivity. This collapses onto a single straight line, as is expected, supporting the existence of 2D fluctuations over a large temperature and magnetic field range, as well as across the phase diagram for $FeSe_{1-x}S_x$. Note that the collapse of all excess conductivity data in magnetic field is achieved with the same A coefficient (see equation 2.30) for all x substitutions (within a small deviation). The implications of this are currently unclear, but it implies that the scaling is universal across the phase diagram of $FeSe_{1-x}S_x$.

8.6 Ginzburg number

Another parameter that can be used to characterise properties of a superconductor and the fluctuations of the superconducting state is the Ginzburg number, Gi, which represents the magnitude of the fluctuations, given by equation 2.33 [114]. The Ginzburg number for $FeSe_{1-x}S_x$ as a function of x is shown in figure 8.7, and has been calculated from upper critical field studies in chapter 7. This has been calculated in the low-temperature limit, using $H_{c2}(T \to 0)$ and the anisotropy of the upper critical field as temperature goes to zero. The most difficult value to estimate is the Ginzburg-Landau order parameter, κ, which is of particular importance as $Gi \propto \kappa^4$. This large exponent means Gi is very sensitive to any changes in κ, even if they are small.

Inside the nematic state κ has been estimated from the upper critical field studies in chapter 7 and magnetisation studies of the lower critical field (see figure D.4 in appendix D). From $\mu_0 H_{c1}$ and $\mu_0 H_{c2}$ the Ginzburg-Landau order parameter κ is estimated using equations 1.24, 1.27 and 1.30 (see figure D.5 in appendix D for an example). A constant value of $\kappa \sim 90$ is found inside the nematic state, up to $x \sim 0.18$. This is in good agreement calculating values of κ for $x \leq 0.11$ using the coherence lengths from the upper critical fields when $H||c$ in chapter 7 and values of the penetration depth (λ_{ab}) from Ref. [220]. Outside of the nematic state, the evolution of κ has been estimated using values of $\mu_0 H_{c2}$ and the penetration depth λ from upper critical field measurements [48] and penetration depth studies from μSR experiments [234], which gives $\kappa \sim 7$ for FeS. κ is likely to drop fairly dramatically across the NEP and into the tetragonal state, like other superconductivity parameters in chapter 7, and so a power law dependence of $\kappa \propto (x - x_c)^{-1/2}$ is used from the end of the nematic phase at $x_c \sim 0.175$. Errors in the Ginzburg number are estimated to be $\sim 7\%$ across the phase diagram of $FeSe_{1-x}S_x$.

Gi is ~ 0.017 across the phase diagram, typical for unconventional high-T_c superconductors showing strong superconducting fluctuations [235]. For FeSe this Ginzburg num-

ber is a factor of ~ 2 larger than reported in Ref. [235], but this is because the values they use for the upper critical fields (especially when $H||(ab)$) are predicted incorrectly, giving a smaller value of the anisotropy and a smaller value of the order parameter, of $\kappa \sim 72$. Given that $Gi \propto \kappa^4$ it is then expected that they would predict a lower value than is reported in this chapter. However, Gi is enhanced by a factor of ~ 3, up to $Gi \sim 0.52$, near the nematic end point, which correlates with the enhanced excess conductivity above the 2D line that is also observed near the nematic end point (figures 8.3**b**-**c**). The enhancement of Gi from upper critical field studies suggests that the enhancement of superconducting fluctuations observed near the NEP is robust, as it is extracted using a different method to the excess conductivity, and not an artefact of the measurements and extraction methods presented in this chapter.

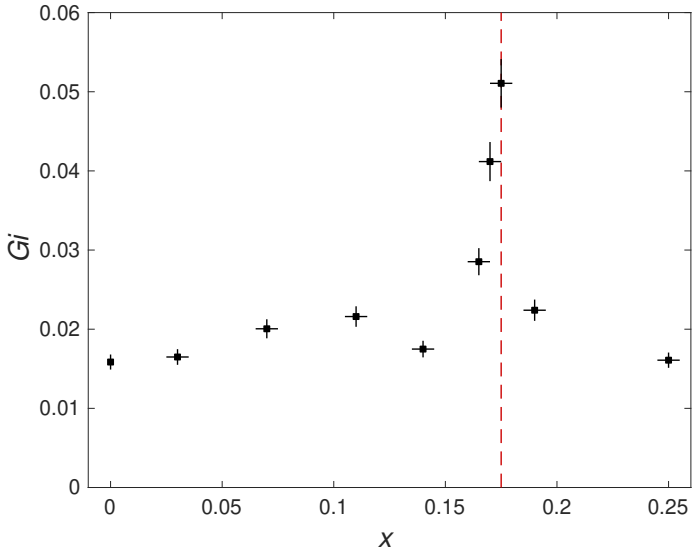


Figure 8.7: The Ginzburg number, Gi, values as a function of sulphur concentration. These values have been calculated from the upper critical field studies in chapter 7 and estimates of the superconducting order parameter κ from magnetisation.

8.7 Discussion

As the sulphur substitution x increases the Fermi surface of $FeSe_{1-x}S_x$ is expected to become more three-dimensional, particularly in the tetragonal phase [41, 43]. As the Fermi surface becomes more 3D, it might be expected that superconductivity, and so also the SCF's, become more 3D as well. This is not what is observed in the experiments presented in this chapter, with the superconductivity remaining 2D across all x substitutions. This may have implications for which, likely highly 2D, Fermi sheets/bands of $FeSe_{1-x}S_x$ are

involved in the Cooper pairing that contributes to superconducting fluctuations that cause the 2D excess conductivity. The persistent 2D fluctuations across the phase diagram may only arise from a particular part of the Fermi surface, i.e. a single band, that remains more 2D. Previous studies have shown that the hole bands undergo a Lifshitz transition at the NEP at the Γ point of the Fermi surface [41, 43]. This gives the hole bands a larger z variation, thus making them more 3D. Hence, this may suggest that the superconducting fluctuations are more likely to occur of the electron band(s) which remain more 2D in character.

Strong low frequency anti-ferromagnetic spin fluctuations have been detected inside the nematic state [44, 45, 223]. The magnitude of the spin fluctuations is largest where $T_{\rm c}$ is at its maximum, suggesting that the spin fluctuations are linked to the increased $T_{\rm c}$. The spin fluctuations are also suppressed across the NEP into the tetragonal state, where $T_{\rm c}$ also drops. Here no change is observed in the dimensionality or extent of the superconducting fluctuations across the NEP, they are 2D and always persist up to $\sim 2.4T_{\rm c}$. This suggests that the spin fluctuations play little or no role on the dimensionality of the superconducting fluctuations, or their persistence to temperatures well above $T_{\rm c}$.

The zero-field $\rho(T)$ superconducting transitions are broader at the NEP than deep inside the nematic state or in the tetragonal phase. One cause of the broadening of resistive transitions could be disorder, which could also affect the nature of the observed superconducting fluctuations. The enhancement of the excess conductivity in figures 8.3**b-c** above the 2D line also seems to occur near the onset temperature of superconductivity, $T_{\rm on}$. This suggests that the broadening of resistive transitions and the enhanced superconducting fluctuations may be intrinsically linked. It is expected that disorder and inhomogeneity in single crystals will actually increase scattering (either in the normal state or of preformed Cooper pairs), which increases the resistivity and should suppress any excess conductivity. This implies that the enhanced superconducting fluctuations near $T_{\rm c}$ at the NEP are unlikely to be caused by disorder or inhomogeneity in samples. Of course, disorder affecting the broadening of resistive transitions cannot be ruled out, but the enhanced superconducting fluctuations could also be causing this broadening. It is not only the zero field $\rho(T)$ resistive transitions that are broader near the NEP, the resistive transitions in magnetic fields are also far broader in this part of the phase diagram, as shown by $\Delta(\mu_0 H_{\rm c2}) = \mu_0(H_{\rm on} - H_{\rm off})$ when $H||(ab)$ in figure 7.2**c** (left-axis). When $H||c$ the broadening of transitions in magnetic field combined with the large amplitude quantum oscillations at low temperature (below ~ 4 K) near the NEP makes defining $\mu_0 H_{\rm on}$ difficult, hence why transitions when $H||(ab)$ have been considered (although the resistive transitions when $H||c$ near the NEP are also clearly broader as well, just not as easily quantifiable). The wider transitions near the NEP in high

magnetic fields could also be linked to an enhancement of the superconducting fluctuations. There are a number of possible reasons for this, which will be considered, although it is worth noting at this point it is unclear of the exact cause. First, it has been detected in the nematic susceptibility (χ_{Nem}) from torque measurements that nematic fluctuations increase near $x \sim 0.17$ [199], close to the nematic end point. These could contribute to enhance superconducting fluctuations. Second, as mentioned previously, it has been suggested that the inner hole band of $FeSe_{1-x}S_x$ goes through a Lifshitz transition at the NEP. This is a strong distortion of the Fermi surface and the carrier density of the inner hole band would be expected to drop dramatically. In low carrier density and low superfluid density systems it has been suggested that phase fluctuations of the superconducting order parameter become important and can significantly enhance the manifestation of fluctuations [224]. Thus, if the hole band that undergoes a Lifshitz transition is involved in preformed Cooper pairing its low density may make it prone to phase fluctuations (as well as amplitude fluctuations), which could in turn further enhance the excess conductivity.

Note that at temperatures above this enhancement $\sigma_{\mathrm{SCF}}(T, H = 0)$ still collapses onto the 2D line over a considerable temperature range, showing the persistence of 2D superconducting fluctuations. Samples near the NEP also show the 2D magnetic field scaling (figures 8.6 and 8.5) even at temperatures inside the superconducting transition. This all implies that the observed 2D fluctuations are not affected by disorder, and are persistent across all sulphur substitutions.

Two-dimensional superconductivity has also been observed in FeSe thin flakes [58] and thin films [55, 56] which might be expected as the thickness of samples approaches the coherence length (as a dimensionality crossover). Both thin flakes and films of FeSe show a Berezinskii-Kosterlitz-Thouless (BKT) transition, characteristic of 2D superconductivity. Note that the 2D BKT behaviour in thin films was found in a film with a thickness of $500\,\mathrm{nm}$, which far exceeds the coherence length (by a factor of ~ 100). T_{c} and H_{c2} are also suppressed in FeSe flakes as the 2D BKT transition is approached [58], which means the superconducting gap is also reduced. This may be consistent with a superconducting smaller gap that dominates the 2D fluctuations in bulk $FeSe_{1-x}S_x$ presented in this chapter. However, it is more likely that the 2D superconductivity in thin FeSe devices is induced by a dimensionality crossover with reducing thickness.

Two-dimensional superconducting fluctuations have been observed in other iron-based superconductors, such as LiFeAs [229, 236]. In this study 2D fluctuations were observed up to $\sim 2.5T_{\mathrm{c}}$, which is very similar to the value of the temperature extent of the superconducting fluctuations that is found in $FeSe_{1-x}S_x$ single crystals in this chapter. This

is in contrast to other iron-based superconductors, such as the Ba-122 system, where 3D fluctuations have been observed despite the layer structure [237, 238].

Perhaps an usual observation in this chapter is that the excess conductivity does not collapse to H_{c2} at low temperatures in figures 8.2**e**-**g** (i.e. $\mu_0 H_{c2} = \mu_0 H^\star$ at $T = 0$), as has been observed previously in the cuprate superconductor $La_{2-x}Sr_xCuO_4$ [239]. In this material the fluctuations have a 3D nature, and so scale in temperature to the coherence length. In this material the superconducting fluctuations are 3D, and so their temperature dependence is governed by the coherence length (see equation 2.24), thus a collapse to H_{c2} at low temperature (which is also set by the coherence length) is expected. The 2D superconducting fluctuations observed here in $FeSe_{1-x}S_x$ are scaled using the c-axis lattice constant, rather than the coherence length, but in a conventional picture one might still expect the fluctuations to collapse to zero at H_{c2}. Next, a reason why this may not be the case is considered.

Different superconducting gaps can have effects on the superconducting state. In chapter 7 the effects of this on the upper critical field were analysed, but this could also propagate into the manifestation of superconducting fluctuations. The coherence length is related to the superconducting gap by $\Delta = \hbar v_F/(1.76 \times 2\pi\xi)$. Substituting in for $\mu_0 H_{c2} = \Phi_0/(2\pi\xi^2)$ gives $H_{c2} \propto \Delta^2$. When $H||c$ the system is only dependent on the coherence length ξ_{ab} in chapter 7 (note $\xi_{ab} = \xi$, as used above in this chapter). Previous reports on FeSe show two superconducting gaps [216], which are $\Delta_1 \sim 2.2\,\text{meV}$ and $\Delta_2 \sim 1.4\,\text{meV}$ (chapter 7). In an isotropic system, the magnitude of the upper critical field at $T = 0$ will be set by the larger gap when $H||c$, and will dictate the $\mu_0 H_{c2}(0)$ value. This predicts that $\mu_0 H'_{c2}(0) \sim 6\,\text{T}$ from the smaller gap for the $x = 0.03$ sample, which is very similar to the value that $H^\star$ tends towards for $T = 0$. The Fermi velocities from upper critical field studies suggest that the α hole band has the larger gap in FeSe, leaving an electron pocket for the second gap (see chapter 7). ARPES shows that the electron band(s) are more 2D in nature than the hole band [29, 40], and so the 2D SCF's may arise from an electron band and the second smaller gap. This provides reinforcement for the hypothesis that the 2D fluctuations arises from the second smaller gap on one of the electron bands. Also note that if one of the bands/gaps manifest 3D SCF's they would give a conductivity contribution ~ 100 times smaller than the 2D fluctuations, and so it is unlikely they would be resolvable where 2D fluctuations are present.

Perhaps the part of the work in this chapter that is brought into question the most is still the method of extracting the excess conductivity. Despite the arguments presented, modelling the resistivity in magnetic fields for $FeSe_{1-x}S_x$ when $H||c$ is complicated, as

discussed in chapter 6. Another approach one could take is to measure the magnetoresistivity with $H||(ab)$, where the field dependence of the resistivity is far simpler due to the lack of orbital contributions and is linear in magnetic field. However, this may invoke some other problems. First, experimentally this is more complicated as the upper critical fields in this orientation are larger, with $\mu_0 H_{\rm on} \sim 35\,$T for $x \sim 0.11$, and so this would require work at a high-field facility at, ideally, similar temperature intervals to this chaper. This would be very time (and not to mention energy) intensive. Second, when $H||(ab)$ FeSe$_{1-x}$S$_x$ is governed by two coherence lengths. This may also manifest in the superconducting fluctuations, and the 3D case (where the excess conductivity is dictated by the coherence length) may prove to be more complicated. Third, in this orientation the Cooper pairs may also not be confined to the Fe(Se/S) layers which will no longer be perpendicular to the field, but parallel to it. This may change the nature of the 2D superconducting fluctuations. Hence, whilst the $H||(ab)$ field orientation may provide an easier method of extracting the excess conductivity from magnetoresistivity data, it may also come with further complications to understand the fluctuations.

8.8 Summary

In this chapter the excess conductivity from superconducting fluctuations in FeSe$_{1-x}$S$_x$ across the nematic end point have been extensively studied using electrical transport in high-magnetic fields up to $16\,$T. The fluctuations are 2D inside the nematic phase, at the nematic end point and in the tetragonal phase, persisting up to $\sim 2.4T_{\rm c}$. The superconducting fluctuations show AL 2D scaling in temperature as well as 2D magnetic field scaling. The excess conductivity near $T_{\rm c}$ is enhanced near the NEP, where resistive transitions in both temperature and magnetic field are also broader. The Ginzburg number, Gi, extracted from the upper critical field studies of FeSe$_{1-x}$S$_x$ in chapter 7 also increases by a factor of ~ 3 near the NEP, indicative of enhanced superconducting fluctuations. This could be an effect of disorder, but this is unlikely as disorder will suppress superconducting fluctuations. The cause of the enhanced excess conductivity, Gi and broader transitions is not clear, but two possibilities are strong nematic fluctuations or phase fluctuations of the superconducting order parameter arising from a low density band. The persistence of 2D superconducting fluctuations across all sulphur substitutions suggests that they are not linked to the antiferromagnetic spin-fluctuations observed in FeSe$_{1-x}$S$_x$ inside the nematic phase, and also seem to be unaffected by changes in the Fermi surface. This suggests that the superconducting fluctuations occur on an electron band that remains more 2D as the Fermi surface evolves.

Chapter 9

Conclusions

In this thesis two iron-based superconductors, $CaKFe_4As_4$ and $FeSe_{1-x}S_x$, have been experimentally studied using a combination of resistivity, magnetization and torque measurements. $CaKFe_4As_4$ offered the opportunity to study superconductivity in a very clean and optimally doped material. $FeSe_{1-x}S_x$ has been studied in detail up to $x = 0.25$, across the nematic end point.

The magnetization results on $CaKFe_4As_4$ show an exceptionally large critical current density above $10^7\,\mathrm{A/cm^2}$ when $H||c$, the highest of any known iron-based material. The vortex pinning force is also extremely large, due to both strong point-like defects ($\Delta\kappa$-pinning) and surface pinning. The vortex phase diagram is complex, showing crossovers from a vortex solid to vortex glass phases dominated by elastic and plastic creep, characteristic of the second magnetization peak when $H||c$. The extremely-high critical current density of $CaKFe_4As_4$ suggests that the vortex core energy is enhanced in this optimally doped superconductor and the reduced symmetry of Fe-As bonds could play an important role in pinning.

Resistivity measurements in pulsed magnetic fields up to $90\,\mathrm{T}$ were performed to map the upper critical field down to $4.2\,\mathrm{K}$, yielding coherence lengths of $\xi_{ab} = 1.83(3)\,\mathrm{nm}$ and $\xi_c = 1.87(6)\,\mathrm{nm}$. Extrapolation of the field sweep data reveal Fermi liquid T^2 behaviour up to ~ 50 and $\rho_0 = 9.2(4)\,\mu\Omega\mathrm{cm}$, giving a mean free path of $\ell \sim 27\,\mathrm{nm}$. This, combined with the sharp superconducting transition, suggests that this material is very clean and has low amounts of disorder, compared to other optimally doped iron-based systems. Single-band models of the upper critical field fail to describe $H_{c2}(T)$ below $\sim 10\,\mathrm{K}$. Using the parameters from the single-band model combined with details of the Fermi surface gave a starting point for describing the upper critical field of this system using the two band model, discussed in section 2.1.5. $CaKFe_4As_4$ can be described in two limits, using parameters consistent with s^{++} and $s^{\pm}$ pairing. This may suggest a competition

between orbitally dominated pairing on different bands (s^{++}), and pairing mediated by spin-fluctuations across two bands ($s^{\pm}$). The H_{c2} data when $H||(ab)$ are consistent with the emergence of an FFLO state below $\sim 14\,\mathrm{K}$. This is similar for both the s^{++} and $s^{\pm}$ pairing limits. The FFLO state is likely to emerge when the Maki parameter is large, as has been found for $CaKFe_4As_4$ with $H||(ab)$, and shallow bands are present close to the Fermi level. There are a number of bands in $CaKFe_4As_4$ close to the Fermi level that could manifest an FFLO state. Note that the upper critical fields in $CaKFe_4As_4$ are very large, $\sim 85\,\mathrm{T}$ at $4.2\,\mathrm{K}$ and almost perfectly isotropic. This, combined with its stoichiometry, small impurity levels and high critical current density, make $CaKFe_4As_4$ an excellent candidate for practical applications, particularly in the low-temperature high-field regime.

Resistivity results on $FeSe_{1-x}S_x$ from chapter 6 show three different characteristic regimes. Two inside the nematic state, the nematic A and nematic B phase, and another past the nematic end point in the tetragonal state. The nematic A and B phases are separated by the emergence of an extra hole pocket at $x \sim 0.1$, which seems to significantly change the high-field electronic behaviour. At low temperatures in $35\,\mathrm{T}$ the resistivity in the nematic A phase has positive gradient, while in the nematic B phase it shows an insulating-like upturn. The entire nematic state shows unconventional transport power laws in magnetic fields, $\rho_{xx}(H)$ at constant temperature give a field exponent of $\delta = 1.55(5)$. This is non-Fermi liquid behaviour, and seems to be characteristic of the nematic state. Outside of the nematic phase boundary, in the tetragonal state, the exponent returns to the convention Fermi-liquid $\delta \sim 2$. In the low-temperature limit high magnetic fields are used to suppress superconductivity and reveal the temperature dependence of resistivity. There is an extended linear regime, followed by a Fermi-liquid like dependence, highly dependent on the composition and impurity level. Anomalous transport properties dominate the nematic phase, and change rather dramatically in the tetragonal state, becoming far more conventional.

The upper critical fields in $FeSe_{1-x}S_x$ have been studied extensively using both resistivity and torque down to $\sim 0.3\,\mathrm{K}$ in two orientations ($H||c$ and $H||(ab)$) in fields up to $38\,\mathrm{T}$. When $H||c$, the upper critical fields are strikingly linear inside the nematic phase. Inside the nematic A phase they collapse onto a single line in H_{c2}/T_c against T/T_c. The ratio H_{c2}/T_c is then suppressed with increasing x across the nematic end point and into the tetragonal state. A number of parameters, such as the coherence lengths and anisotropy increase dramatically across the nematic end point, suggesting a change in the nature of superconductivity here. The transition widths when $H||(ab)$ are also enhanced at the nematic end point. In either field orientation, the temperature dependence of the upper critical field

varies significantly from single-band models. Instead a two-band model in the clean limit was used to describe $H_{c2}(T)$. This model gave access to band coupling constants, Pauli pair-breaking effects (on different bands) and Fermi velocities. First, the Fermi velocities match previous results well. Pauli effects are zero (or very small) when $H||c$, but become relevant when $H||(ab)$. Our results are consistent with the emergence of an FFLO state at low temperatures inside the nematic A phase (below $x \sim 0.1$). This is supported by the larger Maki parameter here and the presence of two bands near the Fermi level which could support this state. The band coupling parameters given by the two-band model suggest a change in pairing across the nematic end point, from $s^{\pm}$ inside the nematic phase to s^{++} in the tetragonal state. This coincides with the increase in coherence lengths, anisotropy, and the decrease in T_c, providing further evidence for the change in pairing across the nematic end point. Using the Fermi velocities from the two-band model the superconducting gaps have been calculated. The dominant band, Δ_1, agrees well with previous STM results. The smaller gap, Δ_2, in FeSe is also close to previous results. The dominant gap also drops significantly across the nematic end point, again supplying evidence for the change in the nature of superconductivity, and so also the change in pairing here. Matching the Fermi velocities to known bands from ARPES suggests that the dominant gap emerges on the larger outer hole band (α), and the smaller gap comes from one of the warped electron pockets.

Despite the significant changes in the electronic and superconducting properties across the nematic phase and into the tetragonal state, the excess conductivity arising from superconducting fluctuations have a persistent two-dimensional nature across the entire phase diagram and persist up to $\sim 2.4T_c$ for all sulphur substitutions. The excess conductivity also shows a two-dimensional magnetic field scaling for all samples, suggesting that the dimensionality found here is robust. This is an interesting result, as it implies that the Cooper pairs are confined to Fe(Se/S) layers (a dimensionality crossover can be excluded as $\xi \gg c$, where c is the z-axis lattice constant). There is an enhancement in the magnitude of the excess conductivity (above the 2D limit) near the nematic end point very close to T_c. An increase in the Ginzburg number, Gi, (found from the upper critical fields) is also observed here which typically characterises the magnitude of superconducting fluctuations, suggesting the enhancement is real and not an artefact of the measurement. At the nematic end point an increase in the width of resistive transitions into the superconducting state is observed, both in magnetic field and at zero field. As the excess conductivity increases at the same point, it is likely that it is not an effect of disorder and is actually linked to the enhanced superconducting fluctuations. The reason for the enhanced excess conductivity, Gi and broader resistive transition currently remains unexplained, but could be linked to the

enhanced nematic fluctuations present at the nematic end point or changes in the Fermi surface (Lifshitz transition) that occur here, giving rise to a small density band on which phase fluctuations could manifest. The consistency of the dimensionality of superconductivity between the nematic and tetragonal states suggest certain characteristics of superconductivity remain robust across the nematic end point. The upper critical field studies suggest there are two gaps, the smaller gap does not change significantly across the nematic end point, and that it emerges on an electron band. The electron bands are warped cylinders, which are more 2D in nature than the hole bands. This may suggest that the 2D fluctuations arise from the electron band and the smaller gap.

$FeSe_{1-x}S_x$ has been extensively studied in the range $0 \leq x \leq 0.25$. The x substitution of this material can be divided into three parts: the nematic A phase ($0 \leq x \lesssim 0.1$), nematic B phase ($0.1 < x \lesssim 0.175$) and the tetragonal state. The nematic A phase is characterised by a drop in the high-temperature magneto-resistivity with decreasing temperature, Fermi-liquid behaviour at in the zero-field resistivity at low temperatures, the emergence of an FFLO state in the upper critical field and an $s^{\pm}$ pairing nature of superconductivity. At the start of the nematic B phase, $x \sim 0.1$, an additional hole band appears at the Fermi level and T_{c} is maximum. Here the low-temperature magnetoresistivity shows an insulator-like upturn and the characteristics of the upper critical field begin to change, showing a smaller Maki parameter, different curvature and no FFLO state. In the tetragonal state, after the nematic end point, the low-temperature electronic behaviour is Fermi-liquid, T_{c} and superconductivity is dominated by s^{++} pairing. This change in pairing shows the change in the nature of superconductivity between the nematic and tetragonal states. The $s^{\pm}$ pairing inside the nematic state is likely caused by spin-fluctuation mediated Cooper pairing. The spin-fluctuations are suppressed in the tetragonal state, where the pairing changes to s^{++}. Despite the changes to the Fermi surface, scattering and superconductivity, the superconducting fluctuations remain two-dimensional in nature across the x phase diagram. This perhaps suggests that the fluctuations arises from one of the more two-dimensional electron bands.

Appendix A

Additional material for chapter 5

This section contains additional information to support the data, analysis and results presented in chapter 5. It will cover the Fermi surface of $CaKFe_4As_4$, the extraction of parameters such as H_{c2} from pulsed field data (figure A.2) and the coherence lengths (figure A.3), and further details of the two-band model of the upper critical field (section A.1 and figure A.4).

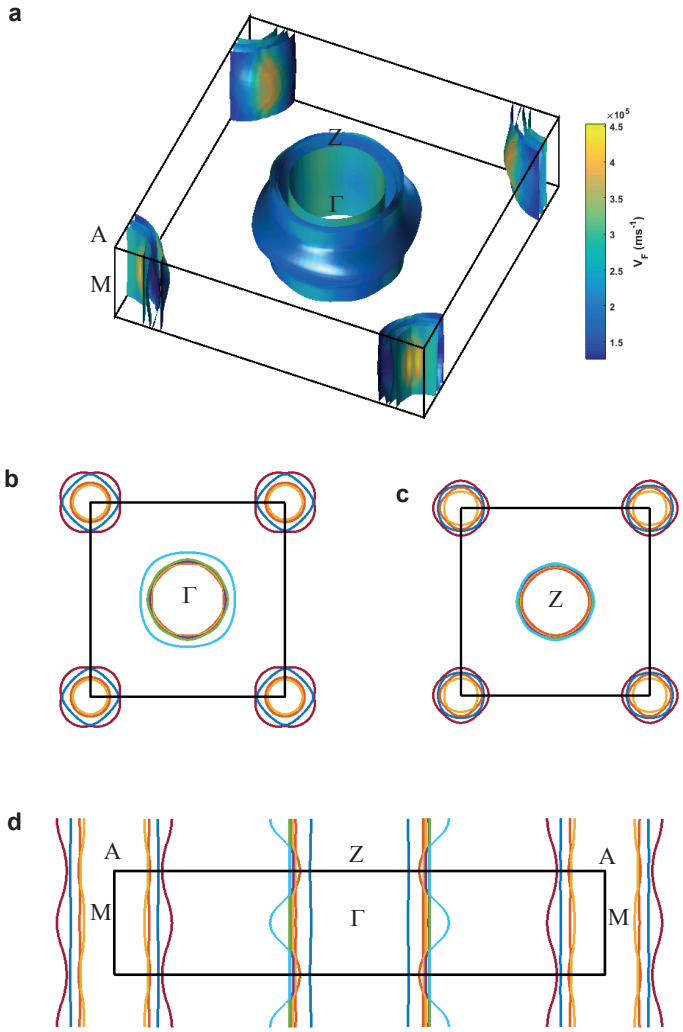


Figure A.1: **Fermi surface of $CaKFe_4As_4$. a** Fermi surface with velocity colour. Slices at the **b** Γ and **c** Z-point indicating the size of the different sheets. Solid lines indicate the Brillouin zone. **d** Fermi surface slice along the [110] diagonal of the Brillouin zone indicated by the solid lines. The calculations were performed using Wien2k and GGA approximation and the experimental lattice parameters described by the $P4/mmm$ symmetry group were $a = b = 3.86590$ Å, $c = 12.88400$ Å[59]. The calculated value of anisotropy, Γ=$\lambda_c/\lambda_{ab} = 313.68/70 = 4.5$ using a similar approached used in Ref. [178]. These calculations are in agreement with previous results reported in Ref. [138]. [This figure was produced by A. Coldea, who also carried out the necessary Fermi surface calculations.]

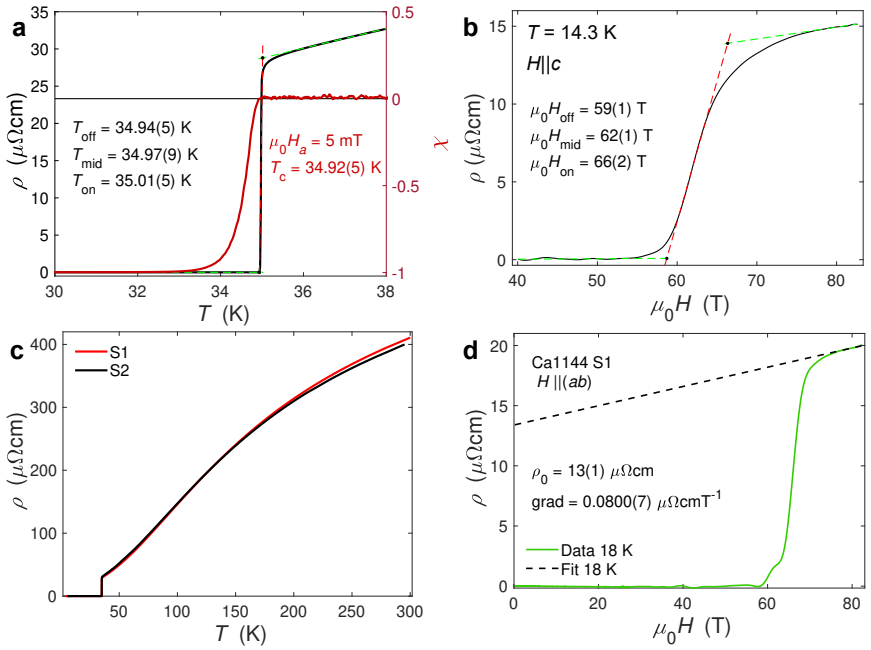


Figure A.2: **Transport data of $CaKFe_4As_4$ as a function of temperature and magnetic field.** **a** Critical temperature extraction from resistivity against temperature in zero magnetic field (left-axis) and a bulk T_c extraction from magnetic susceptibility in a small applied field of 5 mT (right-axis). The midpoint of the transition, T_{mid}, is identified as the peak in the derivative $d\rho/dT$. Linear fits are performed above and below the midpoint transition. The intercepts of these lines are defined as T_{off} and T_{on} and are labelled in the plot. T_c from susceptibility is defined as the point at which diamagnetism occurs and deviates from the high-temperature background. The T_c from susceptibility is closest to the offset temperature in transport, which is why this is chosen as the criteria. Note that critical temperatures that were used to build the phase diagrams in $\mu_0 H > 0$ T were extracted in the same way as in **a** left-axis. **b** The upper critical field extraction from resistivity in pulsed magnetic field data at constant temperature. These values are found using the same method as in **a**. **c** Resistivity against temperature for different samples of $CaKFe_4As_4$ between 300 K and 2 K. The superconducting transition is very sharp, with $T_{c,0} = 35.0$ K and width $\Delta T_c = 0.15$ K from onset ($T_{c,on}$) to offset ($T_{c,off}$). These values are typical of all single crystals in this paper. **d** Resistivity data as a function of magnetic field for the sample S1 when $H||(ab)$ at 18 K. The dashed black line shows the linear extrapolation used to obtain the zero-field resistivity at 18 K and the intercept, $\rho_{H\to 0}(T)$, and gradient are shown. Using this method, the extracted values of zero-field resistivitiy measured at constant temperatures are shown in the main paper in figure 5.1**f**.

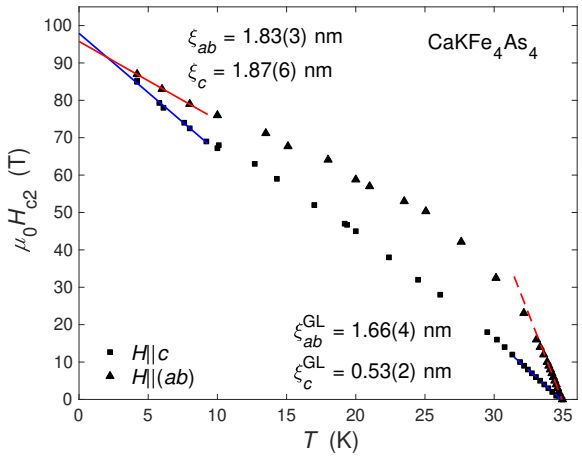


Figure A.3: **Coherence length extraction.** Upper critical fields in $CaKFe_4As_4$ as a function of temperature. The dashed blue and red lines are linear fits near T_c when $H||c$ and $H||(ab)$ respectively. The gradients of these fits (shown in the figure) were used to calculate the coherence lengths using the Ginzburg-Landau theory (equation **??**). The solid blue and red lines are linear fits to the low temperature region when $H||c$ and $H||(ab)$ respectively. The zero-temperature extrapolation of $H_{c2}(T \to 0)$ for the two orientations were used to find the zero-temperature coherence lengths, as shown in the figure.

A.1 The upper critical fields using a two-band model

To describe the entire temperature dependence of $H_{c2}(T)$ for $CaKFe_4As_4$, including the upturn below $\sim 10\,K$ for both orientations, a two-band model in the clean limit is used. This model includes paramagnetic effects and allows the emergence of a FFLO state, as detailed in Ref. [81]. The upper critical fields as a function of temperature are found from simulations using the two-band model developed by A. Gurevich discussed in 2.1.5. The values of the coupling constants allows us to establish the dominant pairing. For s^{++} pairing the parameter $w > 0$ ($w \sim 0.248$ for the case presented in figure 5.3**c** and figure A.4**c**) whereas for $s^{\pm}$ pairing $w < 0$ (figures 5.3**a**, 5.3**b**, A.4**a** and A.4**b**).

Various simulations of upper critical fields using this two-band model are shown in Fig. 2.3. The slope of H_{c2} near T_c of $CaKFe_4As_4$, is ~ -3.3 for $H||c$ and ~ -10.8 for $H||(ab)$, giving an $\epsilon \sim 1/10$. Q is the magnitude of the FFLO modulation and it is found for a given temperature when H_{c2} is maximal ($dH_{c2}/dQ = 0$). The simulations of H_{c2} for $H||(ab)$ assumed that the bands have the same anisotropy parameter $\epsilon_1 = \epsilon_2 = \epsilon$. Parameters from this model are first estimated using previous results and single-band fitting, as above. The velocities are then minimised locally to find an optimum solution. This was done in the different $s^{\pm}$ and s^{++} pairing limits, which are described in section 5.5.

A rescaling of the upper critical field has been performed previously mapping $H^c_{c2} \rightarrow H^{ab}_{c2}$ using $q_{ab} \rightarrow q_c\epsilon^{-3/4}$, $\alpha_{ab} \rightarrow \alpha_c\epsilon^{-1/2}$, $b^{1/2}_{ab} \rightarrow b^{1/2}_c\epsilon^{1/4}$ in U_1, $(\eta_{ab}b_{ab})^{1/2} \rightarrow (\eta_c b^{1/2}_c)\epsilon^{1/4}$ in U_2. The values of the α parameters change as $\alpha_{ab,1} \rightarrow \alpha_c\epsilon^{-1/2}$, and $\alpha_{ab,2} \rightarrow \alpha/(\eta\epsilon^{1/2})$. However, this re-scaling has not been used in this study, as the ratio between the Fermi velocities η is a variable parameter that can be changed between the two field orientations.

Previous studies on $CaKFe_4As_4$ have described the onset upper critical field data up to $60\,T$ using the parameters $\lambda_{11} = \lambda_{22} = 0$, $\lambda_{12}\lambda_{21} = 0.25$, $\eta = 0.2$, $\alpha = 0.5$ and $\epsilon = 1/6$ and the above re-scaling [61]. These parameters clearly fail to describe the full temperature dependence of the onset upper critical field data (open blue and red symbols) of $CaKFe_4As_4$ as shown in figures A.4**a** and A.4**b** (blue and red curves). As discussed in the main body of text, the upper critical field of $CaKFe_4As_4$ can reasonably describe using a two-band model with band parameters for the $s^{\pm}$ and s^{++} pairing (see Table 5.5), as shown in figure A.4**c** and A.4**e**, respectively. Note here that an FFLO state can be stabilized at low temperatures for $H||(ab)$ (figures A.4**c** and A.4**e**, right axis).

In this study the full upper critical phase diagram is fitted down to $4.2\,K$ in both $H||c$ and $H||(ab)$. To do this, sensible starting parameters are first identified. Initial values for velocities are estimated using the calculations in A.1 and Ref. [141]. These can also give

limits on the values for η, which has an extreme minimum value of ~ 0.025. The single-band WHH fits in figure 5.2**c** are used to give initial values for α in both field orientations. Simulations of the reduced field h are produced from equations 2.12-2.14 in different limits, to generate different curves and see which shapes best describe our data. These are shown in figure 2.3. The velocity v_1 is then minimised locally in each limit to the lowest residual error, and so the best fit.

To test the validity of results, both the offset and onset critical fields for both field orientations are modelled in the $s^{\pm}$ and s^{++}. The parameters are shown in Table 5.5. The fits for $\mu_0 H_{\rm off}$ are shown in figures A.4**c** and A.4**e**, and the fits for $\mu_0 H_{\rm on}$ are shown in figures A.4**d** and A.4**f**. The parameters for fitting the offset and onset fields are similar. For $H_{\rm on}$, the values for α are slightly larger than for $H_{\rm off}$. This is expected, as the curvature for $H_{\rm on}$ is greater. The velocities for $H_{\rm on}$ are also slightly smaller, which is expected from the larger slopes near $T_{\rm c}$. The slopes near $T_{\rm c}$ scales as $|dH_{\rm c2}/dT|_{T_{\rm c}} \propto 1/v^2$. Using the values for $H_{\rm off}$ and $H_{\rm on}$, a $\sim 20\%$ difference is expected in velocities when $H||c$, and a $\sim 10\%$ difference when $H||(ab)$. This is in agreement with the velocities in table 5.5. Perhaps the most important result in the comparison between the two different criterion modelling is that both are consistent with the emergence of an FFLO state at low temperatures. This suggest that the stabilization of an FFLO state in $CaKFe_4As_4$ is robust.

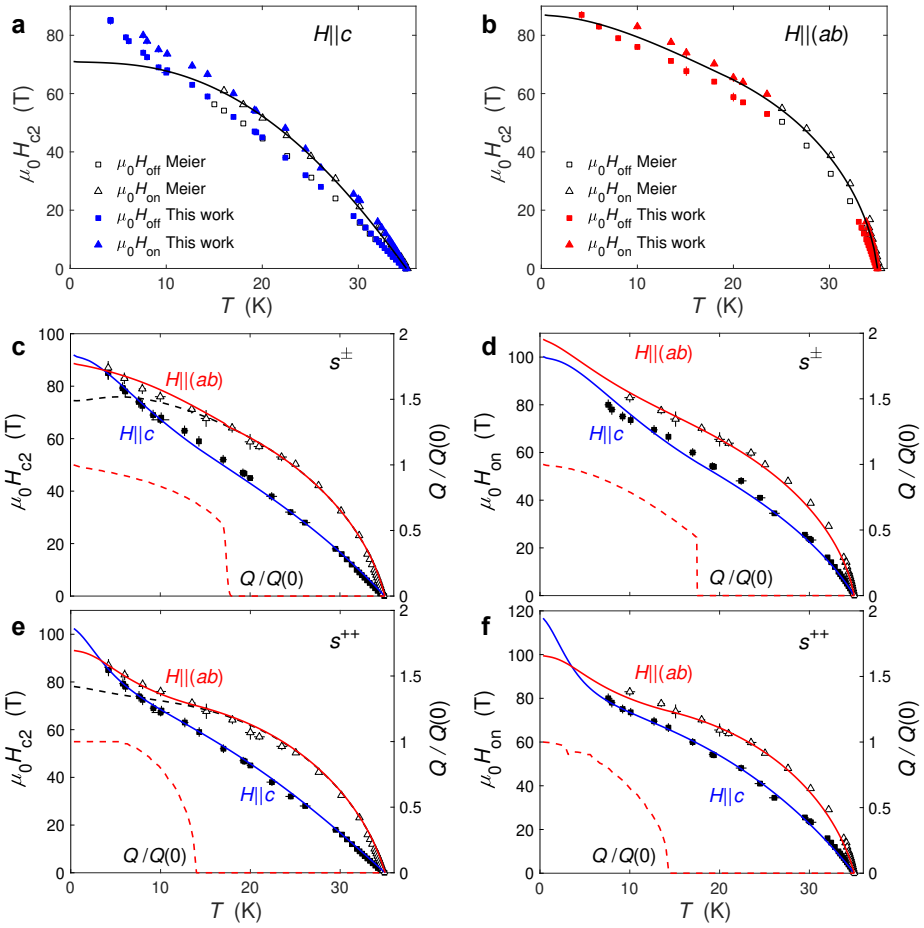


Figure A.4: **Two-band upper critical field models for $CaKFe_4As_4$ using different band coupling parameters.** **a** and **b** $\lambda_{11} = \lambda_{22} = 0$, $\lambda_{12}\lambda_{21} = 0.25$, $\eta = 0.2$, $\alpha = 0.5$ and $\epsilon = 1/6$ used previously to describe the onset upper critical field of $CaKFe_4As_4$ up to 60 T [61] when $H||c$ and $H||(ab)$ respectively. **c** $s^{\pm}$ pairing with $\lambda_{11} = \lambda_{22} = 0$, $\lambda_{12} = \lambda_{21} = 0.5$. Here $\alpha_1 = 0.95$, $\alpha_2 = 0$ and $\eta \sim 0.006$ for $H||c$, and $\alpha_1 = 3.1$, $\alpha_2 = 0.7$ and $\eta \sim 0.04$ for $H||(ab)$. **d** $s^{\pm}$ pairing for the onset critical field using the same parameters as in **c**, but with $\eta \sim 0.008$ and $\alpha_1 = 1.5$ when $H||c$, and $\alpha_1 = 4.2$ when $H||(ab)$. **e** s^{++} pairing with $\lambda_{11} = 0.81$, $\lambda_{22} = 0.29$ and $\lambda_{12} = \lambda_{21} = 0.1$. Here $\alpha_1 = 0.95$, $\alpha_2 = 0$ and $\eta \sim 0.02$ for $H||c$, and $\alpha_1 = 3.1$, $\alpha_2 = 0.0$ and $\eta \sim 0.04$ for $H||(ab)$. **f** s^{++} pairing for the onset critical field using the same parameters as in **e**, but with $\alpha_1 = 1.0$ when $H||c$, and $\alpha_1 = 3.5$ when $H||(ab)$. In **c**-**f** blue lines show the two-band model (with no FFLO state present) when $H||c$, dashed black lines show the two-band model with no FFLO state when $H||(ab)$, and the red lines show the two-band model with an FFLO state when $H||(ab)$. The temperature dependence of the FFLO Q vector is shown by the dashed red lines (the right-axis in **c**-**f**) for $H||(ab)$, and it is scaled to the zero-temperature value $Q(0)$. Note that the FFLO state emerges when $H||(ab)$ regardless of the pairing limit or which critical field criteria is chosen. This reinforces the robustness of this result.

Appendix B

Additional material for chapter 6

This section contains additional figures to support the results and conclusions presented in chapter 6. This includes additional resistivity against magnetic field data (figure B.1) that supports the magnetic field exponents found, and the extraction, fitting and analysis of low temperature $\rho_{H\to 0}(T)$ data inside the superconducting state (figures B.2-B.7).

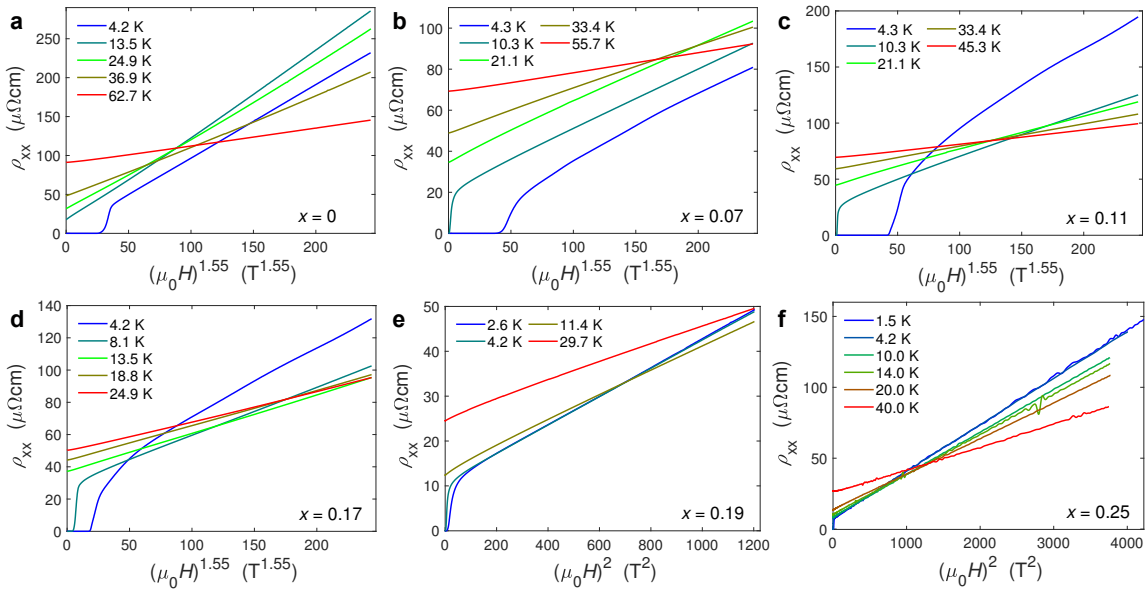


Figure B.1: **Field dependence of the transverse magnetoresistance of $FeSe_{1-x}S_x$ over a large magnetic field window. a-d** Resistivity as function of $(\mu_0 H)^{1.55}$ showing linear dependence for samples inside the nematic phase at constant temperatures below T_s up to a magnetic field of 35 T. At the lowest temperatures, below ~ 4.2 K, the magnetoresistance is dominated by quantum oscillations. **e-f** Resistivity versus $(\mu_0 H)^2$ at constant temperatures for samples in the tetragonal phase. Data for $x = 0.25$ were measured up to ~ 69 T.

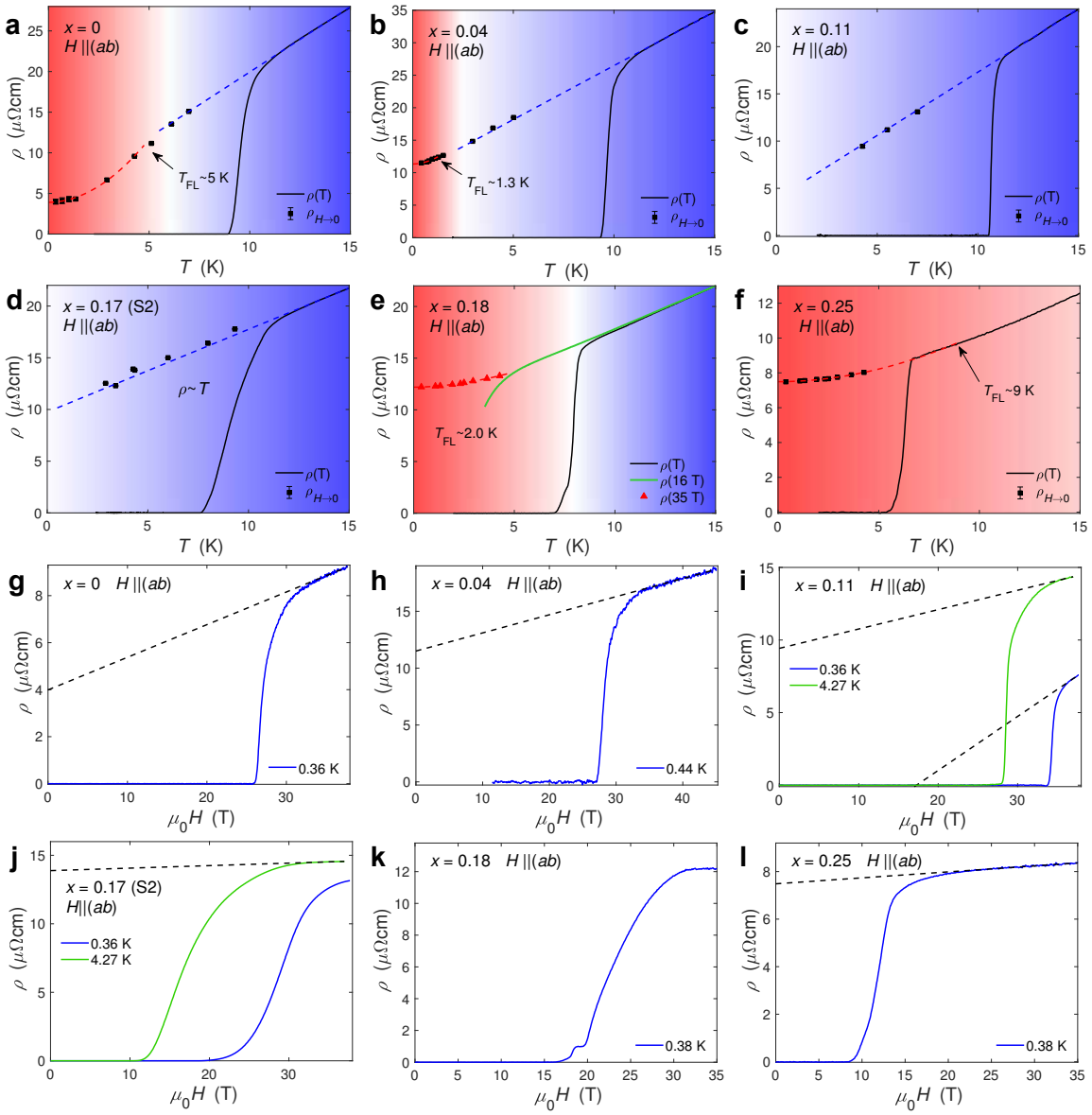


Figure B.2: **The low-temperature resistivity extracted from longitudinal magnetoresistance data of $FeSe_{1-x}S_x$. a-f** Temperature dependence of resistivity at low temperatures for different compositions used to build the low-temperature phase diagram in figure 6.7**b**. Solid squares show the extrapolated normal state resistivity, $\rho_{H\to 0}$ from **g-l**, and the solid triangles in **e** are the resistivity data at 35 T from **k**, when the magnetic field is along the conducting (ab) plane. Solid lines are the zero-field resistivity for each sample. Fermi-liquid like behaviour is observed in certain samples (with the largest resistivity ratio in figure 6.1**c**) below T_{FL}, as indicated by arrows. **g-l** Magnetic field-dependence of the resistivity at the lowest temperature when $H||(ab)$. Dashed lines are the linear extrapolation towards $H \to 0$. For $x = 0.11$ and 0.17, the upper critical field is too large to reach the normal state in magnetic fields up to 38 T in this orientation.

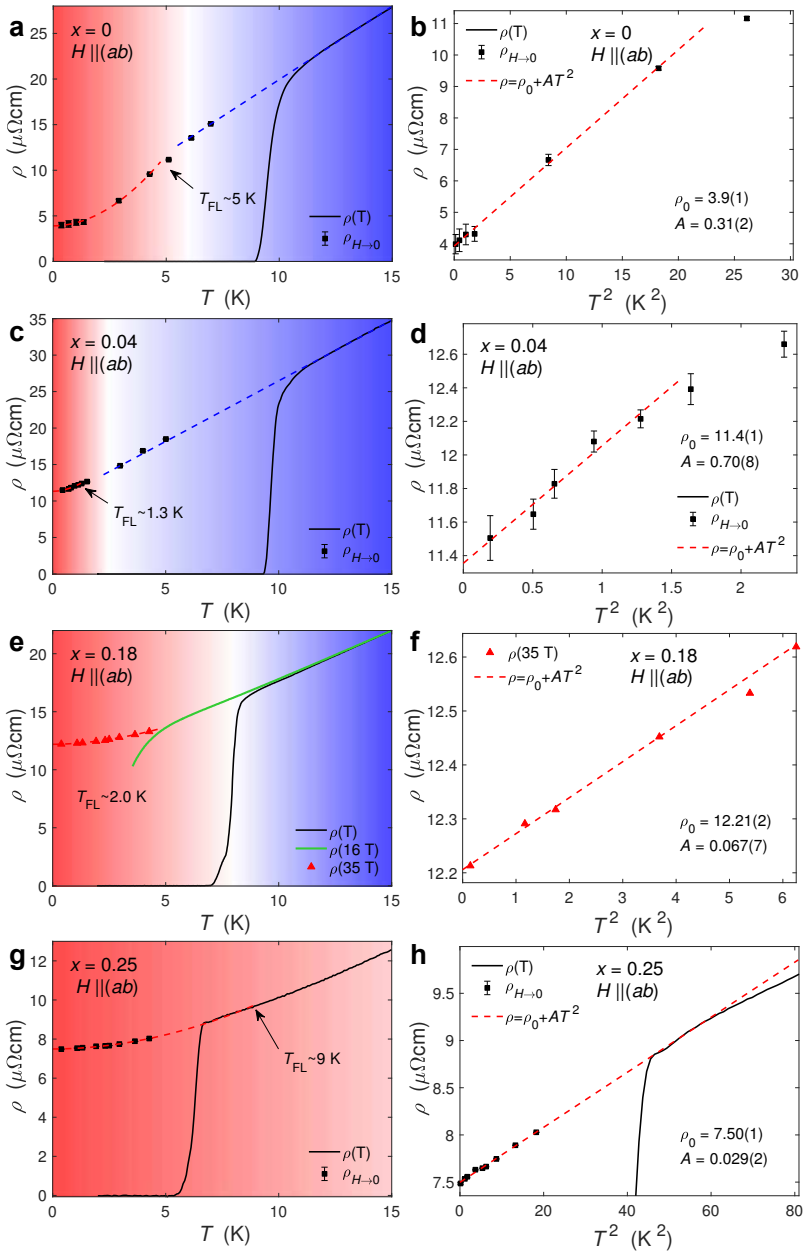


Figure B.3: **Evidence of Fermi liquid behaviour in certain samples of $FeSe_{1-x}S_x$. a**,**c**,**e**,**g** Temperature dependence of resistivity at low temperatures for different samples which show Fermi-liquid behaviour, extracted as detailed previously in figure B.2. The red dashed lines are fits of resistivity to a quadratic temperature dependence below T_{FL}, and the blue dashed lines show a linear dependence between $\sim T_{\mathrm{FL}}$ and T^*. Resistivity data taken at 16 T for $x \sim 0.18$ is also shown in **e** and follows the zero field curve at high temperatures as expected for longitudinal magnetoresistance. **b**,**d**,**f**,**h** The temperature dependence of resistivity against T^2 illustrating the Fermi-liquid behaviour, given by $\rho = \rho_0 + AT^2$. Here the dashed red lines are linear fits in T^2 and the zero-temperature resistivity values, ρ_0, and A parameters are listed in each panel. The samples with larger RRR also display higher T_{FL}.

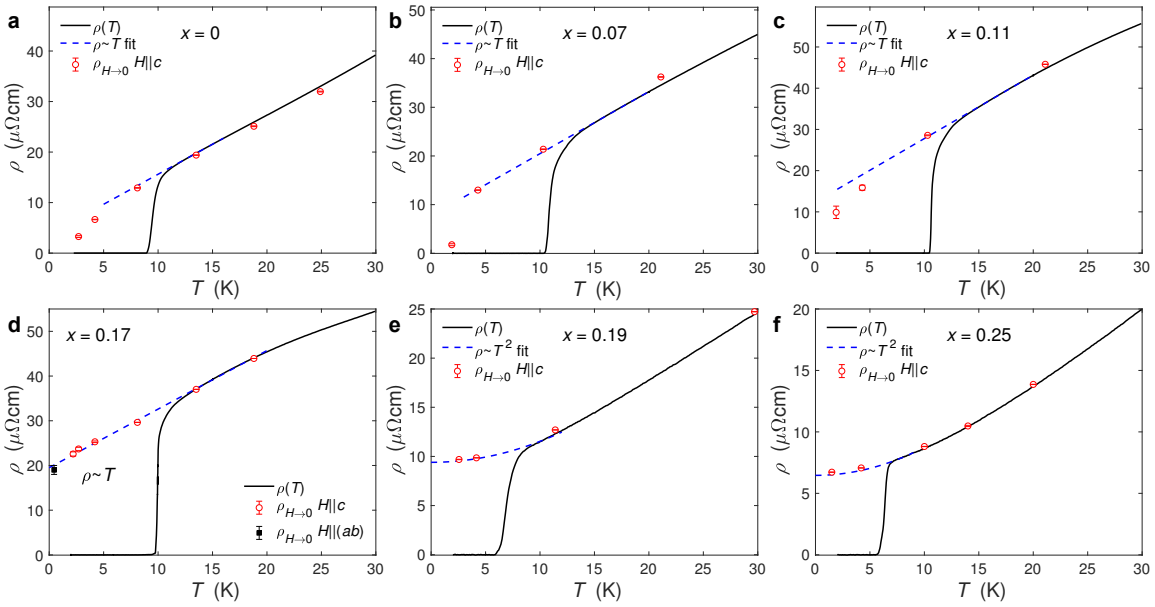


Figure B.4: **The low-temperature transport behaviour based on transverse magnetoresistance for $FeSe_{1-x}S_x$. a-f** Low temperature resistivity against temperature for different compositions. The open circles in each panel correspond to the extrapolated resistivity (from symmetrized magnetic field data) up to 35 T, using the magnetic field exponents of $\delta = 1.55$ inside the nematic state ($x \lesssim 0.18$) and $\delta = 2$ in the tetragonal state ($x = 0.19 - 0.25$), as shown in figure B.1. Inside the nematic phase the presence of quantum oscillations at low temperatures, makes the extrapolation of $\rho_{H\to 0}$ more difficult in this orientation when compared with longitudinal magnetoresistance studies, shown in figure B.2. In the tetragonal phase, Fermi-liquid behaviour is confirmed, similar to the longitudinal magnetoresistance studies in figure B.2**f**. Dashed lines are either linear fits to the resistivity inside the nematic state or quadratic fits in the tetragonal state. Linear resistivity is found in the vicinity of the nematic end point for $x \sim 0.17$ using both transverse and longitudinal magnetoresistance studies.

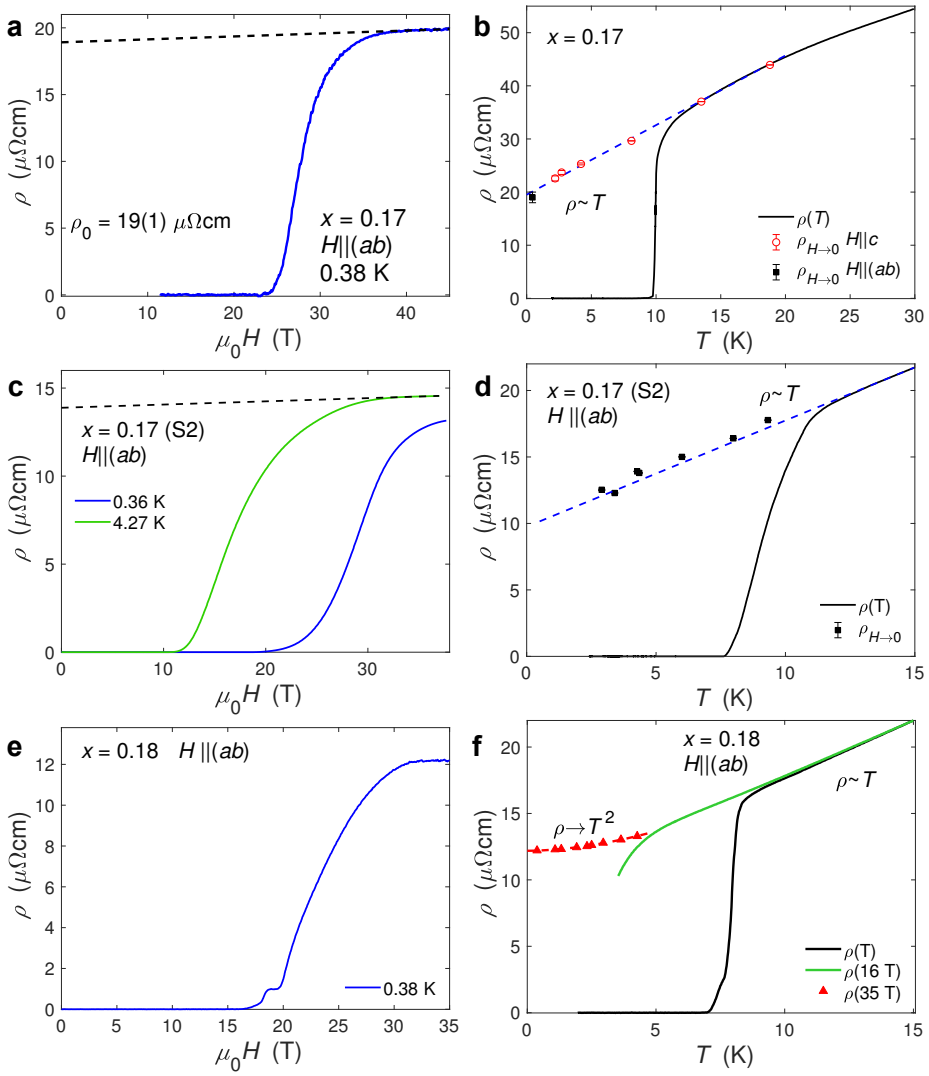


Figure B.5: **The low-temperature transport behaviour in the proximity of the nematic end point in FeSe$_{1-x}$S$_x$.** The nematic end point is defined as the complete suppression of the structural transition at $x_c \sim 0.180(5)$, which agrees with previous reports [43, 199]. **a**,**c**,**e** Resistivity against magnetic field up to $45\,\mathrm{T}$ at the lowest temperatures ($\sim 0.38\,\mathrm{K}$) for three different samples from the same batch with $H||(ab)$. For sample $x \sim 0.17$ (S2) extracting $\rho_{H\to 0}$ at the lowest temperatures is not possible up to $38\,\mathrm{T}$ and measurements at $\sim 4.2\,\mathrm{K}$, are also shown in **c**. **b**,**d**,**f** Resistivity against temperature for the same samples. Here the solid curves show the zero-field resistivity data and solid black squares are the extrapolated $\rho_{H\to 0}$ from $H||(ab)$ field sweeps in **a**, **c** and **e**. Solid triangles in **f** are the resistivity at $35\,\mathrm{T}$ shown in **e**. Dashed blue lines in **b** and **d** show a linear dependence, and the red dashed line in **f** show a Fermi-liquid behaviour for $x \sim 0.18$. The sample that shows Fermi-liquid behaviour has a larger RRR of ~ 24 compared to ~ 16 of the two other samples, suggesting that Fermi-liquid behaviour is observed only in cleaner samples.

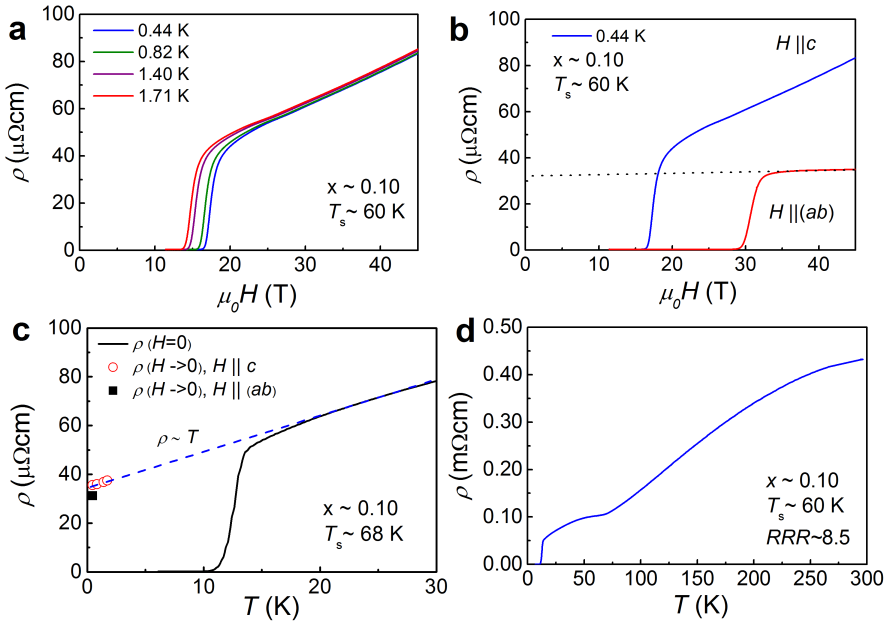


Figure B.6: **Magnetoransport data of a dirtier sample of $FeSe_{1-x}S_x$, with $x \sim 0.10$. a** Resistivity as a function of magnetic field at constant low temperatures with $H||c$. **b** Resistivity against magnetic field for two different orientations at base temperature, $H||c$ and $H||(ab)$. **c** Zero-resistivity data (solid curve) together with zero-field extrapolation using both linear extrapolation for $H||(ab)$ (solid square) from **b** and zero-field extrapolation using a $H^{1.55}$ dependence for $H||c$ (open circles) from **a**. **d** Resistivity versus temperature for $x \sim 0.10$ with $RRR \sim 8.5$. The strong suppression of quantum oscillations and the low RRR in this sample are evidence that it is a dirtier system which also display linear resistivity down to the lowest temperatures measured (~ 0.44 K). [This figure was produced by A. Coldea, who also gathered and analysed the data.]

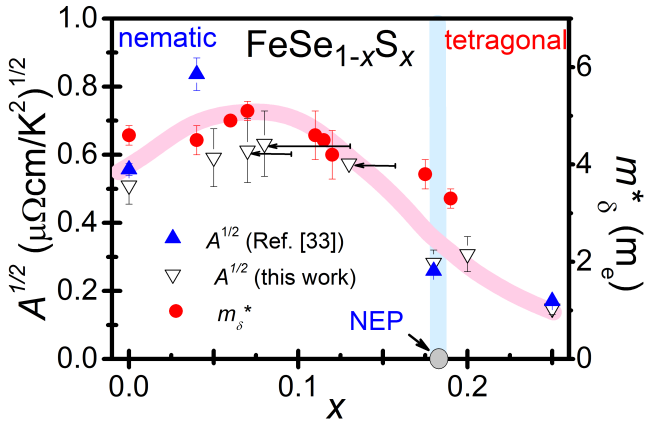


Figure B.7: **Comparison between the $A^{1/2}$ temperature coefficient and the effective masses for different compositions of FeSe$_{1-x}$S$_x$.** The band masses of the δ orbit (from Ref. [43]) are compared to the Fermi liquid coefficient, A, extracted at low temperatures (solid triangles) for compositions that show Fermi-liquid behaviour, as shown in Fig.B.3. Data reported in Ref. [201] are also included for comparison as open triangles. Please note that Ref. [201] uses nominal x_{nom} values which are shifted to smaller values (as indicated by horizontal arrows) to match the real x values based on EDX studies reported previously [43, 199]. The nematic end point (NEP) is indicated by an arrow and circle around $x \sim 0.180(5)$. Solid thick lines are guides to the eye. [This figure was produced by A. Coldea.]

Appendix C

Additional material for chapter 7

This section contains additional information to support the findings presented in chapter 7. First, the raw data, resistivity (figures C.1-C.7) and torque (figures C.8-C.10) against magnetic field, is presented for a selection of samples and all samples near the NEP. All of the two-band fits of the upper critical field are then shown (figures C.11-C.13), finally followed by the two-band parameters (figure C.14) and the Fermi velocities (figure C.15).

C.1 Raw data

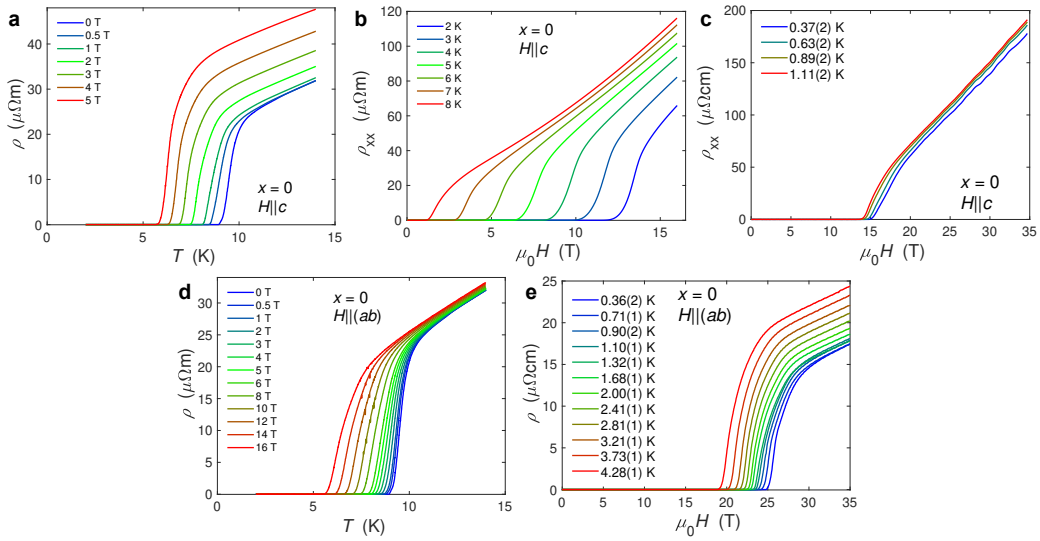


Figure C.1: **Resistivity data for $x = 0$ from which critical fields were extracted.** **a** resistivity against temperature at constant magnetic field when $H||c$. **b** and **c** resistivity against magnetic field at fixed temperatures when $H||c$ up to 16 T in Oxford and 35 T in Nijmegen respectively. **d** resistivity against temperature at constant magnetic field when $H||(ab)$. **e** resistivity against magnetic field at fixed temperatures when $H||(ab)$ up to 35 T.

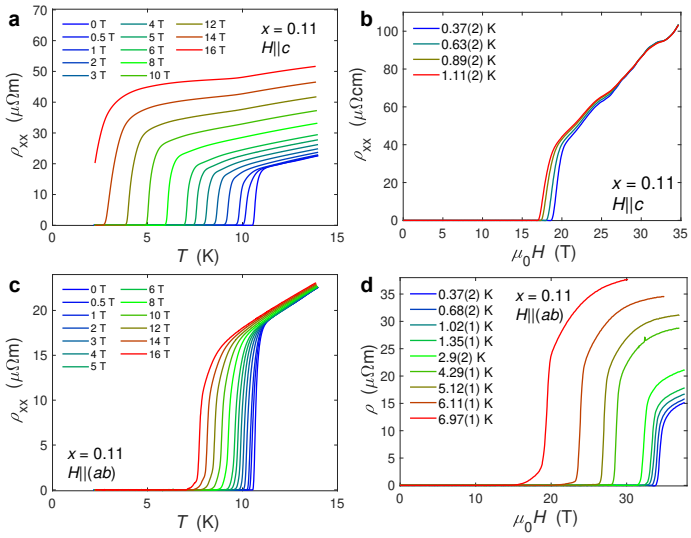


Figure C.2: **Resistivity data for $x = 0.11$ from which critical fields were extracted. a** resistivity against temperature at constant magnetic field when $H||c$. **b** resistivity against applied magnetic field at fixed temperatures up to 38 T when $H||c$. **c** resistivity against temperature at constant magnetic field when $H||(ab)$. **d** resistivity against applied magnetic field at fixed temperatures up to 38 T when $H||(ab)$.

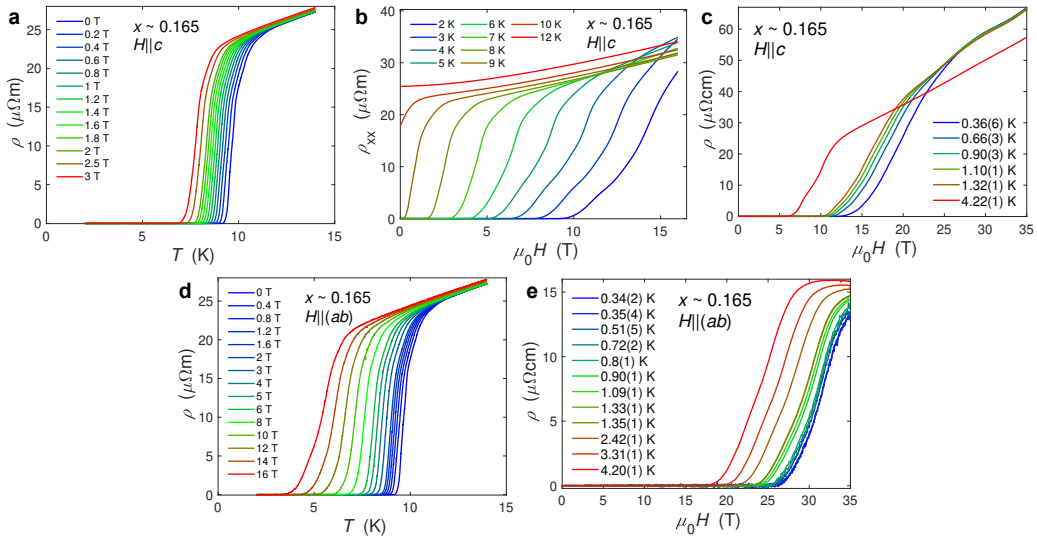


Figure C.3: **Resistivity data for $x \sim 0.165$ from which critical fields were extracted. a** resistivity against temperature at fixed magnetic fields when $H||c$. **b** and **c** resistivity against temperature at constant magnetic field when $H||c$ up to 16 T in Oxford and 35 T in Nijmegen respectively. **d** resistivity against temperature at constant magnetic fields when $H||(ab)$. **e** resistivity against applied magnetic field up to 35 T at fixed temperatures when $H||(ab)$.

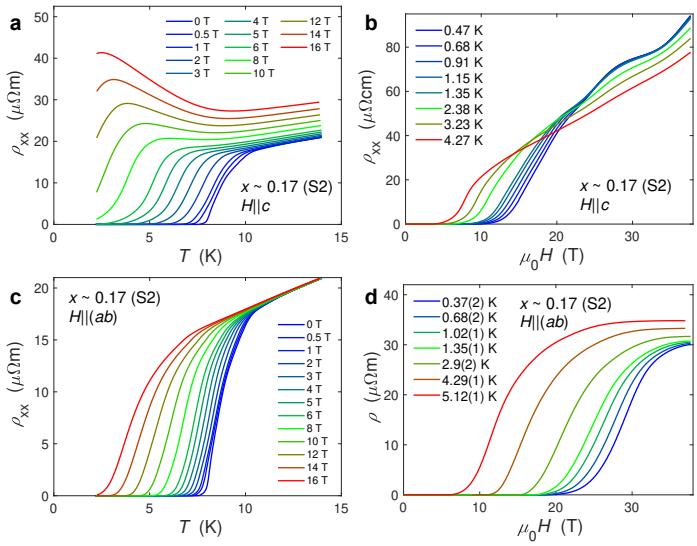


Figure C.4: **Resistivity data for a second sample with $x \sim 0.17$ (S2) from which critical fields were extracted.** **a** resistivity against temperature at constant magnetic field when $H||c$. **b** resistivity against magnetic field at fixed temperatures when $H||c$ up to $\sim 38\,\mathrm{T}$. **c** resistivity against temperature at constant magnetic field when $H||(ab)$ **d** resistivity against applied magnetic field at fixed temperatures when $H||(ab)$ up to $38\,\mathrm{T}$ in taken in Nijmegen.

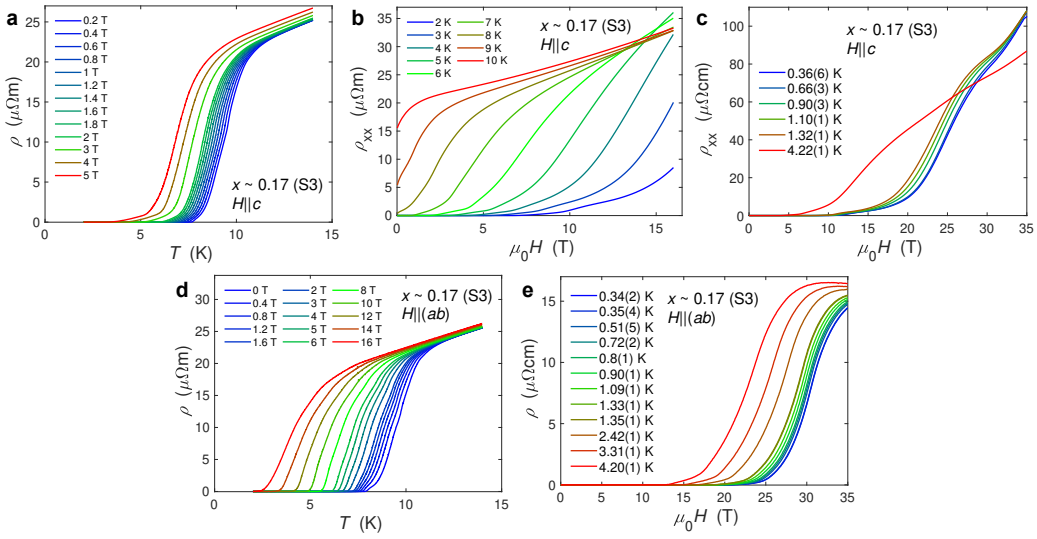


Figure C.5: **Resistivity data for a thrid sample with $x \sim 0.17$ (S3) from which critical fields were extracted.** **a** resistivity against temperature at constant magnetic field when $H||c$. **b** and **c** resistivity against temperature at constant magnetic field when $H||c$ up to $16\,\mathrm{T}$ in Oxford and $35\,\mathrm{T}$ in Nijmegen respectively. **d** resistivity against temperature at constant magnetic field when $H||(ab)$. **e** resistivity against applied magnetic field at fixed temperatures up to $35\,\mathrm{T}$ when $H||(ab)$.

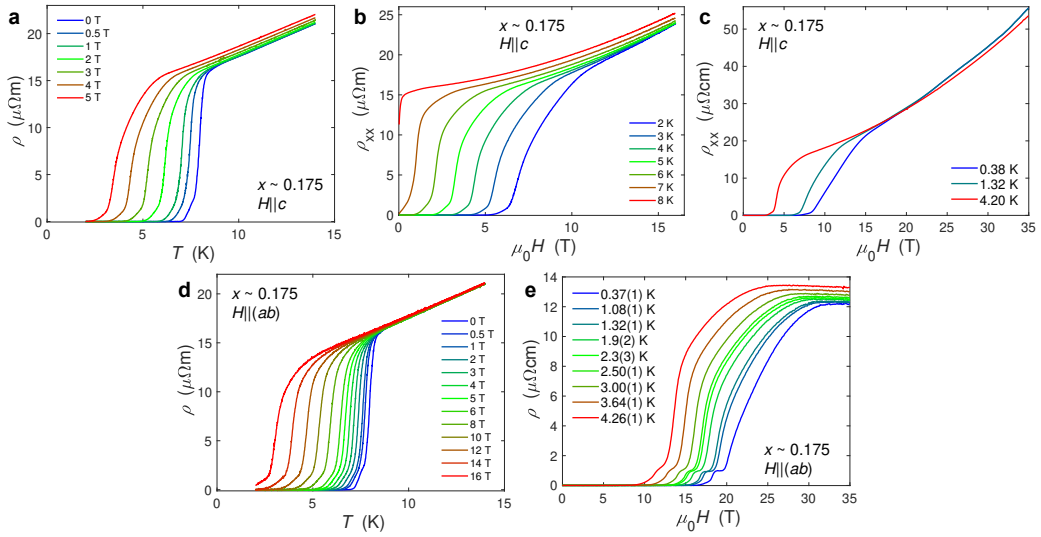


Figure C.6: **Resistivity data for $x \sim 0.175$ from which critical fields were extracted.** **a** resistivity against temperature at constant magnetic field when $H||c$. **b** and **c** resistivity against temperature at constant magnetic field when $H||c$ up to 16 T in Oxford and 38 T in Nijmegen respectively. **d** resistivity against temperature at constant magnetic field when $H||(ab)$. **e** resistivity against applied magnetic field at fixed temperatures up to 38 T when $H||(ab)$.

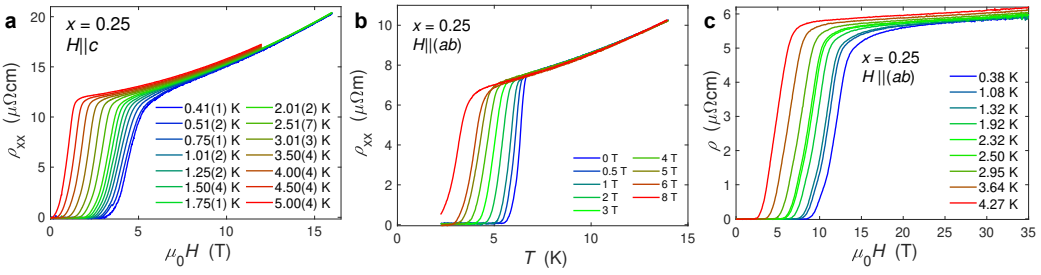


Figure C.7: **Resistivity data for $x = 0.25$ from which critical fields were extracted.** **a** resistivity against magnetic field at fixed temperatures when $H||c$ up to 16 T. **b** resistivity against temperature at constant magnetic field when $H||(ab)$. **c** resistivity against magnetic field at fixed temperatures when $H||(ab)$ up to 35 T.

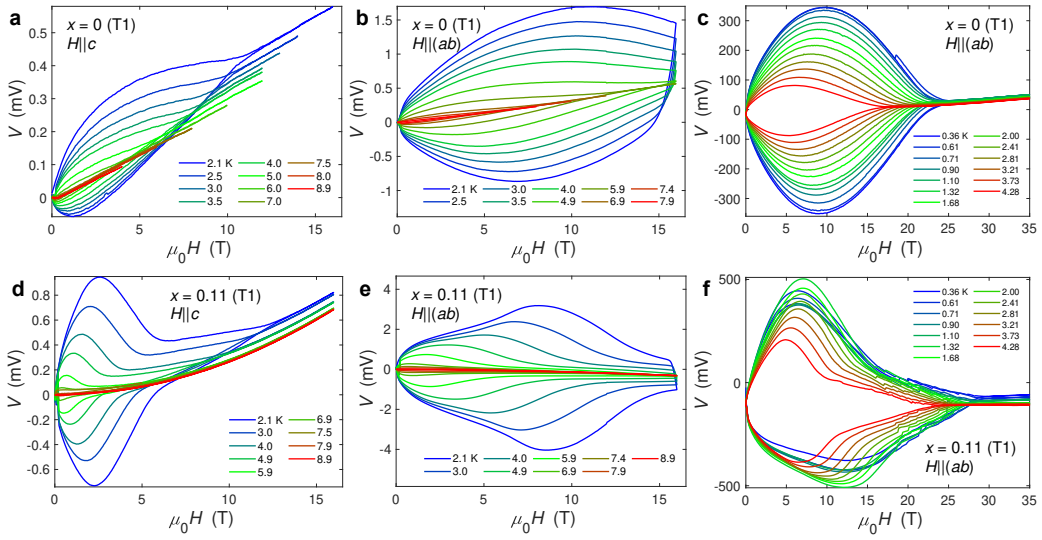


Figure C.8: **Torque data inside the nematic state.** **a** voltage against applied magnetic field torque data at fixed temperatures with $H||c$ for a single crystal of $x = 0$. **b** and **c** voltage against applied magnetic field torque data at fixed temperatures with $H||(ab)$ for a single crystal of $x = 0$, taken up to $16\,\mathrm{T}$ in Oxford and $38\,\mathrm{T}$ in Nijmegen respectively. **d** voltage against applied magnetic field torque data at fixed temperatures with $H||c$ for a single crystal of $x = 0.11$. **e** and **f** voltage against applied magnetic field torque data at fixed temperatures with $H||(ab)$ for a single crystal of $x = 0.11$, taken up to $16\,\mathrm{T}$ in Oxford and $38\,\mathrm{T}$ in Nijmegen respectively.

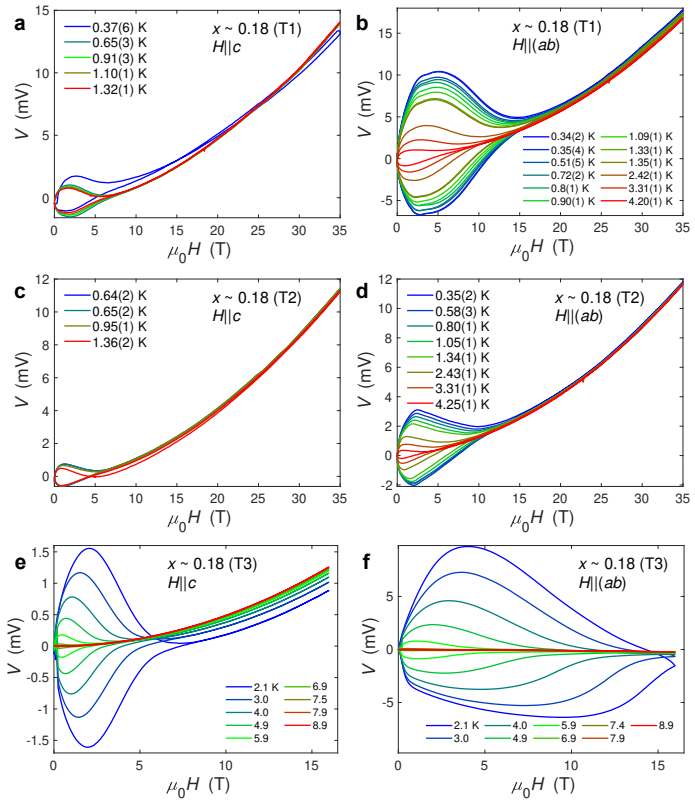


Figure C.9: **Torque data near the nematic end point for 3 different samples.** **a** and **b** voltage against applied magnetic field up to 35 T at fixed temperatures for sample $x \sim 0.18$ (T1) when $H||c$ and $H||(ab)$ respectively. **c** and **d** voltage against applied magnetic field up to 35 T at fixed temperatures for sample $x \sim 0.18$ (T2) when $H||c$ and $H||(ab)$ respectively. **e** and **f** voltage against applied magnetic field up to 16 T at fixed temperatures for sample $x \sim 0.18$ (T3) when $H||c$ and $H||(ab)$ respectively.

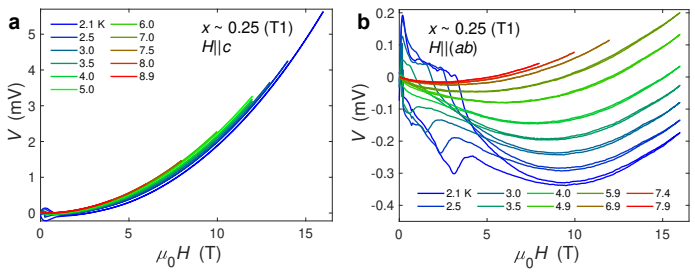


Figure C.10: **Torque data outside of the nematic state.** **a** and **b** voltage against applied magnetic field up to 16 T at fixed temperatures for sample $x \sim 0.25$ (T1) when $H||c$ and $H||(ab)$ respectively.

C.2 Two-band model parameters

This section covers additional information and figures for the parameters from the two-band model of the upper critical field for $FeSe_{1-x}S_x$. First, a comparison of different cases for FeSe is presented before moving on to changes across the phase diagram.

Figure C.11 shows two-band models of the upper critical field for FeSe for different band coupling parameters. Figures C.11**a**-**c** shows offset critical field data from resistivity measurements, and figures C.11**d**-**f** show irreversibility field data extracted from torque measurements. The parameters used for each case are listed in table C.1, where "$s^{\pm}$ dominant" refers to the parameters described in detail in chapter 7. Perhaps the most important parameters to compare in table C.1 is the residual errors (bottom row) between each band coupling limit. These residual errors are calculated as

$$\text{error} = \frac{1}{N}\sum_{i=1}^{N}\frac{(\mu_0 H_{\text{c2}}[i] - \mu_0 H_{\text{model}}[i])^2}{(\mu_0 H_{\text{c2}}[i])^2}, \tag{C.1}$$

where N is the number of data points (excluding T_{c}, where $H_{\text{c2}} = 0$ and the point is ignored), $\mu_0 H_{\text{c2}}$ are the upper critical field data and $\mu_0 H_{\text{model}}$ are the points generated by the two-band model. The residual errors have been normalised to the number of points. These values in table C.1 clearly show that the errors are smallest for the $s^{\pm}$ case with a dominant band ($\lambda_{11} > 0$, $\lambda_{22} = 0$ and $\lambda_{12} = \lambda_{21} = 0.5$) for critical fields extracted from resistivity and torque measurements in both magnetic field orientations. This implies that this band coupling limit provides the best representation of the upper critical field for FeSe.

Table C.1: Two-band parameters for models of the upper critical fields in FeSe in different pairing limits (different band coupling constants). Here the columns labelled "$s^{\pm}$ dominant" refer to the two-band fits that are shown in the main body in chapter 7, with strong inter-band coupling and a large value for λ_{11}, where the larger superconducting gap will be present.

FeSe	$\mu_0 H_{\rm off}$						$\mu_0 H_{\rm irr}$					
	$s^{\pm}$ dominant		pure $s^{\pm}$		s^{++}		$s^{\pm}$ dominant		pure $s^{\pm}$		s^{++}	
$H\|\|$	c	(ab)	c	(ab)	c	(ab)	c	(ab)	c	(ab)	c	(ab)
$T_{\rm c}$ (K)	9.08	9.08	9.08	9.08	9.08	9.08	8.5	8.5	8.5	8.5	8.5	8.5
λ_{11}	0.5	0.5	0	0	0.81	0.81	0.5	0.5	0	0	0.81	0.81
λ_{22}	0	0	0	0	0.29	0.29	0	0	0	0	0.29	0.29
λ_{12}	0.5	0.5	0.5	0.5	0.1	0.1	0.5	0.5	0.5	0.5	0.1	0.1
λ_{21}	0.5	0.5	0.5	0.5	0.1	0.1	0.5	0.5	0.5	0.5	0.1	0.1
α_1	0	1.6	0	1.6	0	1.6	0	1.6	0	1.6	0	1.6
α_2	0	0	0	0.5	0	0	0	0	0	0.5	0	0
v_1 (meVÅ)	355	137	438	153	277	124	340	132	392	151	254	117
v_2 (meVÅ)	42	19	98	68	48	39	40	19	111	43	40	33
η	0.014	0.02	0.05	0.2	0.03	0.1	0.014	0.02	0.08	0.08	0.025	0.08
$T_{\rm FFLO}$ (K)	–	2.8	–	2.2	–	–	–	2.63	–	2.8	–	–
error (10^{-2})	1.37	1.18	1.54	1.70	7.63	1.51	0.14	0.011	0.62	0.86	0.59	0.57

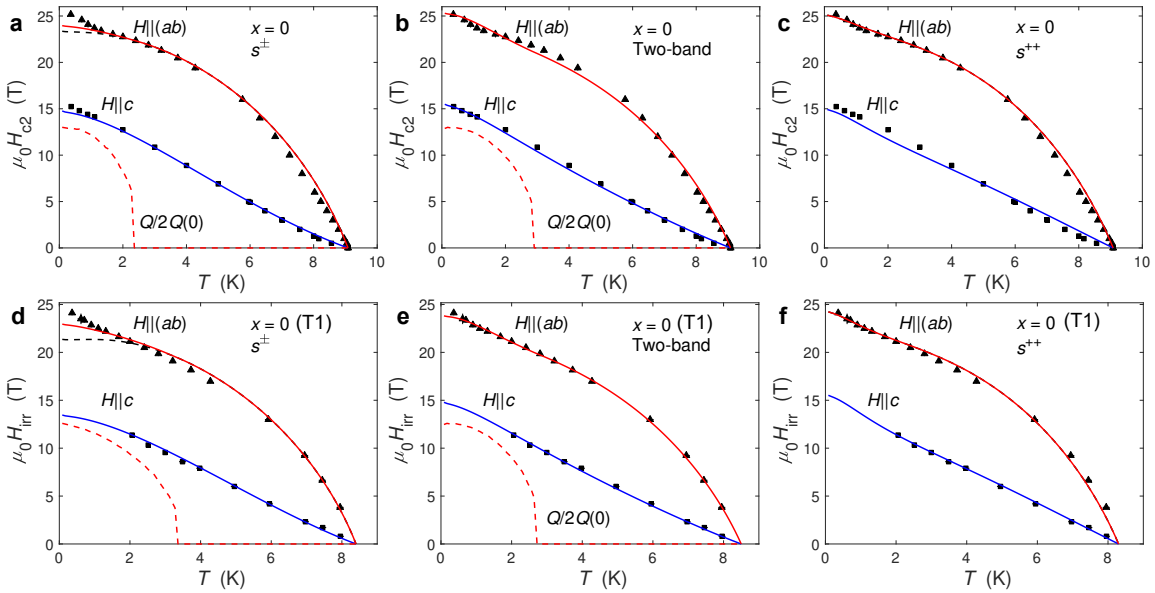


Figure C.11: **Two-band fits to upper critical field data of FeSe in both field orientations in different limits.** Temperature dependence of $\mu_0 H_{c2}$ from resistivity measurements in the **a** pure inter-band limit using $\lambda_{11} = \lambda_{22} = 0$, $\lambda_{12} = \lambda_{21} = 0.5$, $\alpha_{ab,1} = 1.6$, $\alpha_{ab,2} = 0.5$, $\eta_c \sim 0.05$ and $\eta_{ab} \sim 0.2$; **b** inter-band limit with a dominant band using $\lambda_{11} = 0.81$, $\lambda_{22} = 0$, $\lambda_{12} = \lambda_{21} = 0.5$, $\alpha_{ab,1} = 1.6$, $\alpha_{ab,2} = 0$, $\eta_c \sim 0.02$ and $\eta_{ab} \sim 0.02$; and **c** the intra-band limit (s^{++} pairing limit) using $\lambda_{11} = 0.81$, $\lambda_{22} = 0.29$, $\lambda_{12} = \lambda_{21} = 0.1$, $\alpha_{ab,1} = 1.6$, $\alpha_{ab,2} = 0$, $\eta_c \sim 0.03$ and $\eta_{ab} \sim 0.1$. **d-f** two-band models of the irreversibility field extracted from torque data for the same band coupling constants as in **a**-**c**, respectively. When $H||c$ $\alpha_{c,1} = \alpha_{c,2} = 0$ for all panels. Fits when $H||c$ and $H||(ab)$ are represented by blue and red lines respectively. Dashed red lines represent the scaled Q vector of the FFLO state when $H||(ab)$ in **a** and **b**. Note that no FFLO state is necessary when $H||c$, or for the s^{++} case when $H||(ab)$ in **c**. The dashed black line in **a** represents the two-band model when $H||(ab)$ with $Q = 0$ for all temperatures (no FFLO state). The difference between this and the red line at low temperatures is an example of how the FFLO state enhances the upper critical field at low temperatures. The three cases are presented here to compare between different pairing limits. The pure $s^{\pm}$ case in **a** fails at low temperatures for both field orientations. The s^{++} case in **b** works well for $H||(ab)$ with no FFLO state, but does not represent the data when $H||c$ well. The inter-band limit with a dominant band in **b** gives the best description of the data. Similar comparisons to other sulphur substitutions to determine how the parameters vary across the phase diagram. A summary of the parameters for each case are show in table C.1.

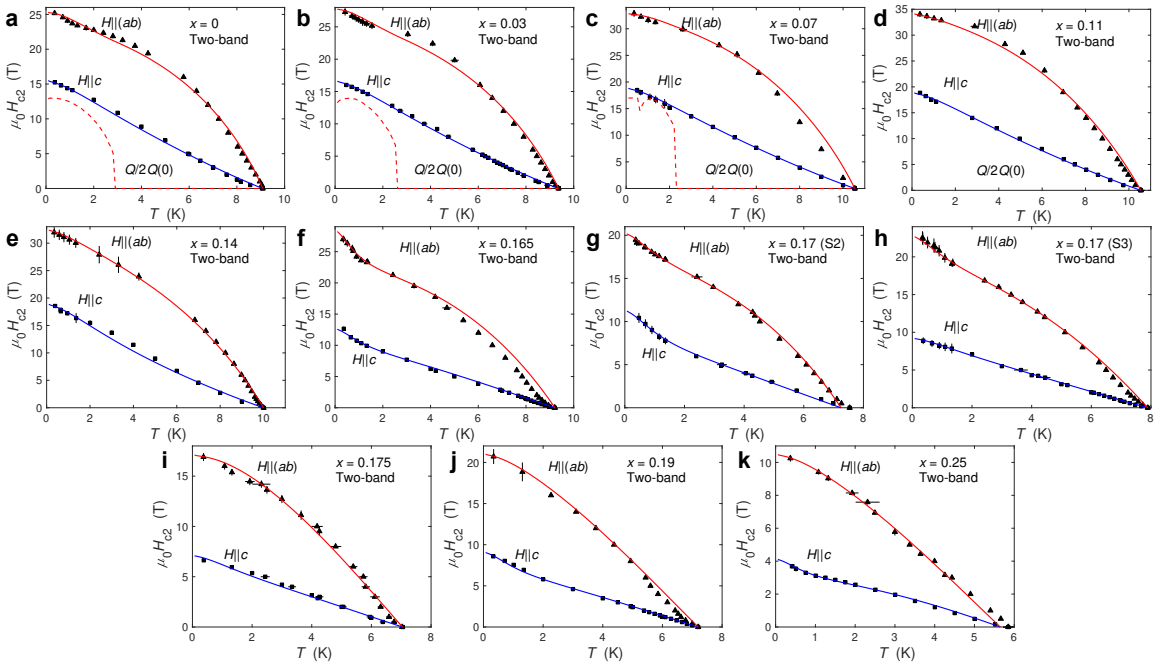


Figure C.12: **Two-band fits to upper critical field data from electrical transport for both $H||c$ (blue) and $H||(ab)$ (red).** Models of the upper critical field, $H_{c2}(T)$, using the Gurevich two-band model for the samples labelled in their respective panels. Here the black squares are the upper critical field data when $H||c$ and the black triangles when $H||(ab)$. The blue lines are the model when $H||c$, and the red lines when $H||(ab)$. The magnitude of the FFLO Q modulation is shown as a dashed red line.

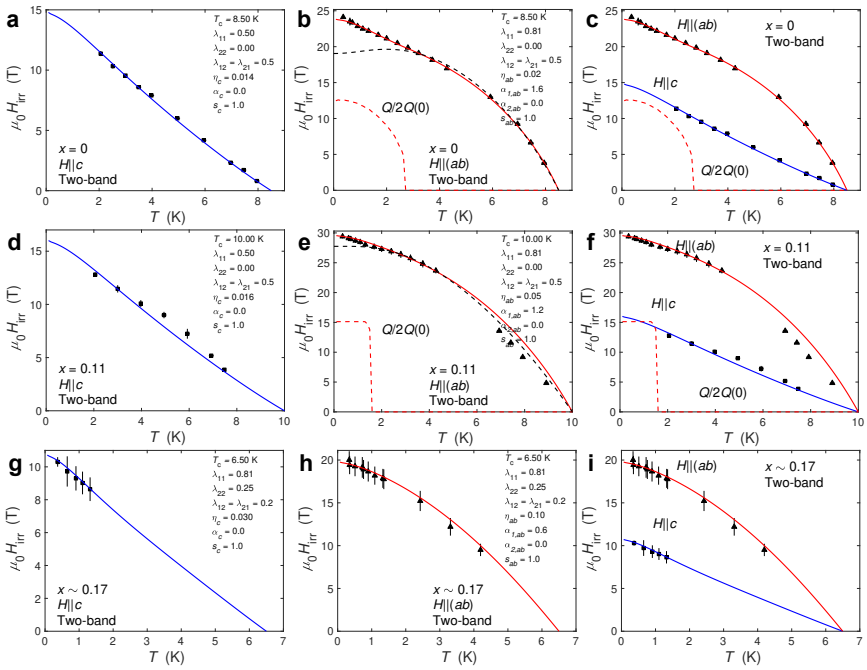


Figure C.13: **Two-band fits to upper critical field data from torque for both $H||c$ (blue) and $H||(ab)$ (red).** Models of the upper critical field, $H_{c2}(T)$, using the Gurevich two-band model for the samples labelled in their respective panels. Here the black squares are the upper critical field data when $H||c$ and the black triangles when $H||(ab)$. The blue lines are the model when $H||c$, and the red lines when $H||(ab)$. The magnitude of the FFLO Q modulation is shown as a dashed red line. The parameters used to produce the models of the upper critical field are shown in each panel.

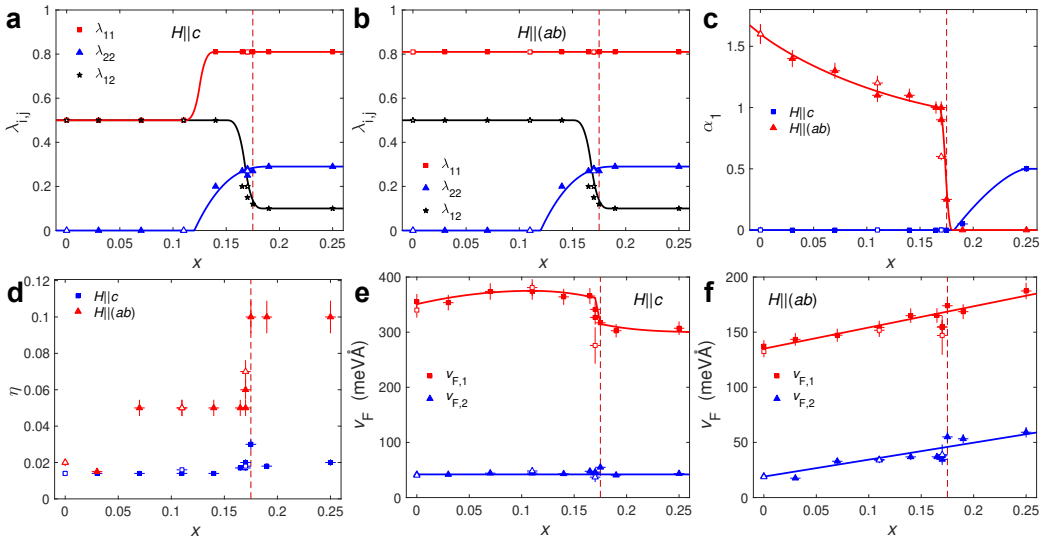


Figure C.14: **Parameters from the two-band model as a function of x in FeSe$_{1-x}$S$_x$. a** and **b** the band coupling constants $\lambda_{i,j}$ as a function of x for $H||c$ and $H||(ab)$ respectively. **c** α_1 as a function of x for $H||c$ (blue) and $H||(ab)$ (red). **d** variation of $\eta = v_2^2/v_1^2$ with sulphur substitution x for $H||c$ (blue) and $H||(ab)$ (red). **e** and **f** Fermi velocities from the two-band upper critical field model as a function of x for $H||c$ and $H||(ab)$ respectively. Here red represents band 1 (the dominant band) and blue band 2.

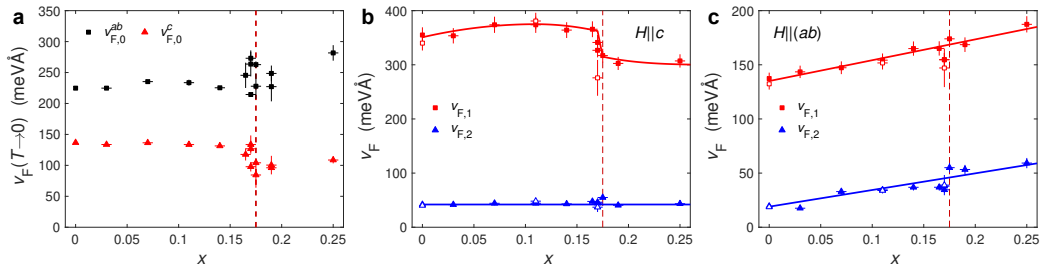


Figure C.15: **Fermi velocities for FeSe$_{1-x}$S$_x$ from the upper critical field data. a** Fermi velocities from coherence lengths as $T \to 0$ for ξ_{ab} (black) and ξ_c (red) extracted using $\xi = (\hbar v_F)/(2\pi k_B T_c)$. **b** and **c** Fermi velocities from the two-band upper critical field model as a function of x for $H||c$ and $H||(ab)$ respectively. Here red represents band 1 (the dominant band) and blue band 2. The Fermi velocities of band 1 (v_1) when $H||c$ in **b** seem to follow the same trend as T_c, with a drop at the NEP, while v_2 remains relatively constant. The behaviour is different when $H||(ab)$ in **c**, with both v_1 and v_2 increasing linearly. This suggests that the behaviour along each orientation may be dominated by a different band. The v_1 values when $H||c$ are well matched to the previously reported values of the outer hole band α, and the values of v_1 when $H||(ab)$ are similar to those reported for the β electron pocket.

C.3 Modelling the Maki parameter

For a single-band superconductor in the clean limit the Maki parameter, α_{M}, for $H||c$ is given by

$$\alpha_{\mathrm{M},c} = \frac{\pi \Delta m^{\star}}{4 E_{\mathrm{F}} m_e}, \tag{C.2}$$

where Δ is the superconducting gap, $m^{\star}$ is the effective mass, E_{F} is the Fermi energy, m_e is the electron mass. For $H||(ab)$ the Maki parameter is given by

$$\alpha_{\mathrm{M},ab} = \frac{\pi \Delta m^{\star} v_{\mathrm{F}}^{ab}}{4 E_{\mathrm{F}} m_e v_{\mathrm{F}}^{c}} = \frac{\alpha_{\mathrm{M},c} v_{\mathrm{F}}^{ab}}{v_{\mathrm{F}}^{c}}, \tag{C.3}$$

where v_{F}^{ab} and v_{F}^{c} are Fermi velocities in the two field orientations.

α_{M} values are modelled for both magnetic field orientations here based on $m^{\star}$ and E_{F} values from APRES and quantum oscillation experiments and Δ from the Δ_1 (of the dominant band) that are found here. The velocity ratio $v_{\mathrm{F}}^{ab}/v_{\mathrm{F}}^{c}$ can be predicted from the upper critical field as $1/v_{\mathrm{F}}^2 \propto |dH_{\mathrm{c2}}/dT|_{T_{\mathrm{c}}}$ and $1/v_{\mathrm{F}}^2 \propto H_{\mathrm{c2}}(T=0)$. This gives us two methods to estimate this ratio, using the slope of H_{c2} near T_{c},

$$\frac{v_{\mathrm{F}}^{ab}}{v_{\mathrm{F}}^{c}} = \sqrt{\frac{|dH_{\mathrm{c2}}^{c}/dT|_{T_{\mathrm{c}}}}{|dH_{\mathrm{c2}}^{ab}/dT|_{T_{\mathrm{c}}}}}, \tag{C.4}$$

and the low temperature value of H_{c2},

$$\frac{v_{\mathrm{F}}^{ab}}{v_{\mathrm{F}}^{c}} = \sqrt{\frac{H_{\mathrm{c2}}^{c}(T=0)}{H_{\mathrm{c2}}^{ab}(T=0)}}. \tag{C.5}$$

This ratio is ~ 0.6.

α_{M} is modelled for different bands (the outer hole band and the two electron bands), and find the the sum of the different contributions gives a relatively good model of the Maki parameter that is experimentally found (see figure C.16).

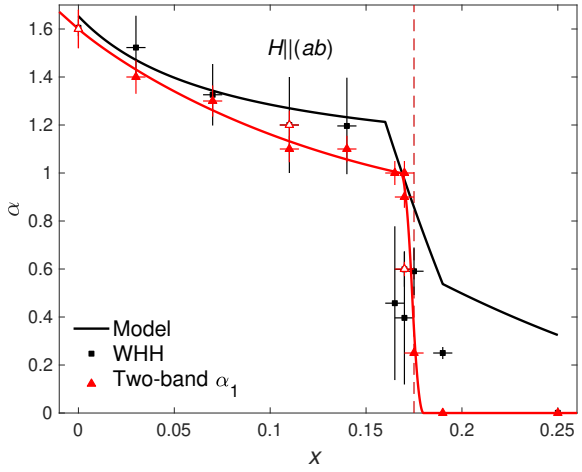


Figure C.16: **Maki parameters from different models in $FeSe_{1-x}S_x$.** The Maki parameter from different models as a function of sulphur concentration when $H||(ab)$. Black points show α_{M} from fits using the WHH model, and red points are α_1 from the two-band model. The solid red line is a guide to the eye for α_1 from the two-band model. The solid black line is the theoretical Maki parameter, calculated as the sum of contributions from the dominant hole band and the electron bands.

Appendix D

Additional material for chapter 8

This section contains supporting information for the conclusions in chapter 8. This includes further evidence of the 2D scaling of σ_{SCF} (figure D.1), and the temperature dependence of σ_{SCF} extracted from $H^{1.55}$ exponent fitting for $x = 0.03$, which also shows 2D scaling (figure **??**).

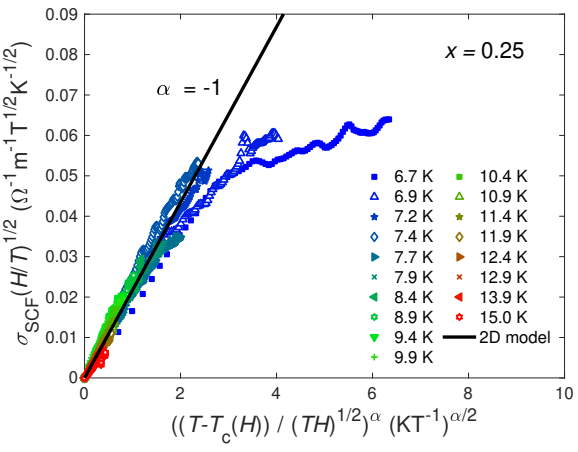


Figure D.1: **Exponent of the magnetic field scaling of the 2D superconducting fluctuations.** Scaling of the superconducting fluctuations from figure 8.6**d** scaled using an exponent of $\alpha = -1$. The colours represent different temperatures. The curves scale onto a single straight line (black), showing the persistence of 2D fluctuations over a large temperature range. The same trend is observed in other samples.

To clarify the dimensionality of the superconducting fluctuations they have been extracted using a different method on the $x = 0.03$ sample, deep inside the nematic phase. For low x values it was established in chapter 6 that the transverse in-plane magnetoresistivity obey a $H^{1.55}$ power law. This exponent is used and fits to the high-field region as $\rho_{\mathrm{n}} = \rho_{H=0} + bH^{1.55}$ are performed, and then the superconducting fluctuations are calculated using $\sigma_{\mathrm{SCF}} = \rho_{\mathrm{xx}}^{-1} - \rho_{\mathrm{n}}^{-1}$. The zero field values are shown as a function of reduced

temperature in figure D.3**a**. Here it is clear that the fluctuations again fall onto the 2D line, with only slight deviation. This shows that the results extracted are robust and independent of the extraction method, and reinforces their 2D nature. Note that if a H^2 power law is used on the $x = 0.25$ sample (in the tetragonal phase, where in chapter 6 a H^2 dependence was determined) then 2D superconducting fluctuations are also observed (see figure D.3**b**).

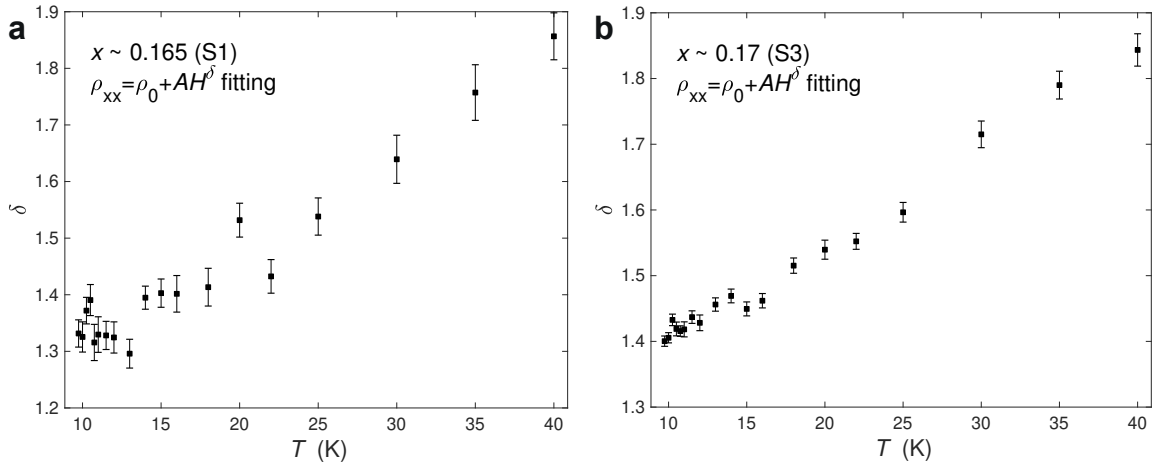


Figure D.2: **a** and **b** Temperature dependence of the magnetic field exponent δ from H^δ fitting used to extracted the excess conductivity for the two samples near the magnetic end point, $x \sim 0.165$ and $\sim 0.17(\mathrm{S3})$ respectively.

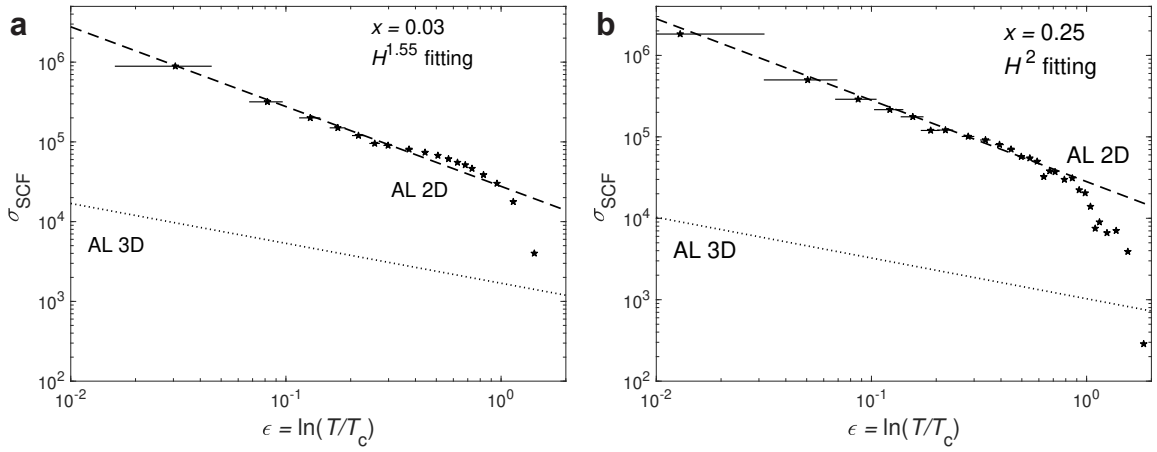


Figure D.3: **a** Temperature dependence of the SCF conductivity extracted from fits using the model $\rho_{\mathrm{xx}} = \rho_{H=0} + aH^{1.55}$ for the $x = 0.03$ sample, which was established to describe the ρ_{xx} magneto-resistivity inside the nematic state in chapter 6 and Ref. [219]. **b** Temperature dependence of the excess conductivity using a model quadratic in magnetic field, $\rho_{\mathrm{xx}} = \rho_{H=0} + aH^2$, for the $x = 0.25$ sample. This exponent was also found to dominate in this part of the phase diagram in chapter 6 and Ref. [219]. σ_{SCF} against reduced temperature again collapses onto the 2D AL line here, suggesting that 2D fluctuations is a robust result, and not dependent on the model used to extract the fluctuating conductivity.

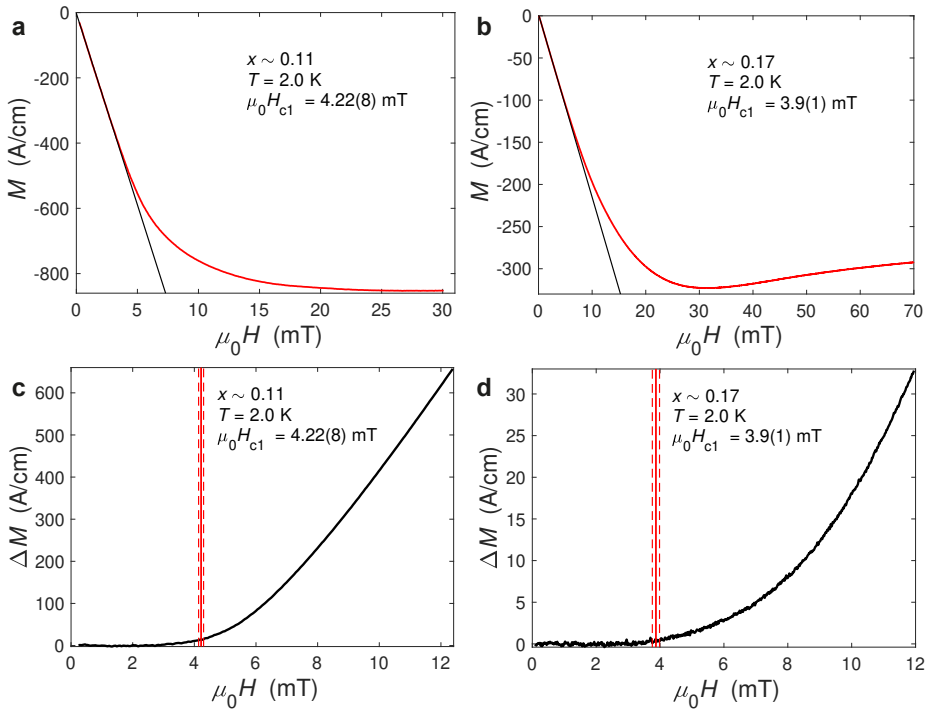


Figure D.4: **a** and **b** Magnetisation against applied magnetic field at 2 K for single crystals with $x = 0.11$ and $x \sim 0.17$ respectively. Red lines show $M(H)$ and black lines show linear fits to the low-field part of the data, where $M(H)$ is linear as the superconductor is in the Meissner state. **c** and **d** ΔM against applied magnetic field, where $\Delta M(H) = M(H) - M_{\mathrm{LinFit}}(H)$, $M(H)$ is the raw magnetisation data and $M_{\mathrm{LinFit}}(H)$ is the linear fit to the Meissner state. The lower critical field, $\mu_0 H_{\mathrm{c1}}$, is defined as the point at which ΔM deviates from the background error (where $\Delta M(H) \sim 0$) by 1 standard deviation, and are listed in each panel.

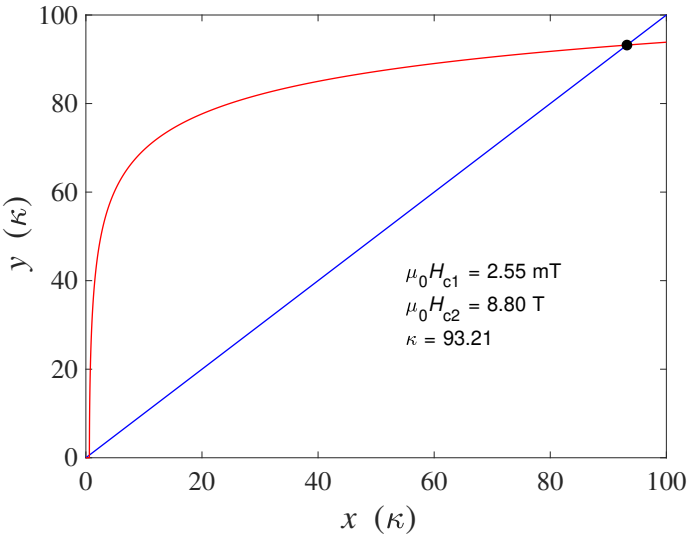


Figure D.5: The extraction of κ from lower critical field, $\mu_0 H_{c1}$, and upper critical field, $\mu_0 H_{c2}$, points. Both the horizontal and vertical axes are in units of κ. The line and curves are generated using equations 1.24, 1.27 and 1.30, and κ is defined as the upper intersection of these curves.

References

[1] H. Kamerlingh Onnes, "The disappearance of the resistivity of mercury," Leiden Comm 119b, 120b, 122b, 124c (1911).

[2] W. Meissner and R. Ochsenfeld, "Ein neuer effekt bei eintritt der supraleitfähigkeit," Naturwissenschaften **21**, 787–788 (1933).

[3] F. London and H. London, "The electromagnetic equations of the supraconductor," Proceedings of the Royal Society of London. Series A-Mathematical and Physical Sciences **149**, 71–88 (1935).

[4] A. B. Pippard and W. L. Bragg, "An experimental and theoretical study of the relation between magnetic field and current in a superconductor," Proceedings of the Royal Society of London. Series A. Mathematical and Physical Sciences **216**, 547–568 (1953).

[5] J. Bardeen, L. N. Cooper, and J. R. Schrieffer, "Theory of Superconductivity," Physical Review **108**, 1175–1204 (1957).

[6] L. N. Cooper, "Bound Electron Pairs in a Degenerate Fermi Gas," Physical Review **104**, 1189–1190 (1956).

[7] E. Maxwell, "Isotope effect in the superconductivity of mercury," Physical Review **78**, 477–477 (1950).

[8] C. A. Reynolds, B. Serin, W. H. Wright, and L. B. Nesbitt, "Superconductivity of isotopes of mercury," Physical Review **78**, 487–487 (1950).

[9] M. Tinkham, *Introduction to Superconductivity*, 2nd ed. (Dover Publications, 2004).

[10] J. F. Annett, *Superconductivity, Superfluids and Condensates*, 1st ed., Oxford Masters Series in Physics (Oxford University Press, 2004).

[11] V. L. Ginzburg and L. D. Landau, "Ginzburg Landau Theory," Zh. Eksperim. i Teor. Fiz. **20**, 1064 (1950).

[12] V. L. Ginzburg and L. D. Landau, "On the theory of superconductivity," in *On Superconductivity and Superfluidity* (Springer, 2009) pp. 113–137.

[13] J. Bardeen, "Critical fields and currents in superconductors," Rev. Mod. Phys. **34**, 667–681 (1962).

[14] N. E. Bickers, D. J. Scalapino, and S. R. White, "Conserving Approximations for Strongly Correlated Electron Systems: Bethe-Salpeter Equation and Dynamics for the Two-Dimensional Hubbard Model," Physical Review Letters **62**, 961–964 (1989).

[15] D. A. Wollman, D. J. Van Harlingen, W. C. Lee, D. M. Ginsberg, and A. J. Leggett, "Experimental determination of the superconducting pairing state in ybco from the phase coherence of ybco-pb dc squids," Phys. Rev. Lett. **71**, 2134–2137 (1993).

[16] Y. Kamihara, H. Hiramatsu, M. Hirano, R. Kawamura, H. Yanagi, T. Kamiya, and H. Hosono, "Iron-based layered superconductor: LaOFeP," Journal of the American Chemical Society **128**, 10012–10013 (2006).

[17] Y. Kamihara, T. Watanabe, M. Hirano, and H. Hosono, "Iron-based layered superconductor La[$O_{1-x}F_x$]FeAs (x =0.05- 0.12) with T_c = 26 K," Journal of the American Chemical Society **130**, 3296–3297 (2008).

[18] P. J. Moll, R. Puzniak, F. Balakirev, K. Rogacki, J. Karpinski, N. D. Zhigadlo, and B. Batlogg, "High magnetic-field scales and critical currents in SmFeAs(O,F) crystals," Nature Materials **9**, 628–633 (2010).

[19] H. Hosono, A. Yamamoto, H. Hiramatsu, and Y. Ma, "Recent advances in iron-based superconductors toward applications," Materials Today **21**, 278–302 (2017).

[20] Q.-Y. Wang, Z. Li, W.-H. Zhang, Z.-C. Zhang, J.-S. Zhang, W. Li, H. Ding, Y.-B. Ou, P. Deng, K. Chang, J. Wen, C.-L. Song, K. He, J.-F. Jia, S.-H. Ji, Y.-Y. Wang, L.-L. Wang, X. Chen, X.-C. Ma, and Q.-K. Xue, "Interface-Induced High-Temperature Superconductivity in Single Unit-Cell FeSe Films on $SrTiO_3$," Chinese Physics Letters **29**, 037402 (2012).

[21] S. He, J. He, W. Zhang, L. Zhao, D. Liu, X. Liu, D. Mou, Y.-b. Ou, Q.-y. Wang, Z. Li, L. Wang, Y. Peng, Y. Liu, C. Chen, L. Yu, G. Liu, X. Dong, J. Zhang, C. Chen, Z. Xu, X. Chen, X. Ma, Q. Xue, and X. J. Zhou, "Phase diagram and electronic indication of high-temperature superconductivity at 65 K in single-layer FeSe films," Nature Materials **12**, 605–610 (2013).

[22] J.-F. Ge, Z.-L. Liu, C. Liu, C.-L. Gao, D. Qian, Q.-K. Xue, Y. Liu, and J.-F. Jia, "Superconductivity above 100 K in single-layer FeSe films on doped $SrTiO_3$," Nature Materials **14**, 285–289 (2015).

[23] A. A. Kordyuk, "Iron-based superconductors: Magnetism, superconductivity, and electronic structure (Review Article)," Low Temperature Physics **38**, 888–899 (2012).

[24] H.-H. Wen and S. Li, "Materials and Novel Superconductivity in Iron Pnictide Superconductors," Annual Review of Condensed Matter Physics **2**, 121–140 (2011).

[25] A. Chubukov, "Pairing Mechanism in Fe-Based Superconductors," Annual Review of Condensed Matter Physics **3**, 57–92 (2012).

[26] Q. Wang, Y. Shen, B. Pan, X. Zhang, K. Ikeuchi, K. Iida, A. D. Christianson, H. C. Walker, D. T. Adroja, M. Abdel-Hafiez, X. Chen, D. A. Chareev, A. N. Vasiliev, and J. Zhao, "Magnetic ground state of FeSe," Nature Communications **7**, 12182 (2016).

[27] A. I. Coldea and M. D. Watson, "The key ingredients of the electronic structure of FeSe," Annual Review of Condensed Matter Physics **9**, 125 (2018).

[28] M. D. Watson, T. K. Kim, A. A. Haghighirad, N. R. Davies, A. McCollam, A. Narayanan, S. F. Blake, Y. L. Chen, S. Ghannadzadeh, A. J. Schofield, M. Hoesch, C. Meingast, T. Wolf, and A. I. Coldea, "Emergence of the nematic electronic state in FeSe," Physical Review B **91**, 155106 (2015).

[29] M. D. Watson, S. Backes, A. A. Haghighirad, M. Hoesch, T. K. Kim, A. I. Coldea, and R. Valentí, "Formation of Hubbard-like bands as a fingerprint of strong electron-electron interactions in FeSe," Physical Review B **95**, 081106 (2017).

[30] M. D. Watson, T. K. Kim, L. C. Rhodes, M. Eschrig, M. Hoesch, A. A. Haghighirad, and A. I. Coldea, "Evidence for unidirectional nematic bond ordering in FeSe," Physical Review B **94**, 201107 (2016).

[31] T. Hanaguri, K. Iwaya, Y. Kohsaka, T. Machida, T. Watashige, S. Kasahara, T. Shibauchi, and Y. Matsuda, "Two distinct superconducting pairing states divided by the nematic end point in $FeSe_{1-x}S_x$," Science Advances **4**, eaar6419 (2018).

[32] Y. Sato, S. Kasahara, T. Taniguchi, X. Xing, Y. Kasahara, Y. Tokiwa, Y. Yamakawa, H. Kontani, T. Shibauchi, and Y. Matsuda, "Abrupt change of the superconducting gap structure at the nematic critical point in $FeSe_{1-x}S_x$," Proceedings of the National Academy of Sciences (PNAS) **115**, 1227–1231 (2018).

[33] P. O. Sprau, A. Kostin, A. Kreisel, A. E. Böhmer, V. Taufour, P. C. Canfield, S. Mukherjee, P. J. Hirschfeld, B. M. Andersen, and J. C. Séamus Davis, "Discovery of Orbital-Selective Cooper Pairing in FeSe," Science **357**, 75 (2016).

[34] Z. Wang, C. Liu, Y. Liu, and J. Wang, "High-temperature superconductivity in one-unit-cell FeSe films," Journal of Physics: Condensed Matter **29**, 153001 (2017).

[35] W. Qing-Yan, L. Zhi, Z. Wen-Hao, Z. Zuo-Cheng, Z. Jin-Song, L. Wei, D. Hao, O. Yun-Bo, D. Peng, C. Kai, W. Jing, S. Can-Li, H. Ke, J. Jin-Feng, J. Shuai-Hua, W. Ya-Yu, W. Li-Li, C. Xi, M. Xu-Cun, and X. Qi-Kun, "Interface-induced high-temperature superconductivity in single unit-cell fese films on srtio 3," Chinese Physics Letters **29**, 037402 (2012).

[36] S. Kasahara, T. Watashige, T. Hanaguri, Y. Kohsaka, T. Yamashita, Y. Shimoyama, Y. Mizukami, R. Endo, H. Ikeda, K. Aoyama, T. Terashima, S. Uji, T. Wolf, H. von Löhneysen, T. Shibauchi, and Y. Matsuda, "Field-induced superconducting phase of FeSe in the BCS-BEC cross-over." Proceedings of the National Academy of Sciences (PNAS) **111**, 16309 (2014).

[37] S. Kasahara, T. Yamashita, A. Shi, R. Kobayashi, Y. Shimoyama, T. Watashige, K. Ishida, T. Terashima, T. Wolf, F. Hardy, C. Meingast, H. v. Löhneysen, A. Levchenko, T. Shibauchi, and Y. Matsuda, "Giant superconducting fluctuations in the compensated semimetal FeSe at the BCS-BEC crossover," Nature Communications **7**, 12843 (2016).

[38] A. Shi, T. Arai, S. Kitagawa, T. Yamanaka, K. Ishida, A. E. Böhmer, C. Meingast, T. Wolf, M. Hirata, and T. Sasaki, "Pseudogap Behavior of the Nuclear Spin–Lattice Relaxation Rate in FeSe Probed by ^{77}Se-NMR," Journal of the Physical Society of Japan **87**, 013704 (2018).

[39] M. C. Rahn, R. A. Ewings, S. J. Sedlmaier, S. J. Clarke, and A. T. Boothroyd, "Strong $(\pi, 0)$ spin fluctuations in $\beta - \mathrm{FeSe}$ observed by neutron spectroscopy," Physical Review B **91**, 180501 (2015).

[40] M. D. Watson, T. K. Kim, A. A. Haghighirad, S. F. Blake, N. R. Davies, M. Hoesch, T. Wolf, and A. I. Coldea, "Suppression of orbital ordering by chemical pressure in $\mathrm{FeSe}_{1-x}\mathrm{S}_x$," Physical Review B **92**, 121108 (2015).

[41] P. Reiss, M. D. Watson, T. K. Kim, A. A. Haghighirad, D. N. Woodruff, M. Bruma, S. J. Clarke, and A. I. Coldea, "Suppression of electronic correlations by chemical pressure from FeSe to FeS," Physical Review B **96**, 121103 (2017).

[42] T. Terashima, N. Kikugawa, H. Lin, X. Zhu, H.-H. Wen, T. Nomoto, K. Suzuki, H. Ikeda, and S. Uji, "Upper critical field and quantum oscillations in tetragonal superconducting FeS," Physical Review B **94**, 100503 (2016).

[43] A. I. Coldea, S. F. Blake, S. Kasahara, A. A. Haghighirad, M. D. Watson, W. Knafo, E. S. Choi, A. McCollam, P. Reiss, T. Yamashita, M. Bruma, S. Speller, Y. Matsuda, T. Wolf, T. Shibauchi, and A. J. Schofield, "Evolution of the low-temperature Fermi surface of superconducting $\mathrm{FeSe}_{1-x}\mathrm{S}_x$ across a nematic phase transition," Nature Physics Journals Quantum Materials **4**, 2 (2019).

[44] Q. Wang, Y. Shen, B. Pan, Y. Hao, M. Ma, F. Zhou, P. Steffens, K. Schmalzl, T. R. Forrest, M. Abdel-Hafiez, X. Chen, D. A. Chareev, A. N. Vasiliev, P. Bourges, Y. Sidis, H. Cao, and J. Zhao, "Strong interplay between stripe spin fluctuations, nematicity and superconductivity in FeSe," Nature Materials **15**, 159 (2016).

[45] P. Wiecki, K. Rana, A. E. Böhmer, Y. Lee, S. L. Bud'ko, P. C. Canfield, and Y. Furukawa, "Persistent correlation between superconductivity and antiferromagnetic fluctuations near a nematic quantum critical point in $\mathrm{FeSe}_{1-x}\mathrm{S}_x$," Physical Review B **98**, 020507 (2018).

[46] S. Medvedev, T. M. McQueen, I. A. Troyan, T. Palasyuk, M. I. Eremets, R. J. Cava, S. Naghavi, F. Casper, V. Ksenofontov, G. Wortmann, and C. Felser, "Electronic and magnetic phase diagram of β-$\mathrm{Fe}_{1.01}\mathrm{Se}$ with superconductivity at 36.7 K under pressure," Nature Materials **8**, 630 (2009).

[47] J. P. Sun, K. Matsuura, G. Z. Ye, Y. Mizukami, M. Shimozawa, K. Matsubayashi, M. Yamashita, T. Watashige, S. Kasahara, Y. Matsuda, J.-Q. Yan, B. C. Sales,

Y. Uwatoko, J.-G. Cheng, and T. Shibauchi, "Dome-shaped magnetic order competing with high-temperature superconductivity at high pressures in FeSe," Nature Communications **7**, 12146 (2016).

[48] T. Terashima, N. Kikugawa, A. Kiswandhi, D. Graf, E.-S. Choi, J. S. Brooks, S. Kasahara, T. Watashige, Y. Matsuda, T. Shibauchi, T. Wolf, A. E. Böhmer, F. Hardy, C. Meingast, H. v. Löhneysen, and S. Uji, "Fermi surface reconstruction in FeSe under high pressure," Physical Review B **93**, 094505 (2016).

[49] Y. Mizuguchi, F. Tomioka, S. Tsuda, T. Yamaguchi, and Y. Takano, "Superconductivity at 27 K in tetragonal FeSe under high pressure," Applied Physics Letters **93**, 152505 (2008).

[50] K. Matsuura, Y. Mizukami, Y. Arai, Y. Sugimura, N. Maejima, A. Machida, T. Watanuki, T. Fukuda, T. Yajima, Z. Hiroi, K. Y. Yip, Y. C. Chan, Q. Niu, S. Hosoi, K. Ishida, K. Mukasa, S. Kasahara, J.-G. Cheng, S. K. Goh, Y. Matsuda, Y. Uwatoko, and T. Shibauchi, "Maximizing $T_{\rm c}$ by tuning nematicity and magnetism in $FeSe_{1-x}S_x$ superconductors," Nature Communications **8**, 1143 (2017).

[51] J. P. Sun, G. Z. Ye, P. Shahi, J.-Q. Yan, K. Matsuura, H. Kontani, G. M. Zhang, Q. Zhou, B. C. Sales, T. Shibauchi, Y. Uwatoko, D. J. Singh, and J.-G. Cheng, "High-$T_{\rm c}$ Superconductivity in FeSe at High Pressure: Dominant Hole Carriers and Enhanced Spin Fluctuations," Physical Review Letters **118**, 147004 (2017).

[52] D. D. Scherer, A. C. Jacko, C. Friedrich, E. Şaşıoğlu, S. Blügel, R. Valentí, and B. M. Andersen, "Interplay of nematic and magnetic orders in FeSe under pressure," Physical Review B **95**, 094504 (2017).

[53] M. Bendele, A. Ichsanow, Y. Pashkevich, L. Keller, T. Strässle, A. Gusev, E. Pomjakushina, K. Conder, R. Khasanov, and H. Keller, "Coexistence of superconductivity and magnetism in $FeSe_{1-x}$ under pressure," Physical Review B **85**, 064517 (2012).

[54] P. Reiss, D. Graf, A. A. Haghighirad, W. Knafo, L. Drigo, M. Bristow, A. J. Schofield, and A. I. Coldea, "Quenched nematic criticality and two superconducting domes in an iron-based superconductor," Nature Physics (2019), 10.1038/s41567-019-0694-2.

[55] R. Schneider, A. G. Zaitsev, D. Fuchs, and H. v. Löhneysen, "Superconductor-Insulator Quantum Phase Transition in Disordered FeSe Thin Films," Physical Review Letters **108**, 257003 (2012).

[56] R. Schneider, A. G. Zaitsev, D. Fuchs, and H. von Löhneysen, "Excess conductivity and Berezinskii–Kosterlitz–Thouless transition in superconducting FeSe thin films," Journal of Physics: Condensed Matter **26**, 455701 (2014).

[57] R. Schneider, A. G. Zaitsev, D. Fuchs, and H. von Löhneysen, "Superconducting and Insulating Phases of Disordered FeSe Thin Films in a Magnetic Field," Journal of Low Temperature Physics **178**, 118–127 (2015).

[58] L. Farrar, M. Bristow, A. A. Haghighirad, A. McCollam, S. J. Bending, and A. I. Coldea, "Suppression of superconductivity and enhanced critical field anisotropy in thin flakes of FeSe," npj Quantum Materials **5**, 29 (2020).

[59] A. Iyo, K. Kawashima, T. Kinjo, T. Nishio, S. Ishida, H. Fujihisa, Y. Gotoh, K. Kihou, H. Eisaki, and Y. Yoshida, "New-Structure-Type Fe-Based Superconductors: $CaAFe_4As_4$ (A=K, Rb, Cs) and $SrAFe_4As_4$ (A=Rb, Cs)," Journal of the American Chemical Society **138**, 3410–3415 (2016).

[60] M. Rotter, M. Tegel, and D. Johrendt, "Superconductivity at 38 K in the Iron Arsenide $(Ba_{1-x}K_x)Fe_2As_2$," Physical Review Letters **101**, 107006 (2008).

[61] W. R. Meier, T. Kong, U. S. Kaluarachchi, V. Taufour, N. H. Jo, G. Drachuck, A. E. Böhmer, S. M. Saunders, A. Sapkota, A. Kreyssig, M. A. Tanatar, R. Prozorov, A. I. Goldman, F. F. Balakirev, A. Gurevich, S. L. Bud'ko, and P. C. Canfield, "Anisotropic thermodynamic and transport properties of single-crystalline $CaKFe_4As_4$," Physical Review B **94**, 064501 (2016).

[62] D. Mou, T. Kong, W. R. Meier, F. Lochner, L.-L. Wang, Q. Lin, Y. Wu, S. L. Bud'ko, I. Eremin, D. D. Johnson, P. C. Canfield, and A. Kaminski, "Enhancement of the Superconducting Gap by Nesting in $CaKFe_4As_4$: A New High Temperature Superconductor," Physical Review Letters **117**, 277001 (2016).

[63] W. R. Meier, Q. P. Ding, A. Kreyssig, S. L. Bud'Ko, A. Sapkota, K. Kothapalli, V. Borisov, R. Valentí, C. D. Batista, P. P. Orth, R. M. Fernandes, A. I. Goldman, Y. Furukawa, A. E. Böhmer, and P. C. Canfield, "Hedgehog spin-vortex crystal stabilized in a hole-doped iron-based superconductor," Nature Physics Journals Quantum Materials **3**, 5 (2018).

[64] K. Iida, M. Ishikado, Y. Nagai, H. Yoshida, A. D. Christianson, N. Murai, K. Kawashima, Y. Yoshida, H. Eisaki, and A. Iyo, "Spin Resonance in the New-Structure-Type Iron-Based Superconductor $CaKFe_4As_4$," Journal of the Physical Society of Japan **86**, 093703 (2017).

[65] P. Drude, "Zur elektronentheorie der metalle," Annalen der Physik **306**, 566–613 (1900).

[66] A. Sommerfeld, "Zur elektronentheorie der metalle auf grund der fermischen statistik," Zeitschrift für Physik **47**, 1–32 (1928).

[67] A. Pippard, *Magnetoresistance in Metals*, Cambridge Studies in Low Temperature Physics (Cambridge University Press, 1989).

[68] J. M. Ziman, *Electrons and Phonons* (Oxford University Press, 1960).

[69] K. K. Huynh, Y. Tanabe, T. Urata, S. Heguri, K. Tanigaki, T. Kida, and M. Hagiwara, "Mobility spectrum analytical approach for intrinsic band picture of $Ba(FeAs)_2$," New Journal of Physics **16** (2014), 10.1088/1367-2630/16/9/093062.

[70] M. D. Watson, T. Yamashita, S. Kasahara, W. Knafo, M. Nardone, J. Béard, F. Hardy, A. McCollam, A. Narayanan, S. F. Blake, T. Wolf, A. A. Haghighirad, C. Meingast, A. J. Schofield, H. v. Löhneysen, Y. Matsuda, A. I. Coldea, and T. Shibauchi, "Dichotomy between the Hole and Electron Behavior in Multiband Superconductor FeSe Probed by Ultrahigh Magnetic Fields," Physical Review Letters **115**, 027006 (2015).

[71] Y. A. Ovchenkov, D. A. Chareev, V. A. Kulbachinskii, V. G. Kytin, D. E. Presnov, O. S. Volkova, and A. N. Vasiliev, "Highly mobile carriers in iron-based superconductors," Superconductor Science and Technology **30**, 035017 (2017).

[72] K. K. Huynh, Y. Tanabe, T. Urata, H. Oguro, S. Heguri, K. Watanabe, and K. Tanigaki, "Electric transport of a single-crystal iron chalcogenide fese superconductor: Evidence of symmetry-breakdown nematicity and additional ultrafast dirac cone-like carriers," Physical Review B **90**, 144516 (2014).

[73] H. v. Löhneysen, A. Rosch, M. Vojta, and P. Wölfle, "Fermi-liquid instabilities at magnetic quantum phase transitions," Rev. Mod. Phys. **79**, 1015–1075 (2007).

[74] J. G. Analytis, H.-H. Kuo, R. D. McDonald, M. Wartenbe, P. M. C. Rourke, N. E. Hussey, and I. R. Fisher, "Transport near a quantum critical point in $BaFe_2(As_{1-x}P_x)_2$," Nature Physics **10**, 194–197 (2014).

[75] A. Rosch, "Interplay of disorder and spin fluctuations in the resistivity near a quantum critical point," Physical Review Letters **82**, 4280–4283 (1999).

[76] A. M. Clogston, "Upper Limit for the Critical Field in Hard Superconductors," Physical Review Letters **9**, 266 (1962).

[77] K. Maki, "Effect of Pauli Paramagnetism on Magnetic Properties of High-Field Superconductors," Physical Review **148**, 362–369 (1966).

[78] N. R. Werthamer, E. Helfand, and P. C. Hohenberg, "Temperature and purity dependence of the superconducting critical field, H_{c2}. iii. electron spin and spin-orbit effects," Physical Review **147**, 295–302 (1966).

[79] A. Gurevich, "Enhancement of the upper critical field by nonmagnetic impurities in dirty two-gap superconductors," Physical Review B **67**, 184515 (2003).

[80] K. D. Usadel, "Generalized Diffusion Equation for Superconducting Alloys," Physical Review Letters **25**, 507–509 (1970).

[81] A. Gurevich, "Upper critical field and the fulde-ferrel-larkin-ovchinnikov transition in multiband superconductors," Physical Review B **82**, 184504 (2010).

[82] P. Fulde and R. A. Ferrell, "Superconductivity in a strong spin-exchange field," Physical Review **135**, A550–A563 (1964).

[83] A. Larkin and Y. N. Ovchinnikov, "Nonuniform state of superconductors," Soviet Physics-JETP **20**, 762–762 (1965).

[84] A. Larkin and I. Ovchinnikov, "Inhomogeneous state of superconductors (Production of superconducting state in ferromagnet with Fermi surfaces, examining Greens function)," Soviet Physics-JETP **20**, 762–769 (1965).

[85] A. Bianchi, R. Movshovich, C. Capan, P. G. Pagliuso, and J. L. Sarrao, "Possible Fulde-Ferrell-Larkin-Ovchinnikov Superconducting State in $CeCoIn_5$," Physical Review Letters **91**, 187004 (2003).

[86] Movshovich, Roman and Bianchi, Andrea and Capan, Cigdem and Jaime, Marcelo and Goodrich, R. G., "Magnetic enhancement of superconductivity from electron spin domains," Nature **427**, 802 (2004).

[87] P. J. Hirschfeld, M. M. Korshunov, and I. I. Mazin, "Gap symmetry and structure of Fe-based superconductors," Reports on Progress in Physics **74**, 124508 (2011).

[88] K. Cho, H. Kim, M. A. Tanatar, Y. J. Song, Y. S. Kwon, W. A. Coniglio, C. C. Agosta, A. Gurevich, and R. Prozorov, "Anisotropic upper critical field and possible Fulde-Ferrel-Larkin-Ovchinnikov state in the stoichiometric pnictide superconductor LiFeAs," Physical Review B **83**, 060502 (2011).

[89] C. Tarantini, A. Gurevich, J. Jaroszynski, F. Balakirev, E. Bellingeri, I. Pallecchi, C. Ferdeghini, B. Shen, H. H. Wen, and D. C. Larbalestier, "Significant enhancement of upper critical fields by doping and strain in iron-based superconductors," Physical Review B **84**, 184522 (2011).

[90] M. Kano, Y. Kohama, D. Graf, F. Balakirev, A. S. Sefat, M. A. Mcguire, B. C. Sales, D. Mandrus, and S. W. Tozer, "Anisotropy of the upper critical field in a co-doped $BaFe_2As_2$ single crystal," Journal of the Physical Society of Japan **78**, 18–22 (2009).

[91] K. W. Song and A. E. Koshelev, "Quantum FFLO State in Clean Layered Superconductors," Physical Review X **9**, 021025 (2019).

[92] L. W. Gruenberg and L. Gunther, "Fulde-Ferrell Effect in Type-II Superconductors," Physical Review Letters **16**, 996–998 (1966).

[93] D. S. James and P. G. De Gennes, "Onset of superconductivity in decreasing fields," Physics Letters **7**, 306–308 (1963).

[94] C. P. Bean, "Magnetization of high-field superconductors," Reviews of Modern Physics **36**, 31 (1964).

[95] D. D. Dew-Hughes, "Flux pinning mechanisms in type II superconductors," Philosophical Magazine **30**, 293 (1974).

[96] P. W. Anderson, "Theory of Flux Creep in Hard Superconductors," Physical Review Letters **9**, 309–311 (1962).

[97] P. W. Anderson and Y. B. Kim, "Hard superconductivity: Theory of the motion of abrikosov flux lines," Rev. Mod. Phys. **36**, 39 (1964).

[98] G. Blatter, M. V. FeigelMan, V. B. Geshkenbein, A. I. Larkin, and V. M. Vinokur, "Vortices in high-temperature superconductors," Rev. Mod. Phys. **66**, 1125 (1994).

[99] T. T. M. Palstra, B. Batlogg, L. F. Schneemeyer, and J. V. Waszczak, "Thermally Activated Dissipation in $\mathrm{Bi_{2.2}Sr_2Ca_{0.8}Cu_2O_{8+\delta}}$," Physical Review Letters **61**, 1662–1665 (1988).

[100] T. T. M. Palstra, B. Batlogg, R. B. van Dover, L. F. Schneemeyer, and J. V. Waszczak, "Dissipative flux motion in high-temperature superconductors," Physical Review B **41**, 6621–6632 (1990).

[101] W. J. Skocpol and M. Tinkham, "Fluctuations near superconducting phase transitions," Reports on Progress in Physics **38**, 1049–1097 (1975).

[102] A. Larkin and A. Varlamov, *Theory of Fluctuations in Superconductors*, International Series of Monographs on Physics (OUP Oxford Science Publications, 2005).

[103] L. G. Aslamasov and A. I. Larkin, "The influence of fluctuation pairing of electrons on the conductivity of normal metal," Physics Letters A **26**, 238–239 (1968).

[104] R. Glover, "Ideal resistive transition of a superconductor," Physics Letters A **25**, 542–544 (1967).

[105] S. Ullah and A. T. Dorsey, "Effect of fluctuations on the transport properties of type-II superconductors in a magnetic field," Physical Review B **44**, 262–273 (1991).

[106] D. H. Kim, K. E. Gray, and M. D. Trochet, "Scaling behavior of fluctuation conductivity of high-temperature superconductors in a magnetic field," Physical Review B **45**, 801–804 (1992).

[107] S. Ullah and A. T. Dorsey, "Critical fluctuations in high-temperature superconductors and the Ettingshausen effect," Physical Review Letters **65**, 2066–2069 (1990).

[108] D. J. Thouless, "Critical Fluctuations of a Type-II Superconductor in a Magnetic Field," Physical Review Letters **34**, 946–949 (1975).

[109] R. S. Thompson, "Microwave, flux flow, and fluctuation resistance of dirty type-II superconductors," Physical Review B **1**, 327–333 (1970).

[110] K. Maki and R. S. Thompson, "Fluctuation conductivity of high-T_c superconductors," Physical Review B **39**, 2767 (1989).

[111] A. G. Aronov, S. Hikami, and A. I. Larkin, "Zeeman Effect on Magnetoresistance in High-Temperature Superconductors," Physical Review Letters **62**, 965 (1989).

[112] D. H. Kim, K. E. Gray, R. T. Kampwirth, and D. M. McKay, "Magnetoconductance of $Tl_2Ba_2CaCu_2O_x$ films in the fluctuation regime," Physical Review B **43**, 2910–2915 (1991).

[113] U. Welp, S. Fleshler, W. K. Kwok, R. A. Klemm, V. M. Vinokur, J. Downey, and B. Veal, "High-Field Scaling Behavior of Thermodynamic and Transport Quantities of $YBa_2Cu_3O_{7-\delta}$ near the Superconducting Transition," Physical Review Letters **67**, 3180–3183 (1991).

[114] G. Blatter, M. V. Feigel'man, V. B. Geshkenbein, A. I. Larkin, and V. M. Vinokur, "Vortices in high-temperature superconductors," Reviews of Modern Physics **66**, 1125–1388 (1994).

[115] *Physical Properties Measurement System Hardware Manual*, Quantum Design, seventh ed. (2011).

[116] *Physical Properties Measurement System Helium-3 Refrigerator System User's Manual*, Quantum Design, tenth ed. (2016).

[117] *Electrical Transport Option (ETO) User's Manual*, Quantum Design, 4th ed. (2013).

[118] C. Kittel, *Introduction to Solid State Physics*, 8th ed. (Wiley, 2004).

[119] S. Foner, "Vibrating sample magnetometer," Review of Scientific Instruments **27**, 548–548 (1956).

[120] *Vibrating Sample Magnetometer (VSM) Option User's Manual*, Quantum Design, 5th ed. (2011).

[121] R. Prozorov and V. G. Kogan, "Effective Demagnetizing Factors of Diamagnetic Samples of Various Shapes," Physical Review Applied **10**, 014030 (2018).

[122] D. X. Chen, E. Pardo, and A. Sanchez, "Demagnetizing factors of rectangular prisms and ellipsoids," IEEE Transactions on Magnetics **38**, 1742–1752 (2002).

[123] M. Sato and Y. Ishii, "Simple and approximate expressions of demagnetizing factors of uniformly magnetized rectangular rod and cylinder," Journal of Applied Physics **66**, 983–985 (1989).

[124] S. Blundell, *Magnetism in Condensed Matter*, 14^{th} ed., Oxford Masters Series in Condensed Matter Physics (Oxford University Press, 2014).

[125] Z. A. Ren, G. C. Che, X. L. Dong, J. Yang, W. Lu, W. Yi, X. L. Shen, Z. C. Li, L. L. Sun, F. Zhou, and Z. X. Zhao, "Superconductivity and phase diagram in iron-based arsenic-oxides ReFeAsO (Re = rare-earth metal) without fluorine doping," Europhysics Letters **83**, 17002 (2008).

[126] S. J. Singh, J. Shimoyama, A. Yamamoto, H. Ogino, and K. Kishio, "Transition Temperature and Upper Critical Field in $SmFeAsO_{1-x}F_x$ Synthesized at Low Heating Temperatures," IEEE Transactions on Applied Superconductivity **23**, 7300605–7300605 (2013).

[127] J. Jaroszynski, F. Hunte, L. Balicas, Y.-j. Jo, I. Raičević, A. Gurevich, D. C. Larbalestier, F. F. Balakirev, L. Fang, P. Cheng, Y. Jia, and H. H. Wen, "Upper critical fields and thermally-activated transport of $NdFeAsO_{0.7}F_{0.3}$ single crystal," Physical Review B **78**, 174523 (2008).

[128] J. Jaroszynski, S. C. Riggs, F. Hunte, A. Gurevich, D. C. Larbalestier, G. S. Boebinger, F. F. Balakirev, A. Migliori, Z. A. Ren, W. Lu, J. Yang, X. L. Shen, X. L. Dong, Z. X. Zhao, R. Jin, A. S. Sefat, M. A. McGuire, B. C. Sales, D. K. Christen, and D. Mandrus, "Comparative high-field magnetotransport of the oxypnictide superconductors $R\mathrm{FeAsO}_{1-x}\mathrm{F}_x$ (R = La, Nd) and $SmFeAsO_{1-\delta}$," Physical Review B **78**, 064511 (2008).

[129] Y. Ma, "Progress in wire fabrication of iron-based superconductors," Superconductor Science and Technology **25**, 113001 (2012).

[130] J. Shimoyama, "Potentials of iron-based superconductors for practical future materials," Superconductor Science and Technology **27**, 044002 (2014).

[131] M. V. Feigelman, V. B. Geshkenbein, A. I. Larkin, and V. M. Vinokur, "Theory of collective flux creep," Physical Review Letters **63**, 2303 (1989).

[132] W. R. Meier, T. Kong, S. L. Bud'ko, and P. C. Canfield, "Optimization of the crystal growth of the superconductor $\mathrm{CaKFe_4As_4}$ from solution in the $\mathrm{FeAs}-\mathrm{CaFe_2As_2}-\mathrm{KFe_2As_2}$ system," Physical Review Materials **1**, 013401 (2017).

[133] E. H. Brandt, "Irreversible magnetization of pin-free type-II superconductors," Physical Review B **60**, 11939 (1999).

[134] S. J. Singh, M. Bristow, W. R. Meier, P. Taylor, S. J. Blundell, P. C. Canfield, and A. I. Coldea, "Ultrahigh critical current densities, the vortex phase diagram, and the effect of granularity of the stoichiometric high-Tc superconductor CaKFe4As4," Physical Review Materials **2**, 074802 (2018).

[135] S. J. Singh, J. Shimoyama, A. Yamamoto, H. Ogino, and K. Kishio, "Significant enhancement of the intergrain coupling in lightly F-doped SmFeAsO superconductors," Superconductor Science and Technology **26**, 065006 (2013).

[136] P. K. Biswas, A. Iyo, Y. Yoshida, H. Eisaki, K. Kawashima, and A. D. Hillier, "Signature of multigap nodeless superconductivity in $CaKFe_4As_4$," Physical Review B **95**, 140505 (2017).

[137] J. Cui, Q.-P. Ding, W. R. Meier, A. E. Böhmer, T. Kong, V. Borisov, Y. Lee, S. L. Bud'ko, R. Valentí, P. C. Canfield, and Y. Furukawa, "Magnetic fluctuations and superconducting properties of $\mathrm{CaKFe_4As_4}$ studied by $^{75}\mathrm{As}$ NMR," Phys. Rev. B **96**, 104512 (2017).

[138] D. V. Suetin and I. R. Shein, "Electronic Properties and Fermi Surface for New Layered High-Temperature Superconductors $CaAFe_4As_4$ (A = K, Rb, and Cs): FLAPW-GGA Calculations," Journal of Superconductivity and Novel Magnetism **31**, 1683–1692 (2018).

[139] Z. S. Wang, H. Q. Luo, C. Ren, and H. H. Wen, "Upper critical field, anisotropy, and superconducting properties of $Ba_{1-x}K_xFe_2As_2$ single crystals," Physical Review B **78**, 140501 (2008).

[140] K. Cho, A. Fente, S. Teknowijoyo, M. A. Tanatar, K. R. Joshi, N. M. Nusran, T. Kong, W. R. Meier, U. Kaluarachchi, I. Guillamón, H. Suderow, S. L. Bud'ko, P. C. Canfield, and R. Prozorov, "Nodeless multiband superconductivity in stoichiometric single-crystalline $\mathrm{CaKFe_4As_4}$," Physical Review B **95**, 100502 (2017).

[141] R. Khasanov, W. R. Meier, Y. Wu, D. Mou, S. L. Bud'ko, I. Eremin, H. Luetkens, A. Kaminski, P. C. Canfield, and A. Amato, "In-plane magnetic penetration depth of superconducting $\mathrm{CaKFe_4As_4}$," Physical Review B **97**, 140503 (2018).

[142] T. Tamegai, T. Taen, H. Yagyuda, Y. Tsuchiya, S. Mohan, T. Taniguchi, Y. Nakajima, S. Okayasu, M. Sasase, H. Kitamura, T. Murakami, T. Kambara, and Y. Kanai, "Effects of particle irradiations on vortex states in iron-based superconductors," Superconductor Science and Technology **25**, 084008 (2012).

[143] G. P. Mikitik and E. H. Brandt, "Critical state in thin anisotropic superconductors of arbitrary shape," Physical Review B **62**, 6800–6811 (2000).

[144] U. Welp, W. K. Kwok, G. W. Crabtree, K. G. Vandervoort, and J. Z. Liu, "Magnetization hysteresis and flux pinning in twinned and untwinned $YBa_2Cu_3O_{7-x}$ single crystals," Applied Physics Letters **57**, 84 (1990).

[145] Y. Yeshurun, N. Bontemps, L. Burlachkov, and A. Kapitulnik, "Dynamic characteristics of the anomalous second peak in the magnetization curves of Bi-Sr-Ca-Cu-O," Physical Review B **49**, 1548 (1994).

[146] R. Lortz, N. Musolino, Y. Wang, A. Junod, and N. Toyota, "Origin of the magnetization peak effect in the Nb_3Sn superconductor," Physical Review B **75**, 094503 (2007).

[147] M. Pissas, S. Lee, A. Yamamoto, and S. Tajima, "Peak Effect in Single Crystal MgB_2 Superconductor for $H||c$-Axis," Physical Review Letters **89**, 097002 (2002).

[148] H. Yang, H. Luo, Z. Wang, and H. H. Wen, "Fishtail effect and the vortex phase diagram of single crystal $Ba_{0.6}K_{0.4}Fe_2As_2$," Applied Physics Letters **93**, 2 (2008).

[149] A. K. Pramanik, L. Harnagea, C. Nacke, A. U. B. Wolter, S. Wurmehl, V. Kataev, and B. Büchner, "Fishtail effect and vortex dynamics in LiFeAs single crystals," Physical Review B **83**, 094502 (2011).

[150] T. Taen, Y. Tsuchiya, Y. Nakajima, and T. Tamegai, "Superconductivity at $T_c \sim 14$ K in single-crystalline $FeTe_{0.61}Se_{0.39}$," Physical Review B **80**, 092502 (2009).

[151] L. Fang, Y. Jia, V. Mishra, C. Chaparro, V. K. Vlasko-Vlasov, A. E. Koshelev, U. Welp, G. W. Crabtree, S. Zhu, N. D. Zhigadlo, S. Katrych, J. Karpinski, and W. K. Kwok, "Huge critical current density and tailored superconducting anisotropy in $SmFeAsO_{0.85}F_{0.15}$ by low-density columnar-defect incorporation," Nature Communications **4**, 2655 (2013).

[152] Y. B. Kim, C. F. Hempstead, and A. R. Strnad, "Flux creep in hard superconductors," Physical Review **131**, 2486 (1963).

[153] S. J. Singh, S. J. Cassidy, M. Bristow, S. J. Blundell, S. J. Clarke, and A. I. Coldea, "Optimization of superconducting properties of the stoichiometric $CaKFe_4As_4$," Superconductor Science and Technology **33**, 025003 (2019).

[154] M. Eisterer, "Magnetic properties and critical currents of MgB_2," Superconductor Science and Technology **20** (2007), 10.1088/0953-2048/20/12/R01.

[155] J. Moore and G. K. Perkins, "Critical fields and critical currents in MgB_2," Superconductor Science and Technology **16**, 176 (2003).

[156] C. Buzea and T. Yamashita, "Review of the superconducting properties of MgB_2," Superconductor Science and Technology **14**, R115 (2001).

[157] R. W. Heussner, J. D. Marquardt, P. J. Lee, and D. C. Larbalestier, "Increased critical current density in Nb-Ti wires having Nb artificial pinning centers," Applied Physics Letters **70**, 901 (1997).

[158] C. S. Yadav and P. L. Paulose, "The flux pinning force and vortex phase diagram of single crystal $FeTe_{0.60}Se_{0.40}$," Solid State Communications **151**, 216 (2011).

[159] L. Klein, E. R. Yacoby, Y. Yeshurun, A. Erb, G. Müller-Vogt, V. Breit, and H. Wühl, "Peak effect and scaling of irreversible properties in untwinned Y-Ba-Cu-O crystals," Physical Review B **49**, 4403–4406 (1994).

[160] H. Wen and Z. X. Zhao, "Fishtail effect and small size normal core pinning in melt-textured-growth YBa_2Cu_3O bulks," Applied Physics Letters **68**, 856 (1996).

[161] S. Ishida, D. Song, H. Ogino, A. Iyo, H. Eisaki, M. Nakajima, J.-i. Shimoyama, and M. Eisterer, "Doping-dependent critical current properties in K, Co, and P-doped $BaFe_2As_2$ single crystals," Physical Review B **95**, 014517 (2017).

[162] R. Prozorov, N. Ni, M. A. Tanatar, V. G. Kogan, R. T. Gordon, C. Martin, E. C. Blomberg, P. Prommapan, J. Q. Yan, S. L. Bud'ko, and P. C. Canfield, "Vortex phase diagram of $Ba(Fe_{0.93}Co_{0.07})_2As_2$ single crystals," Physical Review B **78**, 224506 (2008).

[163] S. Salem-Sugui, L. Ghivelder, A. D. Alvarenga, L. F. Cohen, K. A. Yates, K. Morrison, J. L. Pimentel, H. Luo, Z. Wang, and H.-H. Wen, "Flux dynamics associated with the second magnetization peak in the iron pnictide $Ba_{1-x}K_xFe_2As_2$," Physical Review B **82**, 054513 (2010).

[164] P. Das, A. D. Thakur, A. K. Yadav, C. V. Tomy, M. R. Lees, G. Balakrishnan, S. Ramakrishnan, and A. K. Grover, "Magnetization hysteresis and time decay measurements in $FeSe_{0.50}Te_{0.50}$: Evidence for fluctuation in mean free path induced pinning," Physical Review B **84**, 214526 (2011).

[165] A. Fente, W. R. Meier, T. Kong, V. G. Kogan, S. L. Bud'ko, P. C. Canfield, I. Guillamón, and H. Suderow, "Influence of multiband sign-changing superconductivity on vortex cores and vortex pinning in stoichiometric high-T_{c} $\mathrm{CaKFe_4As_4}$," Physical Review B **97**, 134501 (2018).

[166] R. Griessen, W. Hai-hu, A. J. J. van Dalen, B. Dam, J. Rector, H. G. Schnack, S. Libbrecht, E. Osquiguil, and Y. Bruynseraede, "Evidence for mean free path fluctuation induced pinning in $\mathrm{YBa_2Cu_3O_7}$ and $\mathrm{YBa_2Cu_4O_8}$ films," Physical Review Letters **72**, 1910–1913 (1994).

[167] C. Putzke, P. Walmsley, J. D. Fletcher, L. Malone, D. Vignolles, C. Proust, S. Badoux, P. See, H. E. Beere, D. Ritchie, S. Kasahara, Y. Mizukami, T. Shibauchi, Y. Matsuda, and A. Carrington, "Anomalous critical fields in quantum critical superconductors," Nature Communications **5**, 5679 (2014).

[168] S. L. Bud'ko, T. Kong, W. R. Meier, X. Ma, and P. C. Canfield, " ^{57}Fe Mössbauer study of stoichiometric iron-based superconductor $\mathrm{CaKFe_4As_4}$: a comparison to $\mathrm{KFe_2As_2}$ and $\mathrm{CaFe_2As_2}$," Philosophical Magazine **97**, 2689–2703 (2017).

[169] S. L. Bud'ko, V. G. Kogan, R. Prozorov, W. R. Meier, M. Xu, and P. C. Canfield, "Coexistence of superconductivity and magnetism in $\mathrm{CaK(Fe_{1-x}Ni_x)_4As_4}$ as probed by $^{57}\mathrm{Fe}$ Mössbauer spectroscopy," Physical Review B **98**, 144520 (2018).

[170] W.-L. Zhang, W. R. Meier, T. Kong, P. C. Canfield, and G. Blumberg, "High-T_c superconductivity in $\mathrm{CaKFe_4As_4}$ in absence of nematic fluctuations," Physical Review B **98**, 140501 (2018).

[171] Q.-P. Ding, W. R. Meier, A. E. Böhmer, S. L. Bud'ko, P. C. Canfield, and Y. Furukawa, "NMR study of the new magnetic superconductor $\mathrm{CaK(Fe_{0.951}Ni_{0.049})_4As_4}$: Microscopic coexistence of the hedgehog spin-vortex crystal and superconductivity," Physical Review B **96**, 220510 (2017).

[172] Q.-P. Ding, W. R. Meier, J. Cui, M. Xu, A. E. Böhmer, S. L. Bud'ko, P. C. Canfield, and Y. Furukawa, "Hedgehog Spin-Vortex Crystal Antiferromagnetic Quantum Criticality in $\mathrm{CaK(Fe_{1-x}Ni_x)_4As_4}$ Revealed by NMR," Physical Review Letters **121**, 137204 (2018).

[173] N. Haberkorn, M. Xu, W. R. Meier, J. Schmidt, S. L. Bud'ko, and P. C. Canfield, "Effect of Ni doping on vortex pinning in $\mathrm{CaK(Fe_{1-x}Ni_x)_4As_4}$ single crystals," Physical Review B **100**, 064524 (2019).

[174] S. Ishida, A. Iyo, H. Ogino, H. Eisaki, N. Takeshita, K. Kawashima, K. Yanagisawa, Y. Kobayashi, K. Kimoto, H. Abe, M. Imai, J.-i. Shimoyama, and M. Eisterer, "Unique defect structure and advantageous vortex pinning properties in superconducting $CaKFe_4As_4$," Nature Physics Journals Quantum Materials **4**, 27 (2019).

[175] A. Serafin, A. I. Coldea, A. Y. Ganin, M. J. Rosseinsky, K. Prassides, D. Vignolles, and A. Carrington, "Anisotropic fluctuations and quasiparticle excitations in $FeSe_{0.5}Te_{0.5}$," Physical Review B **82**, 104514 (2010).

[176] D. Braithwaite, G. Lapertot, W. Knafo, and I. Sheikin, "Evidence for Anisotropic Vortex Dynamics and Pauli Limitation in the Upper Critical Field of $FeSe_{1-x}Te_x$," Journal of the Physical Society of Japan **79**, 053703 (2010).

[177] H. Q. Yuan, J. Singleton, F. F. Balakirev, S. A. Baily, G. F. Chen, J. L. Luo, and N. L. Wang, "Nearly isotropic superconductivity in (Ba,K)Fe_2As_2," Nature **457**, 565 (2009).

[178] K. Hashimoto, A. Serafin, S. Tonegawa, R. Katsumata, R. Okazaki, T. Saito, H. Fukazawa, Y. Kohori, K. Kihou, C. H. Lee, A. Iyo, H. Eisaki, H. Ikeda, Y. Matsuda, A. Carrington, and T. Shibauchi, "Evidence for superconducting gap nodes in the zone-centered hole bands of KFe_2As_2 from magnetic penetration-depth measurements," Physical Review B **82**, 014526 (2010).

[179] E. Helfand and N. R. Werthamer, "Temperature and purity dependence of the superconducting critical field, H_{c2}. II," Physical Review **147**, 288–294 (1966).

[180] S. Khim, J. W. Kim, E. S. Choi, Y. Bang, M. Nohara, H. Takagi, and K. H. Kim, "Evidence for dominant Pauli paramagnetic effect in the upper critical field of single-crystalline $FeTe_{0.6}Se_{0.4}$," Phys. Rev. B **81**, 184511 (2010).

[181] A. A. Gurevich, "Iron-based superconductors at high magnetic fields," Rep. Prog. Phys. **74**, 124501 (2011).

[182] B. Maiorov, P. Mele, S. A. Baily, M. Weigand, S. Z. Lin, F. F. Balakirev, K. Matsumoto, H. Nagayoshi, S. Fujita, Y. Yoshida, Y. Ichino, T. Kiss, A. Ichinose, M. Mukaida, and L. Civale, "Inversion of the upper critical field anisotropy in FeTeS films," Superconductor Science and Technology **27**, 044005 (2014).

[183] G. Fuchs, S. L. Drechsler, N. Kozlova, M. Bartkowiak, J. E. Hamann-Borrero, G. Behr, K. Nenkov, H. H. Klauss, H. Maeter, A. Amato, H. Luetkens, A. Kwadrin,

R. Khasanov, J. Freudenberger, A. Köhler, M. Knupfer, E. Arushanov, H. Rosner, B. Büchner, and L. Schultz, "Orbital and spin effects for the upper critical field in As-deficient disordered Fe pnictide superconductors," New Journal of Physics **11**, 075007 (2009).

[184] H. Kontani and S. Onari, "Orbital-Fluctuation-Mediated Superconductivity in Iron Pnictides: Analysis of the Five-Orbital Hubbard-Holstein Model," Physical Review Letters **104**, 157001 (2010).

[185] D. V. Efremov, M. M. Korshunov, O. V. Dolgov, A. A. Golubov, and P. J. Hirschfeld, "Disorder-induced transition between $s_{\pm}$ and s_{++} states in two-band superconductors," Physical Review B **84**, 180512 (2011).

[186] A. A. Golubov, J. Kortus, O. V. Dolgov, O. Jepsen, Y. Kong, O. K. Andersen, B. J. Gibson, K. Ahn, and R. K. Kremer, "Specific heat of MgB_2 in a one- and a two-band model from first-principles calculations," Journal of Physics Condensed Matter **14**, 1353–1360 (2002).

[187] T. Saito, Y. Yamakawa, S. Onari, and H. Kontani, "Revisiting orbital-fluctuation-mediated superconductivity in LiFeAs: Nontrivial spin-orbit interaction effects on the band structure and superconducting gap function," Physical Review B **92**, 134522 (2015).

[188] M. Shahbazi, X. L. Wang, Z. W. Lin, J. G. Zhu, S. X. Dou, and K. Y. Choi, "Magnetoresistance, critical current density, and magnetic flux pinning mechanism in nickel doped $BaFe_2As_2$ single crystals," Journal of Applied Physics **109**, 07E151 (2011).

[189] R. Modler, P. Gegenwart, M. Lang, M. Deppe, M. Weiden, T. Lühmann, C. Geibel, F. Steglich, C. Paulsen, J. L. Tholence, N. Sato, T. Komatsubara, Y. Ōnuki, M. Tachiki, and S. Takahashi, "First-Order Transition between Weak and Strong Pinning in Clean Superconductors with Enhanced Spin Susceptibility," Physical Review Letters **76**, 1292–1295 (1996).

[190] A. Sawada, A. Ishiguro, Y. Inada, M. Suzuki, N. Sato, and T. Komatsubara, "Anomalous flux pinning of UPd_2Al_3," Journal of Low Temperature Physics **101**, 645–650 (1995).

[191] B. J. Ramshaw, S. E. Sebastian, R. D. McDonald, J. Day, B. S. Tan, Z. Zhu, J. B. Betts, R. Liang, D. A. Bonn, W. N. Hardy, and N. Harrison, "Quasiparticle mass

enhancement approaching optimal doping in a high-tc superconductor," Science **348**, 317–320 (2015).

[192] G. S. Boebinger, Y. Ando, A. Passner, T. Kimura, M. Okuya, J. Shimoyama, K. Kishio, K. Tamasaku, N. Ichikawa, and S. Uchida, "Insulator-to-Metal Crossover in the Normal State of $\mathrm{La}_{2-x}\mathrm{Sr}_x\mathrm{CuO}_4$ Near Optimum Doping," Physical Review Letters **77**, 5417–5420 (1996).

[193] T. A. Maier and D. J. Scalapino, "Pairing interaction near a nematic quantum critical point of a three-band CuO_2 model," Physical Review B **90**, 174510 (2014).

[194] S. Lederer, Y. Schattner, E. Berg, and S. A. Kivelson, "Enhancement of Superconductivity near a Nematic Quantum Critical Point," Physical Review Letters **114**, 097001 (2015).

[195] M. A. Metlitski, D. F. Mross, S. Sachdev, and T. Senthil, "Cooper pairing in non-Fermi liquids," Physical Review B **91**, 115111 (2015).

[196] I. M. Hayes, R. D. McDonald, N. P. Breznay, T. Helm, P. J. W. Moll, M. Wartenbe, A. Shekhter, and J. G. Analytis, "Scaling between magnetic field and temperature in the high-temperature superconductor $BaFe_2(As_{1-x}P_x)_2$," Nature Physics **12**, 916–919 (2016).

[197] P. Giraldo-Gallo, J. A. Galvis, Z. Stegen, K. A. Modic, F. F. Balakirev, J. B. Betts, X. Lian, C. Moir, S. C. Riggs, J. Wu, A. T. Bollinger, X. He, I. Božović, B. J. Ramshaw, R. D. McDonald, G. S. Boebinger, and A. Shekhter, "Scale-invariant magnetoresistance in a cuprate superconductor," Science **361**, 479–481 (2018).

[198] V. Grinenko, R. Sarkar, P. Materne, S. Kamusella, A. Yamamshita, Y. Takano, Y. Sun, T. Tamegai, D. V. Efremov, S.-L. Drechsler, J.-C. Orain, T. Goko, R. Scheuermann, H. Luetkens, and H.-H. Klauss, "Low-temperature breakdown of antiferromagnetic quantum critical behavior in FeSe," Physical Review B **97**, 201102 (2018).

[199] S. Hosoi, K. Matsuura, K. Ishida, H. Wang, Y. Mizukami, T. Watashige, S. Kasahara, Y. Matsuda, and T. Shibauchi, "Nematic quantum critical point without magnetism in $FeSe_{1-x}S_x$ superconductors," Proceedings of the National Academy of Sciences (PNAS) **113**, 8139 (2016).

[200] A. E. Böhmer, F. Hardy, F. Eilers, D. Ernst, P. Adelmann, P. Schweiss, T. Wolf, and C. Meingast, "Lack of coupling between superconductivity and orthorhombic distortion in stoichiometric single-crystalline FeSe," Physical Review B **87**, 180505 (2013).

[201] S. Licciardello, J. Buhot, J. Lu, J. Ayres, S. Kasahara, Y. Matsuda, T. Shibauchi, and N. E. Hussey, "Electrical resistivity across a nematic quantum critical point," Nature **567**, 213–217 (2019).

[202] S. Licciardello, N. Maksimovic, J. Ayres, J. Buhot, M. Čulo, B. Bryant, S. Kasahara, Y. Matsuda, T. Shibauchi, V. Nagarajan, J. G. Analytis, and N. E. Hussey, "Coexistence of orbital and quantum critical magnetoresistance in $\mathrm{FeSe}_{1-x}\mathrm{S}_x$," Physical Review Research **1**, 023011 (2019).

[203] Y. Sun, S. Pyon, and T. Tamegai, "Electron carriers with possible Dirac-cone-like dispersion in $\mathrm{FeSe}_{1-x}\mathrm{S}_x$ (x=0 and 0.14) single crystals triggered by structural transition," Physical Review B **93**, 104502 (2016).

[204] L. Fanfarillo, E. Cappelluti, C. Castellani, and L. Benfatto, "Unconventional Hall Effect in Pnictides from Interband Interactions," Physical Review Letters **109**, 096402 (2012).

[205] X. Du, S.-W. Tsai, D. L. Maslov, and A. F. Hebard, "Metal-Insulator-Like Behavior in Semimetallic Bismuth and Graphite," Physical Review Letters **94**, 166601 (2005).

[206] A. Narayanan, M. D. Watson, S. F. Blake, N. Bruyant, L. Drigo, Y. L. Chen, D. Prabhakaran, B. Yan, C. Felser, T. Kong, P. C. Canfield, and A. I. Coldea, "Linear Magnetoresistance Caused by Mobility Fluctuations in n-Doped $\mathrm{Cd}_3\mathrm{As}_2$," Physical Review Letters **114**, 117201 (2015).

[207] J. Singleton, "A simple transport model for the temperature-dependent linear magnetoresistance of high-temperature superconductors," arXiv:1810.01998v1 (2018).

[208] I. Paul and M. Garst, "Lattice Effects on Nematic Quantum Criticality in Metals," Physical Review Letters **118**, 227601 (2017).

[209] X. Wang and E. Berg, "Scattering mechanisms and electrical transport near an Ising nematic quantum critical point," Physical Review B **99**, 235136 (2019).

[210] L. Dell'Anna and W. Metzner, "Electrical resistivity near pomeranchuk instability in two dimensions," Physical Review Letters **98**, 136402 (2007).

[211] D. L. Maslov, V. I. Yudson, and A. V. Chubukov, "Resistivity of a Non-Galilean–Invariant Fermi Liquid near Pomeranchuk Quantum Criticality," Physical Review Letters **106**, 106403 (2011).

[212] S. Kasahara, T. Shibauchi, K. Hashimoto, K. Ikada, S. Tonegawa, R. Okazaki, H. Shishido, H. Ikeda, H. Takeya, K. Hirata, T. Terashima, and Y. Matsuda, "Evolution from non-Fermi- to Fermi-liquid transport via isovalent doping in $BaFe_2(As_{1-x}P_x)_2$ superconductors," Physical Review B **81**, 184519 (2010).

[213] T. Urata, Y. Tanabe, K. K. Huynh, H. Oguro, K. Watanabe, and K. Tanigaki, "Non-Fermi liquid behavior of electrical resistivity close to the nematic critical point in $Fe_{1-x}Co_xSe$ and $FeSe_{1-y}S_y$," arXiv.1608.01044 (2016).

[214] R. X. Cao, J. Dong, Q. L. Wang, X. S. Ye, J. B. Zhang, Y. F. Xu, D. A. Chareev, A. N. Vasiliev, B. Wu, G. Wu, and X. H. Zeng, "Observation of orbital ordering and origin of nematic order in FeSe," arxiv.1810.09639 (2018).

[215] T. Moriya, *Spin fluctuations in itinerant electron magnetism*, Springer series in solid-state sciences (Springer-Verlag, 1985).

[216] P. O. Sprau, A. Kostin, A. Kreisel, A. E. Böhmer, V. Taufour, P. C. Canfield, S. Mukherjee, P. J. Hirschfeld, B. M. Andersen, and J. C. Davis, "Discovery of orbital-selective Cooper pairing in FeSe," Science **357**, 75–80 (2017).

[217] A. Audouard, F. Duc, L. Drigo, P. Toulemonde, S. Karlsson, P. Strobel, and A. Sulpice, "Quantum oscillations and upper critical magnetic field of the iron-based superconductor FeSe," Europhysics Letters **109**, 27003 (2015).

[218] S. I. Vedeneev, B. A. Piot, D. K. Maude, and A. V. Sadakov, "Temperature dependence of the upper critical field of FeSe single crystals," Phys. Rev. B **87**, 134512 (2013).

[219] M. Bristow, P. Reiss, A. A. Haghighirad, Z. Zajicek, S. J. Singh, T. Wolf, D. Graf, W. Knafo, A. McCollam, and A. I. Coldea, "Anomalous high-magnetic field electronic state of the nematic superconductors $FeSe_{1-x}S_x$," Physical Review Research **2**, 013309 (2020).

[220] M. Abdel-Hafiez, Y.-Y. Zhang, Z.-Y. Cao, C.-G. Duan, G. Karapetrov, V. M. Pudalov, V. A. Vlasenko, A. V. Sadakov, D. A. Knyazev, T. A. Romanova, D. A. Chareev, O. S. Volkova, A. N. Vasiliev, and X.-J. Chen, "Superconducting properties of sulfur-doped iron selenide," Physical Review B **91**, 165109 (2015).

[221] S. Kasahara, Y. Sato, S. Licciardello, M. Čulo, S. Arsenijević, T. Ottenbros, T. Tominaga, J. Böker, I. Eremin, T. Shibauchi, J. Wosnitza, N. E. Hussey, and Y. Matsuda, "Evidence for an FFLO state with segmented vortices in the BCS-BEC-crossover superconductor FeSe," arxiv:1911.08237v1 , 1–6 (2019).

[222] X. Yang, Z. Du, G. Du, Q. Gu, H. Lin, D. Fang, H. Yang, X. Zhu, and H.-H. Wen, "Strong-coupling superconductivity revealed by scanning tunneling microscope in tetragonal FeS," Physical Review B **94**, 024521 (2016).

[223] X. Shi, Z.-Q. Han, X.-L. Peng, P. Richard, T. Qian, X.-X. Wu, M.-W. Qiu, S. C. Wang, J. P. Hu, Y.-J. Sun, and H. Ding, "Enhanced superconductivity accompanying a Lifshitz transition in electron-doped FeSe monolayer," Nature Comm. **8**, 14988 (2017).

[224] V. J. Emery and S. A. Kivelson, "Importance of phase fluctuations in superconductors with small superfluid density," Nature **374**, 434–437 (1995).

[225] Y. Wang and J. Zhang, "Revisiting the electronic phase diagram of $YBa_2Cu_3O_y$ via temperature derivative of in-plane resistivity," arXiv:1711.07402v1 (2017).

[226] J. Corson, R. Mallozzi, J. Orenstein, J. N. Eckstein, and I. Bozovic, "Vanishing of phase coherence in underdoped $Bi_2Sr_2CaCu_2O_{8+\delta}$," Nature **398**, 221–223 (1999).

[227] L. Li, Y. Wang, S. Komiya, S. Ono, Y. Ando, G. D. Gu, and N. P. Ong, "Diamagnetism and Cooper pairing above T_c in cuprates," Physical Review B **81**, 054510 (2010).

[228] M. Randeria and E. Taylor, "Crossover from Bardeen-Cooper-Schrieffer to Bose-Einstein Condensation and the Unitary Fermi Gas," Annual Review of Condensed Matter Physics **5**, 209–232 (2014).

[229] F. Rullier-Albenque, D. Colson, A. Forget, and H. Alloul, "Multiorbital effects on the transport and the superconducting fluctuations in LiFeAs," Physical Review Letters **109**, 187005 (2012).

[230] T. Hanaguri, S. Kasahara, J. Böker, I. Eremin, T. Shibauchi, and Y. Matsuda, "Quantum Vortex Core and Missing Pseudogap in the Multiband BCS-BEC Crossover Superconductor FeSe," Physical Review Letters **122**, 077001 (2019).

[231] H. Takahashi, F. Nabeshima, R. Ogawa, E. Ohmichi, H. Ohta, and A. Maeda, "Superconducting fluctuations in FeSe investigated by precise torque magnetometry," Physical Review B **99**, 060503 (2019).

[232] P. M. C. Rourke, A. F. Bangura, C. Proust, J. Levallois, N. Doiron-Leyraud, D. LeBoeuf, L. Taillefer, S. Adachi, M. L. Sutherland, and N. E. Hussey, "Fermi-surface reconstruction and two-carrier model for the Hall effect in $YBa_2Cu_4O_8$," Physical Review B **82**, 020514 (2010).

[233] L. Aslamazov and A. Larkin, "The influence of fluctuations on the properties of a superconductor at temperatures higher than critical," Fiz. Tverd. Tela [Sov. Phys. Solid State 10, 875 (1968)] **10**, 87 (1968).

[234] F. K. K. Kirschner, F. Lang, C. V. Topping, P. J. Baker, F. L. Pratt, S. E. Wright, D. N. Woodruff, S. J. Clarke, and S. J. Blundell, "Robustness of superconductivity to competing magnetic phases in tetragonal FeS," Physical Review B **94**, 134509 (2016).

[235] H. Yang, G. Chen, X. Zhu, J. Xing, and H.-H. Wen, "BCS-like critical fluctuations with limited overlap of Cooper pairs in FeSe," Physical Review B **96**, 064501 (2017).

[236] Y. J. Song, B. Kang, J.-S. Rhee, and Y. S. Kwon, "Thermally activated flux flow and fluctuation conductivity in LiFeAs single crystal," Europhysics Letters **97**, 47003 (2012).

[237] R. I. Rey, A. Ramos-Álvarez, C. Carballeira, J. Mosqueira, F. Vidal, S. Salem-Sugui, A. D. Alvarenga, R. Zhang, and H. Luo, "Measurements of the superconducting fluctuations in optimally doped $BaFe_{2-x}Ni_xAs_2$ under high magnetic fields: Probing the 3D-anisotropic Ginzburg-Landau approach," Superconductor Science and Technology **27**, 075001 (2014).

[238] S. H. Kim, C. H. Choi, M. H. Jung, J. B. Yoon, Y. H. Jo, X. F. Wang, X. H. Chen, X. L. Wang, S. I. Lee, and K. Y. Choi, "Fluctuation conductivity of single-crystalline $BaFe_{1.8}Co_{0.2}As_2$ in the critical region," Journal of Applied Physics **108**, 063916 (2010).

[239] X. Shi, P. V. Lin, T. Sasagawa, V. Dobrosavljević, and D. Popović, "Two-stage magnetic-field-tuned superconductor-insulator transition in underdoped $La_{2-x}Sr_xCuO_4$," Nature Physics **10**, 437–443 (2014).